VITA

Umamaheshwaran Rajasekar

EDUCATION

2011	Ph.D., Geography with specialization in environmental geography and geospatial modeling. Department of Earth and Environmental Systems, Indiana State University, USA.
2005	MSc in geoinformatics from ITC, The Netherlands. September 2003 - May 2005
2002	B.E in civil engineering from School of Building Science and Technology, India. June 1997 - August 2002

EXPERIENCE

Oct 2009 to Present	Senior Consultant, The Action Reseacrch Unit, India
Dec 2010 to Present	Visiting Faculty, School of Planning, Center for Environmental Planning and Technology, India
Jul 2007 to Aug 2009	Director of Communication, Center for Urban and Environmental Change, Indiana State University, USA
Aug 2008 to May 2009	Instructor, Department of Geography, Geology and Anthropology. Indiana State University, USA
May 2005 to Apr 2006	GIS Engineer, Risk Management Solutions, India
Jun 2002 to Aug 2003	Researcher, School of Planning, Center for Environmental Planning and Technology, India

PUBLICATIONS & PRESENTATIONS

- Rajasekar, U. and Weng, Q. (2009). 'Urban Heat Island Monitoring and Analysis by Data Mining of MODIS Imageries'. *ISPRS Journal of Remote Sensing*, 64(1): 86-96.
- Rajasekar, U. and Weng, Q. (2009). 'Spatio-Temporal Modeling and Analysis of Urban Heat Islands by Using Landsat TM and ETM+ Imagery'. *International Journal of Remote Sensing*, 30(13): 3531-3548.
- Rajasekar, U. and Weng, Q. (2009). 'Application of association rule mining for exploring the relationship between urban land surface temperature and biophysical/social parameters'. *PE & RS*, 75(4): 385-396.
- Rajasekar, U., Bijker, W. and Stein, A. (2007). 'Image Mining for Modeling of Forest Fires From Meteosat Images'. *IEEE Transactions on Geoscience and Remote Sensing*. 45(1): 246–253.

ANALYSIS OF URBAN HEAT ISLANDS BY USING MULTI-SENSOR AND MULTI-TEMPORAL REMOTE SENSING IMAGES

A dissertation

Presented to

The College of Graduate and Professional Studies

Department of Earth and Environmental Systems

Indiana State University

Terre Haute, Indiana

In Partial Fulfillment

of the Requirements for the Degree

Doctor of Philosophy

---

by

Umamaheshwaran Rajasekar

August 2011

Keywords: Urban, heat island, environment, data mining, spatial thinking

COMMITTEE MEMBERS

Committee chair: Qihao Weng, Ph. D.

Professor of Geography

Indiana State University

Committee member: Paul Mausel, Ph. D.

Professor Emeritus of Geography

Indiana State University

Committee member: Geoffrey Exoo, Ph. D.

Professor of Mathematics and Computer Science

Indiana State University

Committee member: Susan Berta, Ph. D.

Associate Professor of Geography

Indiana State University

Committee member: Stephen Aldrich, Ph. D.

Assistant Professor of Geography

Indiana State University

ABSTRACT

This doctoral dissertation research has developed models to facilitate in characterization, analysis and monitoring of urban heat islands (UHI). Over the past few years there has been evidence of mass migration of the population towards urban areas which has led to the increase in the number of mega cities (cities with more than 10 million in population) around the world. According to the UN in 2007 around 60% (from 40% in 2000) of world populations was living in urban areas. This increase in population density in and around cities has lead to several problems related to environment such as air quality, water quality, development of Urban Heat Islands (UHI), etc. The purpose of this doctoral dissertation research was to develop a synergetic merger of remote sensing with advancements in data mining techniques to address modeling and monitoring of UHI in space and in time.

The effect of urban heat islands in space and over time was analyzed within this research using exploratory and quantitative models. Visualization techniques including animation were experimented with developing a mechanism to view and understand the UHI over a city. Association rule mining models were implemented to analyze the relationship between remote sensing images and geographic information system (GIS) data. This model was implemented using three different remote sensing images i.e., Advanced Space borne Thermal Emission and Reflection Radiometer (ASTER), Landsat and Moderate Resolution Imaging Spectroradiometer (MODIS). The effect of the spatial resolution on the model and the phenomenon were analyzed in detail to determine variables which strongly associate with land use land cover (LULC) in space and in time.

A non-parametric process convolution model was developed and was used to characterize UHI from MODIS time series images. The resulting characterized images were used to study the relationship between LULC and UHI. The behavior of UHI including its movement and magnitude was analyzed in space and time.

The intellectual merits of these methods are two-fold; first, they will be a forerunner in the development and implementation of association rule mining algorithm within remote sensing image analysis framework. Second, since most of the existing UHI models are parametric in nature; the non-parametric approach is expected to overcome the existing problems within characterization and analysis. Parametric models pose problems (in terms of efficiency, since the implementation of such models are time consuming and need human intervention) while analyzing UHI effect from multiple imageries. These proposed models are expected to aid in effective spatial characterization and facilitate in temporal analysis and monitoring of UHI phenomenon.

ACKNOWLEDGMENTS

I would like to thank Dr. Weng who has helped me in both organizing my personal life and my academic life from the day one. It has been a pleasure working with him.

I would also like to thank my family, especially my mom, dad, who have been supportive during the three years of my study in USA and my wife who has been supportive in the completion of my dissertation. Without their love none of this would have been possible.

I would like to take this opportunity to thank Ajay, Andy, Brian, Heidi, Ryan, Todd, Vijay and Xufei who made sure that my stay in USA was interesting and memorable. The discussions ranging from rationale for my thesis to rationale for life did really help me look at things more critically. Thank you guys.

TABLE OF CONTENTS

LIST OF TABLES

LIST OF FIGURES

ABBREVIATIONS

ASTER	Advanced Space borne Thermal Emission and Reflection Radiometer
ATLAS	Advanced Thermal and Land Applications Sensor
AVHRR	Advanced Very High Resolution Radiometer
BLUHI	Boundary Layer Urban Heat Island
BUBBLE	Urban Boundary Layer Experiment
CLUHI	Canopy Layer Urban Heat Island
DN	Digital Number
EDA	Exploratory Data Analysis
EMR	Electromagnetic Radiation
ENSO	El Nino/ Southern Oscillation
EPA	Environmental Protection Agency
ETM	Enhanced Thematic Mapper
FOV	Field of View
GI	Geo-Information
GIS	Geographical Information Science
IR	Infrared
KDD	Knowledge Discovery in Databases
LC	Land Cover
LST	Land Surface Temperature
LULC	Land Use Land Cover
MAD	Multivariate Alteration Detection
MODIS	Moderate Resolution Imaging Spectroradiometer
NASA	National Aeronautics and Space Administration
NDVI	Normalized Difference Vegetation Index
NOAA	National Oceanic and Atmospheric Administration

RASS	Radio Acoustic Sounding System
RSL	Roughness Sub-Layer
SNDVI	Scaled Normalized Difference Vegetation Index
SODAR	Sound Detection and Ranging
SSUHI	Skin Surface Urban Heat Island
TB	Terra Bytes
TIC	Temporally Invariant Features
TIF	Time-Invariant Features
TIR	Thermal Infrared
TM	Thematic Mapper
UBL	Urban Boundary Layer
UCL	Urban Canopy Layer
UHI	Urban Heat Island
UN	United Nations
UNEP	United Nations Environment Program
USGS	United States Geological Survey
VNIR	Very Near Infrared
WHO	World Health Organization

CHAPTER 1

INTRODUCTION

This research demonstrates models to facilitate in characterization, analysis and monitoring of urban heat islands (UHI). Over the past few years there has been evidence of mass migration of the population towards urban areas which has led to an increase in the number of mega cities (cities with more than 10 million in population) around the world. According to the UN in 2007 around 60% (from 40% in 2000) of world populations are living in urban areas. This increase in population density in and around cities has lead to several problems related to environment such as air quality, water quality, development of UHI, etc. The purpose of this doctoral dissertation research was to develop a synergetic merger of remote sensing with the advancements in data mining techniques to address modeling and monitoring of UHI in space and in time.

The central research question of this dissertation was to model UHI effectively and to use these models to perform spatio-temporal analysis. The impetus of this research was the rapid change in the LULC due to mass migration of people to the urban setting. This has also led to concern among earth scientists of the impact of this change on the environment.

The increase in urban population has led to rapid changes in the land use and land cover within cities during recent years. In the United States of America (USA), the current urban growth rate, based on 1990 and 2000 census figures, is approximately 12.5%, with 80% of population residing within urban areas. As cities continue to grow, to satisfy

various social and economic needs, urban sprawl creates unique problems related to land use, transportation, agriculture, housing, pollution and development for policy makers. Apart from such problems, it is also often observed that air temperatures in densely built urban areas are higher than the temperatures of the surrounding rural country. Among the urban-rural differences, the most notable and well documented is the increase in temperature in urban areas. This phenomenon is known as 'urban heat island' (UHI) effect.

The study of UHI has a lot of importance. UHI effect not only determines the relative difference in temperature but also acts as one of the major factors influencing other phenomena. Earlier research applications have demonstrated that UHI has impact on natural ventilation and urban meteorology. Studies have also shown that UHI has a strong influence on weather leading to anomalies in rainfall patterns and lightning. UHI has negative impacts on aerosols, energy consumption, human health and biodiversity. Apart from these impacts, UHI also plays a major role in the increase in pollution and decrease in environmental conditions. Furthermore, there also exist links between land use land cover (LULC) and temperature. Therefore, it becomes important for urban and environmental researchers to understand, model, quantify and monitor the UHI effect.

1.1 Problem Statement

Within the last four decades, great progress has been made with the advent of space programs associated with Earth observations. Several terra bytes (TB) of Earth science data are being collected from various sensor platforms. Some of the data collected suggests that skin temperatures (also known as surface temperature or land surface temperature) for large areas can be mapped and studied more effectively by using satellite remote sensing data in the infrared region as compared to ground based sensors. Even with satellite measurement it is still difficult to generalize the magnitude, location, and spatial distribution of the UHI for several reasons. These reasons are mainly attributed to the

shape, extent and layout of the city, besides the type and material of surrounding areas, and resolution of imagery used to characterize the phenomenon. These factors not only affect the spatial extent of the UHI but they also affect its magnitude.

Over the years, statisticians have developed several methods of generalization to overcome the issue of characterizing surfaces in a spatial domain. While various approaches of kriging and thin plate spline models have been used successfully for spatial process estimation, they have the weakness of being global models, in which the variability of the estimated process is the same throughout the domain. This failure to adapt to variability of the unknown process is of particular importance in environmental, geophysical, and other spatial datasets. Lastly, a single parametric model can be defined for the analysis of a single image, but, it becomes difficult to apply the same over multi-temporal and multi-sensor images in order to conduct a successful comparative analysis. This aspect gets further complicated due to the changing nature of the land cover and land use and also the uncertainty involved in the boundary between urban and rural areas.

Another major problem is the use of appropriate statistical analysis for quantifying the relation between urban temperatures to other associated factors. The interactions between the LULC and normalized differential vegetation index (NDVI) with UHIs have been studied and quantified previously using linear statistical models and multivariate analysis. These techniques are well established and are effective in analyzing quantitative relationships between limited qualitative variables and general trends. However, these techniques cannot be used to identify and quantify micro-level deviations within earth science processes.

1.2 Research Objective

The primary objective of this dissertation was to study the effect of urban heat islands in space and over time using both the exploratory and quantitative models. This primary objective was achieved through systematic implementation of the following tasks:

1. Development of a visualization technique to study the characteristics of UHI across a city.

2. Implementation of association rule mining models and analysis of the relationship between remote sensing images and GIS data.

3. Implementation of non-parametric process convolution model to images from MODIS to characterize UHI as a continuous function including both urban and rural surfaces. Analysis of non-parametric model results with respect to LULC. Study and identification of the effect of scale on the modeling and on the phenomenon.

4. Development of a method to automate the above process with minimal user intervention i.e. a model for monitoring MODIS time series data set to study the change in the UHI characteristics over time i.e., daily, weekly, monthly, seasonal and annual.

1.3 Hypotheses

Hypotheses that are addressed within this research are:

1. There will be minimal change in confidence of the association rules and associating variables with relation to change in the type of the remote sensing image used especially between ASTER and MODIS.

2. With an increase in the scale of the remote sensing images there will be a relative decrease in the prediction capability of the association rule mining models.

Modeling for monitoring the phenomenon of UHI over time would have impact on the quantified results especially the characteristic descriptors (center, spread, intensity, etc.,) due to diurnal/seasonal effects, but otherwise the phenomenon of UHI will not have a considerable change in its center and spread with respect to minimum change in the LULC over time. This variation in UHI center should be within a particular land use

zoning, difference in spread should be within a county and change in intensity should be well within the LST uncertainty limits.

1.4 Structure of the Thesis

Chapter 2 provides a brief introduction about the phenomenon of UHI and the current state of modeling within the field of spatial science. This chapter also provides a review of the existing problems in the field of data mining and geo-scientific models with reference to the UHI phenomenon under study. The study area and the data that has been used within this thesis are introduced in Chapter 3. The methods and the models that are used within this research are described in Chapter 4. Chapter 5 discusses the results obtained through exploratory data analysis, association rule mining and macro-analysis of UHI phenomenon using MODIS. This chapter also discusses the effect of varying scales (medium to low resolution images) on the method in general and UHI analysis in specific. This chapter also discusses in detail the effect of a model at varying scale and the behavior of the phenomenon over time. This will include day/ night, monthly, seasonal and between years variation of the phenomenon over the city of Indianapolis and its surrounding eight counties. Chapter 6 summarizes the discussions and conclusions of this research.

CHAPTER 2

BACKGROUND

This chapter explains data mining, UHI modeling and monitoring in detail. Section 2.2 of this chapter describes data mining models. This section also differentiates between spatial and non-spatial data mining and explains the importance of implementing such methods within geo-spatial science. Section 2.3 provides a brief introduction to UHI explaining the nature of this phenomenon. This sub-section explains the need for modeling and monitoring of the phenomenon based on the cause and effect relationships associated with other physical and social variables. Section 2.4 elaborates on various types of UHI modeling within the urban context and an overview on the status of current research within the field of heat island modeling and monitoring along with its problems. Section 2.5 discusses the types of heat island, their causes and effect. Section 2.6 lists data and models that are currently being used for studying UHI.

2.1 Knowledge Discovery within Spatial Datasets

The amount of data that has been collected so far is immense and the number is increasing on a daily basis (Kafatos et al., 1998). "The world produces between 1 and 2 Exabyte of unique information per year, which is roughly 250 megabytes for every man, woman, and child on earth. An exabyte is a billion gigabytes or 1018 bytes" (Lyman et al., 2000). However, not enough is being done to analyze all data or to extract all possible information. In general, people collect data for specific purposes but the collected data has

the opportunity to reveal much more information than its intended use. Unfortunately much of the data available is generally used for a specific purpose and is not explored beyond the intended purpose.

This problem of massive increase in data is evident in the field of remote sensing where there have been various advancements in technology over the past several decades. The quantities of remote sensing images (RSI) that are being collected every day from satellites, aerial sensors, telescopes and other sensor platforms are immense. Majority of data are archived before information can be extracted (Ding et al., 2003). Even though remote sensing images have the ability to reveal much information in comparison to their textual counterpart, it becomes very difficult or in some cases impossible for the human mind to look at every image from massive storage, analyze it and assess its relationship with the previous images of varying time stamps.

In order to overcome the above limitations the process of Knowledge Discovery in Databases (KDD) has been developed and is currently being advanced by scientists and business professionals alike. According to Heckel and Zendulka (2004), "The knowledge discovery process can be defined as a nontrivial process of identifying valid, novel, potentially useful and ultimately understandable patterns in data. Data mining is the key step in the process where intelligent methods are applied in order to discover knowledge in data". Even though the process of KDD is vast as compared to data mining and data mining is only a part of the whole process which deals with processing of the data in a predefined efficient manner to find meaningful information, within this study the term data mining will be used alternatively to KDD. In short, within this study the term data mining means 'the process of extracting previously unknown, valid and actionable information from large databases' (Cabena, 1998) or 'the process of searching and discovering valuable information and knowledge from large volumes of data' (Velickov et al., 2000).

Data mining initially started in late 1980's as the computational capability of the

computers began to increase. Since its inception its major uses have proved to be in the fields of defense, finance, marketing, stock prediction, fraud detection, etc., where the amount of data collected is high and, at the same time, it is humanly impossible to go through it manually and retrieve information. Data mining encompasses principles and techniques from statistics, machine learning, pattern recognition, numeric search and scientific visualization to accommodate the new data types and data volumes being generated (Miller and Han, 2001). According to Groth (1999) "80% of the fortune 500 companies are involved in the process of data mining".

There has been considerable development in the field of data mining on handling market-basket (relational data bases) data sets but there have been limited developments in the area of spatial databases which include image and vector datasets. Since a spatial database is not the same as a non-spatial database, these data types are to be considered as a special case of data mining.

2.2 Geo-spatial Data Mining

Knowledge mining from image and raster datasets can be viewed as a case of spatial data mining. Table 1 illustrates some of the data mining tasks and techniques. According to Koperski et al. (2002) most database research on the analysis of geospatial data has concentrated on data retrieval, and on simple queries that involve spatial joins and spatial selections. Such systems also perform analysis on single images. But when we deal with large collections of remotely sensed images, current systems do not scale well. Therefore, new algorithms and new indexing methods are needed to enable the analysis of the spatial data provided by the sensor systems. According to Openshaw (1999) some of the requirements in the tools for spatial data mining are as follows:

1. Serve basic spatial data exploratory needs,

2. Have the potential to create new insights, ideas, and hypotheses from the analysis,

3. Offer artistic impressions of pattern structure to stimulate the imagination,

4. Spot major unusual localized database patterns and detect empirical location-based irregularities, and

5. Be easy to use and meet basic GIS ability criteria.

Conceptually what is stated above may appear simple, but the implementation of the concepts within the spatial data mining systems are complex due to the inherent complexity of the spatial data sets. Researches are being carried out at institutes, universities and research laboratories to develop more efficient tools and techniques to assist spatial data miners (Takahara et al., 2002).

Table 1

Data mining tasks and techniques (Miller and Han, 2001)

Type	Task	Technique
Segmentation	Clustering: Determining a finite set of implicit classes that describes the data	Cluster analysis, Bayesian classification and Decision or Classification trees
	Classification: mapping data items into pre-defined classes	Artificial neural networks
Dependency analysis	Finding rules to predict the value for some attribute based on the value of the other attribute	Bayesian networks and Association rules
Deviation and outliner analysis	Finding data items that exhibit unusual deviations from expectations	Clustering and other data mining methods, outliner detection
Trend detection	Lines and curves summarizing the database, often over time	Regression and Sequential pattern extraction
Generalization and characterization	Compact descriptions of the data	Summary rules and Attribute-oriented induction

2.3 Problems within Geo-spatial Data Mining

Every spatial scientists' dream is that geospatial analysis tools expand to become a sophisticated spotter of patterns with the ability to suggest highly plausible hypotheses, and with the capability to handle hundreds of different layers that may contain thousands of millions of data points (Estiville-Castro and Lee, 2004). But the use of traditional approaches within geospatial analysis often require significant manual intervention and expertise in the field of statistics and geospatial analysis (Fayyad and Smyth, 1999). These limitations of the conventional statistical methodologies incorporated within the existing spatial analytical systems can lead to a variety of problems for knowledge extraction. Further, spatio-temporal objects and relationships tend to be more complex than the objects and their relationships in non-geographic databases. The diversity and limitation in the techniques to analyze the spatial data contributes to the development of geographic data mining (Openshaw, 1999). Furthermore, Uncertainty has long been recognized as being important in geo-information (GI) science it is, however, still a problematical issue (Foody, 2003).

Many of the current systems which are being developed in the area of geospatial data mining are based on the developments in the market basket analysis. Ding et al. (2002) extracted association rules from remote sensing imagery by considering set ranges of the spectral bands to be items and the pixels to be transactions. Tešić et al. (2003) implemented perceptual association rule to a image data set to prove the fact that presence of a crop A near a Crop B leads to high yield and vice versa. These examples are very similar to that of the market basket analysis where the analysis aims at finding a relationship such as if customer A buys a product X, he/she also buys the product Y.

However, according to Brunsdon et al. (1999) "there is a major potential problem in that if you use conventional data mining tools then you are implicitly forced to accept the key assumption that geographical data is the same as any other data and that there

is nothing special about geographical information or indeed geographical analysis that will prevent it being performed by conventional methods". For example, if you provide the spatial location information within many of the conventional data mining tools they assume it as an attribute and not as the location element of an attribute. This basic error in assumption would lead to less useful results.

Openshaw (1999) argues that what is needed now are new types of data mining tools that can handle the special nature of spatial information and also capture the spirit and essence of geography that a GIS inclined data miner would expect to have available. There is an additional problem that needs to be dealt with. If you simply equate geographical data mining with exploratory spatial analysis then maybe some analysts will be misled into believing that this problem has already been solved. However this assumption overlooks the massive difference between exploring a manageable small data set with few variables and the need to perform the same process on massive databases (with two or three orders of magnitude in most cases) and possibly high levels of multivariate complexity.

The above mentioned problems gets further complicated due to the data types and distinction between various geospatial datasets i.e. GIS and remote sensing data types and the various domains that they cover. First, the imagery in itself is of no use, until and unless, it is supported by the auxiliary alpha-numeric information which might range from anything to everything depending upon the purpose. Many of the models developed based on the market basket study may work well for GIS data but not remote sensing images and vice versa. Secondly, a researcher from the domain of environmental analysis would be least interested in the amount of minerals found in a place but the fact that certain minerals are present there and their mining is taking place and is causing environmental problems that might be of interest. Therefore, even though the domain may not be directly related to a topic of study the information or data source may result in interesting conclusions for such a topic. Therefore, models have to be developed such

that they can be used by analysts' of indirectly related fields of study. Conversely, asking the computer to find all such interesting patterns from a given set of remote sensing data source might be expensive in terms of time (processing) as it is directly proportional to amount of the images, the processor capacity and the location or the medium in which data files are stored. Due to the nature of the image data sets, the size and type of remote sensing images vary drastically from relational data structures. Thirdly, it is not mandatory that the results obtained through the process of data mining are easily interpreted by a remote sensing scientist. Since, there exists a possibility that the results that are obtained may not be from the researchers area of expertise.

In order to overcome these problems it would be better if the researcher mines the data to a certain extent, then analyses the results and subsequently guides further the data mining process in a direction that may be of interest. This will save considerable amount of processing time.

2.4 Models and Tools

The models within data mining can be broadly classified into two categories i.e. descriptive modeling and predictive modeling (refer Table 2). Descriptive modeling is a class of models that tend to summarize the data into meaningful information. Predictive modeling is model that provides analytical projections based on sample sets (training data). Some of the software tools which are available to facilitate the successful execution of the above models within spatial data sets are Spatial Stats Module by S-Plus, Spatial Module for R to assist in spatial prediction or pattern mining, Spatial Statistics Toolbox for Matlab for computing simultaneous and conditional spatial auto regression and mixed regression, Spatial Ecometrics Library for Matlab, Cluster SEER/Boundary Seer/ Space Stat by TeraSeer for supporting spatial clustering, spatial autocorrelation analysis and classification, NEM for Neighborhood clustering, GeoMiner by Systems Research laboratories for mining characteristic patterns, comparison & association patterns in geospatial

database and Spin by Leeds University for mining in Geo-referenced data (Zhang and Zhang, 2002).

Table 2

Types of data mining models (Hand et al., 2001)

Predictive Models		Descriptive Models
Classification	Regression	Probability distribution and density functions
Perceptron	Linear models	
Linear discriminants	Generalized linear models	
Nearest neighbor methods	Non-parametric 'Memory-Based' local models	Probabilistic model based clustering using mixture models
Tree models		
Logistic discriminant analysis	Artificial neural networks	Clustering algorithms
Native bayes		

2.5 Urban Heat Island Phenomenon

Over the past few decades the world has experienced a sudden increase in migration. This migration is not only of the number of people moving between continents and countries due to the advancement in the transportation but also in the number of people moving from the rural areas to the urban areas due to changes in the economy and work profile. Figure 1 shows the percentage of population in the urban areas during 2007 and the projected values for the years 2025 and 2050. From the figure we can infer that in the United States of America (USA), the current urban growth rate is approximately 12.5% and 80% of population is residing within urban areas. From Figure 2 we can infer that if the trend of migration of people towards the urban areas increases, then by 2010 more than 50% of the world's population will be living in urban localities.

This increase of the urban population has also led to rapid changes in the land use and land cover within cities during recent years, causing problems related to traffic

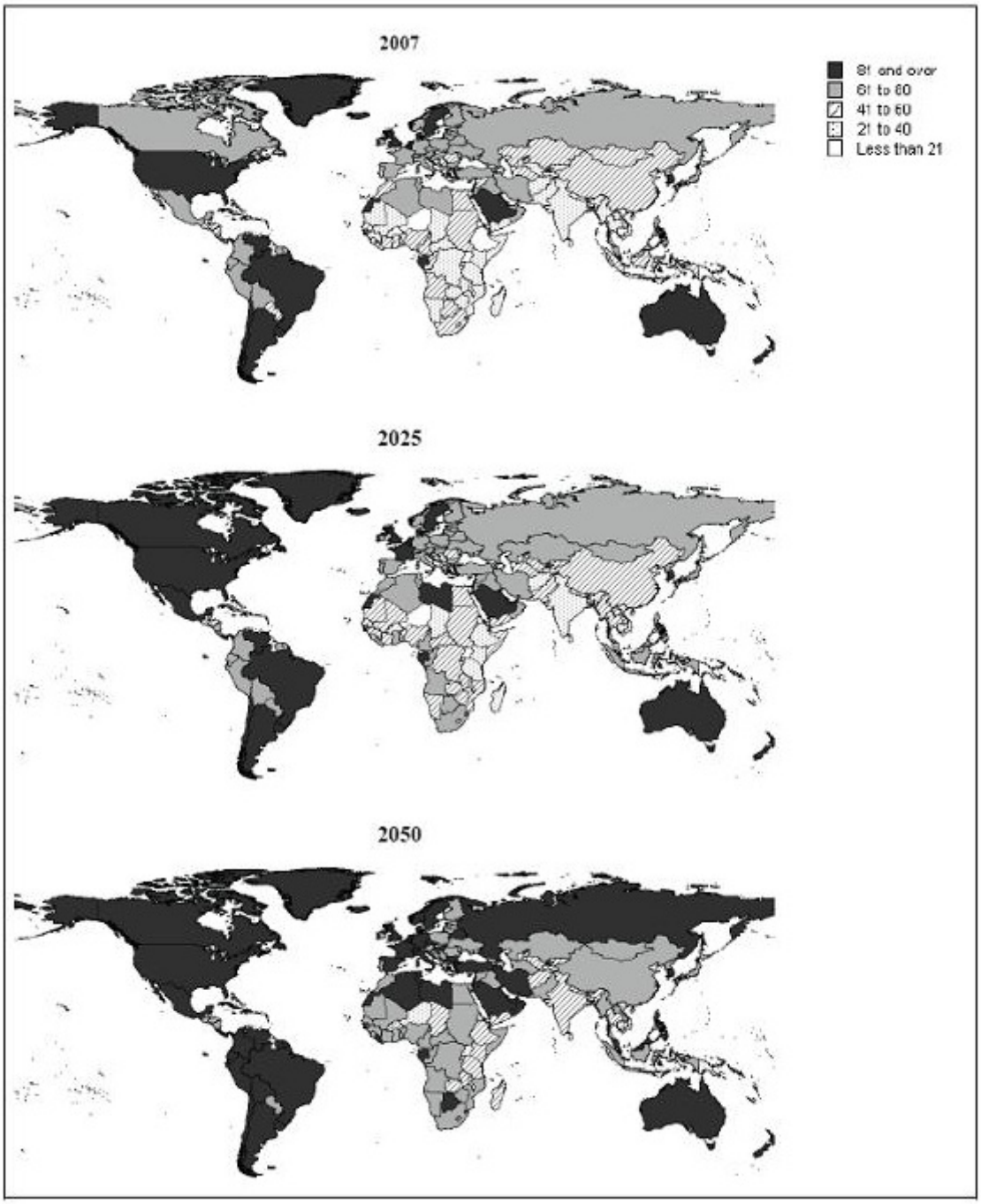

Figure 1. Percentage of population in the urban areas

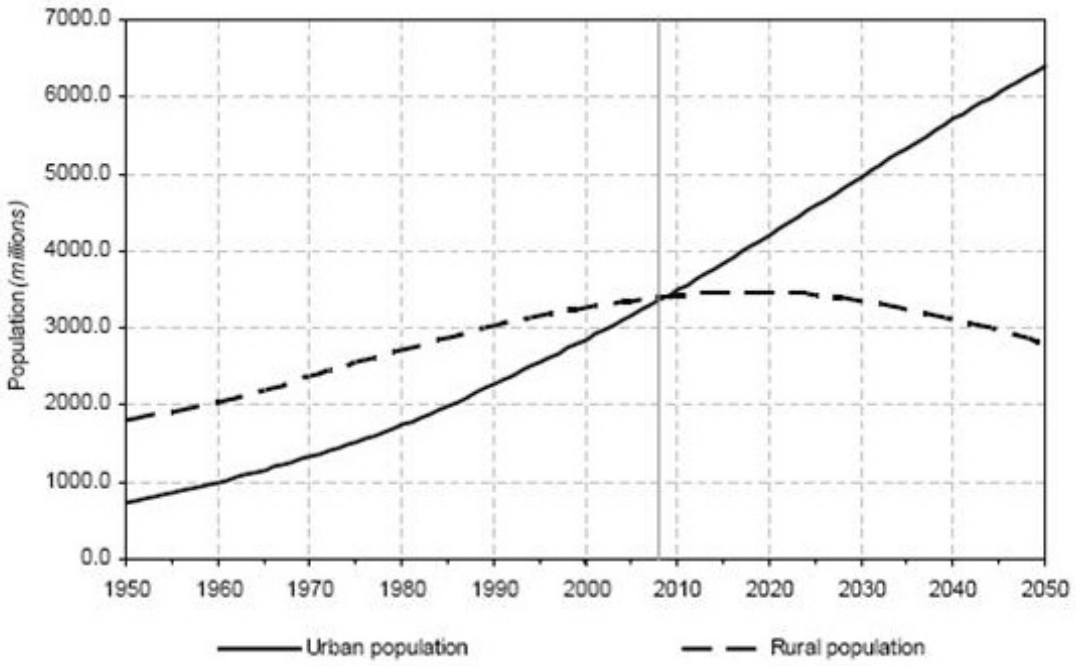

Figure 2. Urban and rural population of the world, 1950-2050 (source: United Nations, Population Division, 2007)

congestion, increase in pollution, water supply and sanitation. These physical changes affect the quality of the environment, contributing to other phenomenon such as increase in air temperature. Scientiests have observed that air temperatures in densely built urban areas are higher than the temperatures of the surrounding rural country. This increase in temperatures within urban areas is known as the 'urban heat island' (UHI) phenomenon. According to Voogt (2005), UHI can be defined as "closed isotherms indicating an area of the surface that is relatively warm; most commonly associated with areas of human disturbance such as towns and cities. The physiographic analogy derives from the similarity between the pattern of isotherms and height contours of an island on a topographic map. Heat islands commonly also possess 'cliffs' at the urban-rural fringe and a 'peak' in the most built-up core of the city". The temperature differences strongly vary at micro scale, both in rural and urban areas because of varying radiant load. For example, a concrete surface may have a different radiant load as compared to water in a

lake. This could be observed both within the urban and the rural environment. But, the thermal characteristics of the overall urban terrain constitute a basic factor in creating the UHI effect which is not only observable at a micro level but also at the macro level.

Types of UHI

There has been a significant amount of research conducted using thermal measurement data which support the idea that urban and suburban characteristics lead to the well known UHI effect. UHI studies carried out over the past few years can be broadly classified into two categories:

1. studies aimed at modeling UHI
2. studies demonstrating the cause and effect relationships

Based on the methods used to measure, modeling of UHI can be broadly classified into three main categories (Grimmond, 2006; Oke, 1987). They are:

1. Canopy layer urban heat island (CLUHI)
2. Boundary layer urban heat island (BLUHI)
3. Skin surface urban heat island (SSUHI)

CLUHI phenomenon is formed due to the change in near surface air temperature between the urban and rural setting. According to Voogt and Oke (2003) one can define CLUHI as that layer of the urban atmosphere extending upwards from the surface to approximately mean building height. There are various factors that influence the CLUHI, such as building infrastructure and the underlying urban surface characteristics (Friedl, 2002). CLUHI are usually measured using readings taken either by weather stations or data loggers placed within the study area. Even though the measuring of heat and air turbulence within any area is generalized, the interactions between various elements

within urban surrounding involve meso-scale modeling of the phenomenon and its associated processes (Chin et al., 2005).

Urban boundary layer heat islands can be defined as the layer above the buildings and roof tops (refer Figure 3). A clearer definition of the urban boundary layer (UBL) is provided by Arnfield (2003):

"the air layers immediately above horizontally uniform surface types with tall roughness elements, conventional flux-profile relationships and Monin-Obukhov similarity theory are likely to be invalid. In this layer, termed the roughness sublayer, flow consists of the interacting wakes and plumes (of heat, humidity and pollutants) introduced by individual roughness elements. At some height above the canopy, the blending effect of turbulent mixing will erase the significance of individual roughness elements and create a layer (the inertial sub layer, surface layer or constant-flux layer) in which turbulent fluxes are constant with height, permitting measurement of landscape-scale energy balance fluxes and Reynolds stress. The roughness and overlying surface layer constitute the lowest portion of the UB. The nature of the urban surface, with its rigid buildings of different heights and physical characteristics, separated by trees, canyons and open spaces, makes it particularly susceptible to the development of a roughness sub layer of significant depth, perhaps several times the average building height".

The heat island formed within this region can be broadly defined as the boundary layer urban heat island (BLUHI). Even though scientists have defined the phenomenon using numerical models (Atkinson, 2003), in order to quantitatively measure the BLUHI one might need more specialized sensor platforms such as tall towers, radiosonde or tethered balloon flights, or aircraft-mounted instruments (Voogt and Oke, 1998a). Due to the complicated nature of the equipment, very few extensive studies have been carried out to measure and model the BLUHI. One of the recent studies that has demonstrated the boundary layer heat island analysis is the Basel UrBan Boundary Layer Experiment (BUBBLE) which was carried out in the city of Basel, Switzerland (Rotach et al., 2005).

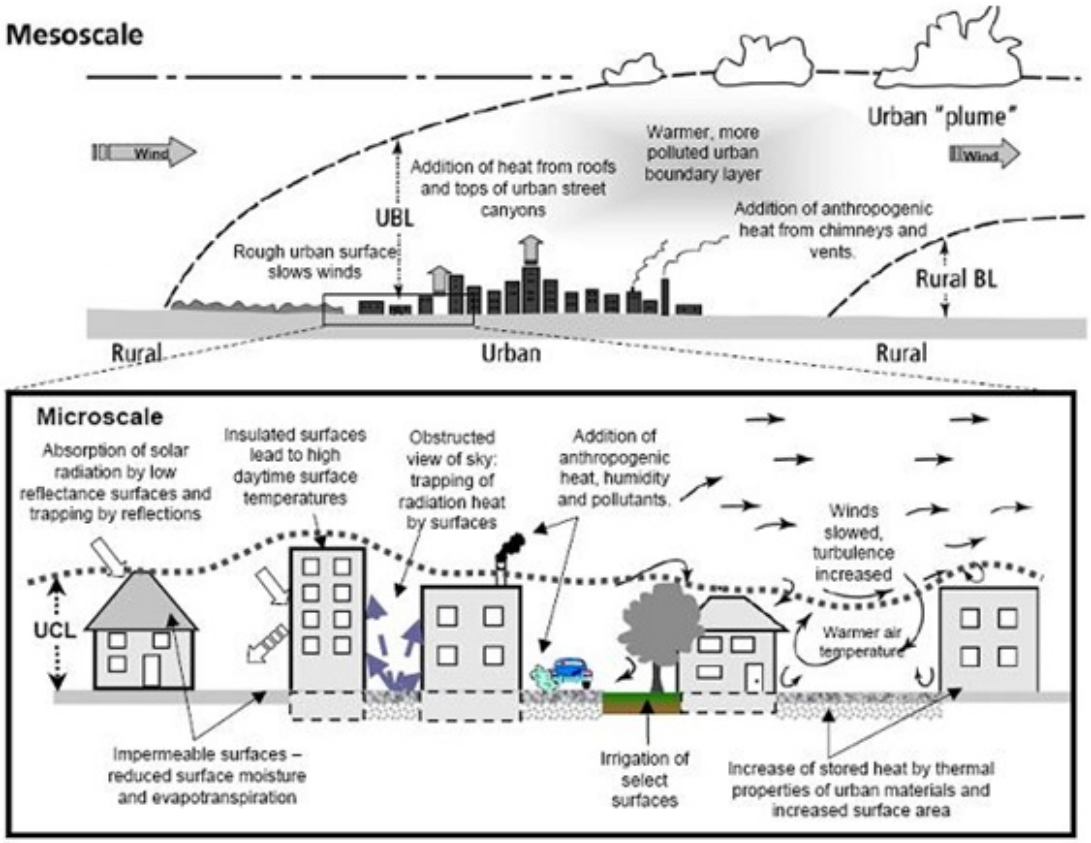

Figure 3. Illustration of the urban heat island processes (Voogt, 2005)

Within this study the researchers set up towers at several locations with their size being at least twice that of surrounding obstacles. These were set up for a period of one month to study air turbulence at various levels. This study conducted at such a detailed level concluded by stating that on a closer look at temperatures at all sites, the nocturnal release of storage heat results in a nocturnal urban heat island. The huge daytime intake of heat by the density of building materials in the urban environment produces an urban cold island (Rotach et al., 2005). This result was found to compliment similar air temperature studies using weather station data demonstrated the presence of night-time heat island within many cities (Bottyán and Unger, 2003; Fast et al., 2005; Kim and Baik, 2005).

Skin surface is defined as the surface of the objects on the ground as seen by any remote sensing platform. The SSUHI can be defined as the heat island characterized by images representing measurements as sensed by the sensors within the thermal window of the electromagnetic spectrum. Due to the advent of the sensor platforms and imaging technology in recent decades, there have been several studies examining SSUHI. Lambin and Ehrlich (1996) investigated the use of Land Surface Temperature (LST) and Normalized Difference Vegetation Index (NDVI) over the African continent. He used a decade of Advanced Very High Resolution Radiometer (AVHRR) global area coverage data to study the relationship between temperature and bio-physical characteristics. In a similar study, Owen et al. (1998) modeled the regional scale climate impact of urbanization using vegetation index and temperature data computed from AVHRR. In another study, Gallo and Owen (1999) went a step further and analyzed the UHI effect using multi-sensor approach employing AVHRR and Landsat images.

A number of other studies have considered UHI in other locales including Streutker (2002) measured the growth of UHI in Houston, Texas using the split-window infrared channels of AVHRR. Jung et al. (2005) used airborne hyperspectral imageries to study the effect in Hungarian villages. Hung et al. (2006) assessed the UHI within Asian mega cities using images from Aqua and Terra missions.

With the help of sensors, it also becomes convenient to analyze the cause and effect of this phenomenon at a pixel-level using associated remote sensing and GIS information. Xiao and Weng (2007) analyzed the effect of deforestation and change in land cover type on the UHI effect in the Guizhou Province of southern China. Xiao et al. (2008) analyzed the impact of bio-physical variables on land surface temperature and its characteristics. Weng and Lu (2008) completed a sub-pixel analysis of the effect of urbanization on land surface temperature. There have also been several studies conducted by scientists using remotely sensed images to analyze the effect of surface temperature on other related phenomena. Gillies et al. (1997) calculated the surface soil water content from the surface radiant flux measurements obtained using an airborne sensor. Sobrino and Raissouni (2000) analyzed the regional response of the soil-vegetation system to climate in arid zones by applying theoretical models to obtain parameters such as Land Surface Temperature (LST) and Normalized Difference Vegetation Index (NDVI) derived from AVHRR sensor. Goward et al. (2002) used satellite-derived surface temperatures and biosphere model to approximate soil moisture conditions on the ground. Weng and Yang (2006) used thermal imagery and land use information to quantify atmospheric pollution. Voogt and Oke (1998b) analyzed the effect of surface geometry on temperature. Kato and Yamaguchi (2005) analyzed the heat balance during daytime and nighttime using Landsat Enhanced Thematic Mapper (ETM+) and Advanced Spaceborne Thermal Emission and Reflection Radiometer (ASTER) images.

Causes of UHI

Over the past decade UHI presence has been studied and documented for several cities around the world. As the name suggests, the cause of phenomenon is urban landscape in general, there are several bio-physical factors that contribute its presence and spread. In a broader perspective every human being wants to live in a developed environment or an environment where there is an easy access to resources and their benefits. With the

advent of technology and modern transportation systems, access to resources/benefits has become easier and such facilities have been achieved in many cities within the developed nations. However, ease in accessibility comes with the price of change in land use and land cover. In this case it is not only the monetary price that one has to invest to achieve such things but also other qualitative prices that one has to pay through the process. One such price is the quality of the living environment.

According to Golany (1996), during the early years of development of a city "the design without designer method was traditionally and fanatically passed from one generation to another, versus our contemporary design style produced on the drafting table with little or no observation of the diversified natural forces action on the field". The traditional method of planning would be to include environmental considerations within the design. But, the lack of such a process within the methodology has lead environmental scientists to look back and analyze the various effects of natural and built forms within the urban surrounding.

Weather

When we discuss UHI effect, we are essentially discussing a component of the boundary layer, canopy layer or surface layer weather system. Similar to weather systems UHI effects have a strong relationship with weather parameters such as wind and cloud. In a smaller scale (individual building scale) experiment by Hall et al. (1999) many of the meteorological and climate characteristics were analyzed. The research demonstrated that aspect ratio, wind direction, wall thickness of buildings, presence of openings and surface clutter have significant effects on the heating and cooling of the surfaces, often altering them by orders of magnitude. Apart from such spatial arrangements the study of UHI in Athens by Mihalakakou et al. (2004) demonstrated that synoptic-scale circulation is a predominant input parameter, affecting the heat island intensity considerably and on a much larger scale. In this study it was demonstrated that high pressure ridge mostly favor heat island phenomenon whereas, intense northerly winds are responsible for its

nonappearance.

Size and spread of the urban sprawl

According to de Schiller and Evans (1996) "The ability to design with urban microclimates depends on the architects' and planners' skills to identify significant variations in the regional climate in urban areas, develop awareness of the possible future modifications produced by changes in the urban tissue and its potential during the process at different scales of applications". City forms such as size, geometry and the materials used in the construction of urban spaces define the UHI effects characteristics. For example two cities with 'X' amount of population but differing urban geometry, allocation of spaces and the type of construction material used would have two entirely different UHIs.

Scherer et al. (1999) demonstrated this behavior and came up with criteria to effectively maintain natural ventilation within a city environment, reduce risks of hazards caused by wind, to help transport fresh air and reduce air pollution in sensitive areas and to reduce heat load while simultanously reducing negative effects of frost and cold stress. These criteria were incorporated to help urban planners in addressing the issue of urban climate within their planning process.

Streutker (2003) analyzed the presence of UHI in the city of Houston, Texas and quantified it in terms of spatial spread and magnitude. In this study, the author demonstrated that there is a inverse relationship in temperature profiles between urban areas and their surrounding rural areas. Gaffin et al. (2006) documented the presence of UHI within the city of New York, New York. Within their preliminary research they were able to identify a linear correlation between air temperature and surface temperature heat islands. Weng (2003) performed a similar analysis to establish the presence of heat island in Guangzhou, China and to quantify the spatial distribution of surface radiant temperatures using fractal analysis. In his study, the author, apart from analyzing the variation of UHI intensity over different zones, demonstrated the changes in fractal dimensions in different seasons. These changes were found to be caused by solar illumination and climatologic

conditions related to soil moisture and air temperature, topographic variation and spatial arrangement and areal extent of different land cover types.

Geometry

The geometry of a building or any built form is also an important constituent of the much larger UHI effect. According to the study performed by Hoyano et al. (1999) on sensible heat flux from exterior surfaces of buildings it was demonstrated that the variation in difference between surface temperature and air temperature is 20 - 30 C during the day and 5 - 10 C at night in summer and winter respectively. The study also showed that the difference between roof and air temperature was around 14 - 25 C depending upon the time of the day. In yet another study by Lagouarde et al. (2004) using an airborne TIR camera, the influence of time on UHI effect at a large scale was analyzed. In this study, first four plots were obtained over the city centre at different dates and times and subsequent data from these plots were used to illustrate a dependence on sun illumination. From the results, all plots showed thermal 'hot spot' effect with maximum temperature observed when aiming at a surface opposite to the sun (with the sun behind). Also, direction of the hot spot moved during the day and was consistent with the sun displacement.

Function of the city

Quality of life aspects such as energy use, water use and pollution have a bilateral relationship with the UHI effect. In one of the studies carried out by Grant and Wong (1999) within the suburban neighborhood of Lafayette, Indiana, USA, the effect of canopy layer and boundary layer air circulation with respect to the land surface temperature (LST) was analyzed. In their study, they demonstrated the effect of air circulation on air pollutants (especially oxidants) at various levels, thereby, establishing an indirect relationship between temperature and air pollution levels within city. A study by Sarrat et al. (2006) also demonstrated similar results, establishing an indirect relationship

between surface temperature and air pollution within an urban environment.

In spite of several studies related to quality of life it is very important for us to understand the effect of these variables with respect to UHI effect. The main reason is that even though some aspects of a particular variable may contribute to a decrease in UHI effect but they may still contribute to an increase in hazardous phenomena. A study byTaha (1997) demonstrated that the use of high albedo materials would lead to a significant reduction in ozone (decrease of 12%) and a decrease in population- weighted exposure to this pollutant. A similar study by Bretz et al. (1998) demonstrated that the use of high albedo materials would favor in the mitigation of the UHI, leading to a substantial decrease in energy demands. But in order to achieve high albedo within the urban settings, some form of synthetic material may have to be used as a coating to existing surfaces which might lead to other forms of health hazards. In some cases, the presence of vegetation, especially trees in the suburban neighborhood, may reduce the summer air conditioning demand. On the other hand, this dense vegetation canopy structure might intercept the incoming solar energy during winter months, thereby increasing the winter heating load (Simpson and McPherson, 1998).

Geography

The physical, human and environmental geography of a city including topography, rural surroundings and climate are some of the criteria that have been long studied in relation to UHI effect. These studies were carried out mainly because of two main reasons. First, these parameters could be effectively quantified using statistics and second, the collection and documentation of primary data was relitavely straightforward. The primary parameter that defines much of urban space is its climate. The UHI phenomenon may vary with respect to the local climate, which is generally controlled by the geographic location of the city on Earth. For example, the UHI phenomenon in a tropical climate may behave differently during different times than the UHI phenomenon in a non-tropical setting.

A detailed study of the climatic variation, using a city's available climatic data and physical simulations of the thermal field in urban areas is presented in a study by de Assis and Frota (1999). In their study, they demonstrated that the design requirements for varying climatic regions during different seasons vary strongly and have to be taken into account before arriving at any mitigation strategies. Local topography and location of the main commercial and industrial sectors are also an important variable while analyzing the UHI effect. In the analysis executed by Kim and Baik (2005) near the borderline of Seoul, it was found that temperatures were relatively low in the city, except near the southwestern and southeastern borderlines where several warm cores were observed. These are the regions where urbanization is in progress and are pronounced by industrial complexes, highly commercialized complexes with high-story buildings and heavy traffic.

Since the urban population distribution values are closely related to land-use zoning within the USA, one can assume that this may contribute to the generation of anthropogenic heat and thus towards the overall UHI effect. In order to analyze this hypothesis Weng et al. (2006) analyzed effect of urban population by census block group and LST measurements. The results of this study showed that population density from the 2000 Census is moderately positively correlated with LST (coefficient: 0.547) in the city of Indianapolis, Indiana. From the above facts, one can conclude that the distribution of urban vegetation may be an important intermediary between patterns of human settlement and regional climate spatial variability.

Furthermore, research by Jenerette et al. (2007) was carried out to test the above hypothesis. In their research they analyzed to identify relationships between surface temperatures, regional climate, vegetation, and human settlement patterns in Phoenix, AZ, USA region. The results of their study concluded that higher income neighborhoods were associated with increased vegetation cover and higher density neighborhoods were associated with decreased vegetation variability. Thus suggesting that the settlement patterns in central Arizona influences regional climate through multiple pathways. These

pathways are further heterogeneously distributed throughout the city.

Effects of UHI

It is imperative to understand the UHI effect is evident in urbanized and urbanizing regions. This presence of UHI within such environment poses several threats to human life, plants, animals, regional climate and global climate patterns. These impacts can be broadly classified into two classes i.e. effect on climate and effect on living environment.

Effect on climate

The UHI phenomenon affects both the regional and the global climatic patterns (Golden, 2004). The bias involved with the global models is far greater and is always an aspect of discussion. All the same, strong conclusions resulting from some of the regional experiments encourage environmental scientists to believe in the scale of UHI impacts.

In a research conducted by Chin et al. (2005) using a three dimensional mesoscale model inferred that the urban canopy produces a nocturnal warming along the urban zone with a maximum value of 1.8 C and a corresponding hydrostatically induced negative pressure anomaly zone at a level of 10 m above the ground. On further analysis Chin et al. (2005) were able to identify that this warming is a result of weaker nighttime cooling within the urban canopy due to urban heat release at night. Furthermore, research by Ghiaus et al. (2006) arrived at a similar conclusion, stating that the UHI effect has a strong negative influence on natural ventilation potential.

Anthropogenic heat is one of the significant parameters that affects energy balance within urban surroundings ((Cenedese and Monti, 2003; Offerle et al., 2006). A drastic change in this parameter during both summer and winter has considerable impact on both local air circulation and latent heat flux which mainly contributes to evaporation and therefore rainfall. There have been several studies that have demonstrated the impact of UHI on weather leading researchers to speculate that UHI influences anomalies in rainfall patterns and lightning (Childs and Raman, 2005; Gedzelman et al., 2003; Rozoff et al.,

2003). In a study by Lensky and Drori (2007) on cloud formation, they demonstrated that temperature difference is greater for clouds that develop over more polluted and/or warmer surfaces than those resulting from smoke and urban pollution and/or urban heat island,. Furthermore, through a case study over Southeast Asia, Lensky and Drori (2007) were able to demonstrate that the difference in temperatures are around 1 - 6 C for tropical maritime clouds, 8 - 15 C for tropical clouds over land, 16 - 26 C for urban air pollution, and 18 - 39 C for clouds ingesting smoke from forest fires. Furthermore, from an experiment conducted by Mihalakakou et al. (2004) it was concluded that daytime air temperature was a single input parameter that contributed between 24 and 31% of regional climate models accuracy.

Therefore, based on the above results one can conclude that nighttime and daytime estimations of urban air temperature is one of the predominant input parameters on urban climatic conditions, thus emphasizing the importance of the heat island phenomenon

Livable environment

According to the world health organization (WHO) anthropogenic warming claims more than 150,000 lives on an annual basis (refer Figure 4). According to Patz et al. (2005) these heat related mortalities can be classified into two broad divisions. First, direct heat related mortality and morbidity, and second a climate-mediated change on the incidence of infectious diseases. The primary is mortality caused due to considerable difference between temperature extremes especially between the mean and the maximum during a particular period. This has more effect during early summer months when people are in the process of getting familiar to higher temperatures. A sudden change in the temperature during these days instead of gradual increase might affect many who are less prepared for that change, especially old people. Such sudden increases in temperatures are termed as heat waves (Souch and Grimmond, 2004). These effects arise because of one or more meteorology-related factors such as an increase in number of consecutive hot days, higher effective temperatures, increased humidity, stagnation,

accelerated photochemical smog, pollutant emissions, and particulate formation (Taha et al., 2004). Such heat waves can cause severe thermal environmental stress leading to health impediment and increased mortality. The worst such effect was experienced by the people of Europe in the year 2003 which caused heat related mortality in tens of thousands and property damages in billions due to the subsequent forest fires (UNEP, 2004).

According to an Environmental protection Agency (EPA) study in 2003 and Samenow (2007), heat waves were much more severe in Western Europe than in countries to the east. The studies found that temperature deviations were generally higher for maximum, rather than minimum, temperatures. Of major European cities, Paris exhibited the greatest deviations where the temperature increased to more than 17 C. Even though the occurrence was a once in a lifetime event, according to the UN, projections indicate that such extreme changes may be quite common in future climate scenarios. As urban populations grow in the future, their vulnerability towards such heat-related mortality would also be likely to grow.

Apart from heat waves, another effect which is evident in our everyday life is the increase in pollution within urban centres. Even though the UHI phenomenon does not contribute to an increase in the air pollution, it does substantially contribute to its dispersion. The Department of Environment of Australia commissioned a study to analyze wind patterns and their effect on air pollutants in south-east Queensland air shed to analyze the significance of anthropogenic heat. From the results of their experiments by Khan and Simpson (2001) inferred that anthropogenic heat in urban areas can substantially affect the wind and temperature regime. Through their experiments they were able to demonstrate that the meteorological conditions have strong correlation with the extent and intensity of pollution. Furthermore, their model simulations identified clear patterns of pollutant movement within a strong sea breeze during summer months. Some of their simulation results demonstrated that in scenarios where the onshore sea

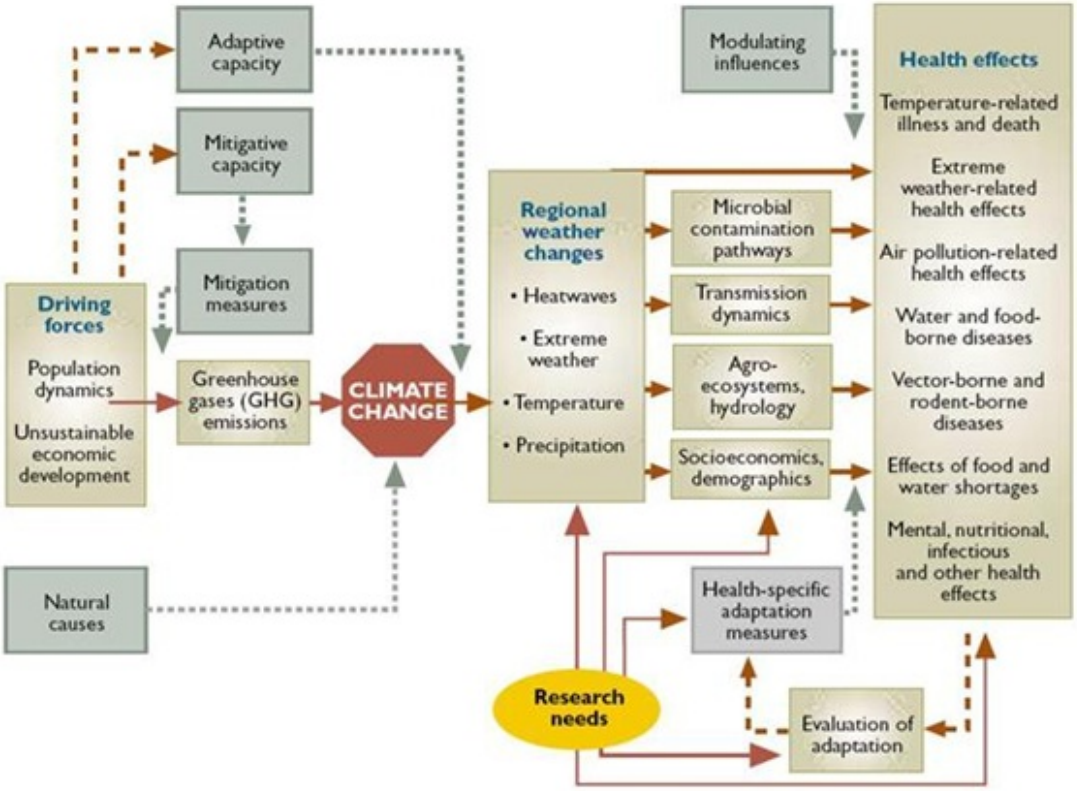

Figure 4. Climate change and possible health impacts (Source: WHO, 2003)

breeze is strong, then it would be capable of carrying pollutants as far as 100 km inland. If analyzed in relevance to the experiment carried out by Childs and Raman (2005) to realize the potential of bio-terrorism hazards, this projects a catastrophic scenario. The authors further state that if any biological attacks do coincide with such environmental conditions then the hazardous elements would travel to the entire city of Queensland and in some cases extend to neighboring cities. This scenario was validated after the September 11th attack, by Gedzelman et al. (2003) where they analyzed the dispersion of debris (pollutants) after the attack within the city at various times of the day and night for four months.

In a research Taha (1997) demonstrated that mitigating UHI has a positive effect on mitigation of air pollution within that environment. In this study, the author analyzed the effects within Salt Lake City, Baton Rouge, and Sacramento using both mesoscale meteorological data and air quality modeling. The results of these simulations indicated that for these three cities a decrease of 1 - 2 C in the UHI effect would lead to a drastic decrease in air-pollution concentration.

Apart from heat related mortality, many prevalent human diseases are also linked to climatic fluctuations. This includes, cardiovascular mortality and respiratory illnesses due to heat waves, to altered transmission of infectious diseases and malnutrition from crop failures. According to Patz et al. (2005), El Nino/Southern Oscillation (ENSO) has been found to be related to incidences of malaria in South America, rift valley fever in east Africa, dengue fever in Thailand, hantavirus pulmonary syndrome in the southwestern USA, childhood diarrheal disease in Peru and cholera in Bangladesh. The authors further state that "it is unclear at this stage whether global warming will significantly increase the amplitude of ENSO variability, but if so, the regions surrounding Pacific ocean and Indian ocean are expected to be most vulnerable to associated changes in health risks".

There have also been instances of such heat fluctuations leading to an increase in tornadoes and wind storms. On one hand, in the USA, air mass temperature contrast

leads to creation of a powerful jet stream in the upper atmosphere and this jet stream in turn provides wind shear, which serves as a source of rotation for tornadoes (Halverson, 2006). On the other hand, in Europe, wind speeds have significantly increased over the second half of the twentieth century (Pryor et al., 2005). Even though increase in wind speeds has lead to an increase in wind energy generation in certain regions, this effect has led to an overall increase in both the frequency and the amount of wind storms across Europe.

Another dimension of the effect of UHI can be felt in terms of the economy and the increase in consumption of both renewable and non-renewable energies. Guhathakurta and Gober (2007), found that during summer months, especially during days when the UHI effect is at its relative maximum water consumption within Phoenix, Arizona increased by 60%. The authors demonstrated that for every 0.55 C increase in a census tract's low temperature, average water use in single-family unit increased by 1.7% or 290 gallons per month. Furthermore, a similar increase in warmer temperature during night would increase water use by 681 gallons. A similar study conducted by Rosenzweig et al. (2006) towards electricity consumption and the results demonstrated a strong association between higher temperatures and an increase in electricity demand.

2.6 Urban Heat Island: Data, Models and Methods

There are various types of UHI models that have been developed over the past four decades. These models vary based on the input data i.e. remote sensing instrument, type of reading, details within the reading, the spatial resolution, spectral resolution, temporal resolution and uncertainty of measurement.

"The study of urban weather and climate possesses a perspective that is almost unique. So unlike other environments of interest, where it is sufficient to study the atmosphere for its own sake or value, in urban areas there is interest to know about urban effects. This means assessing possible changes to meteorological variables as an urban area grows or

develops over time, compared to what would have happened had the settlement not been built. This is a question that is essentially unanswerable because the settlement has been built, and even if it hadn't the landscape may well have evolved into a different state than the pre-existing one anyway. The assessment of urban effects is therefore fraught with methodological difficulties and no 'truth' is possible, only surrogate approximations", Oke (2006).

Numerical/ empirical UHI models

On a broad scale, the types of models could be distinguished as either numerical or empirical (statistical). If the amount of data collected is exhaustive, or does possess the potential to explain the phenomenon at hand, then empirical or statistical models are sufficient. For large scale studies, such as in global climate simulations, numerical models tend to be a better choice (Masson, 2006). For example, Balling and Brazel (1998) used realistic surface temperature measurements derived from AVHRR to model temperature patterns in Phoenix, Arizona, USA. Within this study empirical models including mean and standard deviation were used to analyze the results. They inferred that temperatures within residential and commercial areas varied by 2 C. Similarly, in another case Kikegawaa et al. (2003) analyzed how this temperature difference corresponds with peak energy demands. In order to simulate this they developed a numerical simulation system adopting one-dimensional urban canopy meteorological model.

Models based on measurements/instrument types

Since most climate related information is collected by weather stations and local meteorological laboratories. The temperature readings from weather stations/ towers are one of the primary data used in UHI studies (Emeis and Schafer, 2006; Scheeringa, 2006). Apart from the weather stations, scientists have also attempted modeling UHI using profilers.Mihalakakou et al. (2002) tested for estimation of heat island intensity in Athens,

Greece using measurements from 23 temperature profilers. Hawkins et al. (2004) used a denser network of temperature and humidity sensors to study the UHI effect in Phoenix, Arizona. In both the above studies, the researchers were able to identify existence of one UHI.

In an another study Khaikine et al. (2006) used microwave profilers to measure temperatures up to 600m in height to determine boundary layer heat island within the city of Moscow, Russia. The results of this study demonstrated the presence of two UHIs one with a higher heat dome at all levels and another, with a low heat dome along with cold air above (UBL and UCL). These deviations in measurements were attributed to change in instrument type and the information collected.

Apart from profilers, there are several other remote sensors which are available to scientists for studying the UHI phenomenon. Some of the instruments are;

SODAR (Doran et al., 2002)

Sound Detection and Ranging (SOSAR). These are also known as Rawinsondes. These are used along with weather balloons to obtain profiles of winds, temperatures, and humidity.

RASS (Doran et al., 2002)

Radio acoustic sounding systems (RASSs). A RASS is capable of measuring profiles of virtual temperature up to heights in excess of 1 km above the surface, although performance varies with ambient conditions. In this dissertation, RASS data, in conjunction with measurements from tethered sondes, rawinsondes and surface instruments provide information to construct a three-dimensional representation of the temperature structure.

Ceilometers (Emeis and Schafer, 2006)

These are instruments that use the optical backscattering principle to obtain measurements of cloud heights and aerosol intensities. The main advantage of a ceilometer in comparison to SODAR and RASS is that it can easily be used in urban areas, because it has no negative

impacts on its surroundings and it can measure up to several kilometers whereas the SODAR are limited to a few.

Imaging sensors (Thermal infra red)

Imaging sensors are instruments (on board a satellite or aircraft) that record electromagnetic radiation (EMR) that is reflected/ radiated from the objects on the earth's surface. The information recorded in the thermal infrared part of the spectrum is widely used in understanding the UHI effect. For example, a study conducted by Gallo and Owen (1999) demonstrated a variation of less than 40% between the temperature measurements derived from AVHRR sensor (satellite) and ground based weather stations.

Scale and scalability of measurements and models within UHI research (Oke et al., 2004)

The concept of scale is very important to geography and variation in the scale can be regarded as both strength and weakness of geography (Lam and Quattrochi, 1992). The various scales that are of importance within UHI research are as follows:

Microscale

Urban microclimates are defined by dimensions of individual elements such as buildings, trees, roads, streets, courtyards, gardens, etc., extending from less than one to hundreds of meters. The aim of microscale measurements is to achieve climate observations free of extraneous microclimate signals to characterize local climates. Avoiding anomalous microclimate influences is hard to achieve.

Mesoscale

This scale quantifies the city's influence on weather. Climate at the scale of a whole city extends typically tens of kilometers. An essential difference between the climate of urban areas and that of open-country sites is that the vertical exchanges of momentum, heat and moisture occur in a layer of significant thickness - called the urban canopy layer (UCL). The height of the UCL is approximately equivalent to the mean height of the main

roughness elements (buildings and trees). Microclimatic effects of individual surfaces and obstacles persist for a short distance away from their source and they blend in the horizontal and vertical directions by turbulence. The distance depends on the magnitude of the effect, the wind speed and the stability. Effects may persist up to a few hundred meters horizontally. In the vertical, individual element effects are discernable in the roughness sub layer (RSL) up to blending height.

Local scale

This scale includes climatic effects of landscape features, such as topography, but excludes microscale effects. In cities this means the climate of neighborhoods with similar types of urban development (surface cover, size and spacing of buildings, activity). Typical scales are one to several kilometers.

Other factors on which the scale and scalability of heat measurements depend are:

1. source (point or area) of the measurement
2. field of view (nadir or angular) of the sensor
3. resolution (high or low) of the sensor
4. radiometric characteristics of the sensor.

Sensor or image

Temperature readings from weather stations and readings measured using thermal imaging sensors pose a unique problem within the urban meteorology. The readings from weather stations are usually of high temporal resolution and of very sparse or low spatial resolution. It is quite the opposite in the case of the thermal imaging sensors especially AVHRR readings. In the study conducted by Gallo and Owen (1998) over a region of 41 km x 41 km, mean differences in satellite sensor-based predicted bias and observed bias of the readings ranged from 0.04 C to 0.92 C for maximum and minimum temperature

bias respectively. This bias was also found to vary depending upon the location of the sensors and their distribution.

Angular or nadir (Soux et al., 2004)

A sensor viewing an urban area from different points may 'see' a different mix of surface elements, i.e., different parts of the complete surface are obscured from certain views. What is 'seen', and hence the area from which a remote sensor with a given field-of-view (FOV) acquires its input, is a combination of many surface facets, both sunlit and shaded. This highly three-dimensional surface structure, in combination with varying solar azimuth and altitude, leads to a directional variation of the measured radiance (anisotropic radiance distribution, referred to as anisotropy). Soux et al. (2004) in their research project 'SUM' modeled to estimate the variation in temperature of roof, wall and ground facets (sunlit or shaded) at different times of the day. The results showed that in certain urban terrain a variation of +/- 3 C and +/- 5 C is possible with a change in vertical and horizontal viewing angles respectively.

Spatial resolution

With the advent of sensor and satellite technology there are a range of satellite and terrestrial instruments available to record information in the thermal part of the electromagnetic radiation (EMR). Some of the previous researches conducted using low to high spatial resolutions are:

Jin et al. (2005) used Moderate Resolution Imaging Spectroradiometer (MODIS) instrument on board National Aeronautics and Space Administration (NASA) Terra satellite measures. This instrument apart from recording thermal emissivity also records other information such as surface spectral and radiative temperatures. These additional measurements help provide a better understanding of the climate impact of urbanization as well as our ability to specify the parameters needed by climate models to compute impacts of urbanization. Satellite observations provide a basis for characterizing the

physical modifications that result from urbanization.

Stathopoulou et al. (2004) used National Oceanic and Atmospheric Administration's (NOAA) AVHRR images to model UHI in Greece. The main advantage of using this sensor is its low cost and time-synchronous coverage of urban areas. Li et al. (2003) used land surface temperature (Ts) derived from Landsat 5 Thematic Mapper (TM) and Landsat 7 Enhanced Thematic Mapper (ETM) thermal band. The main advantage of these images is the increase in resolution i.e. 120 m and 90 m of Landsat 5 and Landsat 7 respectively in comparison with 1 km and 250 m resolution of MODIS and NOAA/ AVHRR respectively. Instead of using conventional satellite remote sensing Lo et al. (1997) researched the UHI effect using day and night airborne thermal infrared image data of 5m spatial resolution acquired with the 15-channel (0.45 μm +/- 12.2 μm) Advanced Thermal and Land Applications Sensor (ATLAS). The results demonstrated that high-resolution thermal infrared images match the complexity of the urban environment. The main disadvantage of using such sensor is the cost and time associated with collecting the data and in performing the initial processing.

Models used for characterization

Apart from the various types of UHI models that have been proposed, one of the important criteria that affect the outcome of results is the selection of an appropriate model for calculation of land surface temperature from the remote sensing measurements (digital numbers (DN)). Sobrino et al. (2004) in their research analyzed the effect of three of the most common models (radiative transfer, mono-window algorithm and single-channel algorithm) to retrieve the LST from thermal infrared data supplied by band 6 of the Thematic Mapper (TM) sensor onboard the Landsat 5 satellite. The results demonstrated that the minimum root mean square deviation (rmsd) for emissivity (0.009) and land surface temperature (1 K) was by a single-channel algorithm. It should be noted that these results would not prove true with a change in sensor platform and study area.

Intervals between measurements

UHI is a phenomenon that keeps changing constantly with time. A research conducted by Akai et al. (2002) using RASS over Tokyo metropolitan area during end of February 2000, demonstrated a decrease in temperature within a short period of time (variability between hours). This variation was caused due to cold airflow into the measurement sites, and the occurrence of an inversion layer. They concluded their research by stating that such rare meteorological phenomena are quite common within an urban terrain but it requires detail measurements using sophisticated devices to detect and model such changes. Hudischewskyj et al. (2001) investigated the variation of UHI between days of the same season and concluded that a variation of 0.3 C between readings from 14th and 15th July was observed. The more evident annual changes of UHI due to land use and land cover (LULC) were discussed by Weng (2001) over Zhujiang delta, China and demonstrated a difference of 3 C for urban or barren lands.

Remote sensing of UHI: Problems and pitfalls

Within the last four decades, great progress has been made in remote sensing with the advent of space programs and sensors associated with Earth observations (Tan et al., 2002). With differences in various data collection systems some researchers have demonstrated that field measurements and remote sensing measurements show considerable agreement. These studies reinforce the conclusions of other recent studies that have demonstrated the compatibility of two-layer energy balance models with remote sensing observations and, by extension, the viability of using thermal remote sensing to model surface energy balance (Friedl, 2002).

Some researches also demonstrated that surfcae temperatures for large areas could be mapped and studied more effectively by using satellite remote sensing data in the infrared region as compared to ground based sensors (Stathopoulou et al., 2004). Furthermore, even with satellite measurement, it is still difficult to generalize about the magnitude,

location, and spatial distribution of the UHI for several reasons. These reasons are mainly attributed to the shape, extent and layout of the city, the type and material of surrounding areas, and the resolution of imagery used to characterize the phenomenon (Arnfield, 2003). These factors not only affect the spatial extent of the UHI but they also affect its magnitude.

Over the years, statisticians have developed several methods of generalization to overcome the issue of characterizing surface in spatial domain. While various approaches of kriging and thin plate spline models have been used successfully for spatial process estimation, they have the weakness of being global models, in which the variability of the estimated process is the same throughout the domain. This failure to adapt to variability, or heterogeneity, in the unknown process is of particular importance in environmental, geophysical, and other spatial datasets, in which domain knowledge suggests that in most cases the phenomenon may be non-stationary (Paciorek and Schervish, 2006). Lastly, a single parametric model can be defined for analysis of a single image, but, it becomes difficult to apply the same over multi -temporal and multi-sensor images in order to conduct a successful comparative analysis. This aspect gets further complicated due to the changing nature of land cover and land use and also the fuzziness involved within the boundary between urban and rural areas.

Another major problem is the use of appropriate statistical analysis for quantifying the relation between urban temperatures to other associated factors. The interactions between the LULC (Dousset and Gourmelon, 2003; Golden, 2004; Weng et al., 2004) and NDVI (Eliasson, 1996; Gillies et al., 1997; Lo, 1995) with UHIs have been studied and quantified using linear statistical models and multivariate analysis. These techniques are well established but are effective in analyzing the quantitative relationship between limited qualitative variables, general trend and not specific micro level deviations (Bottyán and Unger, 2003).

This research attempts to address some of these problems stated above within the

field of UHI modeling and monitoring. This research intends to solve problems through developing and experimenting with methods adopting techniques of data mining. The methodology incorporates issues addressing both spatial and temporal resolution though using data from varying sensor platforms.

2.7 Summary

To summarize, problems associated with UHI exist and are of serious concern. Even though many algorithms have been developed for modeling there is a lack of systems for continuous monitoring of UHI using remote sensing instrument. Based on inspiration from recent developments, this research analyzes the UHI effect using both high temporal (MODIS) and medium spatial resolution imagery (ASTER and Landsat) in modeling the phenomenon for monitoring and analyzing UHI behavior in space and over time. This research, explores the concept of implementing some of the data mining models within the areas of UHI research to overcome some of the limitations described by earlier researches. The next chapter describes the data and study area that will be taken as a sample case for analysis.

CHAPTER 3

DATA AND STUDY AREA

This chapter briefly explains about the nature of the study area that was taken as a case to test the model and its results. Section 3.2 provides a description of the study area and its geography. Section 3.3 discusses the data that were used within this study. In this section, the data types were classified into four major types i.e., remote sensing images, raster, vector and statistical or tabular data. These data types, along with their associated datasets were also explained in detail.

3.1 Study Area

Indianapolis, Indiana, USA, was chosen as the study area (refer Figure 5). It possesses several characteristics that make this area an appropriate choice for the study proposed. Indianapolis has a single central city. Large urban areas in the vicinity have not influenced its growth. The city is located on a flat plain and is relatively symmetrical, having possibilities of expansion in all directions. Like many other American cities, Indianapolis is rapidly increasing in population and in area. According to the 2000 Census, its population is 791,926, making it Indiana's most populous city and the 12th largest city in the U.S. The U.S. Census July 1, 2004 estimate for the Consolidated City of Indianapolis is 794,160 and a metropolitan area population of 1,595,377. The larger combined statistical area (an agglomeration called the Nine-County Region) has a population approaching two million residents (1,939,349). Indianapolis is the third largest city in the Midwest after

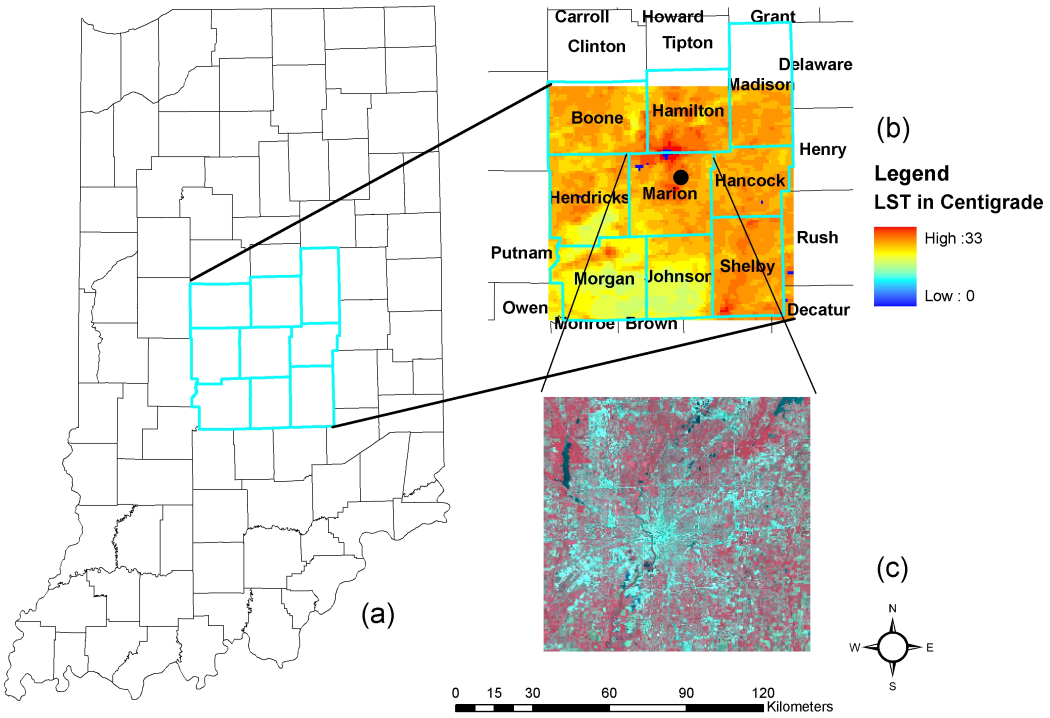

Figure 5. (a) Depicts the state of Indiana and its counties, (b) The counties that are adjacent to the Marion County and (c) False color composite of Landsat ETM+ October 2000

Chicago and Detroit and is one of only three major cities in the Midwest with a growth rate above 5%. As of 2005, Marion County's population is 863,133. The total area of the nine counties is 7900 km^2. The current expansion is occurring through encroachment into adjacent agricultural and non-urban land. Certain decision-making forces, such as density of population, distance to work, property value, and income structure, encourage some sectors of metropolitan Indianapolis to expand faster than others.

3.2 Data

The datasets to be used in this study are classified into four categories based on their nature and type as follows:

- Remote sensing images
- Pre-classified raster images
- Vector data
- Census statistics

Remote sensing images

In this research, satellite derived thermal infrared data were used instead of ground based air surface temperature data. In spite of the advancement in ground sensors for measuring the air temperature at a high temporal scale, it is satellite remote sensing which helps in attaining high spatial resolution data of the land surface temperature. Further, the number and spread of existing air surface temperature data loggers situated in and around the study area were inadequate to cover the entire study area with the precision necessary for a local study. Varying satellites acquire the scene differently due to their sensor characteristics and each and every sensor is designed for specific purposes. Therefore, within this study, varying remote sensing images were used to satisfy the varying requirement of the proposed study. Higher resolution images such as aerial photos (acquired on 2003) and ASTER were used for field study selection, exploratory analysis and micro analysis of the LST.

The relatively lower resolution images of Landsat-TM (thematic mapper) and one image from Landsat-ETM+ (enhanced thematic mapper) and Moderate Resolution Imaging Spectroradiometer (MODIS) were used for analysis. Landsat missions are the oldest for acquisition of multispectral data from satellite used for Earth resources and this

makes it the suitable choice for analyzing the spatial change over a long period of time at medium resolution. The TM sensors on board Landsat were specifically designed for quantitative analysis of the Earth's land surfaces (Vogelmann et al., 2001). Further, since the spectral window of Landsat TM, ETM+ and MODIS are around the similar ranges i.e. 10.4μm to 12.5μm in the case of Landsat and 10-15 m in the case of MODIS. These factors make Landsat and MODIS images the best available resource for this study of UHI over Indianapolis in space and over time. A total of two thousand nine hundred and twenty two day and night images from MODIS between period 2003 - 2006 were used for the analysis. Further care was taken that the amount of cloud cover was relatively limited in all the images used.

Pre-classified raster images

Information extracted from remote sensing images in the form of pre-classified raster datasets (NLCD and MODIS LST) was used along with the remote sensing images to facilitate the temporal monitoring requirements of the proposed research. The rationale for using these images are: (1) The images are currently available at no cost, (2) The time frequency that is used for generating these image products satisfy the initial requirements of this proposed project, (3) The 1991 and 2001 NLCD was useful for analyzing the relation between the land cover and temperatures for the periods 1985, 1995 and 2000, and (4) The daily day and night MODIS LST products was useful in studying the diurnal and seasonal behavior of the UHI.

The U.S. Geological Survey (USGS), in cooperation with the U.S. Environmental Protection Agency, have produced land cover dataset for the conterminous United States. The NLCD is a component of the USGS Land Cover Characterization Program. The NLCD contains 21 categories of land cover information and is currently distributed by State as 30-meter resolution raster images in an Albers Equal-Area map projection (United States Geological Survey, 2008).

The UHI effects are found in terms of surface temperature anomalies at both the daytime and nighttime (Jin et al., 2005). Therefore the satellite-measured skin temperature (Tskin) derived from long-wave bands that detect surface emissions will be highly useful for UHI study. In this research, LST information will be derived from analysis of selected bands collected from the MODIS satellite Terra sensor. The main rational for selecting the MODIS imagery was its high temporal resolution. The MODIS LST team disseminates the global daily day-time and night-time LST daily. The assumption was that, this data will aid in understanding UHI on a spatial and temporal scale. MODIS is carried on the NASA's Terra satellite launched in May 2000 and later on the Aqua satellite. On Terra, it measures the earth's surface characteristics through seven solar and three thermal spectral bands at 1030 LT and 2230 LT daily. The 36-band MODIS satellite scanner has 1km by 1km pixels at nadir for the thermal infrared bands. A daily LST map of both day and night time temperatures are being developed and distributed. The present algorithm is based on the work by Snyder et al. (1998). It employs the radiance and emissivity in band-31 (10.8-11.3 μm) and band-32 (11.8-12.3 μm). The emissivity variation represents approximately 70% of the globe-year land surface. The day/night LST algorithm is generated from pair of daytime and nighttime L1B data using the seven thermal infrared (TIR) bands, atmospheric temperature and water vapor (Wan 2006). The algorithm has previously shown promising results in LST estimation (Dash et al., 2002).

Vector data

The vector datasets used in this study include road network layout (for determining the influence of transportation and quantifying their contribution within the UHI effect), zoning data (to study the impact of specific land use zones), state/county/district boundaries and blocks/tracts/block group areas.

Census statistics

The 2000 United States census statistics of demographics as distributed by the U.S. Census Bureau were used within this study. The rationale for using demographic data was to study the influence of population density on the UHI effect.

3.3 Software

This research was carried out to demonstrate efficiency of models for the analysis of UHI. At the time of research there was no software available which could execute all the models. Therefore, multiple software were used to experiment different models. The list of software which were used for running the selected models were ArcScene a GIS software, R a statistical software, geospatial data acquisition library (GDAL) and Apriori as developed by Christian Borgelt. The description of these software and their usages are detailed within the Chapter Methods and Results.

3.4 Summary

To summarize, the city of Indianapolis was taken as a case for this research. The city is located on a flat plain and is relatively symmetrical, having possibilities of expansion in all directions. The population of the city has increased drastically over the past two decades and this makes it a near perfect case to study the temporal change in the UHI effect with respect to the change in the physical characteristics of the city. These factors, along with several other characteristics, make the City of Indianapolis metro area an appropriate choice for this research. Based on the availability, remote sensing images from ASTER, Landsat and MODIS were used for analysis. The pre-classified raster images include the daily, weekly and monthly data sets of MODIS LST and MODIS derived NDVI data sets from 2003 to 2006. Vector information such as the road network and zoning data has been used in tandem with census 2000 statistical information.

The forthcoming chapter describes the methodology that was adapted in this research. Apart from describing the methods, the chapter also provides the information about the rationale, underlying model, its parameters and the steps involved within execution.

CHAPTER 4

METHODS

The methods section is divided into two sub-sections. The initial section will discuss the methods that were implemented for generating the information from the base datasets. The latter explains the models that were developed to extract knowledge from the information.

4.1 Primary Information Generation

Information creation is the intermediate aspect of knowledge discovery. In this research, varying information sources from the raw data have been developed with the intention of studying their relative importance on the behavior of UHI in space and time. Some of the variables which were extracted from the remotely sensed images are the LULC, vegetation and surface temperature. The variables which were extracted from secondary information sources were the population density grid and transportation buffer zones.

This research involves images of varying spatial and temporal resolution for modeling and monitoring the UHI phenomenon. Therefore, to compare the results between these images, base imagery becomes necessary. Within this research, ASTER 2000 image was used as the base image for geometric correction. The rationale for selecting ASTER image was its relatively higher spatial resolution in comparison with the rest of the images (e.g., Landsat 7) used in this study.

The procedures for the generation of the base information from the datasets are

described below:

Land use land cover (LULC)

The LULC data used within this study was developed from the ASTER 2000 image using semi-automatic technique. I would like to thank Dr. Hua Liu who assisted us in ASTER image acquisition and processing of land use and land cover classification. This data set was created using unsupervised classification method (Iterative Self-Organizing Data Analysis) and reclassification based on expert knowledge. Post classification smoothing and image refinement were conducted to improve classification accuracy. (For further information about the data set and its quality please refer to Liu and Weng (2008)).

Land surface temperature -ASTER

In this study, ASTER band 13 ($10.25 - 10.95\mu m$) has been used to calculate the LST due to the spectral width of this band being close to the peak radiation of the black-body spectrum given off by urban surface within a study area (Lu and Weng, 2006). There were two steps which were involved in the computation of LST. First, the conversion of sensor derived spectral radiance to the at-sensor brightness temperature, i.e., considering that the emitting source is a perfect black body. The second step is the conversion of the black body temperature to spectral emissivity

The conversion formula for the first step as derived by Dash et al. (2002). The formula used is as follows:

$$T_c = \frac{C_2}{\lambda_c ln\left(\frac{C_1}{\lambda_c^5 \pi L_\lambda} + 1\right)} \tag{4.1}$$

Where T_c is the brightness temperature in Kelvin (K) from the central wavelength, L_λ is the spectral radiance in $Wm^{-3}sr^{-1}$, λ_c is the sensor's central wavelength, in this case the central wavelength of the band 13 of the ASTER imagery, C_1 is the first radiation constant ($3.74151 * 10^{-16} Wm^{-2}sr^{-1}\mu m^{-1}$), and C_2 is the second radiation constant ($0.0143879 mK$)

The resulting black body temperature imagery, T_c, has been corrected for the spectral emissivity (ϵ). This was done using the LULC classification derived from ASTER data (using optical and thermal bands). The LULC categories were then assigned an emissivity value according to the scheme provide by Snyder et al. (1998).

The emissivity corrected LST has been computed using the following equation (Lu and Weng, 2006):

$$LST = \frac{T_c}{1 + \left(\frac{\lambda * T_c}{\rho}\right) ln\epsilon} \tag{4.2}$$

Where λ is the wavelength of the emitted radiance (for which the peak response and the average of the limiting wavelengths was used), $\rho = h * c/\sigma$ where, σ = Boltzmann constant ($1.38 * 10^{-23} JK^{-1}$), h = Planck's constant ($6.626 * 10^{-34} J.s$) and c = velocity of light ($2.998 * 10^{8} ms^{-1}$), which equals to $1.438 * 10^{-2} mK$.

Geometric correction - Landsat

The geometric corrections of all the Landsat images (Landsat 5 and Landsat 7) were done based on image to image geo-rectification. Since, the available Landsat images were of correction level 'systematic'. A geometrically corrected ASTER image of 15m resolution has been used as a base image for the correction of individual time series images. Sample points have been selected based on the user knowledge and from earlier field survey data. The thermal infrared bands (TIR) within Landsat 5 and Landsat 7 have been resampled to a constant resolution, i.e., to the spatial resolution of TIR band of Landsat 5 (120 m).

LST generation and radiometric normalization - Landsat

There were several different radiometric correction methods available. Choosing the right method for this study was based on the available data and the task at hand. There are several methods for absolute radiometric calibrations and relative radiometric calibrations. The context of this study was to analyze the UHI effect for the same region from time

series images and to compare the results obtained. To acheive consistent images, relative radiometric calibration using absolute normalization has been performed. The selection of sample points, i.e., pseudo invariant features (PIF) in all the images is an important task in the relative radiometric calibration process. Multivariate-alteration detection (MAD) (Schroeder et al., 2006), post-correction evaluation index (Quadratic Difference Index) (Paolini et al., 2006) and statistical selection of features using principle component analysis (Du et al., 2002) were some of the few from the vast selection of methods available. Some of them depended on field data and some purely depended on statistical models. In this study, based on field data and knowledge of the area under study, a semi-statistical approach (Haute, 1988) using temporally invariant features (TIC (Chen et al., 2005)) has been implemented.

The initial normalization of the five imageries has been accomplished by converting the digital numbers (DN) to exoatmospheric radiance or black body temperature (Weng and Lu, 2008). The DN values of the Landsat 5 and Landsat 7 TIR band have been converted to spectral radiance using Equation 4.3 adopted from Markham and Barker (1985) and equation 4.4 adopted from Landsat user handbook.

$$L_\lambda = 0.0056322 * DN + 0.1238 \tag{4.3}$$

$$L_\lambda = 0.0370588 * DN + 3.2 \tag{4.4}$$

The spectral radiance of the TIR bands were then converted into blackbody temperature using equation 4.5 (Wukelic et al., 1989)

$$T_B = \frac{K_2}{ln\left(\frac{K_1}{L_\lambda} + 1\right)} \tag{4.5}$$

where T_B is the effective at-satellite temperature in Kelvin (K), L_λ the spectral radiance in $Wm^{-2}sr^{-1}\mu m{-}1$; and K_1 and K_2 are the pre-launch calibration constants. For Landsat-

5 TM images, $K_1 = 60.776\ mWcm^{-2}sr^{-1}\mu m$, $K_2 = 1260.56K$ and for Landsat-7 ETM+ images $K_1 = 1282.71\ mWcm^{-2}sr^{-1}\mu m$, $K_2 = 666.09K$

After the conversion of the images to black body temperatures, time-invariant features (TIFs) between images have been selected for normalization. Within this study, selection of TIFs has been based on previous field survey, available building history and visual examination of the true color and pseudo true color images over time. A single image has been selected as 'master' and the rest have been considered as 'dependent' or 'slave images'. The final process then involved the extraction of the brightness component (temperature values at TIF locations) from the 'master' and 'slave images'. A simple linear regression model has been developed from the scatter plot of the slave and master image values for the same locations and this formula has been then used to convert the 'slave' image to match the 'master'.

Scaled normalized difference vegetation index (SNDVI)

The SNDVI in this study has been calculated from the ASTER images using equation 4.6. The resulting image has been scale transformed from scale -1 - 1 to 0 - 2. The assumption was that by doing so it would help in increasing the efficiency of the processing. The resulting image has been converted into categorical data of 10 classes using the algorithm that best suited the model. This selection of the algorithm was based on sensitivity analysis conducted over sample datasets.

$$NDVI = \frac{NIR - R}{NIR + R} \tag{4.6}$$

Where, NIR and R refer to very near infrared bands VNIR-Band3N (B3) and VNIR-Band2 (B2) respectively (within the ASTER image data set).

Population density dataset

The reason for inclusion of population data was to study the relation between population density and LST. Population is one of the major factors that indicate urban sprawl. Population is one of the reasons why UHI effect is proved to be more prominent in the developed cities. The map of population zones along with block identifiers (by Indiana Geological Survey) and population (2000 population census) were used in this study. There were three levels of population data representing block, block group and tract level data. Block group level population statistics (658 blocks within the Marion County/the city proper of Indianapolis) have been selected for this study, since they were a more detailed representation as compared to the other two. The assumption was that more variation at a pixel level would improve the strength of relationships between the variables of interest. The population map was converted into population density raster dataset by dividing population by map area, i.e., block group population data divided by the area of the specific block group. The resultant density raster has been further classified into interval dataset. This selection has been based on the sensitivity analysis (similar to the creation of SNDVI). Care has been taken that a constant model was used for all such cases to reduce the variability within data generation.

4.2 UHI Analysis Models and Methods

In this research, three different models were used to study UHI. These were, an exploratory model (for realizing the existence of UHI within a region), micro model and macro model (for quantifying the effect of UHI).

Exploratory data analysis

Exploratory data analysis (EDA) can be described as data-driven hypothesis generation where an examination of the data is performed in search of structures that may indicate

deeper relationships between cases or variables using principles from cartography and/or statistics (in this case cartography) (Klosgen and M.Zytkow, 2002). EDA contrasts with hypothesis testing, which begins with a proposed model or a hypothesis and undertakes statistical manipulations to determine the likelihood that the data arose from such a model (Hand et al., 2001). Cartography as a discipline has a significant stake in the evolving role of maps within systems for scientific visualization, within spatial decision support systems, within hypermedia information access systems, and within virtual reality environments. Further, 'spatial analysis' and 'spatial simulation' could be considered prototypical components of scientific visualization (MacEachren and Kraak, 1997).

Visual representation of data and concepts are also indispensable materials in the construction of scientific knowledge. Moreover, quantitative data about the environment, once in short supply, now exceeds our capacity to learn from them. In this research, 3D visualization through animation has been used as a method for exploratory analysis of the UHI phenomenon. Figure 6 illustrates the process diagram of the data analysis. Although cartographers have been interested in the potential of the animated maps for decades, compared to static maps, animated maps have always been difficult to make, distribute and access. The computer revolution has given cartographers the means to more easily create animated maps and map users a way to view animated maps (Harrower, 2004).

Association rule mining using spatial datasets

In this research, the technique of association rule mining has been specially utilized to study and understand the quantitative relationship between LULC patterns and other environmental, physical and demographic data at a micro level. Even though the very nature of urban LULC is dependent upon various influencing factors, the nature of dependence between LULC and LST has proved to be strong. Therefore, the main rationale of this research was to model, analyze and quantify this relationship. An

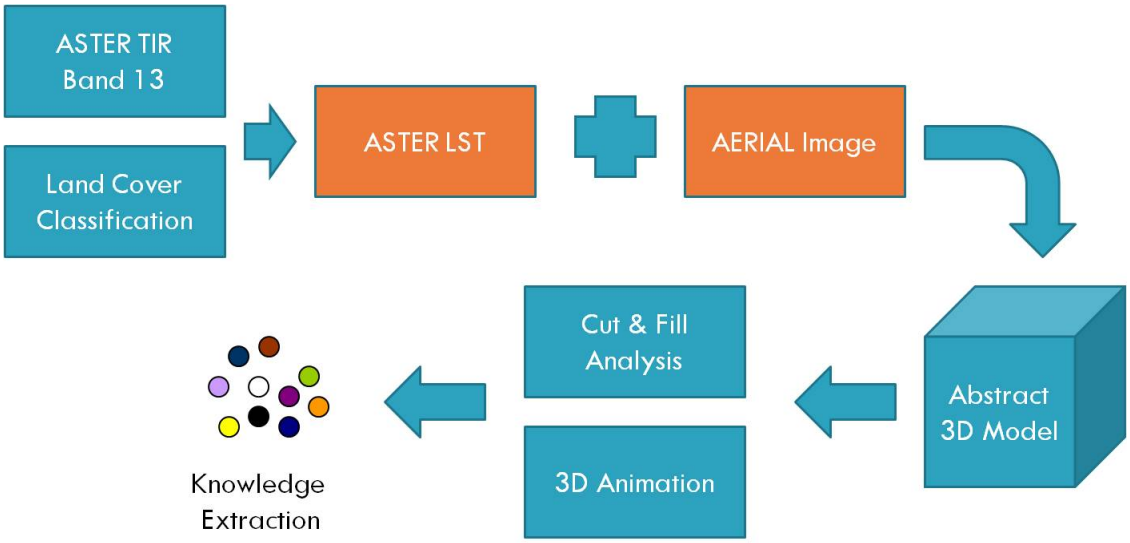

Figure 6. Model describing the steps involved in the exploratory data analysis

association rule is a relationship of the form $X \geq Y$, where X and Y are sets of items. X is called antecedent and Y the consequence. There are two primary measures, support and confidence, used in assessing the quality of the rules. The goal of association rule mining is to find all the rules with support and confidence exceeding user specified thresholds (Ding et al., 2003).

The brief explanation of the terms support and confidence are as follows (modified from Borgelt and Kruse (2002)):

Let T be the set of all transactions under consideration, i.e., let T be the set of all the attributes (in this research LULC, population density, LST, NDVI, zoning and distance to the major roads) which were recorded on an image v. Let LC be a subset of a certain type which contains a particular set of attributes. Then the support of type LC is the percentage of pixels in T which cover similar attributes. For example, LC is a subset which has the attributes: LULC = urban, temperature = $20°C$ and distance = $400m$ from the road network. Then if ϵ is the set of all pixels within the image T which contains all the attributes of LC, then

$$support\,(LC) = (|\epsilon| \,/\, |T|) * 100\% \tag{4.7}$$

where $|\epsilon|$ and $|T|$ are the number of pixels in ϵ and T, respectively.

The confidence of an association rule is the measure used to evaluate association rules. The confidence of a rule $R = A\ and\ B \Rightarrow C$ is the support of the set of all items that appear in the rule divided by the support of the antecedent of the rule, i.e.

$$confidence\,(R) = (support\,(\{A, B, C\}) \,/\, support\,(\{A, B\})) * 100\% \tag{4.8}$$

The confidence of a rule is the number of cases in which the rule is correct relative to the number of cases in which it is applicable. For example, let R = *urban land cover and distance from highway 400m belongs to* $20^{\circ}C$ *temperature*. It means that, for a given pixel, if LULC is urban and if its location is around $0 - 400m$ from the major highways, then the temperature value recorded for such region is $20^{\circ}C$. It also means that for a given pixel, if LULC is not urban, the location is not around $0 - 400m$ or neither, then the rule is not applicable, and does not say anything about the resulting temperature values. If the rule is applicable, it means that the resulting temperature can be expected to be $20^{\circ}C$. At the same time, if the rule is found to be applicable, but the temperature is not as expected, then the rule may not be correct. The interest is in how good the rule is, i.e., how often its prediction for a given attribute type turns out a constant temperature. The rule confidence measures the percentage of cases in which the rule is correct. It computes the percentage relative to the number of cases in which the antecedent holds, since these are the cases in which the rule makes a prediction that can be true or false. If the antecedent does not hold, then the rule does not make a prediction, so these cases are excluded.

According to the support–confidence framework (Zhang and Zhang, 2002), and rules of association by Silverstein et al. (1997), support of a rule can be enumerated as follows:

1. $X \cap Y = \emptyset$,

2. $p(X \cup Y) \geq minsupp$,

3. $p(Y|X) \geq minconf$ $(e.g., conf(X \rightarrow Y) \geq minconf)$, and

4. $\left| \frac{p(X \cup Y)}{p(X)p(Y)} - 1 \right|$

The valid association rule $X \rightarrow Y$ can be extracted to a valid rule of interest. The above set of rules describe the method of extracting association rules, further conditions could be added to generate positive association rules within which the confidence of the rules are higher and negative association rules within which the confidence of the rules are lower. An initial scenario was able to to find the positive relationship between objects (e.g., if LULC type A is present, then the temperature should be within range 'X'). The latter helped find the negative relationship between objects (e.g., if LULC type A is present then the temperature will most likely not be within range 'X'). This research was aimed at extracting the parameters which have impact on LST with the main concentration has been towards extracting positive association rules.

Figure 7 illustrates the process model of micro-anlayis that has been undertaken by this research.

Descriptive analysis of UHI

The macro-analysis includes two main components. The first is the characterization of the UHI from the infrared images and the second is the comparison of the characterized urban heat effect with LULC. In this research, MODIS LST images have been used for the time series analysis due to their relatively high temporal resolution (daily day and night images) and Landsat 5 and Landsat 7 derived LST has been used for the analysis of the relationship with LULC due to its relatively high spatial resolution and also its availability over long time periods. Due to the large number of images that have been used for this analysis a non-parametric process convolution(kernel convolution) model has been used to characterize UHI from LST images.

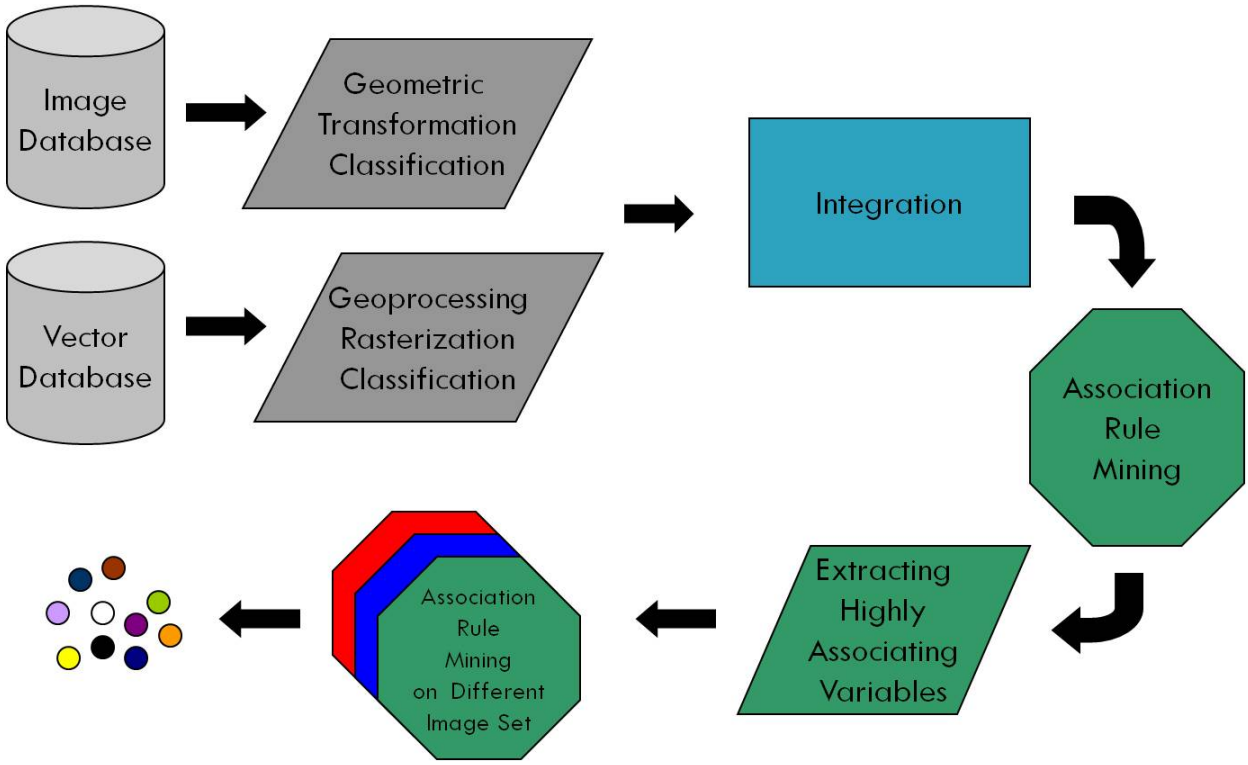

Figure 7. Model describing the steps involved in the micro-analysis

There are several methods that are available to characterize the phenomenon over the space. For example, filters, splines, surface interpolations, non-linear least square. These well documented methods are readily available within many of the conventional spatial analysis software. Two of the main drawbacks with these parametric approaches are: 1) they are user dependent, and 2) they are image dependent. The above methods are user dependent because they need users to provide them with initial parameters and these mostly change over time and over space. The methods were also image dependent because as the size of the image changes or as the distribution of no-data values within the image change they tend to either fail or provide inconsistent results. In this research, several MODIS images with varying degrees of cloud cover were analyzed using a non-parametric process convolution approach. This approach is less user dependent. It also provides the least variation in image characteristics.

Kernel smoothing refers to a general class of techniques for non-parametric estimation

of functions. The kernel is a smooth positive function $w(z,h)$ which peaks at 0 and decreases monotonically as z increases in size. The smoothing parameter h controls the width of the kernel function, hence, the degree of smoothing applied to the data.

As the smoothing parameter increases, the resulting estimate misses some details and as the smoothing parameter decreases, the estimator begins to track the data too closely interpolating the observed points (Bowman and Azzalini, 1997).

One can define a Kernel as a function k that for all $x,z \in X$ satisfies (Taylor and Cristianini, 2004)

$$k(x,z) = \langle Œ(x), Œ(z) \rangle, \tag{4.9}$$

where ϕ is a mapping from X to an (inner product) feature space F

$$Œ : x \longrightarrow Œ(x) \in F \tag{4.10}$$

The degree of smoothing to be performed by the kernel is defined by its bandwidth, h. The value of h increases as the degree of smoothing increases and vice versa. When the value of h starts to decrease beyond a certain threshold, the degree of smoothing starts to over fit the data points leading to interpolation between the values. Similarly, when h starts to increase beyond a certain threshold it tends to over-fit the data, leading towards a straight line. Therefore, the selection of a suitable bandwidth is very important for capturing patterns. In this research the bandwidth has been selected through sensitivity analysis of the parameter h on Landsat and MODIS images.

The process defined by the kernels have been convoluted to yield a single image in time. The convolution of f and g could be written as $f * g$. It is defined as the integral of the product of the two functions after one is reversed and shifted.

$$(f * g)(t) = \int f(ø)\, g(t - ø)\, dt \tag{4.11}$$

If X and Y are two independent variables with probability densities f and g, then the probability density of the sum $X + Y$ is given by the convolution $f * g$. For discrete functions, one can use a discrete version of the convolution. It is given by equation 4.12.

$$(f * g)(m) = \sum_{n} f(n)\, g(m - n) \tag{4.12}$$

Discrete kernel estimation of $\psi_{(a,b)}$ requires $O(n^2)$ kernel evaluations making the computation very expensive for large sample sizes, especially remote sensing images. In order to reduce the cost of computation IFourier transform methods have been used to compute the required convolution. The discrete Fourier transform of a complex vector $z = (z_0, \ldots, z_{n-1})$ is the vector of $Z = (Z_0, \ldots, Z_{N-1})$ where,

$$Z_j = \sum_{l=0}^{N-1} z l e^{2\beta i l j / N}, j = 0, \ldots, N - 1 \tag{4.13}$$

The vector z can be recovered from its Fourier transform, Z, by applying the inverse discrete Fourier transform formula.

$$z_l = N^{-1} \sum_{l=0}^{N-1} z l e^{2\beta i l j / N}, l = 0, \ldots, N - 1 \tag{4.14}$$

Discrete Fourier transforms and their inverses can be computed in $O(N \log N)$ operations using the fast Fourier transform(FFT) algorithm. The algorithm is fastest when N is highly composite such as a power of 2. The discrete convolution of two vectors can be computed quickly using the FFT by appealing to the discrete convolution theorem: multiply the Fourier transforms of two vectors element-by-element and then invert the result to obtain the convolution vector.

The above processes have resulted in a series of UHI images in space over time. In order to analyze these images with respect to LULC in space and UHIs in time Kullback Leibler divergence (Kullback and Leibler, 1951) has been used. In the work presenteed here,

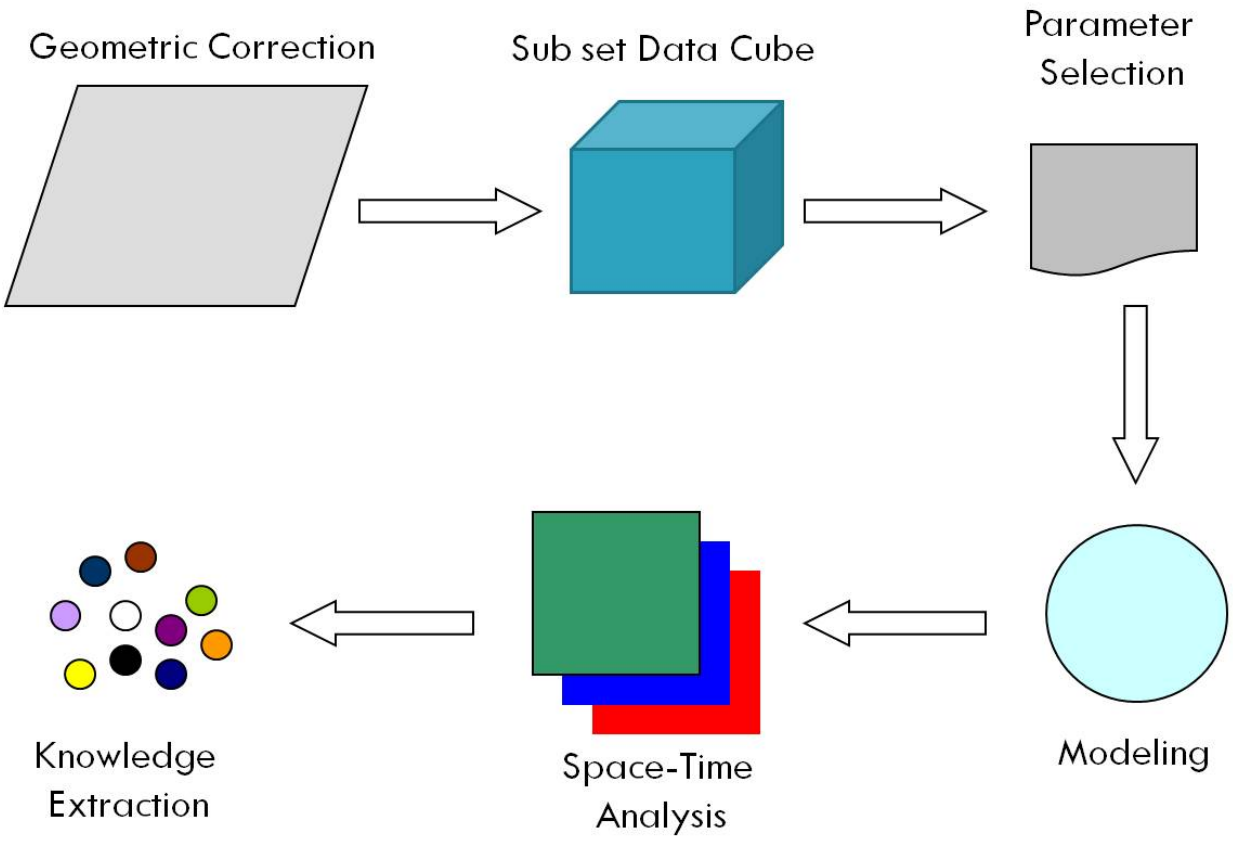

Figure 8. The schema for mining series of images, from observation, through modeling and analysis towards prediction

measures of divergence between MODIS time series images were calculated to analyze seasonal behavior and annual variation of UHI. Figure 8 illustrates the flowchart of the descriptive analysis from image correction through modeling, analysis to information extraction.

The model also includes a series of analyses involving visualization techniques such as animation and overlays to effectively understand the end results.

4.3 Summary

This chapter described in detail the data used, their preprocessing and the methodologies that were adapted for the analysis of UHI. The primary information generation from the

data sets included land use land cover information from image dataset, generation of land surface temperature from the image spectral information, radiometric normalization, scaled normalization of associated information and geometric correction of spatial dataset.

Three models for UHI visualization, identification and extraction were later described in detail. These models included exploratory data analysis, association rule mining of spatial dataset and descriptive analysis of the UHI phenomenon using non-parametric kernel convolution. The rationale and process involved within each models were explained using analogies, process diagrams, mathematical derivation and examples where necessary.

The next chapter describes in detail the results obtained from each of these models and their interpretation. This chapter also provides the discussions of the results with respect to the real world scenario where necessary to enable broader impact of the study and its possible applications.

CHAPTER 5

RESULTS

This chapter explains the results obtained from the models detailed in chapter 4. This chapter is divided into three sections based on the type of model used and their respective results. Section 5.1 outlines the results obtained through visualization. Subsections within this section shed light on the result of analysis over different land use land cover types namely; residential, commercial, roads, open areas and water bodies. Section 5.2 presents results of association rule mining model. Within this section the results are broadly classified into three subsections. The first subsection describes the data used, while the second and third subsections describe results of the classification schema and the mining algorithm. This section also highlights the effect of image resolution on association mining results. Section 5.3 describes results obtained from the implementation of non-parametric kernel convolution model over MODIS time series images. The section is divided into three subsections describing the results from analysis of land surface temperature, urban heat island (UHI) and the effect of UHI in space and over time.

5.1 Visualization of UHI

3D modeling was used for visualization of thermal data with land cover data. ArcMap 9.1, a product of ESRI (Environmental Systems Research Institute), was used for visualization of results. In this research, experiments using Bertin's visual variables such as position, color (including transparency), shape and size (through 2.5D abstractions, since there was

no volume involved but will be referred to as 3D within this research) were carried out to visualize and analyze the urban heat island effect.

In the resultant abstract model, computed land surface temperature was used as base heights for an aerial photograph image drape. In other words, objects were given heights not with respect to their actual elevation from the ground, but by the relative heat radiated by them. Even though visually one would not be able to quantify the amount of heat, one would be able to identify the relative difference in the surrounding land cover types thereby facilitating a qualitative comparison. In this study, five land use types namely Residential, Commercial, Water Bodies, Open lands and Roads were analyzed for anomalies visually.

For a scientist, the desired outcome of visual thinking is scientific insight i.e., noticing meaningful patterns or anomalies in data (DiBias et al., 1992). In this case, to analyze the heat in and around downtown Indianapolis, cut and fill operations were performed to various segments of the image subset and also to the subset as a whole. This analysis is similar to hydrological modeling, where, given a city's digital elevation model (DEM) and varying flood height, the submergence level is simulated. In this research, instead of using the DEM an abstract "terrain model" of temperature was used for analysis. Varying degree of heat levels were used for the simulation and the relative temperature differences for varying land cover types were analyzed. The amount of variation in heat radition by objects relates to the presence/absence of heat islands.

In order to communicate the information to viewers a fly-by/ animation was created. A fly-by is a sequence of views of a static surface or volume in which the view point of the camera used for animation changes gradually. A track, including land use types (which were analyzed during the visual thinking stage), was outlined and the camera was maneuvered along this track thereby giving viewers a picture of the entire scene. The scene provides the viewers with the visual information on influence of land cover types and human activities in the formation of UHI. Due to the amount of memory (computer

processor) that was consumed for the process, certain compromises had to be made in order to execute the model. After experimentation with the entire city of Indianapolis (Marion County), Indiana, the time required for the software to refresh the screen in order to run the animation and to display the image was too high. Therefore, the option of a subset was chosen, where only a selected portion of the city encompassing downtown and the neighboring areas to the west and east of the White River were selected and used for the animation. Care was also taken that the selected subset comprised of all the five land cover types under study, in order to make an effective analysis and comparison. Furthermore, resolution of the aerial imagery was too high. Even with advancement in terms of computing technology (Intel Pentium IV processor with 3.00 Ghz of processing and 1 gigabyte of random access memory (RAM)) display of the subset in actual scale was not possible. In order to overcome this problem the resolution of the aerial image was scaled down to 1/3 of its original resolution for the animation and analysis. This drastically reduced the quality of the presentation, but nevertheless buildings and other objects were not difficult to identify. Even though the reduction in resolution proved to be a compromise in the quality of the 3D model, it increased overall efficiency of the process.

One important aspect which has to be taken into consideration is that this research addresses the relative temperature difference at the urban centre alone. Theoretically, the mean, the minimum and the maximum temperature under discussion are relatively higher than the mean, minimum and maximum temperature of the rural setting surrounding the city of Indianapolis for the same day.

In spite of the well known phenomenon i.e., urban temperatures are relatively higher than rural temperatures, this study attempted to shed more light on the UHI effect at the macro and micro level. Overall urban temperature is a combined effect caused due to the presence of vegetation (Weng, 2001), by the characteristics of the impervious material (Quattrochi and Ridd, 1994) and their spatial distribution. All these aspects are clearly identified through the 3D visualization and the cut and fill operation. The results obtained

by various land cover types such as residential, commercial, water bodies, open lands and roads are discussed below. The maximum, minimum and mean temperatures for the given subset were 283, 306 and 293 degree Kelvin respectively. Even though calculations were made on the basis of actual recorded values in reality these values change altogether on a day to day basis depending upon cloud cover and season. In order to overcome this, relative temperature measurements (with respect to the minimum, maximum and mean temperatures for each classes) were used for analysis.

Residential

Residential areas within this study were classified by the presence of low-rise buildings, which are well spaced and have not so dense vegetation around them. Since heat within most of the areas is also influenced by neighboring regions, two separate residential areas were selected for analysis. One along the eastern side, near Interstate-70 and another at the southeastern side of Indianapolis. Figure 9 and 10 depict residential areas around downtown Indianapolis. From these two images and the result of the simulation as illustrated in the Figures 9 (b) & (c) and 10 (b), (c) & (d) it was found that around 50% of the residential areas were within the mean temperature range. But in some areas maximun heat was a degree Celsius more than the mean level. These areas are of commercial buildings among the residential areas (refer Figures 9 and 10). It was also noted that, at a macro level, irrespective of their high vegtation index, residential areas which were closer to commercial buildings and open impervious parking spaces tend to be influenced by the surrounding higher temperatures.

Commercial

Commercial areas within downtown Indianapolis are completely different from many other commercial establishments found within the city mainly due to the structure and type of buildings. The commercial class within this study also includes industrial

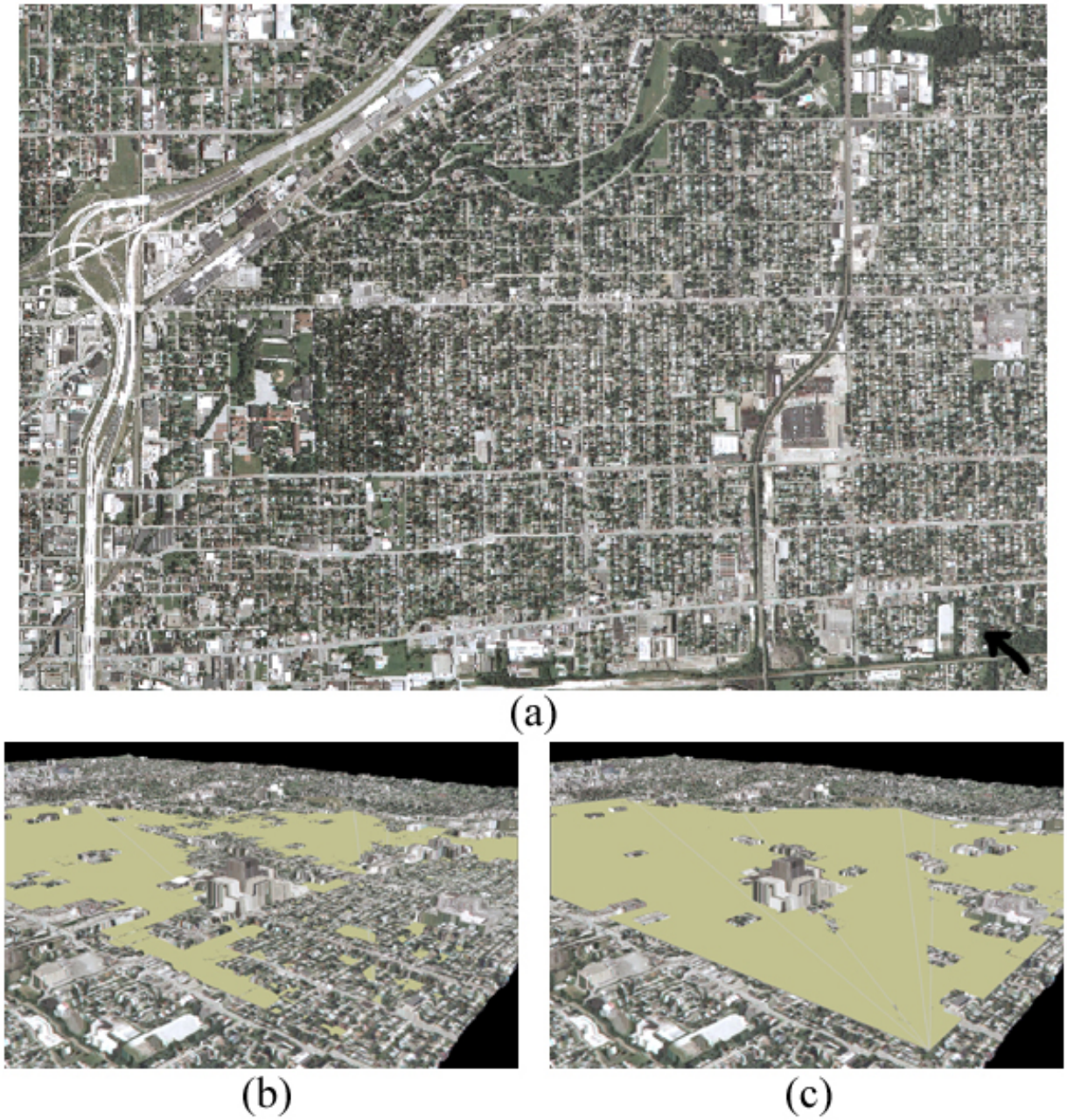

Figure 9. Figure (a) represents the aerial view of the residential area along eastern side of Indianapolis close to Interstate–70. The arrow within the figure (a) at the right bottom corner of the image shows the position of the camera from which the perspectives (b) and (c) were captured. The figure (b) and (c) are the results of the simulation of heat level 19 and 21 C respectively. The yellow color depicts the varying levels of submergence for the varying heat thresholds.

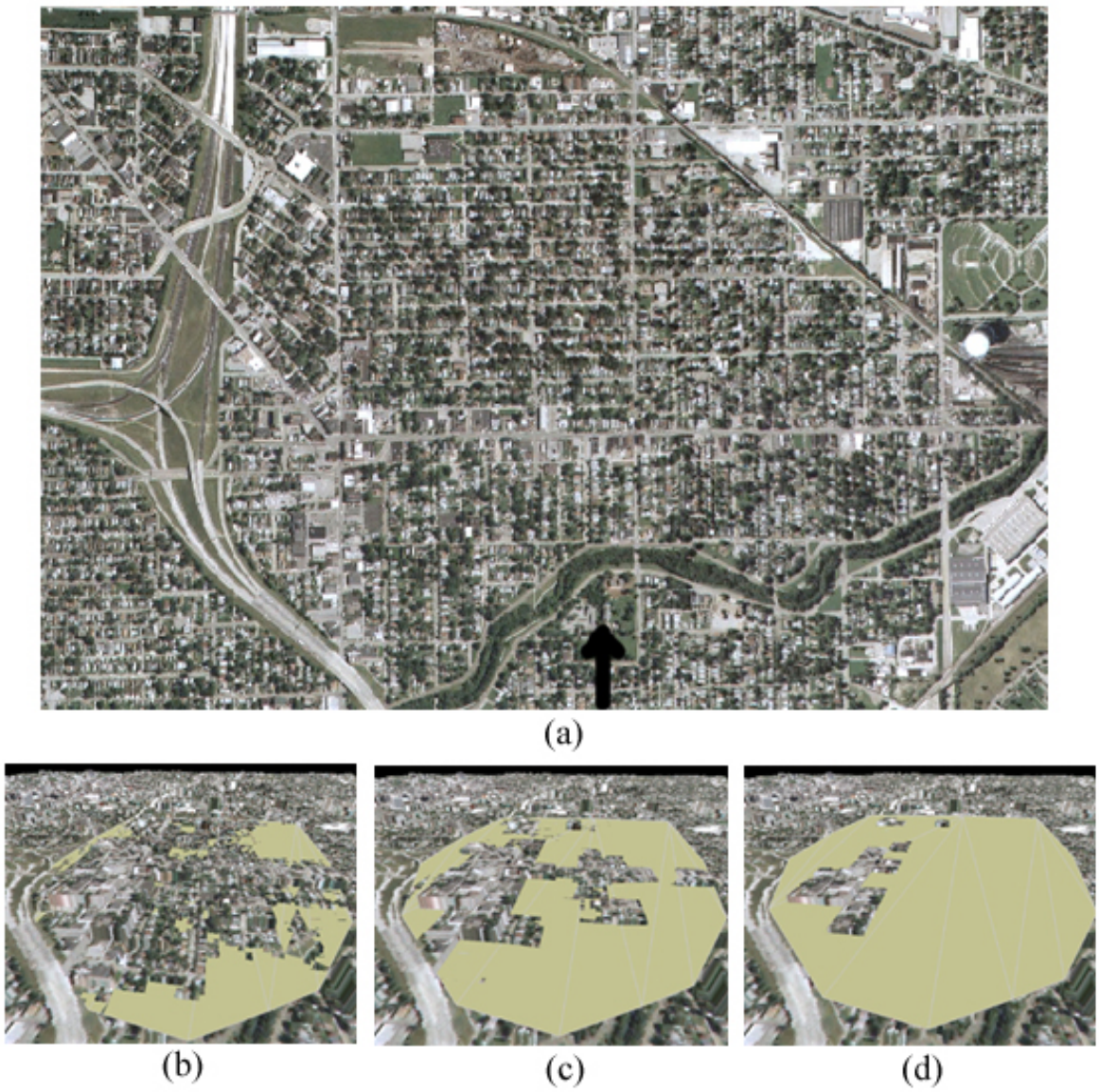

Figure 10. Figure (a) represents the aerial view of the residential area along eastern side of Indianapolis close to Interstate–65. The arrow within the figure (a) at the bottom of the image shows the position of the camera from which the perspectives (b), (c) and (d) were captured. The figure (b), (c) and (d) are the results of the simulation of heat level 19, 21 and 23 C respectively. The yellow color depicts the varying levels of submergence for the varying heat thresholds

structures. The overall heat level around downtown was $2^{\circ}C$ above the mean except for the RCA dome at central Indianapolis. Due to the type of material, its color and its structure, the dome has a radiant heat of $15^{\circ}C$ which was $5^{\circ}C$ less than the average temperature. Furthermore, all sky scrapers around central Indianapolis were also found to be cooler. The average temperatures recorded around these buildings were found to be very near the global mean temperature. This is visualized in Figure 11 (c). The reason for this anomaly was attributed to the roof type of these high-rise buildings (mostly slanting) and also the fact that most of the buildings are relatively tall; therefore, the shadow cast by these buildings prevents the heat from directly reaching the ground. These reductions in the incident energy contribute mainly to the above effect. The RCA dome was also found to radiate the least heat among the downtown commercial structures. The buildings which were found to radiate the most heat, in downtown were commercial buildings adjacent to the RCA dome (including the Circle center mall) and the Chevrolet motor division on the west side of downtown and the White River. Apart from these regions, there were several other commercial buildings and open parking areas which were found to radiate relatively high heat. This aspect can be be seen in Figure 12 (b), (c) & (d).

From the above analysis it appears that the relative heat around commercial buildings was $5 - 7^{\circ}C$ higher than the global mean. Based on detailed analysis of the aerial image, it could be inferred that roof type negatively affects the heat radiation budget of buildings, whereas other aspects such as the location of air conditioning elements on roof tops positively affects the radiation. Nevertheless, further detailed study along with field work is required to analyze the exact reasons and influencing factors for high heat over these selected regions which contribute to a great extent towards the overall cahrecter of UHI.

Apart from the study of UHI, the strong temperature difference observed between residential and commercial areas could be used for land use classification. Further analysis on the thermal behavior of buildings in combination with a DEM could lead to the development of a robust land use classification technique, based on heat differential.

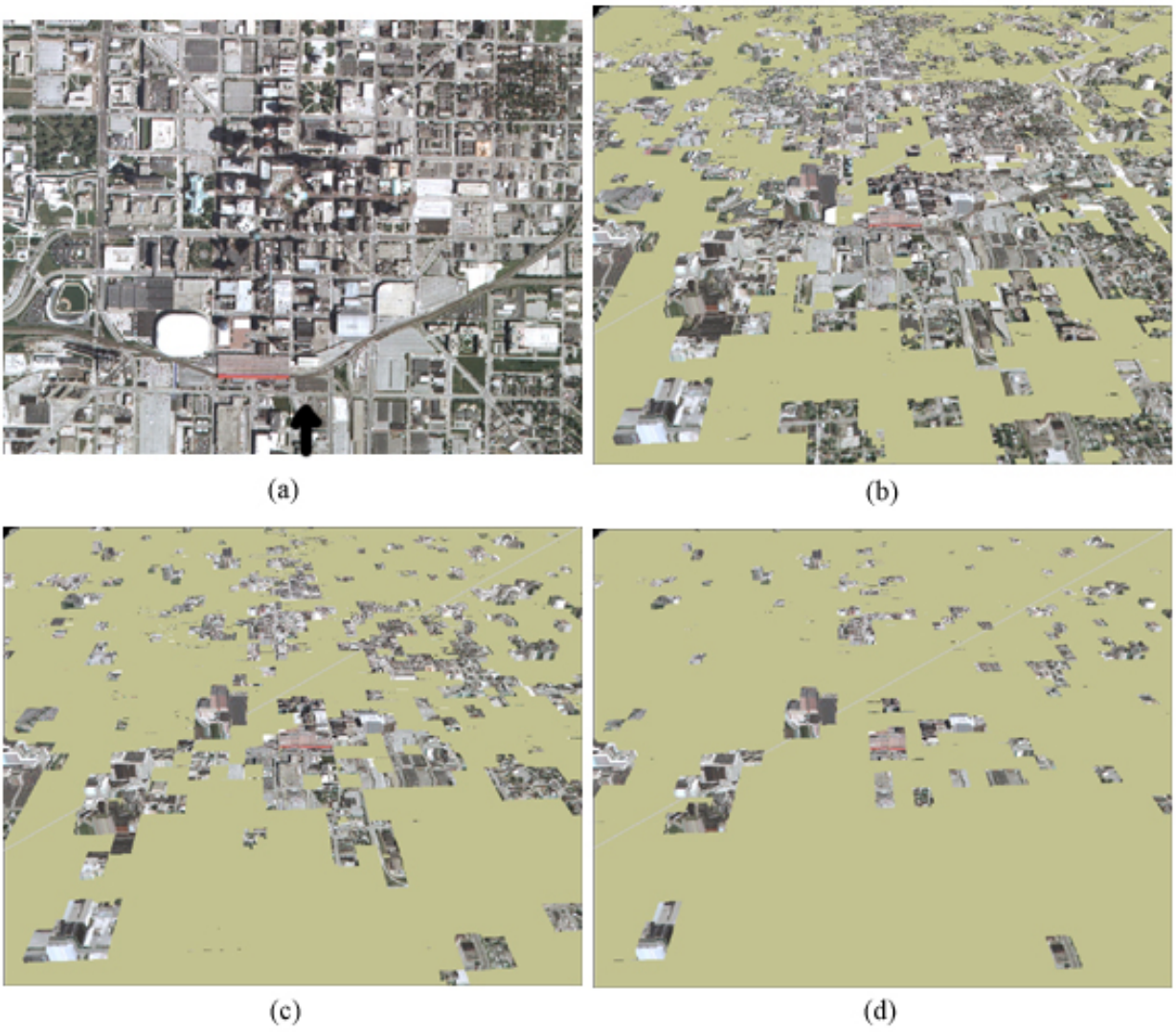

Figure 11. Figure (a) represents the aerial view of the commercial area in the downtown Indianapolis. The arrow within the figure (a) at the bottom of the image shows the position of the camera from which the perspectives (b), (c) and (d) were captured. The figure (b), (c) and (d) are the results of the simulation of heat level 21, 23 and 25 C respectively. The yellow color depicts the varying levels of submergence for the varying heat thresholds

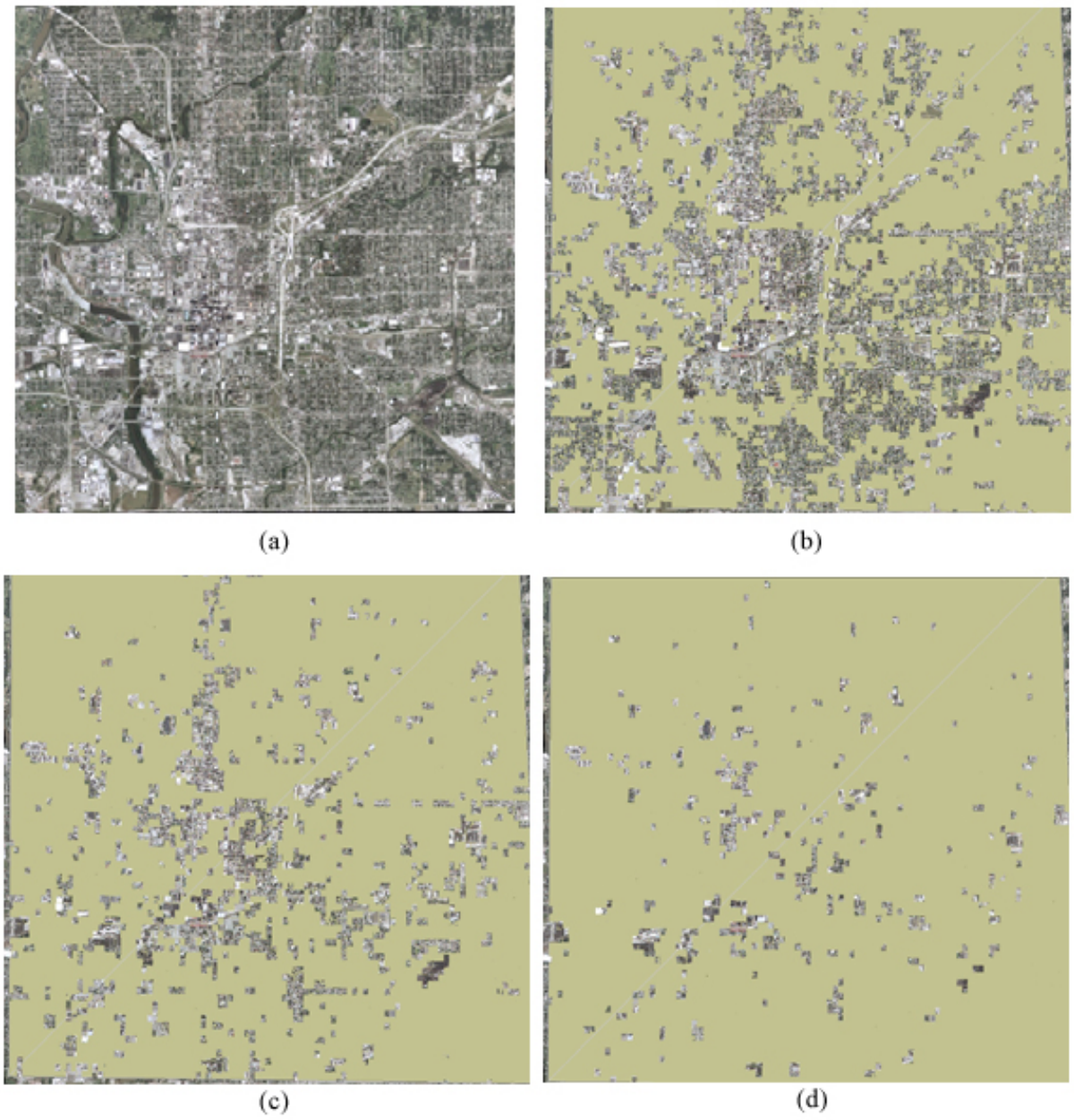

Figure 12. Figure (a) represents the aerial view of the entire subset of the imagery (Indianapolis downtown). The figure (b), (c) and (d) are the results of the simulation of heat thresholds at 21, 23 and 25 C respectively. The yellow color depicts the varying levels of submergence for the varying heat thresholds. It can be observed that the level of submergence is minimal at $294^{\circ}K$ and occupies both commercial and a few residential areas. One can visualize from the simulation (b) that with an increase of $2^{\circ}C$ almost all the residential, water bodies and road networks are covered and only the commercial establishments are left out. With a further increase of $2^{\circ}C$ simulation (c) we can see only the roof tops of most of the commercial buildings

Roads

Within this research, two road sections near downtown Indianapolis were analyzed. One section was from interstate-70 and the other was from interstate-65. Figure 13 (a), (b), (c) and (d) illustrate the road sections and the result of the simulations. The main reasons for selecting interstates rather than streets were, first they were broad enough to be captured by the ASTER TIR bands. Second, the probability of shadows from adjacent buildings and trees would be almost negligible. There were a few major roads which were initially analyzed but most of their sections were influenced by the heat of adjoining buildings and it was difficult to differentiate the influence due to mixed pixel effect.

From the simulations of the major interstate sections within the city of Indianapolis,it appears that the radiation of heat from highways is almost equivalent to that of the overall mean heat level. It was also found that interstate-65 was $2^{\circ}C$ hotter than interstate-70. The major reason for this could be difference in the construction materials used for the sections analyzed (i.e., difference in radiation of heat between asphalt and reinforced cement concrete). Further investigation and field work needs to be done to analyze this discrepancy of radiation between these two interstate sections.

Open areas and water

Figure 14 and 15 qualitatively depict the heat radiation from the water bodies and open areas respectively. From the analysis it was concluded that water bodies radiated the least amount of heat with an average of $13^{\circ}C$ over the sections of White river. This is $10^{\circ}C$ less than the effect observed in central Indianapolis. Open areas on the other hand were about the same as residential areas with a mean of $21^{\circ}C$. On a detailed analysis it became claer that structures near water bodies also show less heat and areas with green vegetation radiate less heat. The amount of variation from normal temperatures is not a constant factor, and a detailed analysis of each and every type of land cover and their

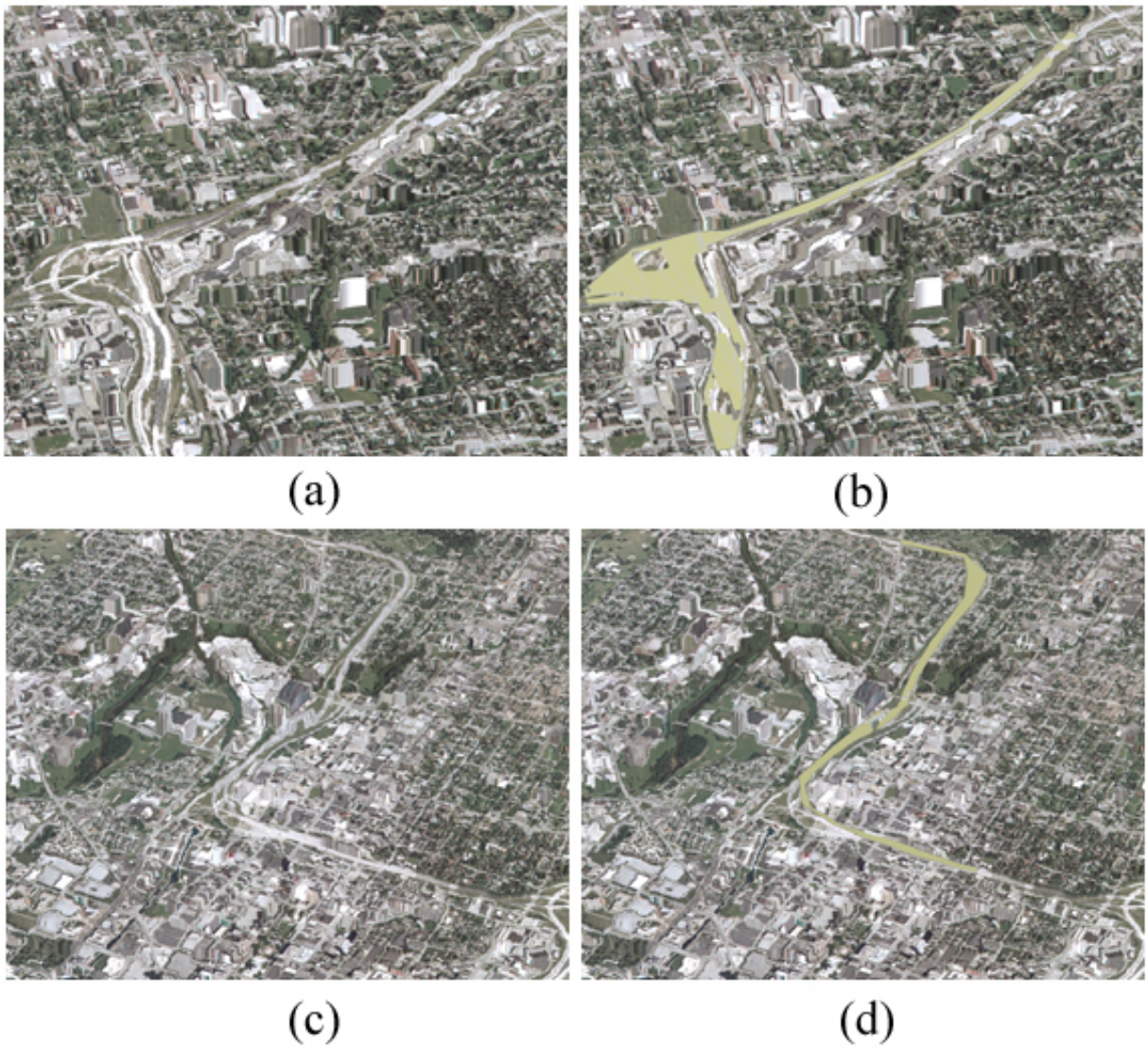

Figure 13. Figure (a) and (c) represents the perspective views of the interstate-70 and 65 respectively before the simulation. Figure (b) and (d) represents the section at a heat level of $292^{\circ}K$ and $294^{\circ}K$ respectively

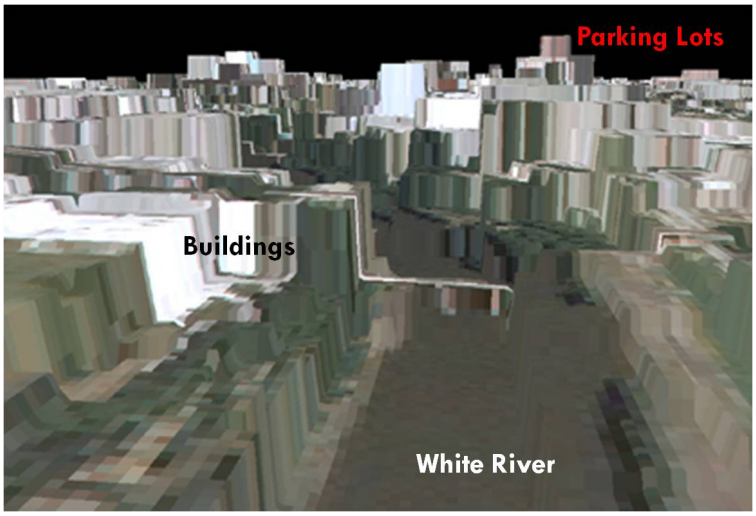

Figure 14. A 3D scene of the river front area along the White River on the southern side of Indianapolis. From the image one can visualize the difference in the heat radiated by the water bodies and the adjacent land covers such as buildings and vegetations.

association with their surrounding structures, needs to be analyzed in detail.

5.2 Association Rule Mining

Association rule mining over spatial dataset is a complex process riddled with uncertainty. This is mainly due to non uniform representation of information at both spatial and temporal scales. Furthermore, the complexity involved in linking raster datasets, which exhibit uniformity of representation over an area, with vector datasets, which exhibit the flexibility of representing objects of varying spatial scales, poses a challenge. In this research, land surface temperature (LST) is derived from three different sensors namely, the Enhanced thematic mapper (ETM+), the Moderate Resolution Imaging Spectroradiometer (MODIS) and the Advanced Spaceborne Thermal Emission and Reflection Radiometer (ASTER).Date from these sensors were used to test association rule mining model and to analyze the effectiveness of this algorithm in understanding the relationship of UHI and land use and land cover (LULC).

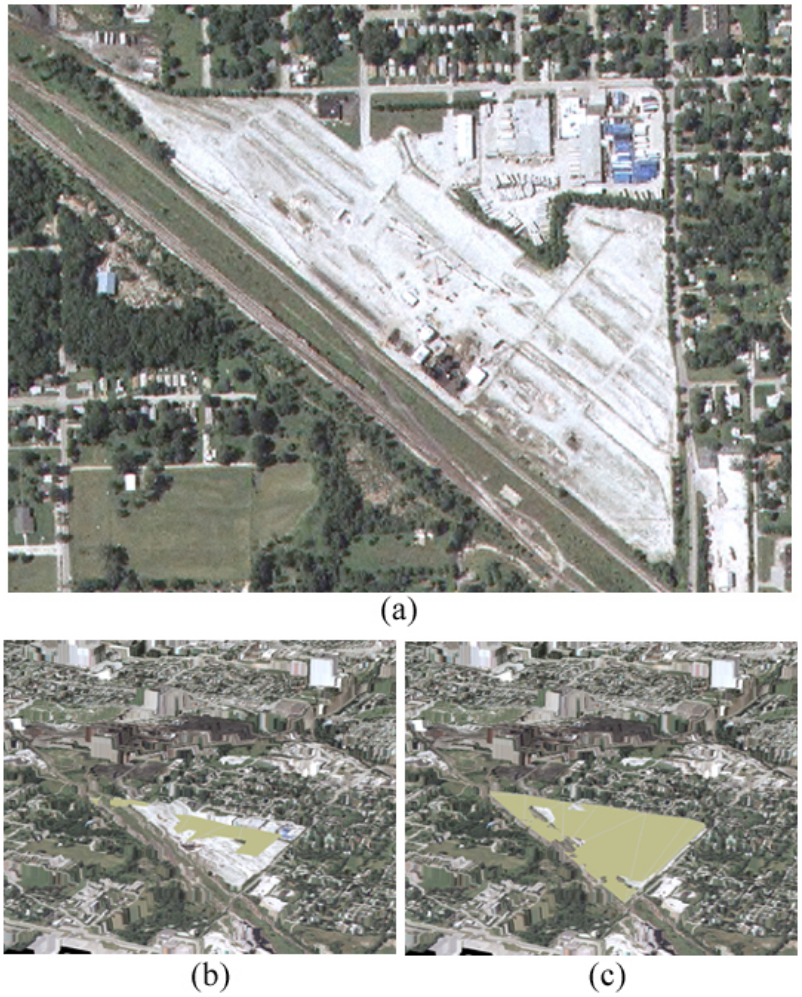

Figure 15. Figure (a) represents the aerial view of an open area on the south eastern side of Indianapolis close to industrial area. The figure (b) and (c) are the results of the simulation of heat level 19 and 21 C respectively. The yellow color depicts the varying levels of submergence for the varying heat thresholds

Data used

The data used within this experiment can be broadly classified into two different categories namely a) image or raster data set and b) vector data set. The image/ raster dataset used for the study are as:

1. LST derived from ASTER at 30m resolution re-sampled to 15m, dated 05th April, 2004.
2. NDVI derived from ASTER at 15m resolution, dated 05th April, 2004.
3. LST derived from Landsat ETM+ at 60m resolution, resampled to 15m resolution dated 12th April, 2003.
4. NDVI derived from Landsat ETM+ at 15m resolution, dated 12th April, 2003.
5. LST derived from MODIS at 1 km resolution, dated 20th June, 2004
6. NDVI derived from MODIS 1 km resolution, dated 25th June, 2004
7. National Land Cover Database (NLCD) at 16m resolution, developed and distributed by United States Geological Survey, dated 2001

During designing of the experiment and before the collection of necessary datasets, the rationale was to standardize temporal characteristics of the datasets to compare the effect of spatial and spectral resolution on the characteristics of UHI. Unfortunately, non-availability of information of uniform temporal characteristics led to variations in the datasets. Nevertheless, in order to successfully compare the results from image products, due consideration was taken to ensure that all images are from summer months with minimal cloud cover. In this study, cloud cover of less than 10% was considered acceptable.

Irrespective of efforts taken to standardize the temporal dimension of the datasets, there were minor deviations in achieving this. The reasons for such deviation include a)

non-availability of cloud free images over the study area and b) irregularity or problems with the sensor and image characteristics during the selected time period. The data used within this experiment had variations in both spatial and temporal resolution of the images used for this study. Therefore, normalization through classification was executed over these dataset to minimize the effect of problems within the satellite images (e.g. haze).

To complement the image data sets, vector datasets representing anthropogenic characteristics of land use and land cover, such as zoning and demographics, were used for analysis. The demographic information used for analysis included population density, average households, average family size, percentage of houses or buildings that are vacant within that area and the median age of the people living there. This information was collected from the 2001 census and was assembled at the block group level. The rationale for using demographic indicators was to analyze if there is a relationship between demographics and urban land surface temperature.

Results of classification and normalization

LST as derived from three sensors represents the temperatures as rational values. In order to successfully execute association mining, the rational data was converted into interval data types. There are several classification algorithms which facilitate the conversion of rational data types to interval data types. The most common of these classification algorithms include natural breaks, equal intervals, quantiles and standard deviation. Each of these algorithms has their set of advantages and disadvantages. Since, in this study, one of the main rationales was to develop an algorithm to perform association rule mining with minimal human intervention and to arrive at a method that could be replicated irrespective of the spatial and temporal characteristics of the dataset, a sensitivity analysis of the above algorithms was carried out. The results from the sensitivity analysis are presented in the Figure 16.

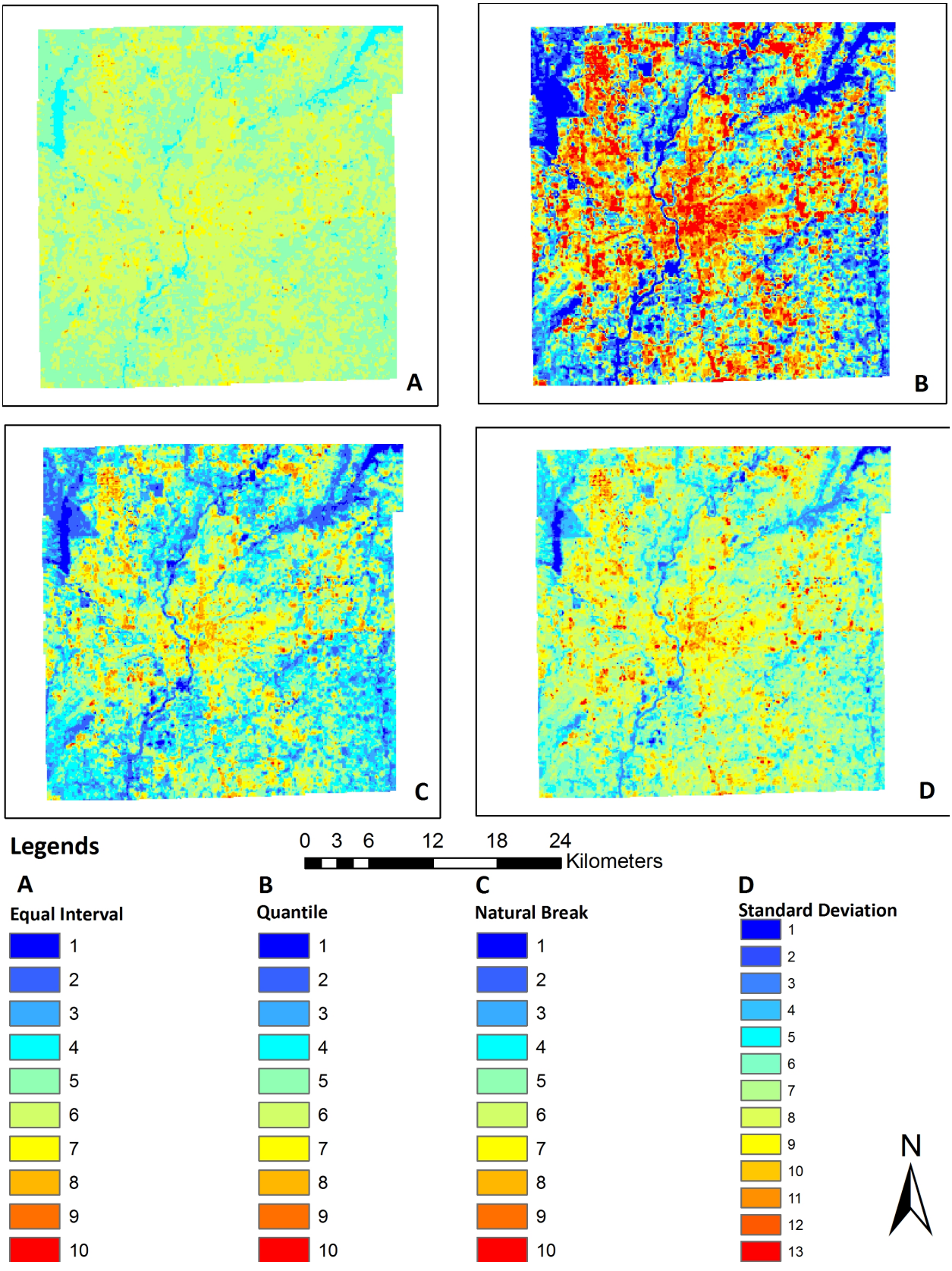

Figure 16. Result from the sensitivity analysis of four classification algoirthms

From the results of the sensitivity analysis, it is evident that, distinct categorization of LST over study area is possible through the quantile classification, whereas outliers or small scale anomalies, which are inclusive of variations, are evident using the equal interval classification. The remaining two classification techniques namely the natural breaks and standard deviation, were not as useful as equal interval and quantile.

Based on the sensitivity analysis, in this research, the classification algorithms that provided the two extreme representations of LST were considered for analysis. Furthermore, equal interval classification usually classifies the variation of temperature values by equally distributing them, starting from minimum or $0^{\circ}C$ (whichever is lower) to maximum (within-image) degree C. On the other hand, quantile classification incorporates the variation from minimum temperature to maximum temperature. The latter therefore provides a relatively better classification of LST images in space and over time for a fixed geographic location, while the equal interval classification may be of use while comparing the temperature anomalies across varying geographic locations. For example, comparing two cities.

LST and NDVI information derived from three sensors was classified separately using both the equal interval and quantile algorithms. The numbers of classes were limited to 10 to avoid over fitting and under fitting of the results. The equal interval and quantile classification schema for ASTER, Landsat ETM+ and MODIS are presented in Tables 3 through 5.

The NLCD 2000 and Land Zoning Map were used without any modification. The classes which were evident within the study area, their abbreviations and their brief descriptions are presented in Tables 6 and 7.

The demographic information, which was represented spatially at the block group level, was normalized to a scale of 1 to 10. The number of classes was selected to match the raster data classification. The normalization method was used for achieving maximum-minimum normalization, as mentioned in the chapter on methodology,

Table 3

Equal interval and quantile classification schema for NDVI and LST derived from ASTER

	NDVI					Temperature			
	Equal Interval		Quantile			Equal Interval		Quantile	
Class	From	To	From	To	Class	From	To	From	To
1	-0.55	-0.43	-0.55	-0.43	1	0.00	4.15	0.00	14.10
2	-0.43	-0.31	-0.43	-0.31	2	4.15	8.31	14.10	15.56
3	-0.31	-0.18	-0.31	-0.18	3	8.31	12.47	15.56	16.40
4	-0.18	-0.06	-0.18	-0.06	4	12.47	16.62	16.40	17.07
5	-0.06	0.06	-0.06	0.06	5	16.62	20.78	17.07	17.66
6	0.06	0.18	0.06	0.18	6	20.78	24.94	17.66	18.28
7	0.18	0.30	0.18	0.30	7	24.94	29.09	18.28	18.98
8	0.30	0.42	0.30	0.42	8	29.09	33.25	18.98	19.84
9	0.42	0.54	0.42	0.54	9	33.25	37.41	19.84	21.14
10	0.54	0.67	0.54	0.67	10	37.41	41.56	21.14	41.56

Table 4

Equal interval and quantile classification schema for NDVI and LST derived from Landsat

	NDVI					Temperature			
	Equal Interval		Quantile			Equal Interval		Quantile	
Class	From	To	From	To	Class	From	To	From	To
1	-1.00	-0.80	-1.00	-0.09	1	0.30	3.05	0.30	14.93
2	-0.80	-0.60	-0.09	-0.06	2	3.05	5.80	14.93	15.23
3	-0.60	-0.40	-0.06	-0.04	3	5.80	8.55	15.23	15.53
4	-0.40	-0.20	-0.04	-0.02	4	8.55	11.30	15.53	15.83
5	-0.20	0.00	-0.02	0.00	5	11.30	14.05	15.83	16.13
6	0.00	0.20	0.00	0.01	6	14.05	16.80	16.13	16.43
7	0.20	0.40	0.01	0.03	7	16.80	19.55	16.43	16.73
8	0.40	0.60	0.03	0.07	8	19.55	22.30	16.73	17.32
9	0.60	0.80	0.07	0.11	9	22.30	25.05	17.32	17.91
10	0.80	1.00	0.11	1.00	10	25.05	27.80	17.91	27.80

Table 5

Equal interval and quantile classification schema for NDVI and LST derived from MODIS

NDVI					Temperature				
	Equal Interval		Quantile			Equal Interval		Quantile	
Class	From	To	From	To	Class	From	To	From	To
1	-0.64	-0.49	-0.64	0.07	1	0.00	3.67	0.00	24.79
2	-0.49	-0.34	0.07	0.22	2	3.67	7.35	24.79	25.22
3	-0.34	-0.19	0.22	0.31	3	7.35	11.03	25.22	25.77
4	-0.19	-0.04	0.31	0.40	4	11.03	14.71	25.77	26.42
5	-0.04	0.11	0.40	0.47	5	14.71	18.39	26.42	27.38
6	0.11	0.26	0.47	0.53	6	18.39	22.07	27.38	28.44
7	0.26	0.41	0.53	0.59	7	22.07	25.75	28.44	29.45
8	0.41	0.56	0.59	0.64	8	25.75	29.43	29.45	30.35
9	0.56	0.71	0.64	0.69	9	29.43	33.11	30.35	31.61
10	0.71	0.86	0.69	0.86	10	33.11	36.79	31.61	36.79

with a modification to scale data between values of 1 to 10. The revised equation for normalization is presented in Equation 5.1

$$Normalization = \frac{D_i - Min(D)}{Max(D) - Min(D)} * (Max(R) - Min(R)) + Min(R) \qquad (5.1)$$

Where 'D' is the demographic variable for which the values range from $i = 1, 2,...,N$. 'R' is the range within which the normalized values of 'D' have to be scaled. here, the range of normalized values were bounded between 1 and 10. Therefore, $Max(R) = 10$ and $Min(R) = 1$. The classification schema of the demographic indicators are presented in Tables 8 to 12.

The vector and raster data were integrated. Association rule mining algorithm 'apriori' as initially developed by (Borgelt and Kruse, 2002) was chosen for mining the association within LST and other LULC indicators. A minimum support of 10 and confidence ranging from 0 to 100 were selected as the initiation parameters. Minimum confidence of 0 was chosen to identify negative association rules.

Table 6

Land cover as mapped over study area their abbreviation and detailed description (NLCD, 2000)

Abb	LULC Class	Description
BR	Barren Land	Barren areas of bedrock, desert pavement, scarps, talus, slides, volcanic material, glacial debris, sand dunes, strip mines, gravel pits and other accumulations of earthen material
DE	Deciduous Forest	Areas dominated by trees generally greater than 5 meters tall, and greater than 20% of total vegetation cover
DHI	Developed, High Intensity	Includes highly developed areas where people reside or work in high numbers
DLI	Developed, Low Intensity	Includes areas with a mixture of less constructed materials and more vegetation
DMI	Developed, Medium Intensity	Includes areas with a mixture of more constructed materials and less vegetation
EHW	Emergent Wetlands	Areas where perennial herbaceous vegetation accounts for greater than 80 percent of vegetative cover and the soil or substrate is periodically saturated with or covered with water
EV	Evergreen Forest	Areas dominated by trees generally greater than 5 meters tall, and greater than 20% of total vegetation cover
GR	Grassland	Areas dominated by grammanoid or herbaceous vegetation, generally greater than 80% of total vegetation
OS	Developed, Open Space	Includes areas with a mixture of some constructed materials, but mostly vegetation in the form of lawn grasses
OW	Open Water	All areas of open water, generally with less than 25% cover of vegetation or soil
PA	Pasture/Hay	Areas of grasses, legumes, or grass legume mixtures planted for livestock grazing or the production of seed or hay crops, typically on a perennial cycle
RC	Cultivated Crops	Areas used for the production of annual crops, such as corn, soybeans, vegetables, tobacco, and cotton, and also perennial woody crops such as orchards and vineyards
SS	Shrub/Scrub	Areas dominated by shrubs; less than 5 meters tall with shrub canopy typically greater than 20% of total vegetation
WW	Woody Wetlands	Areas where forest or shrub land vegetation accounts for greater than 20 percent of vegetative cover and the soil or substrate is periodically saturated with or covered with water

Table 7

Land use zoning as mapped over study area their abbreviation and detailed description

Zone Type	Abbreviation	Area (Sq.Km)
Airport	A	2.73
Commercial	C	9.68
Central Business District	CBD	0.45
Agriculture	DA	18.51
Hospital	HD	0.53
High Density Housing	HDH	1.03
Historical Preservation	HP	0.01
Industrial	I	9.86
Low Density Housing	LDH	42.96
Medium Density Housing	MDH	4.33
Park	PK	5.19
Special Uses	SU	8.61
University	UQ	0.38

Table 8

Classification schema for population density

Population Density Classes	From	To
1	0	472
2	472.1	1392.2
3	1392.3	2319.5
4	2319.6	3271
5	3271.1	4242.1
6	4242.2	5119.2
7	5119.3	8347.7
10		> 8347.7

Table 9

Classification schema for mean age of induviduals residing in that area

Mean Age Classes	From	To
1	0	0
3	19.3	23
4	23.1	31.3
5	31.4	40.2
6	40.3	49.1
7	49.2	62.3
8	62.4	67.7
9	67.8	80.4
10		> 80.5

Table 10

Classification schema for percentage of vacant housing

% Vacant Classes	From	To
1	0	10.00
2	10.01	20.00
3	20.01	30.00
4	30.01	40.00
5	40.01	50.00
6	50.01	60.00
7	60.01	70.00
8	70.01	80.00
9	80.01	90.00
10	90.01	100.00

Table 11

Classification schema for average household size

Household Size Classes	From	To
1	0	0
4	1	1.38
5	1.38	1.75
6	1.76	2.15
7	2.16	2.54
8	2.55	2.93
9	2.94	3.51
10		> 3.52

Table 12

Classification schema for average family size

Family Size Classes	From	To
1	0	0
5	2	2.3
6	2.31	2.81
7	2.82	3.32
8	3.33	3.84
9	3.84	4.6
10		> 4.6

Rules and knowledge

The association rule mining algorithm was executed using various combinations of the dataset. The initial model was tested using LST (ASTER), NDVI (ASTER), LULC and demographic indicators. Similarly, in succeeding experiments, LST and NDVI information of ASTER was substituted with LST and NDVI information from Landsat and MODIS. Within these initial experiments, the relationship between information from different sensors was not tested. This helped identify sensitivity of the model towards spectral information. In later experiments, the existence of relationships between information from different sensors (ASTER, Landsat, and MODIS) was tested by using combinations of dataset (LST and NDVI).

Due to the nature of the association rule mining algorithm, some of the rules that were obtained as a part of the experiments did not necessarily include LST parameters within their conditional statements. Such rules which may be of interest to urban research community in general are therefore presented as part of this study. Since the primary objective of this study was to analyze the relationship between urban heat (land surface) and its associated LULC characteristics, further detailed analysis of the rules were not carried out. The results are presented in the following sub-subsections in order of the experiments that were conducted.

Table 13

Results from association mining presented as confusion matrix: Confidence of NDVI with respect to LST. Classification of the ASTER NDVI and LST datasets were done using equal interval algorithm

Tc/ NDVI	1	2	3	4	5	6	7	8	9	10
1	0%	0%	0%	0%	0%	0%	0%	0%	0%	0%
2	0%	0%	1%	2%	0%	0%	0%	0%	0%	0%
3	0%	63%	81%	40%	3%	2%	3%	1%	1%	3%
4	100%	33%	14%	35%	13%	22%	33%	29%	31%	37%
5	0%	4%	4%	17%	42%	58%	56%	64%	63%	57%
6	0%	0%	0%	4%	33%	17%	7%	6%	5%	3%
7	0%	0%	0%	1%	6%	1%	0%	0%	0%	0%
8	0%	0%	0%	1%	1%	0%	0%	0%	0%	0%
9	0%	0%	0%	0%	0%	0%	0%	0%	0%	0%
10	0%	0%	0%	0%	0%	0%	0%	0%	0%	0%
Total	100%	100%	100%	100%	100%	100%	100%	100%	100%	100%

ASTER

In this scenario, ASTER-derived LST and NDVI information, which was classified into 10 classes based on equal interval and quantile classification techniques, was analyzed with respect to land use land cover and demographic indicators to mine meaningful relationships. The results obtained through this analysis are summarized in Tables 13 to 18.

Equal interval classification results, and their respective association rules, indicate that low NDVI does not always correspond to low LST. In case of ASTER derived LST, the association with NDVI is non-linear. Low NDVI, i.e., class 1 (range of -0.55 to -0.43), demonstrated strong association with LST class 4 (range of 12.47 to 16.42 C), with a confidence of 100%. While, NDVI classes 2 and 3 (range of -0.43 to -0.18) demonstrated strong association with LST class 3 (range of 8.31 to 12.47 C), with a confidence of 63% and 81% respectively. Similar patterns of low NDVI and high LST are also evident within NDVI class 5 (range of -0.06 to 0.06). NDVI class 5 demonstrates association with LST

Table 14

Results from association mining presented as confusion matrix: Confidence of NDVI with respect to LST. Classification of the ASTER NDVI and LST datasets were done using quantile algorithm

Tc/ NDVI	1	2	3	4	5	6	7	8	9	10
1	22%	5%	6%	11%	18%	13%	7%	5%	4%	4%
2	6%	5%	8%	9%	12%	12%	11%	10%	10%	10%
3	4%	6%	9%	9%	9%	11%	11%	11%	12%	13%
4	4%	7%	9%	9%	9%	10%	12%	13%	13%	16%
5	4%	7%	9%	10%	9%	10%	12%	12%	13%	14%
6	5%	8%	10%	10%	9%	10%	12%	13%	13%	13%
7	6%	9%	11%	11%	10%	10%	12%	12%	12%	11%
8	7%	12%	13%	11%	10%	10%	11%	11%	10%	9%
9	11%	17%	15%	11%	9%	8%	9%	8%	8%	7%
10	30%	24%	11%	7%	5%	5%	5%	5%	5%	4%
Total	100%	100%	100%	100%	100%	100%	100%	100%	100%	100%

class 6 (range of 20.78 to 24.94 C), with a confidence of 33%. While, NDVI class 6 through 10 (range of 0.6 to 0.67) also demonstrate association with LST class 6 through 10 (20.78 to 41.56 C), with a confidence of 17%. In general, NDVI of class 6 through 10 associate with LST class 5, with a support of 51% and confidence > 56%.

Results from association mining using quantile interval classified data demonstrate no strong relationship between NDVI and LST classes. These results further strengthen uncertainty of the relationship between NDVI and LST. This uncertainty was high in the association between NDVI class 1 (range of -0.55 to -0.43) and LST. NDVI class 1, which had a support of 10%, exhibited association with LST of classes 1 (range of 0 to 14 C) and 10 (range of 21.14 to 41.56 C), with a confidence of 22% and 30% respectively.

Irrespective of temperature ranges (which are usually subjected to climatic conditions in space and over time), the classification gives a relative picture which can be used for extrapolating or generalizing the relationships between indicators. In case of NDVI and LST, association rules were not found to be linear, mainly due to the nature of vegetation. For example, a crop can have poor health, and therefore low NDVI value, but can still

Table 15

Results from association mining presented as confusion matrix: Confidence of NLCD with respect to LST. Classification of ASTER LST was done using equal interval algorithm. Please refer Table 6 for the detailed description of the abbreviations

Tc	BR	DE	DHI	DLI	DMI	EHW	EV
1	13%	62%	3%	1%	2%	64%	32%
2	11%	23%	3%	3%	3%	17%	32%
3	32%	7%	3%	6%	3%	5%	9%
4	29%	3%	4%	9%	4%	5%	8%
5	2%	2%	4%	11%	5%	2%	4%
6	4%	1%	5%	15%	7%	2%	6%
7	5%	1%	7%	17%	10%	1%	5%
8	1%	1%	9%	17%	16%	2%	3%
9	1%	0%	15%	13%	26%	2%	1%
10	3%	0%	47%	7%	27%	0%	0%
Total	100%	100%	100%	100%	100%	100%	100%

Tc	GR	OS	OW	PA	RC	SS	WW
1	30%	8%	79%	7%	6%	71%	89%
2	23%	16%	9%	21%	14%	14%	6%
3	8%	16%	4%	24%	17%	6%	3%
4	11%	16%	2%	18%	17%	3%	0%
5	7%	13%	1%	12%	14%	2%	0%
6	10%	11%	1%	9%	11%	1%	1%
7	6%	8%	1%	4%	9%	0%	0%
8	1%	6%	1%	3%	5%	1%	0%
9	0%	4%	1%	1%	3%	1%	0%
10	4%	2%	0%	1%	2%	0%	0%
Total	100%	100%	100%	100%	100%	100%	100%

Table 16

Results from association mining presented as confusion matrix: Confidence of NLCD with respect to LST. Classification of the ASTER LST was done using quantile algorithm. Please refer Table 6 for the detailed description of the abbreviations

Tc	BR	DE	DHI	DLI	DMI	EHW	EV
1	0%	0%	0%	0%	0%	0%	0%
2	0%	0%	0%	0%	0%	0%	0%
3	4%	21%	1%	0%	1%	38%	17%
4	56%	72%	9%	12%	7%	49%	60%
5	37%	7%	38%	78%	58%	12%	23%
6	3%	0%	40%	9%	31%	1%	0%
7	0%	0%	9%	0%	2%	0%	0%
8	0%	0%	2%	0%	0%	0%	0%
9	0%	0%	1%	0%	0%	0%	0%
10	0%	0%	0%	0%	0%	0%	0%
Total	100%	100%	100%	100%	100%	100%	100%

Tc	GR	OS	OW	PA	RC	SS	WW
1	0%	0%	0%	0%	0%	0%	0%
2	0%	0%	1%	0%	0%	0%	0%
3	13%	2%	64%	1%	1%	18%	70%
4	50%	44%	27%	57%	41%	75%	28%
5	33%	52%	7%	41%	54%	6%	2%
6	3%	3%	0%	1%	3%	1%	0%
7	1%	0%	0%	0%	0%	0%	0%
8	0%	0%	0%	0%	0%	0%	0%
9	0%	0%	0%	0%	0%	0%	0%
10	0%	0%	0%	0%	0%	0%	0%
Total	100%	100%	100%	100%	100%	100%	100%

Table 17

Results from association mining presented as confusion matrix: Confidence of zoning with respect to LST. Classification of the ASTER LST was done using equal interval algorithm. Please refer Table 7 for the detailed description of the abbreviations

Tc / Zone	A	C	CBD	DA	HD	HDH	HP
1	0%	0%	0%	0%	0%	0%	0%
2	0%	0%	0%	0%	0%	0%	0%
3	3%	1%	4%	3%	0%	2%	0%
4	27%	14%	6%	49%	11%	8%	0%
5	65%	49%	35%	46%	50%	67%	8%
6	4%	32%	49%	1%	37%	22%	92%
7	1%	3%	4%	0%	1%	0%	0%
8	0%	1%	1%	0%	0%	0%	0%
9	0%	0%	1%	0%	0%	0%	0%
10	0%	0%	0%	0%	0%	0%	0%
Total	100%	100%	100%	100%	100%	100%	100%

Tc / Zone	I	LDH	MDH	PK	SU	UQ
1	0%	0%	0%	0%	0%	0%
2	0%	0%	0%	0%	0%	0%
3	4%	2%	4%	21%	8%	3%
4	23%	24%	14%	39%	32%	17%
5	48%	67%	54%	35%	47%	52%
6	19%	7%	27%	5%	10%	27%
7	4%	0%	0%	0%	2%	1%
8	1%	0%	0%	0%	0%	0%
9	0%	0%	0%	0%	0%	0%
10	0%	0%	0%	0%	0%	0%
Total	100%	100%	100%	100%	100%	100%

Table 18

Results from association mining presented as confusion matrix: Confidence of zoning with respect to LST. Classification of the ASTER LST was done using quantile algorithm. Please refer Table 7 for the detailed description of the abbreviations

Tc / Zone	A	C	CBD	DA	HD	HDH	HP
1	8%	3%	5%	12%	3%	4%	0%
2	8%	4%	2%	18%	3%	3%	0%
3	10%	5%	2%	18%	4%	3%	0%
4	13%	7%	1%	17%	5%	3%	0%
5	13%	7%	2%	13%	7%	3%	0%
6	16%	7%	4%	10%	8%	7%	0%
7	16%	8%	6%	6%	7%	17%	0%
8	7%	11%	8%	4%	11%	19%	0%
9	3%	17%	18%	2%	21%	26%	39%
10	5%	31%	50%	1%	30%	16%	61%
Total	100%	100%	100%	100%	100%	100%	100%

Tc / Zone	I	LDH	MDH	PK	SU	UQ
1	8%	6%	7%	38%	18%	10%
2	8%	9%	4%	11%	10%	5%
3	8%	9%	5%	8%	10%	5%
4	8%	10%	6%	8%	10%	3%
5	8%	11%	6%	7%	9%	5%
6	9%	13%	7%	7%	8%	5%
7	8%	14%	10%	6%	8%	9%
8	9%	14%	13%	6%	8%	15%
9	12%	11%	20%	6%	8%	24%
10	21%	4%	21%	4%	10%	20%
Total	100%	100%	100%	100%	100%	100%

provide sufficient roughness over the surface to prevent absorption or radiation of heat. This phenomenon has been identified within the visual analysis, the results of which are presented in the previous chapter. The results from this study indicate that recreational grassland (e.g., parks) with relatively high NDVI exhibited association with high LST. This may be due to the nature of the vegetation. Nevertheless, the areas that exhibit high NDVI and also radiate relatively high temperatures have to be studied in detail. Such study would aid in understanding the behavior of urban vegetation and radiant heat of surfaces they occupy.

Land cover type, namely deciduous forest (DE), emergent wetlands (EW), open water (OW), shrubs (SS) and woody wetlands (WW) demonstrated association with LST class 1 (range 0 to 4.15 C), with confidence greater than 60%. The woody wetlands were found to be more strongly associated with LST (confidence of 89%) than open waters (confidence of 79%). This variation between land cover elements may be due to their location within the study space. The woody wetlands of Marion County are mostly situated in peri-urban areas and are therefore less influenced by urban heat effect, whereas, open waters (especially White River) that flow through the city are, in part influenced by urban heat. Water depths in parts of the city are also considerably low, thereby contributing to more heat radiation. Developed high intensity (DHI) areas demonstrated a strong association with LST class 10 (range37.41 to 41.56 C), with a confidence of 47%, followed by developed medium intensity (DMI) areas (confidence of 27%). Land cover classes including pastures (PA), evergreen forest (EV) and grasslands (GR) demonstrated partial association (confidence varying between 15 to 25%) with LST classes 2 to 5 (range of 4.15 to 20.78). Developed low intensity (DLI) along with DHI and DMI exhibited partial association with LST classes 6 through 9 (range of 20.78 to 37.41 C). Barren land (BR) demonstrated an association with LST class 3 and 4 (range of 12.47 to 16.62 C), with a confidence of 51%. This indicates that much of the barren land radiates less heat than developed spaces but more heat than forests, wetlands and water.

Association rules between land cover and LST classified using quantile algorithm were similar to the results obtained from LST classified using equal interval algorithm, with minor variation in LST ranges. The results demonstrated that open waters and woody wetlands are associated with quantile LST class 1 (range of 14.10 to 15.56), with high confidence intervals of 64% and 70% respectively. LST class 4 is associated with barren lands (confidence of 56%), deciduous forests (72%), evergreen forests (60%), grasslands (50%), pastures (57%) and shrubs (75%) with relatively high confidence. LST class 5 (range of 16.62 to 20.78 C) has association with developed medium intensity (confidence of 58%), developed low intensity (78%), developed open space (52%) and cultivated crops (54%). LST classes 5 and 6 (range of 16.62 to 24.94 C) are associated with developed high intensity, with a confidence of 78%. From the above results, it is evident that antropogenic changes have positive association with LST.

The association between zoning and LST can be broadly classified into two categories. Categories which fall within LST classes 4 and 5 (range of 12.47 to 20.78 C), and classes 5 and 6 (range of 16.62 to 24.94 C). LST classes 4 and 5 are strongly associated with airport (confidence of 92%), agricultural land (95%), low density housing (91%), industrial areas (71%), parks (74%) and special uses (79%). The occurrence of agricultural land and airport within the same classification is mainly a seasonal characteristic; since the image was captured in the month of April, there is a small possibility of vegetation being present over agricultural areas, making these areas barren or semi-barren. This could have been the reason for high thermal radiation from agricultural zones in comparison with airport. LST classes 5 and 6 demonstrated their association with commercial zones (81%), the central business district (84%), hospitals (87%), high density housing (89%), medium density housing (81%) and university area (79%). Areas which are under historical preservation demonstrated association with LST class 6 (range of 20.78 to 24.94), with high confidence of 92%.

The results obtained from quantile classification reiterated the results obtained from

experiments with equal interval classification. Central business districts and historical preservation areas demonstrated a strong association with LST class 10 (range of 37.41 to 41.56 C), with a confidence of 50% and 61% respectively. Parks demonstrated an association with low LST i.e., class 1 (range of 0 to 14.10 C), with a confidence of 38%.

LST class 4 (range of 12 to 16 C in equal interval classification) demonstrated association with average family size of 2.82 to 3.32, with a high support (27.5%) and confidence (84%). Furthermore, LST class 4 is strongly associated with low intensity developed land, which includes areas with a mixture of constructed materials and vegetation, high NDVI in the range of 0.18 to 3, high average household size, low vacant areas (less than 10%) and low population density, all with high confidence (> 80%). This indicates that households with large family size generally prefer to stay in suburban areas or areas with more open green spaces. These spaces have low radiative capacity and therefore may contribute little to the local heat effect. Further, it appears that the majority of people who have relatively large families living in areas with relatively low thermal radiation zones are also those with a mean age of 31 to 40, with high confidence (91.5%). These areas were also found to consist of buildings with very low vacancy rates, with high confidence (91.3%). This may mean that most people with relatively large families prefer to live in areas with relatively less thermal radiation. But it is also important to note that LULC characteristics including the population density and building occupancy are based on 2001 data. These are more likely to change after the recent decline in the housing sector.

Highly developed areas, where people reside or work in high numbers, were found to have a strong association (belong to) with the relatively higher land surface thermal characteristics of class 5 (equal interval classification). This relationship exists with support of 19.6% and confidence of 84.2%. These highly developed areas were also mostly found to be composed of low density housing. LST class 5 (equal interval classification) was found to have similar association characteristics with population density, NDVI, average household size, average family size and zoning as class 4 (equal

Table 19

Results from association mining presented as confusion matrix: Confidence of NDVI with respect to LST. Classification of the Landsat ETM+ NDVI and LST datasets were done using equal interval algorithm

Tc/ NDVI	1	2	3	4	5	6	7	8	9	10
1	0%	0%	0%	0%	0%	0%	1%	1%	0%	0%
2	0%	0%	0%	0%	0%	0%	1%	2%	0%	0%
3	0%	0%	0%	0%	0%	0%	1%	1%	1%	0%
4	0%	0%	0%	0%	2%	0%	1%	4%	2%	1%
5	4%	0%	1%	4%	4%	1%	4%	17%	11%	7%
6	90%	31%	35%	84%	53%	82%	59%	46%	65%	63%
7	5%	62%	57%	9%	37%	16%	28%	24%	18%	26%
8	1%	7%	8%	3%	2%	0%	6%	5%	2%	3%
9	0%	0%	0%	0%	0%	0%	0%	0%	0%	0%
10	0%	0%	0%	0%	0%	0%	0%	0%	0%	0%
Total	100%	100%	100%	100%	100%	100%	100%	100%	100%	100%

interval classification), with a confidence of above 80%.

Landsat

In this scenario, Landsat ETM+ derived LST and NDVI information which was classified into 10 classes based on equal interval and quantile algorithms were analyzed in tandem with LULC database and demographic indicators. A summary of the results obtained are presented in Tables 19 to 24.

Similar to ASTER, the results from Landsat ETM+ LST and Landsat NDVI classes generated using equal interval classification indicate that there is a non-linear relationship between the two variables. Much of the study area (44.7%) is included under LST class 6 (range of 14 to 16 C) and NDVI class 6 (range of 0 to 0.2). This rule has a high confidence of 82.2%. Due to the high support percentage of these two classes, their dominance was also evident within the association mining rules that were derived. Many of the rules that were obtained had a relationship which was indicative of either LST class 6 or NDVI class 6 (equal interval classification). LST class 6 (range of 14.05 to 16.80 C) was found

Table 20

Results from association mining presented as confusion matrix: Confidence of NDVI with respect to LST. Classification of the Landsat ETM+ NDVI and LST datasets were done using quantile algorithm

Tc/ NDVI	1	2	3	4	5	6	7	8	9	10
1	14%	22%	12%	12%	13%	12%	10%	10%	13%	24%
3	7%	8%	9%	13%	15%	15%	16%	18%	24%	23%
4	5%	7%	8%	10%	11%	12%	14%	16%	18%	14%
5	5%	7%	9%	10%	11%	13%	15%	16%	14%	10%
6	5%	6%	8%	8%	10%	11%	12%	12%	10%	6%
7	7%	8%	11%	12%	13%	14%	14%	13%	10%	7%
8	12%	12%	17%	18%	17%	15%	13%	11%	8%	6%
9	14%	13%	16%	11%	8%	6%	4%	3%	2%	4%
10	31%	17%	10%	5%	3%	2%	2%	1%	1%	6%
Total	100%	100%	100%	100%	100%	100%	100%	100%	100%	100%

to be strongly associated with NDVI class 1 (range of -1 to -0.8), with a confidence of 90%. But NDVI classes especially classes 2 and 3 (range of -0.8 to -0.4) were found to be associated with LST class 7 (range of 16.8 to 19.55 C), with a confidence of 62% and 57% respectively. The remaining NDVI classes 4 through 10 were associated with LST classes 1 through 5, with a high confidence (more than 50% upto 84%). This indicates that NDVI is not directly proportional to LST and may vary.

The association mining results from the dataset derived using quantile classification further strengthens the above conclusion of non-linearity between LST and NDVI. Nevertheless, there exists a weak link between the two variables. For example, the results indicate that LST class 10 (range of 17.91 to 27.80 C) is positively associated with NDVI class 1 (range of -1.0 to -0.09), with a confidence of 31%. Similarly, NDVI class 10 (range of 0.11 to 1.0) is associated with LST classes 1 through 3 (temperature < 15.53 C). The remaining NDVI and LST classes did not demonstrate an association (either positive or negative).

The rules did highlight the presence of a relationship between LST and land cover

Table 21

Results from association mining presented as confusion matrix: Confidence of NLCD with respect to LST. Classification of Landsat ETM+ LST was done using equal interval algorithm. Please refer Table 6 for the detailed description of the abbreviations

Tc	BR	DE	DHI	DLI	DMI	EHW	EV
1	0%	0%	0%	0%	0%	0%	0%
2	0%	0%	0%	0%	0%	0%	0%
3	0%	0%	0%	0%	0%	0%	0%
4	0%	0%	1%	0%	0%	1%	0%
5	32%	7%	4%	1%	2%	46%	12%
6	67%	92%	28%	62%	34%	49%	84%
7	1%	1%	55%	36%	62%	3%	4%
8	0%	0%	11%	0%	2%	1%	0%
9	0%	0%	1%	0%	0%	0%	0%
10	0%	0%	1%	0%	0%	0%	0%
Total	100%	100%	100%	100%	100%	100%	100%

Tc	GR	OS	OW	PA	RC	SS	WW
1	0%	0%	0%	0%	0%	0%	0%
2	0%	0%	0%	0%	0%	0%	0%
3	0%	0%	0%	0%	0%	0%	0%
4	0%	0%	44%	0%	0%	0%	0%
5	14%	2%	43%	2%	3%	3%	52%
6	81%	90%	13%	96%	89%	95%	47%
7	2%	8%	1%	3%	7%	3%	0%
8	3%	0%	0%	0%	0%	0%	0%
9	0%	0%	0%	0%	0%	0%	0%
10	0%	0%	0%	0%	0%	0%	0%
Total	100%	100%	100%	100%	100%	100%	100%

Table 22

Results from association mining presented as confusion matrix: Confidence of NLCD with respect to LST. Classification of Landsat ETM+ LST was done using quantile algorithm. Please refer Table 6 for the detailed description of the abbreviations

Tc	BR	DE	DHI	DLI	DMI	EHW	EV
1	56%	43%	8%	3%	4%	76%	50%
3	24%	33%	4%	6%	4%	12%	25%
4	13%	12%	4%	9%	5%	4%	9%
5	4%	6%	5%	12%	6%	3%	6%
6	2%	3%	4%	13%	6%	1%	4%
7	0%	2%	7%	19%	11%	1%	2%
8	1%	1%	12%	23%	21%	1%	3%
9	0%	0%	15%	10%	23%	1%	1%
10	0%	0%	40%	4%	20%	2%	0%
Total	100%	100%	100%	100%	100%	100%	100%
Tc	GR	OS	OW	PA	RC	SS	WW
1	48%	15%	94%	24%	20%	24%	90%
3	29%	25%	3%	35%	23%	36%	8%
4	8%	19%	1%	19%	17%	19%	1%
5	6%	15%	1%	10%	14%	9%	0%
6	3%	10%	0%	5%	9%	5%	0%
7	1%	9%	0%	4%	8%	4%	0%
8	1%	6%	0%	2%	6%	2%	0%
9	1%	2%	0%	1%	1%	1%	0%
10	4%	1%	0%	0%	1%	0%	0%
Total	100%	100%	100%	100%	100%	100%	100%

Table 23

Results from association mining presented as confusion matrix: Confidence of zoning with respect to LST. Classification of the Landsat ETM+ LST was done using equal interval algorithm. Please refer Table 7 for the detailed description of the abbreviations

Tc	A	C	CBD	DA	HD	HDH	HP
1	0%	0%	0%	0%	0%	0%	0%
2	0%	0%	0%	0%	0%	0%	0%
3	0%	0%	0%	0%	0%	0%	0%
4	0%	0%	1%	0%	0%	0%	0%
5	2%	2%	4%	4%	1%	3%	0%
6	88%	43%	19%	91%	43%	30%	0%
7	9%	50%	65%	5%	54%	66%	89%
8	1%	4%	10%	0%	3%	1%	11%
9	0%	0%	1%	0%	0%	0%	0%
10	0%	0%	1%	0%	0%	0%	0%
Total	100%	100%	100%	100%	100%	100%	100%

Tc	I	LDH	MDH	PK	SU	UQ
1	0%	0%	0%	0%	0%	0%
2	0%	0%	0%	0%	0%	0%
3	0%	0%	0%	0%	0%	0%
4	2%	0%	2%	11%	2%	0%
5	6%	2%	4%	7%	5%	6%
6	54%	69%	42%	68%	73%	44%
7	33%	29%	51%	14%	18%	48%
8	5%	0%	0%	0%	2%	2%
9	1%	0%	0%	0%	0%	0%
10	0%	0%	0%	0%	0%	0%
Total	100%	100%	100%	100%	100%	100%

Table 24

Results from association mining presented as confusion matrix: Confidence of zoning with respect to LST. Classification of the Landsat ETM+ LST was done using quantile algorithm. Please refer Table 7 for the detailed description of the abbreviations

Tc	A	C	CBD	DA	HD	HDH	HP
1	16%	7%	7%	23%	5%	6%	0%
3	26%	7%	1%	27%	9%	3%	0%
4	19%	7%	3%	18%	9%	3%	0%
5	13%	7%	3%	14%	7%	5%	0%
6	8%	7%	3%	8%	6%	5%	0%
7	7%	9%	6%	6%	8%	12%	0%
8	4%	15%	14%	3%	15%	26%	0%
9	2%	16%	15%	1%	18%	26%	20%
10	3%	24%	48%	0%	24%	16%	80%
Total	100%	100%	100%	100%	100%	100%	100%

Tc	I	LDH	MDH	PK	SU	UQ
1	16%	7%	10%	35%	22%	16%
3	11%	11%	6%	22%	21%	8%
4	9%	11%	6%	11%	13%	4%
5	9%	13%	7%	8%	10%	5%
6	7%	12%	7%	5%	6%	7%
7	10%	16%	11%	6%	7%	11%
8	13%	18%	18%	7%	8%	21%
9	9%	8%	18%	4%	5%	16%
10	16%	3%	15%	2%	7%	13%
Total	100%	100%	100%	100%	100%	100%

classes. The results from LST equal interval classification indicate that LST classes 6 and 7 (range of 14.05 to 19.55 C) are associated with DHI, DMI and DLI land cover classes, with confidence of 83 96% and 98% respectively. Further, LST class 6 (range of 14.05 to 16.80 C) exhibits strong association with deciduous forest (confidence of 92%), evergreen forest (84%), grassland (81%), developed open spaces (90%), pastures (96%), rice crops (89%) and shrubs (95%). Unlike the results from ASTER derived LST and land cover analysis, open waters was found to be associated with lower temperatures (range of 8.55 to 14.5 C with confidence of 87%) in comparison with woody wetlands (temperature range of 11.3 to 16.8 C with a confidence of 99%). Barren land and emergent wetlands were also found to be associated with temperature ranges similar to those of woody wetlands (range of 11.3 to 16.8 C), with confidence of 99% and 95% respectively. The variation in the results between the two dataset (ASTER and Landsat) may be due to the spectral characteristics of the sensors and variation in land cover characteristics throughout the year. With the lack of strong rules to support the LST relationship with NDVI, land cover characteristics have to be studied in detail with respect to their radiative properties. Study of percentage of mixed pixels within the derived information may also aid in developing generalized rules for particular months/seasons within a year.

The results from the Landsat derived LST classified based on quantile classification produced rules for two broad ranges of land cover classes. First, LST class 1 (range of 0.3 to 15.53 C) was strongly associated with barren land (with confidence of 80%), deciduous forest (76%), emergent wetlands (88%), open water (97%) and woody wetlands (98%). Second, developed high intensity areas were associated with LST class 10 (range of 17.91 to 27.80 C) with a confidence of 40%. The rest of the land cover classes demonstrated no distinct relationships with LST.

Zoning class associations with equal interval classified LST can be broadly summarized into three categories; zones which fall under LST class 6 (range of 14.05 to 16.80 C), class 7 (range of 16.80 to 19.55) and zones which fall in between classes 6 and 7. The zones which

are associated with LST class 6 are airport (with a confidence of 88%) and agricultural land (91%). The zones which are associated with LST class 7 are historical preservation areas. The zones which are more stringly associated with class 6 and less with class 7 are low density housing (confidence of 69% and 29% respectively), parks (68% and 14%) and special uses (73% and 18%). The zones which are associated with class 7 more than class 6 are commercial (class 6 confidence is 43% and class 7 confidence is 50%), central business district (19% and 65%), hospital (43% and 54%), medium density housing (51% and 42%) and universities (48% and 44%).

The results from quantile classification of LST with zoning areas did not add much to the knowledge derived from the earlier experiments. The results indicate that LST class 10 is positively associated with historical preservation areas, with a confidence of 80% and with central business district, with a confidence of 48%.

In general, LST was found to have strong association with land cover and demographic variables. The association with agriculture, low intensity developed areas (which includes areas with a mixture of constructed materials and vegetation), high intensity developed areas (which includes highly developed areas where people reside or work in high numbers), low density housing, high family size, high household size and low population density, all with high confidence (>80%).

From the rules derived it appears that the temperatures in class 7 (range of 16.8 to 19.5) are the transition range. Within this range, the rules derived by rule mining show an association with similar indicators as exhibited by LST class 6. However, the degrees of association within these indicators varies with variation in LST. This variation was prominent among demographic indicators such as family size and population density. In 20% of the cases the associations of the indicators with LST were not constant. In around 30% of the cases LST class 7 was associated with demographic characteristics similar to that of LST class 6. Ultimately, in 50% of the cases the association with similar indicators exhibit an inverse relationship with family size, median age and population

density. From these results, it appears that people in their mid 20s to early 30s have relatively small family/household size and prefer to stay in highly populated areas. These areas are usually towards the city center and have less tree cover, contributing to more surface heat radiation. Furthermore, LST class 7 is associated with low, medium and high intensity developed areas, which are mainly comprised of residential, commercial and industrial structures. LST class 7 exhibits an association with commercial and industrial spaces, with a confidence of 62% and 33% respectively. The developments along these commercial and industrial areas are of medium intensity, with a mixture of constructed materials and vegetation.

Overall, the rules indicate that population density is associated with LST. But, the above association holds true only for temperatures within a certain range (low to medium). Beyond specific ranges the relationships have weak confidence levels (below 10%) therefore reduce the possibility of generalizing many of the rules that were extracted.

MODIS

In this scenario, MODIS derived LST and NDVI information were classified (10 classes) based on equal interval and quantile algorithms and then analyzed in tandem with LULC and demographic indicators. The summarized results from MODIS analysis are presented in Table 25 to 30.

Unlike ASTER and Landsat derived LST and NDVI information,the same attributes derived from MODIS and classified using equal interval algorithm demonstrated an association. Rules derived indicate the presence of a linear relationship between NDVI and LST. Even though many of the NDVI classes were associated with more than one LST class, in general low NDVI classes were associated with high LST classes and vice versa. NDVI classes 1, 2 and 3 (range of -0.64 to -0.19) were associated with LST of class 9 (range of 33.11 to 36.79 C), with a confidence of 100%, 52% and 60% respectively. NDVI classes 4, 5, 6 and 7 (range of -0.19 to 0.49) were associated with LST classes 8 and 9, with confidence of 76%, 86%, 89% and 91% respectively. In this case, NDVI classes were more

Table 25

Results from association mining presented as confusion matrix: Confidence of NDVI with respect to LST. Classification of the MODIS NDVI and LST datasets were done using equal interval algorithm

Tc/ NDVI	1	2	3	4	5	6	7	8	9	10
1	0%	6%	4%	1%	0%	0%	0%	0%	0%	0%
7	0%	0%	0%	1%	1%	3%	7%	23%	60%	72%
8	0%	11%	17%	24%	27%	33%	47%	59%	39%	27%
9	100%	52%	60%	52%	59%	56%	46%	18%	2%	1%
10	0%	31%	19%	22%	12%	8%	1%	0%	0%	0%
Total	100%	100%	100%	100%	100%	100%	100%	100%	100%	100%

Table 26

Results from association mining presented as confusion matrix: Confidence of NDVI with respect to LST. Classification of MODIS NDVI and LST datasets were done using quantile algorithm

Tc/ NDVI	1	2	3	4	5	6	7	8	9	10
1	1%	1%	3%	2%	5%	7%	3%	15%	26%	33%
2	0%	1%	2%	3%	3%	10%	15%	22%	24%	22%
3	1%	0%	1%	2%	6%	14%	19%	26%	14%	17%
4	1%	2%	4%	3%	8%	14%	20%	16%	16%	12%
5	1%	3%	4%	12%	16%	19%	23%	12%	13%	9%
6	8%	10%	13%	16%	15%	13%	12%	6%	5%	7%
7	14%	17%	22%	21%	17%	8%	2%	2%	2%	1%
8	17%	22%	18%	19%	15%	10%	2%	1%	0%	1%
9	20%	19%	20%	16%	13%	4%	2%	0%	0%	0%
10	37%	25%	14%	6%	2%	1%	0%	0%	0%	0%
Total	100%	100%	100%	100%	100%	100%	100%	100%	100%	100%

Table 27

Results from association mining presented as confusion matrix: Confidence of NLCD with respect to LST. Classification of MODIS LST was done using equal interval algorithm. Please refer Table 6 for the detailed description of the abbreviations

Tc	BR	DE	DHI	DLI	DMI	EHW	EV
1	0%	0%	0%	0%	0%	0%	2%
7	100%	23%	25%	22%	20%	13%	14%
8	0%	51%	42%	41%	42%	44%	43%
9	0%	23%	29%	33%	34%	39%	34%
10	0%	3%	4%	3%	4%	5%	8%
Total	100%	100%	100%	100%	100%	100%	100%

Tc	GR	OS	OW	PA	RC	SS	WW
1	0%	0%	0%	0%	0%	0%	0%
7	52%	24%	24%	52%	60%	6%	7%
8	39%	41%	47%	32%	38%	73%	73%
9	9%	30%	24%	15%	2%	19%	19%
10	0%	4%	5%	0%	0%	2%	1%
Total	100%	100%	100%	100%	100%	100%	100%

associated towards LST class 9 than class 8. NDVI classes 8, 9 and 10 (range of 0.49 to 0.81) were associated with LST classes 7 and 8 (range of 22.07 to 29.43 C), with confidence of 82%, 99% and 99% respectively. While NDVI class 8 was more associated with LST class 8, NDVI classes 9 and 10 were more associated with LST class 7.

This inverse linear relationship between NDVI and LST was also evident in the association mining results obtained through the quantile classification dataset. In this case, even though the linear relationship was evident, each of the NDVI classes was associated with more than one LST class. This prevented the derivation of generalized rules (rules with high confidence) from the results. Nevertheless, NDVI class 1 (range of -0.64 to 0.07) and class 10 (range of 0.69 to 0.86) were found to be highly (relative to the rest of the NDVI classes) associated with LST class 10 (range of 31.69 to 36.79 C) and class 1 (range of 0 to 24.79 C), with a confidence of 37% and 33% respectively.

Based on the results obtained from ASTER, Landsat and MODIS derived data one can infer that NDVI is associated with LST, but the relationship is usually non-linear

Table 28

Results from association mining presented as confusion matrix: Confidence of NLCD with respect to LST. Classification of MODIS LST was done using quantile algorithm. Please refer Table 6 for the detailed description of the abbreviations

Tc	BR	DE	DHI	DLI	DMI	EHW	EV
1	94%	10%	8%	6%	6%	3%	10%
2	0%	8%	9%	9%	7%	5%	4%
3	6%	5%	8%	8%	7%	4%	1%
4	0%	5%	8%	10%	8%	4%	3%
5	0%	7%	11%	11%	12%	11%	6%
6	0%	20%	12%	9%	10%	18%	24%
7	0%	19%	12%	12%	13%	10%	11%
8	0%	12%	10%	13%	11%	21%	17%
9	0%	6%	13%	12%	14%	10%	15%
10	0%	8%	10%	10%	11%	13%	9%
Total	100%	100%	100%	100%	100%	100%	100%
Tc	GR	OS	OW	PA	RC	SS	WW
1	20%	6%	9%	31%	27%	1%	0%
2	31%	10%	10%	12%	14%	3%	6%
3	1%	9%	5%	11%	21%	2%	1%
4	13%	9%	2%	12%	16%	5%	4%
5	26%	10%	11%	6%	12%	8%	15%
6	0%	11%	24%	8%	6%	32%	42%
7	0%	11%	11%	5%	3%	27%	12%
8	0%	13%	9%	12%	2%	9%	11%
9	9%	10%	6%	3%	0%	5%	3%
10	0%	10%	14%	0%	0%	7%	6%
Total	100%	100%	100%	100%	100%	100%	100%

Table 29

Results from association mining presented as confusion matrix: Confidence of Zoning with respect to LST. Classification of the MODIS LST was done using equal interval algorithm. Please refer Table 7 for the detailed description of the abbreviations

Tc	A	C	CBD	DA	HD	HDH	HP
1	0%	0%	0%	0%	0%	0%	0%
7	94%	28%	0%	47%	10%	0%	0%
8	6%	41%	9%	42%	37%	22%	0%
9	0%	27%	91%	9%	51%	75%	100%
10	0%	5%	0%	1%	1%	2%	0%
Total	100%	100%	100%	100%	100%	100%	100%

Tc	I	LDH	MDH	PK	SU	UQ
1	0%	0%	0%	1%	0%	0%
7	22%	20%	21%	9%	26%	0%
8	48%	40%	45%	66%	46%	20%
9	26%	36%	30%	25%	25%	78%
10	4%	4%	5%	0%	4%	1%
Total	100%	100%	100%	100%	100%	100%

in higher resolution images and tends to become linear with lower resolution images. Furthermore, NDVI of a particular range was found not to exhibit similar thermal absorption or radiation. The nature of the relationship between NDVI and LST was made evident through the results of association mining algorithm. Nevertheless, a detailed characteristic of different urban features will have to be mapped at both low and high scale to generalize their thermal behavior.

Only three land cover classes were able to demonstrate clear rules in LST dataset classified using equal interval algorithm. Barren lands demonstrated an association with LST class 7 (range of 22.07 to 25.75 C), with a confidence of 100%. Woody wetlands and shrubs exhibited an association with LST class 8 (range of 25.75 to 29.43 C), with a confidence of 73% and 73% respectively. In case of the LST dataset which was classified using the quantile algorithm, once again barren lands were found to be associated with LST class 1 (range of 0.00 to 24.79 C), with a confidence of 94%. The other classes were not found to exhibit any strong (confidence of more than 30%) association with any one

Table 30

Results from association mining presented as confusion matrix: Confidence of zoning with respect to LST. Classification of the MODIS LST was done using quantile algorithm. Please refer Table 7 for the detailed description of the abbreviations

Tc	A	C	CBD	DA	HD	HDH	HP
1	44%	11%	0%	16%	0%	0%	0%
2	45%	8%	0%	14%	3%	0%	0%
3	5%	8%	0%	19%	8%	1%	0%
4	1%	9%	0%	15%	9%	3%	0%
5	3%	11%	0%	13%	6%	1%	0%
6	1%	10%	2%	7%	8%	1%	0%
7	1%	11%	7%	5%	20%	16%	0%
8	0%	8%	36%	6%	0%	19%	0%
9	0%	11%	55%	2%	1%	45%	100%
10	0%	12%	0%	2%	46%	13%	0%
Total	100%	100%	100%	100%	100%	100%	100%

Tc	I	LDH	MDH	PK	SU	UQ
1	8%	5%	3%	4%	8%	0%
2	6%	8%	6%	5%	10%	0%
3	10%	8%	13%	1%	8%	0%
4	9%	9%	8%	2%	7%	9%
5	12%	10%	11%	13%	11%	4%
6	13%	9%	10%	28%	16%	0%
7	14%	11%	15%	23%	13%	8%
8	9%	16%	9%	12%	10%	42%
9	7%	13%	10%	7%	8%	37%
10	13%	10%	13%	5%	10%	1%
Total	100%	100%	100%	100%	100%	100%

particular class of the LST. This lack of association between MODIS and NLCD dataset is mainly due to the variation in resolution. MODIS LST has a spatial resolution of 1 km, while NLCD posesses a resolution 16 m. These variations in resolution usually contain mixed land cover pixels contributing to a single land surface temperature. The effects of mixed pixels negate the possibility of extracting generalized association rules in such mixed pixel cases.

The LST dataset and land use zoning demonstrated strong association rules in comparison with association of LST with land cover dataset. From the results it was evident that agriculture areas are associated with LST class 7 (range of 28.44 to 29.45 C), with confidence of 94%. Central business district and historical preservation areas are assoicaiated with LST class 9 (range of 30.35 to 31.61), with a confidence of 91% and 100% respectively. Areas zoned as industrial , LDH, MDH, parks and special uses had similar association characteristics with LST classes 7 to 9 (range of 28.44 to 31.61 C), with more confidence in association with class 8 (range of 29.45 to 30.35 C).

From the results of the analysis it was also evident that many of the rules (over 95%) which were obtained using the association mining algorithm were for the temperature range of 22 to 29 C. Upon a detailed analysis, it was evident that around 69% of the study area exhibited a temperature characteristic of this range. This may be one of the primary reasons why many of the rules had a bias towards this range. Within the classification schema which was used for MODIS derived measurements this range fell within two classes (classes 7 and 8) in the equal interval classification and LST classes 1 through 7 in the case of quantile classification.

The results demonstrated similar knowledge characteristics as that of ASTER and Landsat. Low population density and moderate temperature range (equal interval class 7) exhibited association with large family size (with a confidence of 93.7%). This association of large family size to a specific range of temperature (class 5) was also evident in the rules derived using quantile classification.

5.3 MODIS LST Analysis Results

There were a total of 2,922 MODIS LST images analyzed for the study of UHI in and around the city of Indianapolis. From this large dataset only a portion were suitable for analysis as the area is prone to frequent cloud cover. Furthermore, the MODIS LST algorithm has trouble characterizing surface temperature over areas which are subjected to irregular snow or water cover. Care was taken so that the selected images have less than 30% cloud cover. This is mainly because cloud cover was found to have a strong negative relationship with LST. The relationship between cloud cover and temperature variation is presented in Figure 17. Based on the above criterion, of the 2,922 images only 242 daytime LST images and 200 nighttime LST images were selected for further analysis. Therefore, it appears for Indianapolis on an average about 20% of MODIS LST images can be used for UHI analysis. In spite of this generalized variation, the number of images which are suitable for analysis varies considerably with respect to seasons. The distribution of images selected for further analysis is presented in Figure 18.

From Figure 18, it is clear that the availability of cloud free images varies with respect to the periods of rain and snow in the study region. The availability of well characterized LST is little to none during the months of January and February when snow cover is high. The summer showers also impact LST especially during the months of May, June and July. For the city of Indianapolis and its surroundings, the best time to acquire LST images for UHI analysis is the month of April followed by August to October.

The subset of images which were used for analysis indicate the mean and maximum day time temperatures were lowest in the month of January and gradually increase to the months of July to August, decreasing thereafter. In the case of nighttime temperatures, the February mean and maximum temperatures were found to be lower than January mean and maximum temperatures. Furthermore, unlike daytime temperatures peak night time temperature was realized in the months of June and July. Figures 19 and 20 illustrate

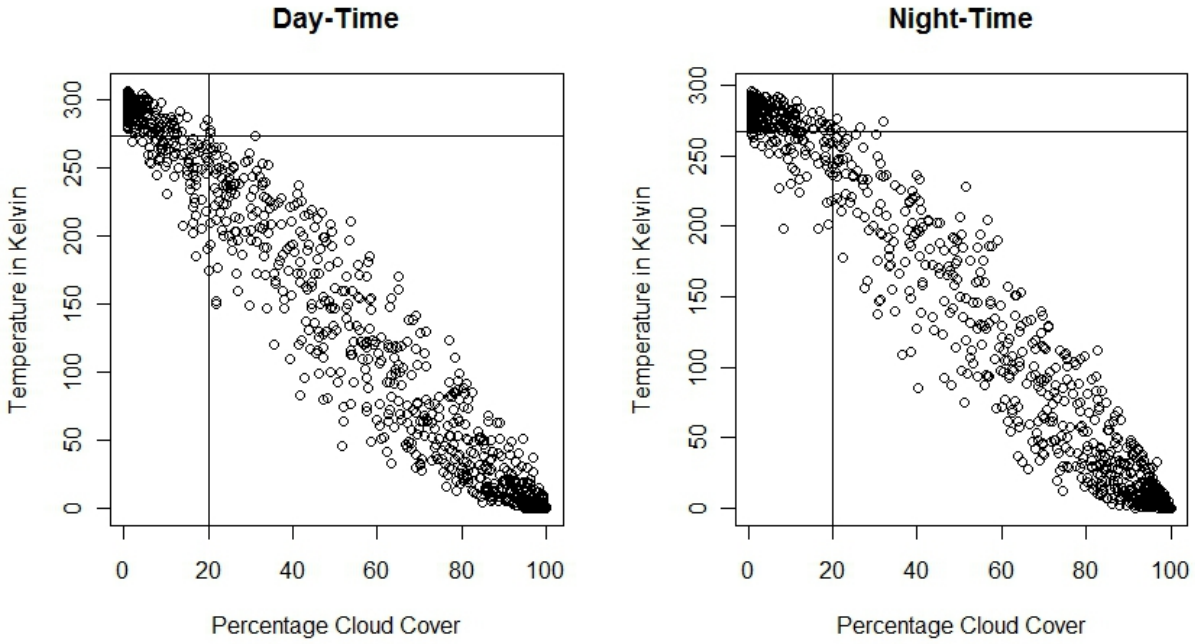

Figure 17. Relationship between cloud cover and its effect on LST

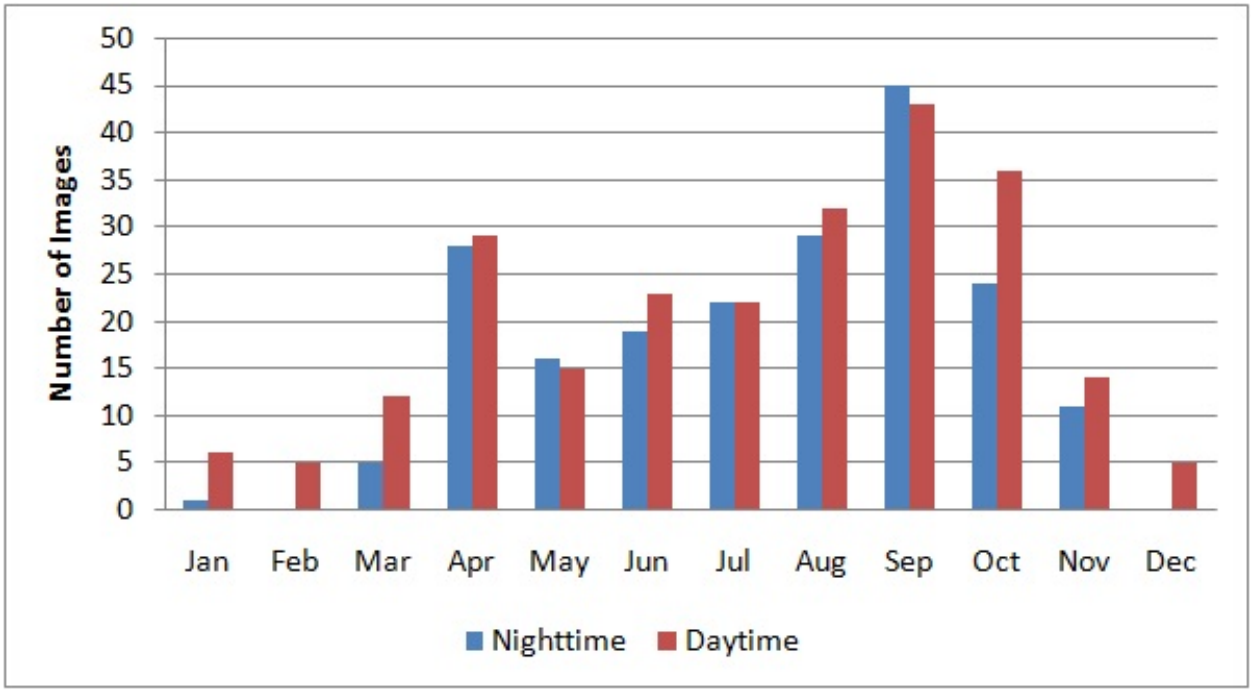

Figure 18. Month wise number of images used for analysis

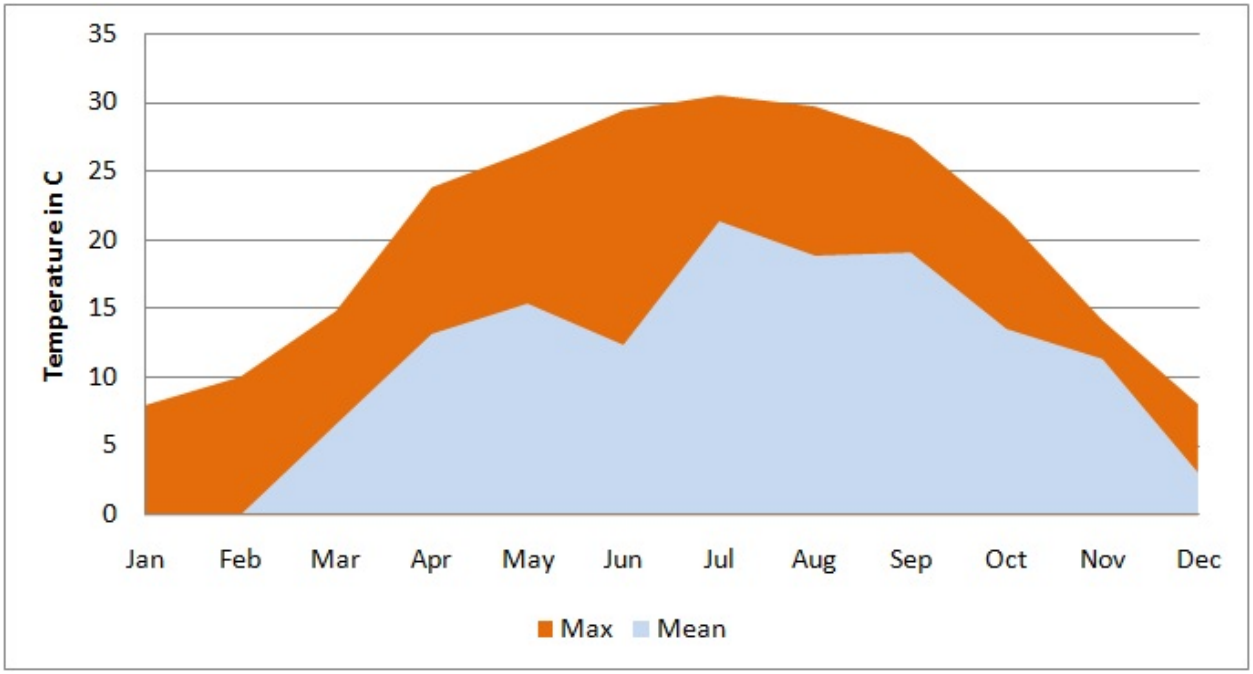

Figure 19. Average of mean and maximum daytime temperatures

the variation in average mean and maximum daytime and nighttime temperatures.

Land surface temperature analysis

The results from selected LST images indicated variation in their intensity. The variations in mean and maximum temperatures within the daytime and nighttime images are presented in Figures 21 and 22. Daytime temperatures indicate that variations in mean temperatures are greater than variations in maximum temperatures. Additionally, except for winter months, the variation in maximum temperature (within each particular month) is within one degree centigrade. On the other hand, variation in mean daytime temperature is greater during the spring and summer months than in autumn and winter months. The high variation during the month of April can be due to transition weather experienced within the study area i.e., transition from winter to spring which may have days of cold weather followed by pleasant weather. Such variations do impact the characteristics of the LST. This is also apparent in LST observation through little variation

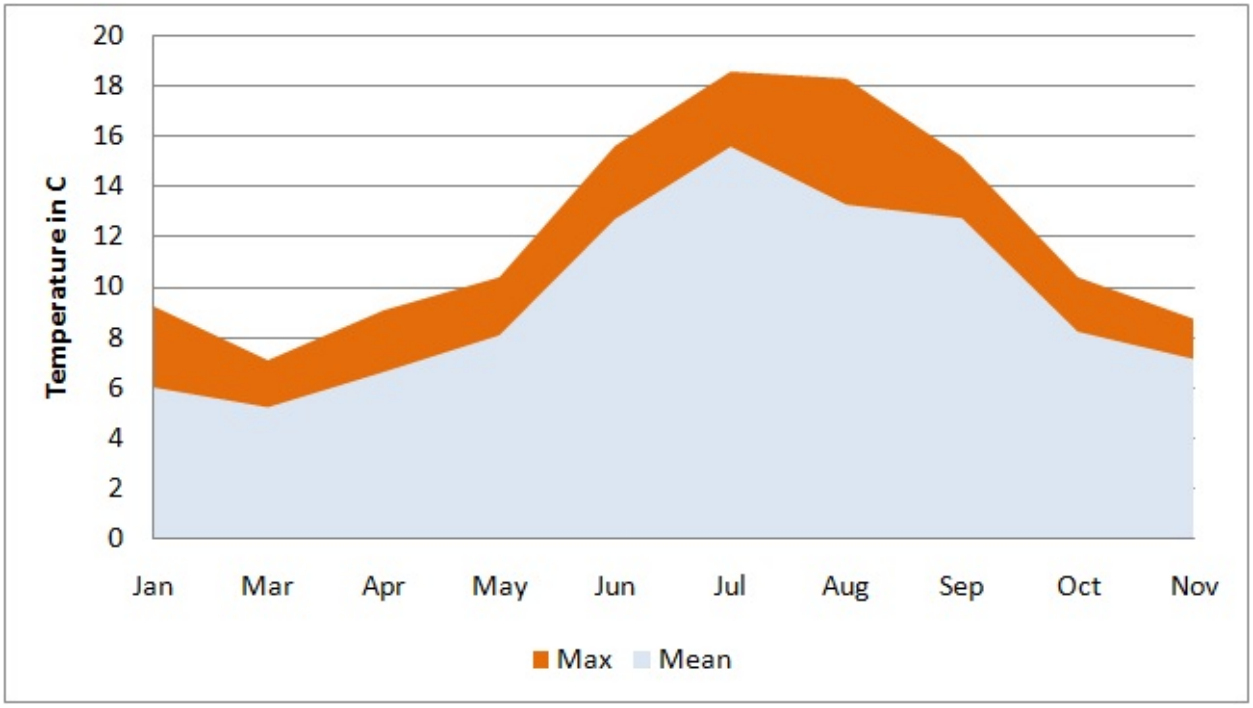

Figure 20. Average of mean and maximum nighttime temperatures

evident during the month of May. This occures because, by the end of April, the transition from winter to spring is usually complete, therefore leading to little variation during the month of May. In the case of June and July, these summer months have hot weather followed by summer showers, including extreme conditions favoring tornados, along the peri-urban areas of Indianapolis. Such weather does not last for a long, but contributes to high variation in mean temperatures. This analysis indicates that such variations can lead to an average temperature difference of over 12 C. The variation in mean temperature is constant during the autumn months. This variation is within a range of 5.5 to 6.5 C, and also exhibits a decreasing trend from August to October.

Nighttime temperatures exhibited less variation in comparison to daytime temperatures. While the maximum variations in temperatures are over 10 C in the case of daytime LST, maximum variation in the nighttime mean and maximum temperatures do not exceed 3.5 C. Maximum variation in nighttime temperatures is evident for the month of April (3.4 C) followed by July and October. These months are also the transition

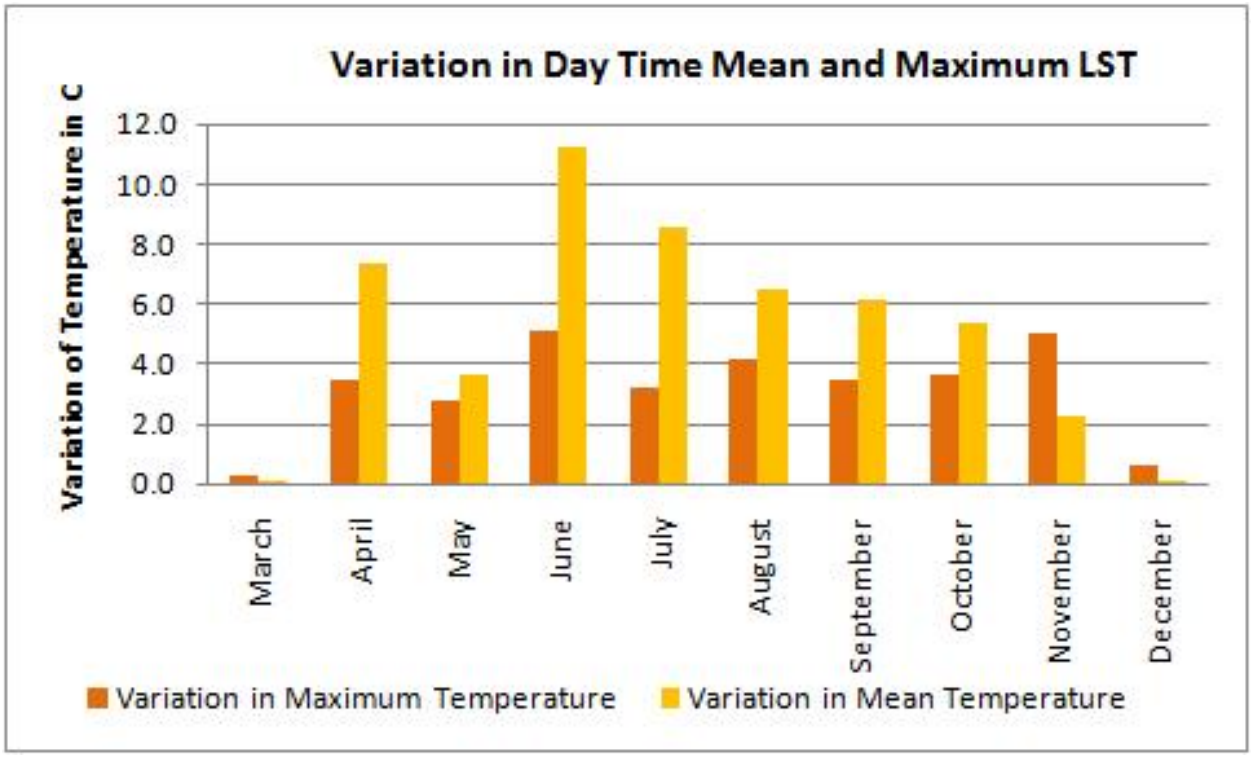

Figure 21. Variation in daytime mean and maximum LST

months between seasons i.e., from winter to spring, summer to autumn and autumn to winter. The analysis indicates that nighttime temperature patterns are sensitive to the change in seasons. The results also indicate that, unlike daytime temperatures, mean and maximum nighttime temperatures exhibit similar variation patterns. Also, in most months the variations in maximum nighttime temperature are higher than mean nighttime temperatures.

The magnitude of daytime and nighttime LST for Marion County and its surrounding regions is presented in Figure 23. It is evident that LST is higher during the daytime than nighttime. This difference in temperature ranges between 2 to 17 C in case of daytime LST, to 1.6 to 5 C in case of nighttime LST. The magnitude of temperature difference is highest during June for daytime LST, and it is highest during the month of August for nighttime LST. While the average magnitude is around 9.2 C, with a variation of 3.5 C for daytime LST, the average magnitude is only 2.7 C, with variation of less than 1 C for nighttime

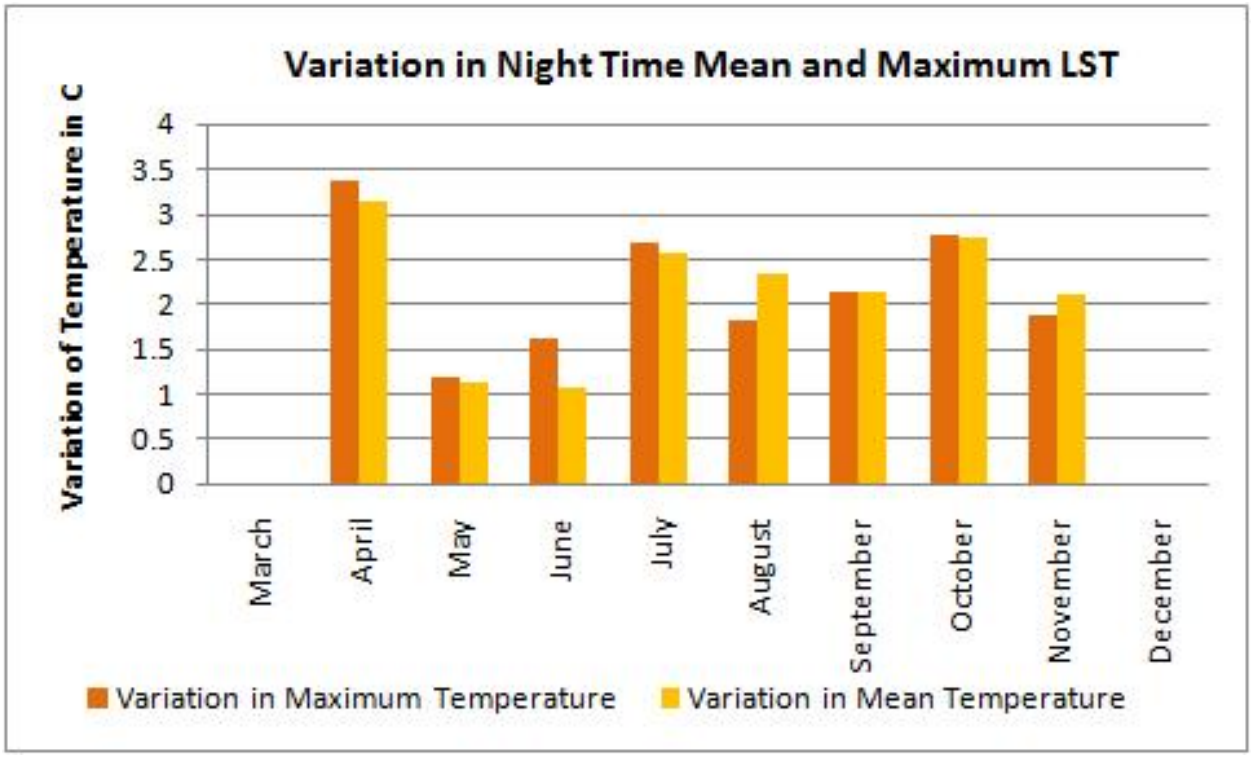

Figure 22. Variation in nighttime mean and maximum LST

LST. This magnitude may not necessary correspond to the magnitude of UHI but does provide us with a range of possible variations over the study area irrespective of month, season or year. A 17 C variation within the study area is a matter of concern. Vulnerable populations (children below 6 and people aged above 65) are likely to experience severe stress in these high magnitude heat pockets.

Urban heat island analysis

LST with minimum cloud cover MODIS images were used to characterize UHI using the non-parametric kernel convolution model as described in the methods section. Non-parametric modeling aided in filling data gaps which were present due to cloud cover, and also aided in characterizing UHI spacially. The result of kernel convolution for an image is presented in Figure 24. The results indicate that LST with minor variations decreases the possibility of identifying the presence of UHI. The process of kernel convolution

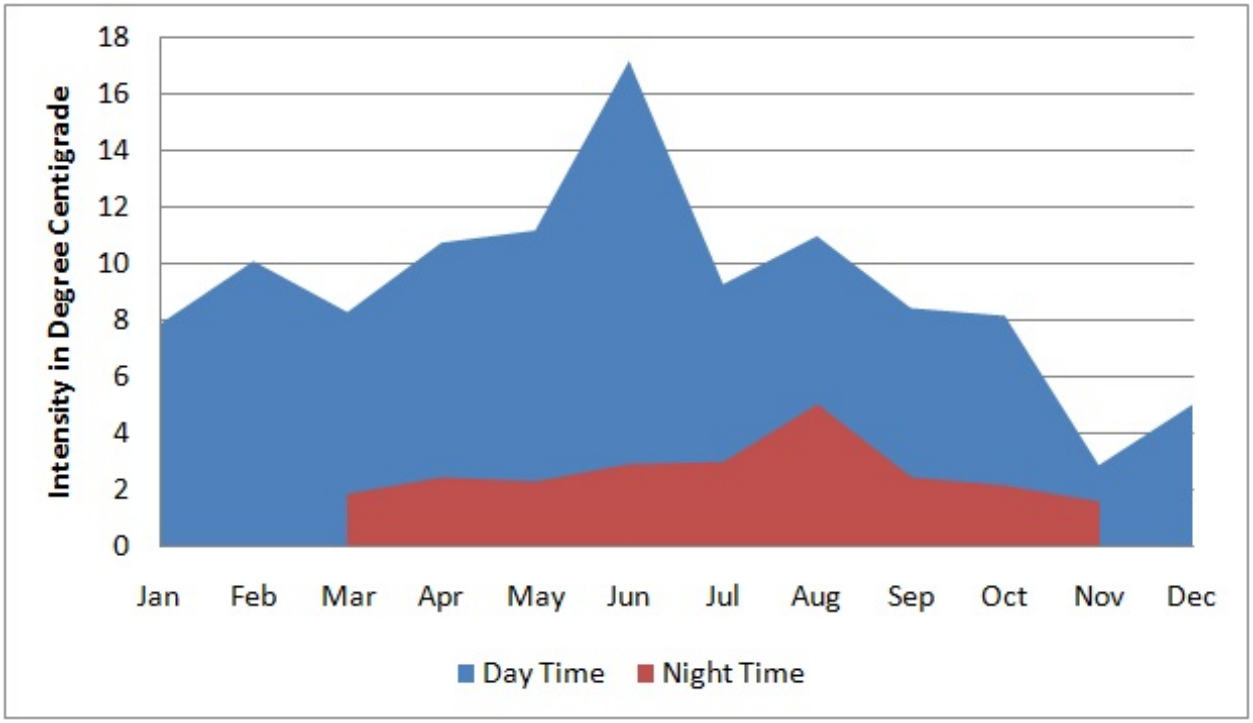

Figure 23. Average magnitude of daytime and nighttime LST

aided in characterizing the image while maintaining its mean temperature. This process demonstrates the effectiveness of an algorithm in identifying the presence of phenomenon by exaggerating or smoothing background noise where necessary. The degree of such smoothing can be controlled by users based on their knowledge and understanding of the phenomena of interest. This degree of smoothing varies from 0 to 100, where 0 is likely to produce an image similar to the original LST and the number 100 is likely to produce an image where variation within the image is equal to the mean.

Kernel convolution did manage to maintain the mean temperature of the LST images while characterizing the heat island through reducing/exaggerating the variations between maximum and minimum temperatures. Figure 25 illustrates the diurnal characteristics of mean LST before and after convolution; it appears that the variation in the actual and modeled mean temperature is minimal.

Figure 26 illustrates the diurnal characteristics of Mean LST after kernel convolution. The results indicate that variation in mean nighttime temperature exhibits a strong pattern

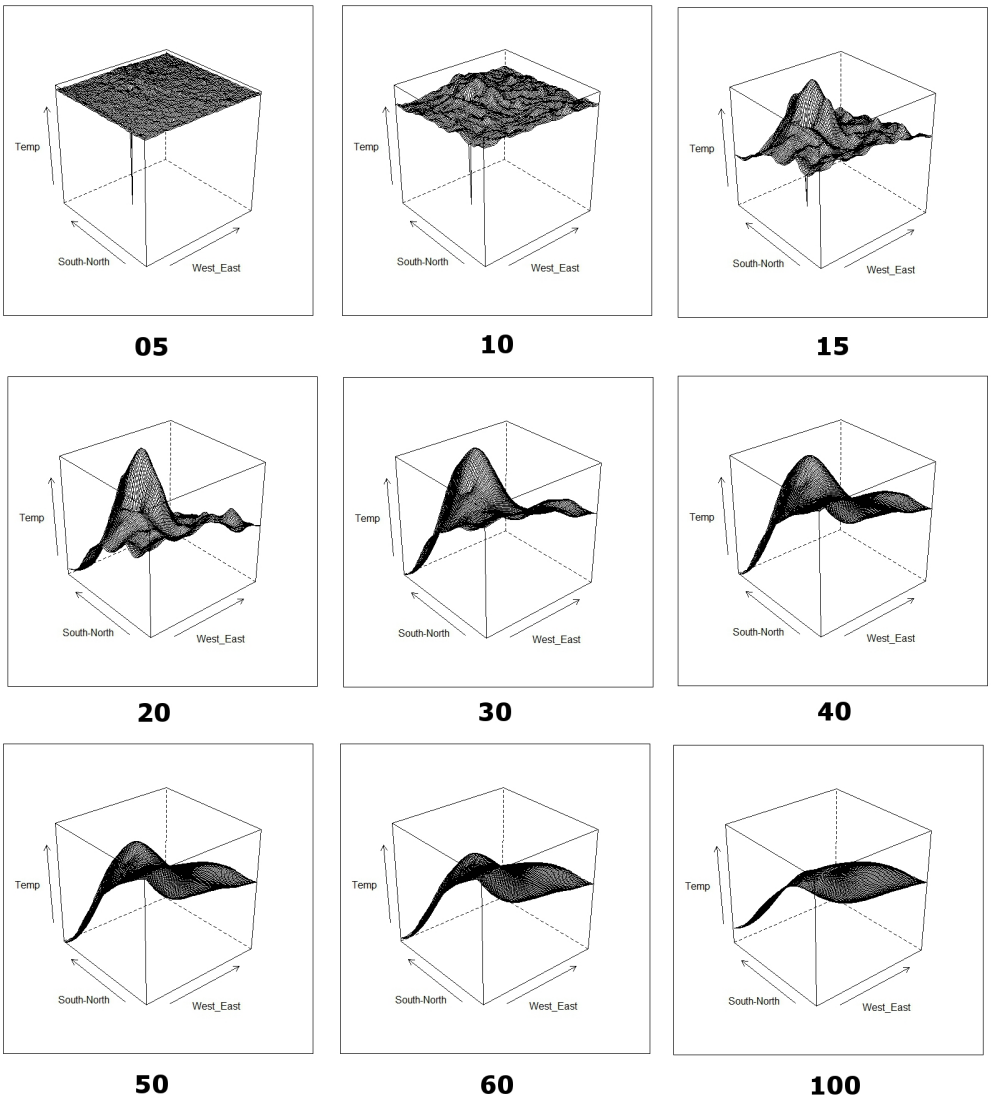

Figure 24. From Top to bottom and left to right represents the stages in Kernel Convolution for 23 February 2006 MODIS LST. The top left image represents the actual images with minor variation in its LST. The top right image illustrates the intermediate process in characterization. The bottom image represents the final image after characterization using kernel convolution.

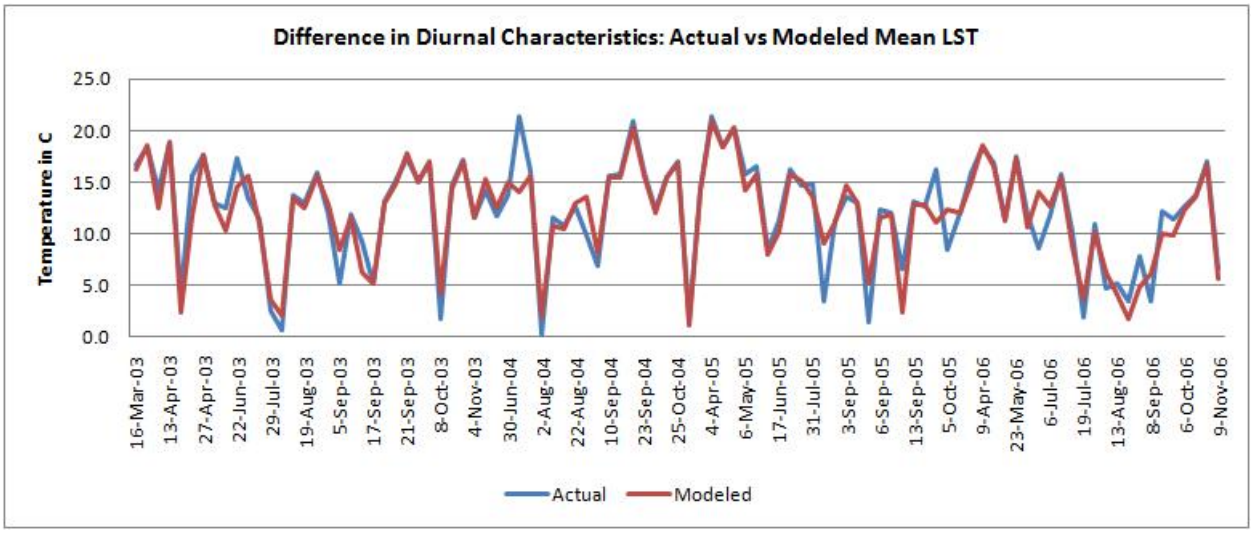

Figure 25. Diurnal characteristics of actual and modeled mean LST

of increase from April to August, and a gradual decrease thereafter. Such patterns were not evident for mean daytime temperatures. Mean daytime temperatures does decline during the months of January through March and between October through December. But, this reduction in temperature does not follow a pattern, as in the case of nighttime mean surface temperature. This may be due to the effect of other disturbances on surface temperature during daytime.

Figure 27 illustrates the diurnal variation in pattern for maximum surface temperatures, i.e., difference between the daytime and nighttime maximum temperatures for selected images. Within the span of four years only limited number of cloud free daytime and nighttime LST were available. The analysis of such modeled LST images indicates that there is an average difference of 14 C between the maximum daytime and maximum nighttime temperatures across all seasons. The diurnal temperature is high during the month of April where the difference is around 18 C and is minimum during July where the difference is around 10 C. It should be noted that corresponding day and night images were not available for the months of January, February and December.

Kernel convolution process does have its limitations. One such limitation is the sensitivity of parameterization to the local mean (in this case mean LST). Variation in

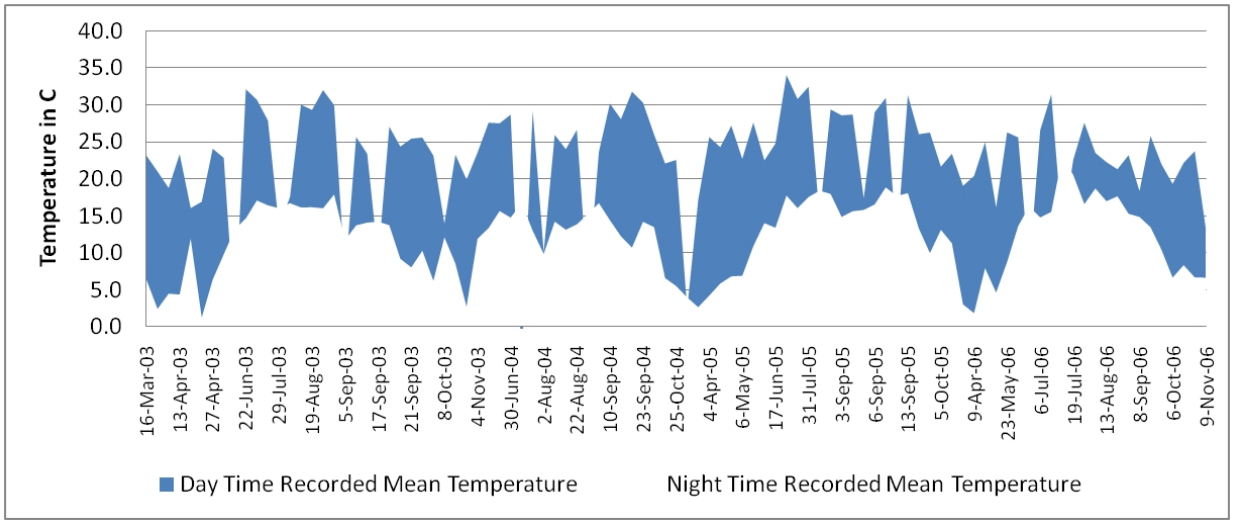

Figure 26. Diurnal characteristics of mean surface temperature

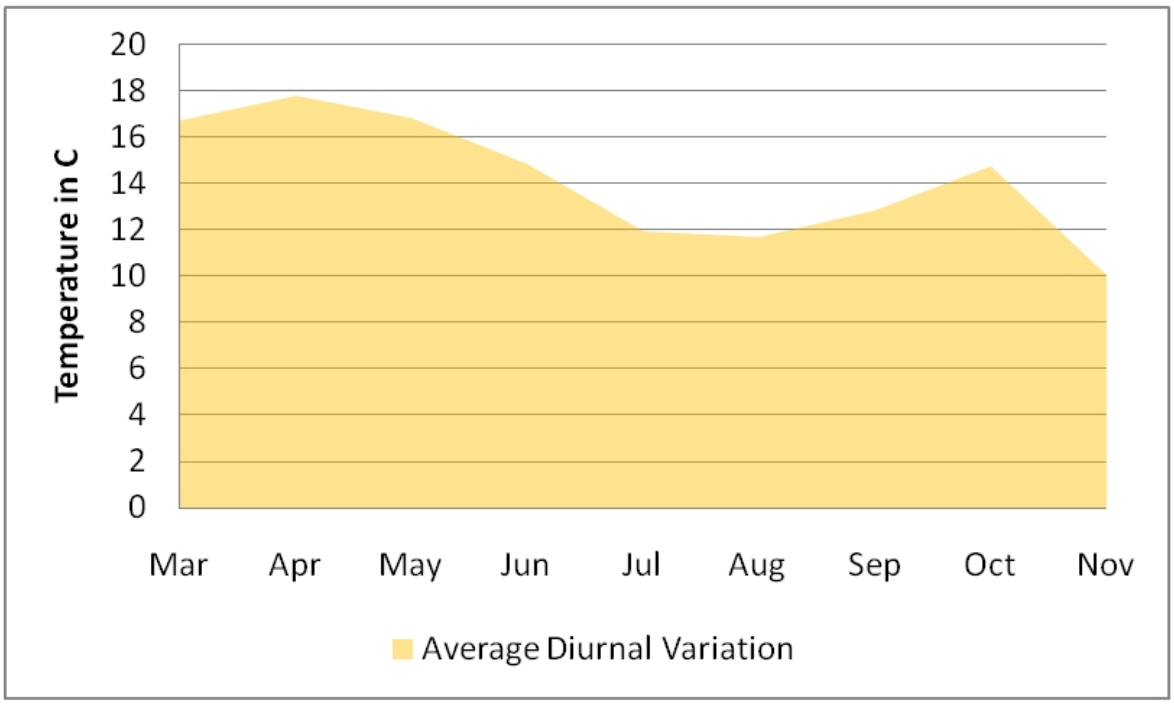

Figure 27. Average month wise diurnal variation in maximum surface temperature

mean temperature will have an impact on the model results. Therefore, the algorithm may not be best suitable for characterizing UHI over a large area. In such cases, presence of more than one heat island, and drastic variation of temperatures within the region, may have impact on results. Therefore, the process of kernel convolution should be limited to smaller regions. Nevertheless, the resulting image and the subsequent conversion of UHI into suitable Gaussian bi-variant functions will be valuable to scientists in compressing information and comparing the effect in space and over time.

Results from the characterization of UHI for Marion County and its surrounding areas can be classified into three categories based on the results obtained from kernel convolution. The results from kernel convolution led to LST being characterized as positive heat islands, negative heat islands and absence of heat islands.

Positive heat islands are those where the central core of the island is hotter than its surroundings. This is similar to the typical heat island phenomenon. Figure 28 illustrates such a heat island with examples from the results of positive heat island effect for Marion County and its surroundings. In these images one can observe the presence of UHI in the north of Marion County. The presence of one UHI is evident in the northern part of the County.

Negative heat islands are those where the central core of the island is colder than the surrounding areas. This is similar to inverse heat island effect, where temperature gradually increases from the core of an island to its surrounding. In this case, the mean temperature is higher than the core of the heat island and therefore, the magnitude is usually lower than the mean. Such areas can also be defined as cold zones, i.e., areas within the urban zone where temperature is usually lower than average for the city. Figure 29 illustrates the presence of negative heat islands within the study area.

These negative heat islands may also be caused by an error within the MODIS LST algorithm. In most images, the MODIS algorithm is designed to identify cloud cover within the land surface and denote such areas as 'no-data'. In spite of the efficiency of the

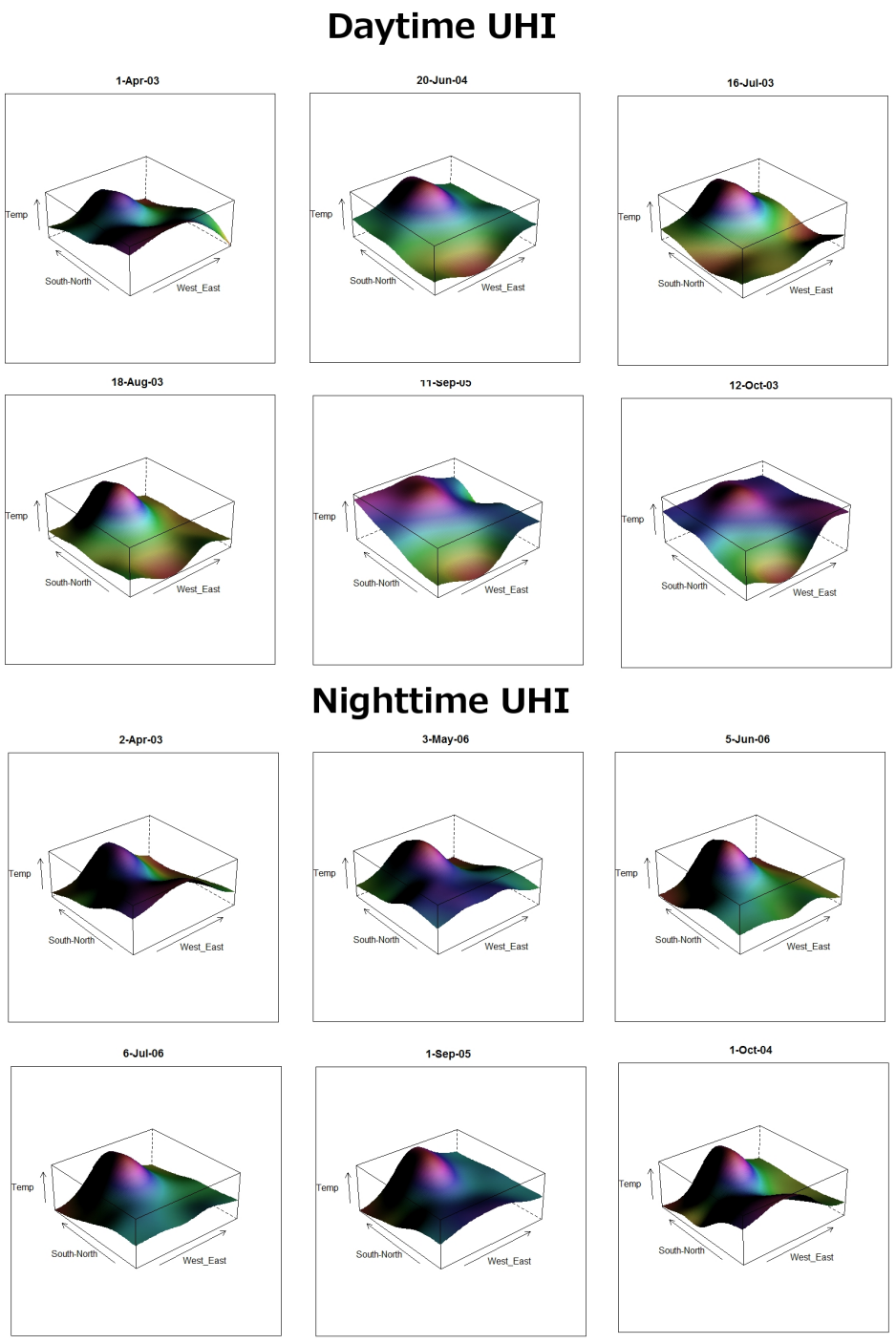

Figure 28. Illustration of positive heat island effect as characterized by kernel convolution method

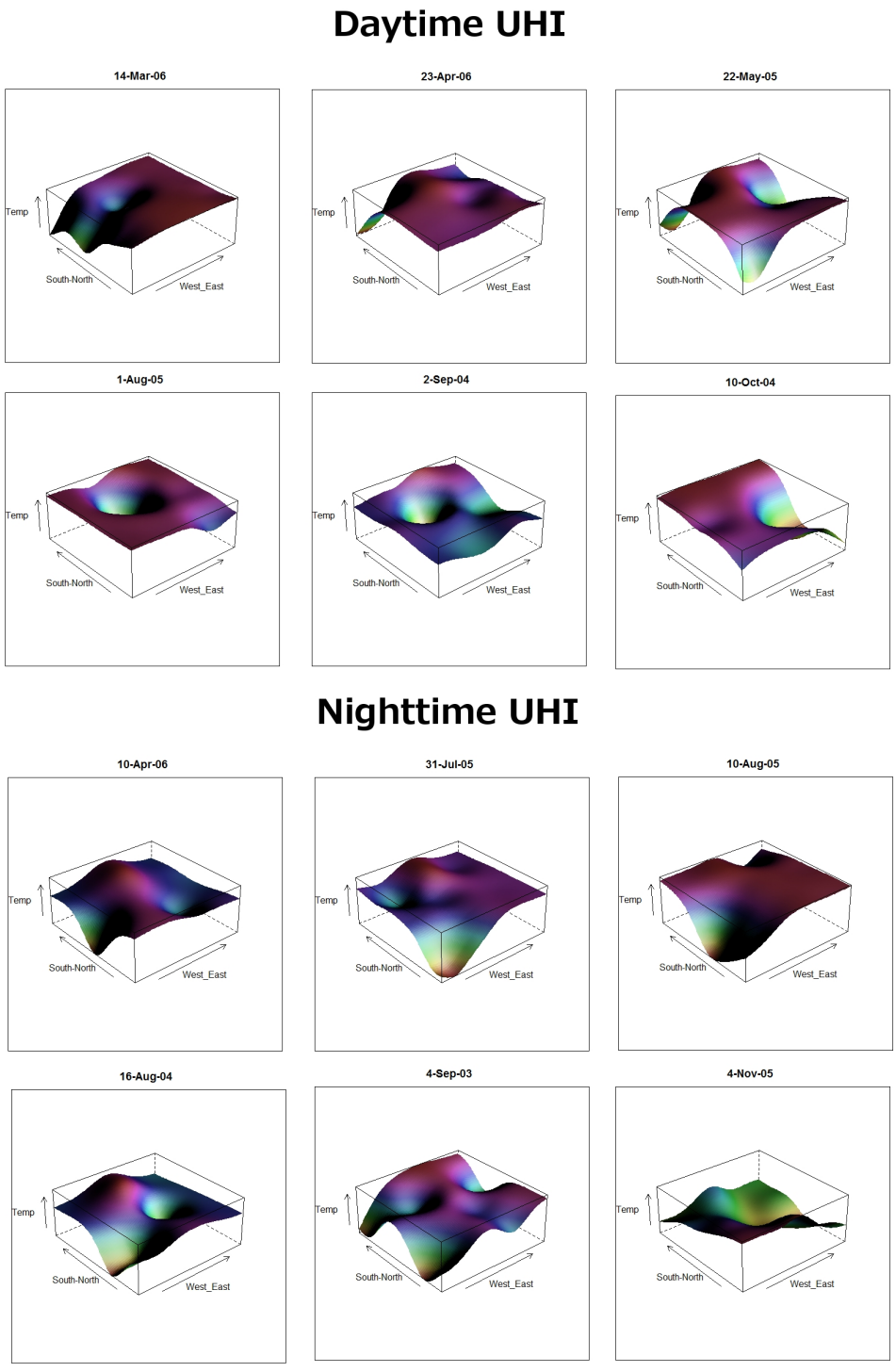

Figure 29. Illustration of negative heat island effect as characterized by kernel convolution method

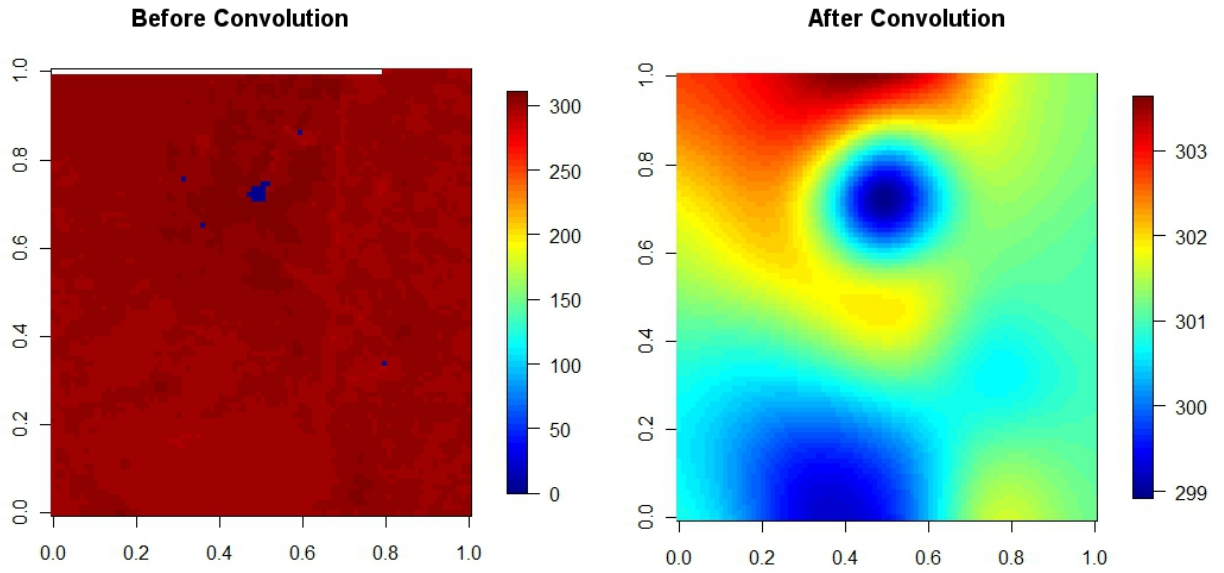

Figure 30. Comparison of MODIS cloud prone LST before convolution and after convolution

algorithm in identifying and differentiating cloud prone areas within most images, the algorithm failed in classifying clouds that were scattered over the 1 km pixel area yielding a mixed pixel effect. The extent of variation in LST (as modeled by MODIS algorithm) depends upon the spread and intensity of cloud cover. This leads the algorithm to assign a probable temperature values to regions which exceed the possible range. For example, there are instances where temperature values for Marion County and its surroundings are less than 0 C even during Spring and Summer months. An example of such a case of cloud cover before convolution and after convolution is presented in Figure 30.

From the Figure 30, it is evident that the kernel convolution method managed to smooth values in areas which have relatively low temperatures based on their surrounding values. But, the result of such smoothing did not aid the desired characterization of UHI. As with the spatial filters of specified dimension, the kernel convolution method is also influenced by the size of cloud cover within the image and uncertainty within LST as modeled by MODIS for a particular region.

It was also evident from this analysis that once the percent cloud cover within a certain region increases beyond a certain threshold, the characterization of LST becomes meaningless. The exact percentage of cloud cover that could lead to such results could not be ascertained in this study due to lack of sufficient data. Nevertheless, it is evident from these results that it is not only percent cloud cover that impacts results, but, it is also the distribution of that cloud cover. Figure 31 illustrates the effect of concentrated cloud cover (cloud cover not evenly distributed over space) on UHI characterization.

Figure 32 illustrates the number of images which were classified into the three different categories after kernel convolution. From the results, it is evident that the presence or absence of heat island does not have any correlation with either month or season but is only proportional to the number of relatively cloud-free images which were used for analysis.

The largest number of images which have well defined UHI effect are from the months of August and September, wherein due to minimal percentage cloud cover more than 10 images are available over a four year span. Apart from these two months, for the rest of the months from April to December the number of cloud free images on an average is of one image per month per year. The Figure 31 highlights the low probability of acquiring a cloud-free image during the months of January, February, March and December, showing that the average number of images that were acquired over a four year period is less than one per month per year. These limitations prevent the detailed analysis of UHI with respect to months and seasonality in this studuy area. Nevertheless, the extent of MODIS images that would be available in the near future (over one decade) will allow the possibility of a detailed analysis of the phenomenon.

This problem can be overcome by identifying the cloud prone pixels in space and populating these cloud prone areas with realistic temperature values for that particular time (day, month or season). This could be achieved by the following means: a) populating temperature values within LST based on real-time ground observation, b) knowledge

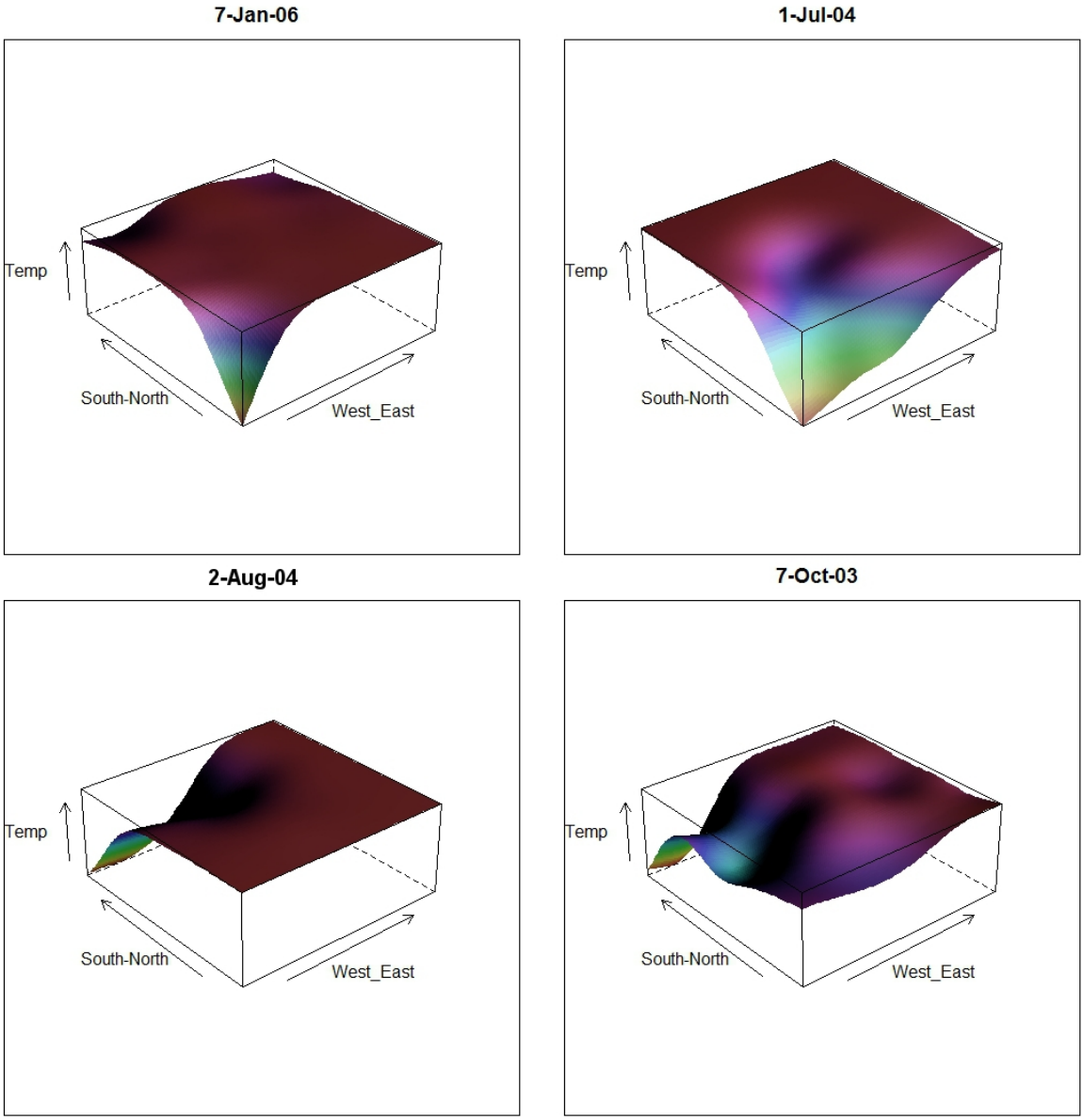

Figure 31. Absence of heat island on LST with concentrated cloud cover

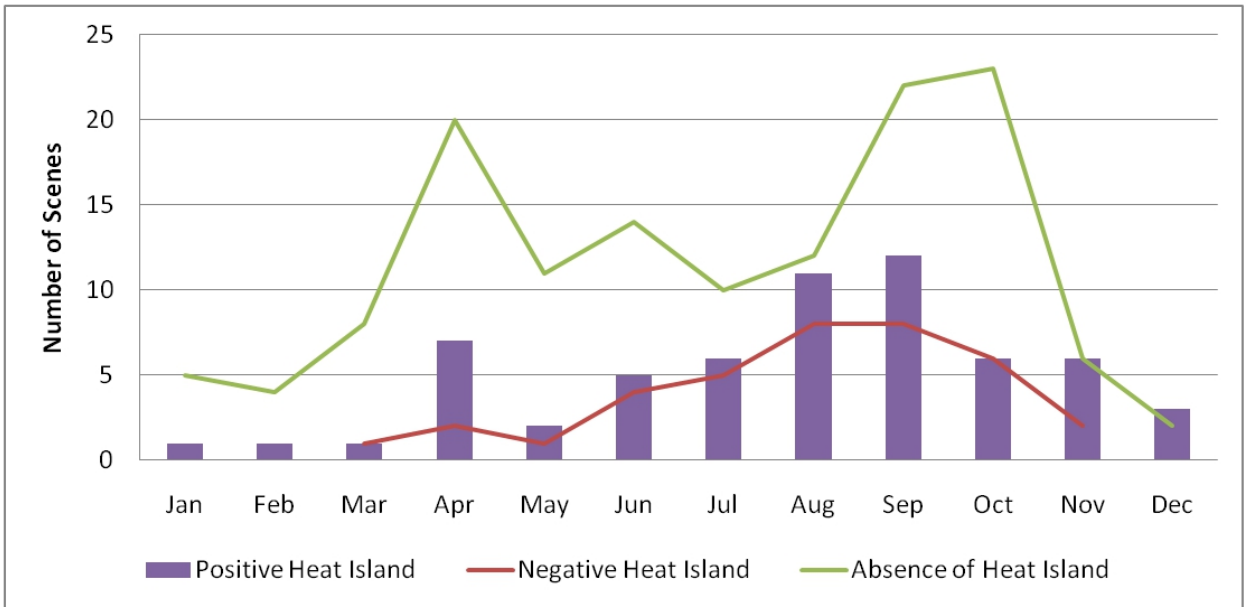

Figure 32. Monthwise distribution of number of positive, negative and absence of UHI within selected relatively cloud free LST images

of the behavior of MODIS algorithm for the study area based on observation over time (especially using 100% cloud-free data), c) populating the possible cloud covered areas with indicative values based on average LST from observations over time, or d) substituting the regions exceeding standard variation using indicative temperature values based on associated land use or land cover parameters.

In this study, since options (a), (b) and (c) were not feasible due to the lack of required data, option (d) was explored using normalized differential vegetation index (NDVI) as one of the indicative parameters. In general, LST is inversly proportional to NDVI. Therefore, an attempt was made to correlate the monthly average NDVI with the monthly average LST to identify patterns that could be used to populate cloud-prone areas.

Month-wise temperature analysis was carried out for characterized surface temperature. The results were also compared with NDVI to identify the existence of any strong correlation with respect to the UHI effect. Since the NDVI is more prominent for the study area between the months of May through October, the image statistics of characterized

surface temperature from these months were used. In order to identify annual variations the temperature and NDVI characteristics were distinguished based on their month and year of acquisition. NDVI for the year 2003 was not available, therefore NDVI results from the years 2004, 2005 and 2006 are presented in this research. The results of the analysis for daytime and nighttime surface temperatures are presented in Figures 33 through 38.

The analysis of May and June daytime modeled surface temperature characteristics with respect to NDVI indicate no strong correlation. NDVI for the month of May was found to be almost constant for all three years (2004-06), with the mean being lower than 0.5 while in the case of June the mean is within the range of 0.55 to 0.6. Also, the standard deviations of NDVI values are higher for May while they are relatively low for June. The mean temperatures for early summer months, i.e., May and June, show a relatively varied picture, with May 2004 exhibiting maximum variation. The result of temperature analysis indicates that the mean and maximum temperatures are low in the years with maximum variation.

Nighttime temperature analysis indicates a similar mean and maximum temperature across all years except May 2004. The results also indicate that the difference between the average of mean nighttime temperature and average of maximum nighttime temperature is very low for May and June. Additionally, the ranges of variations evident within nighttime temperatures for a given month are high in comparison with daytime temperatures. This variation is higher in June than May. The reason for high variation in surface temperatures could be the use of central air conditioning systems. These air conditioning systems are usually located on the rooftops and generate more heat contributing to the high variation. Nevertheless, a detailed analysis of such variation has to be studied using ground survey techniques to understand the cause of such variation, especially for nighttime surface temperatures.

Similar to May and June, the months of July and August indicate a relatively higher NDVI with little variation. There is also some evidence of increase in outliers in July and

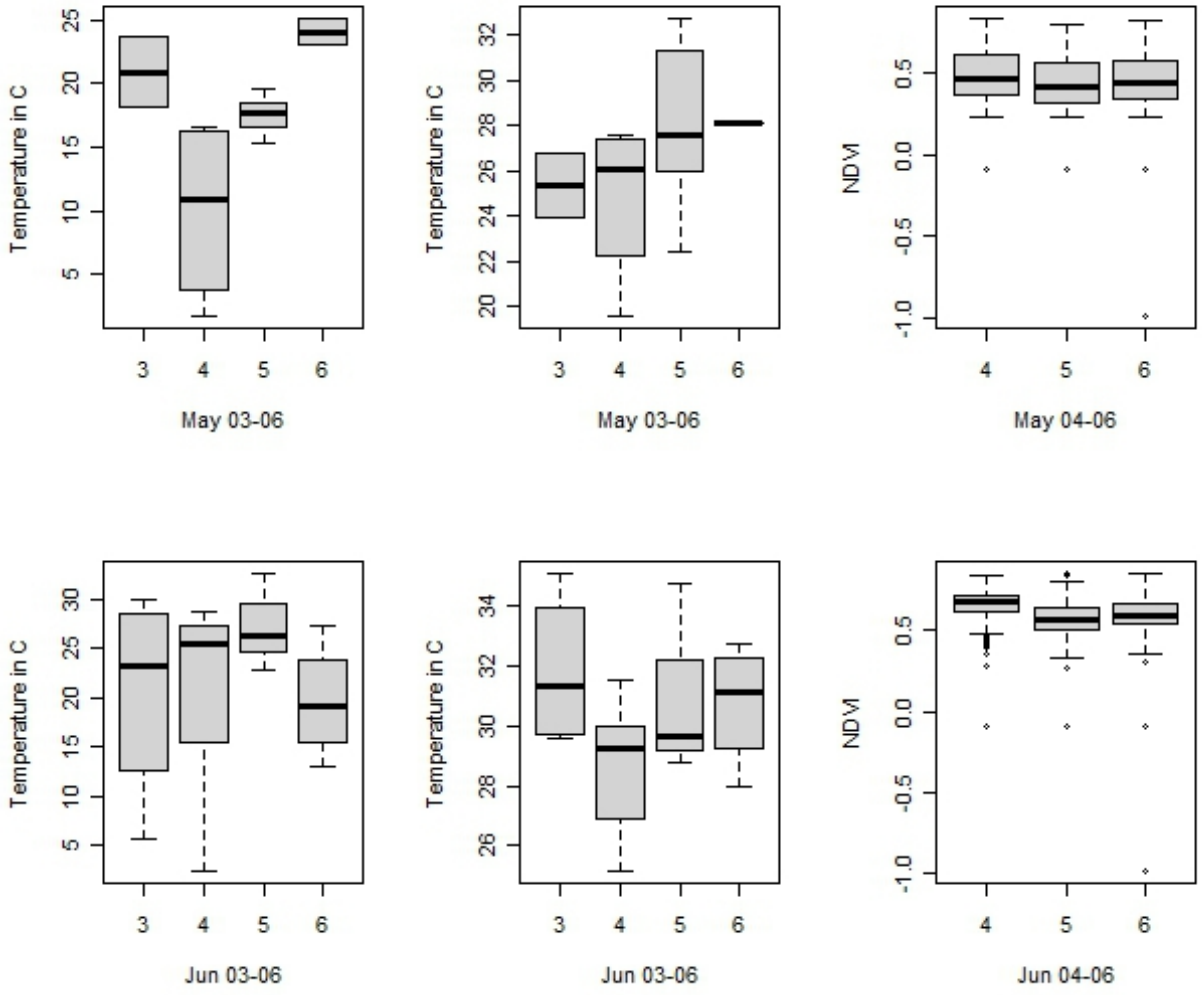

Figure 33. From left to right and top to bottom are box plots representing the distribution of mean daytime surface temperature, maximum daytime surface temperature and NDVI for the months of May and June respectively

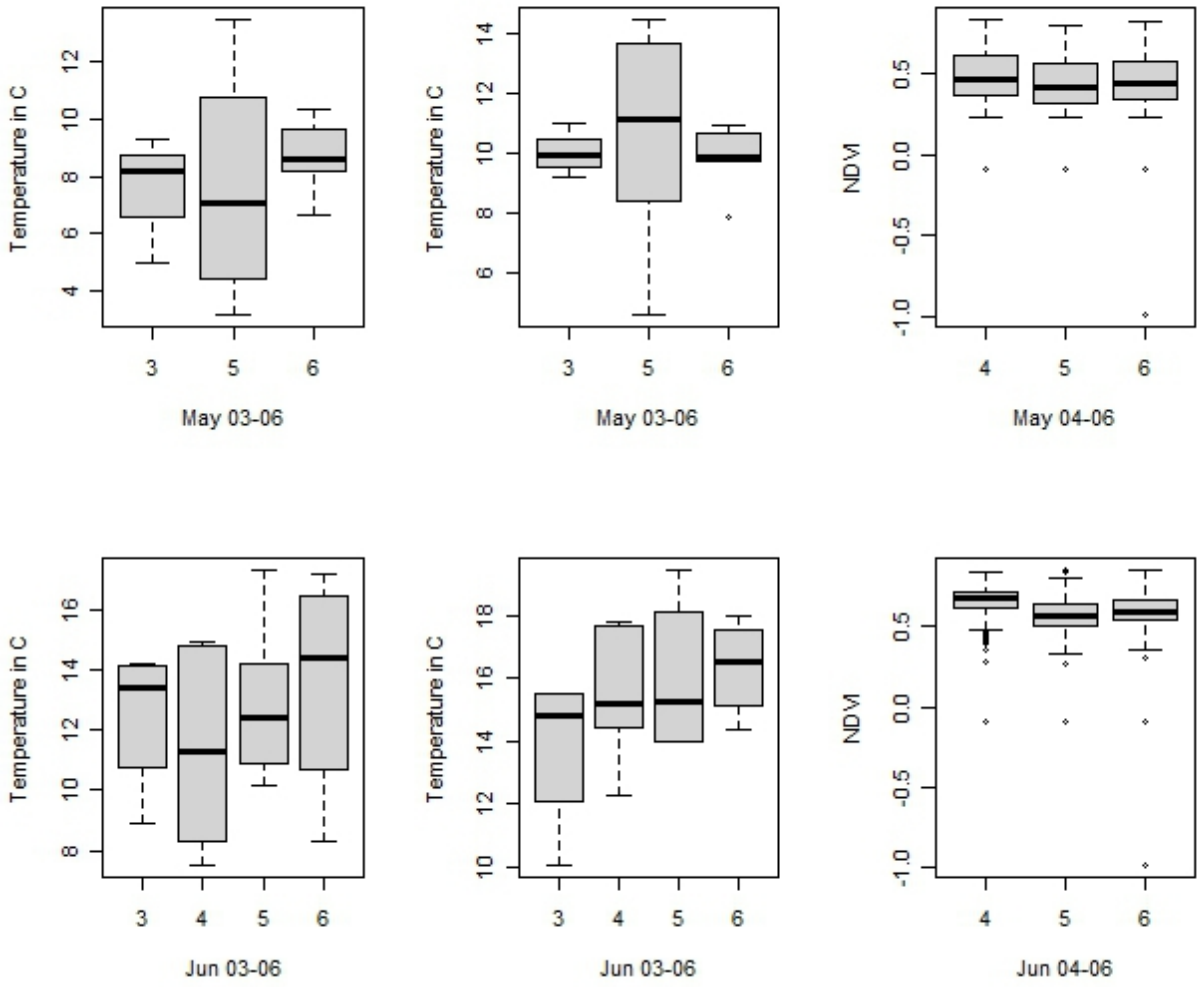

Figure 34. From left to right and top to bottom are box plots representing the distribution of mean nighttime surface temperature, maximum nighttime surface temperature and NDVI for the months of May and June respectively

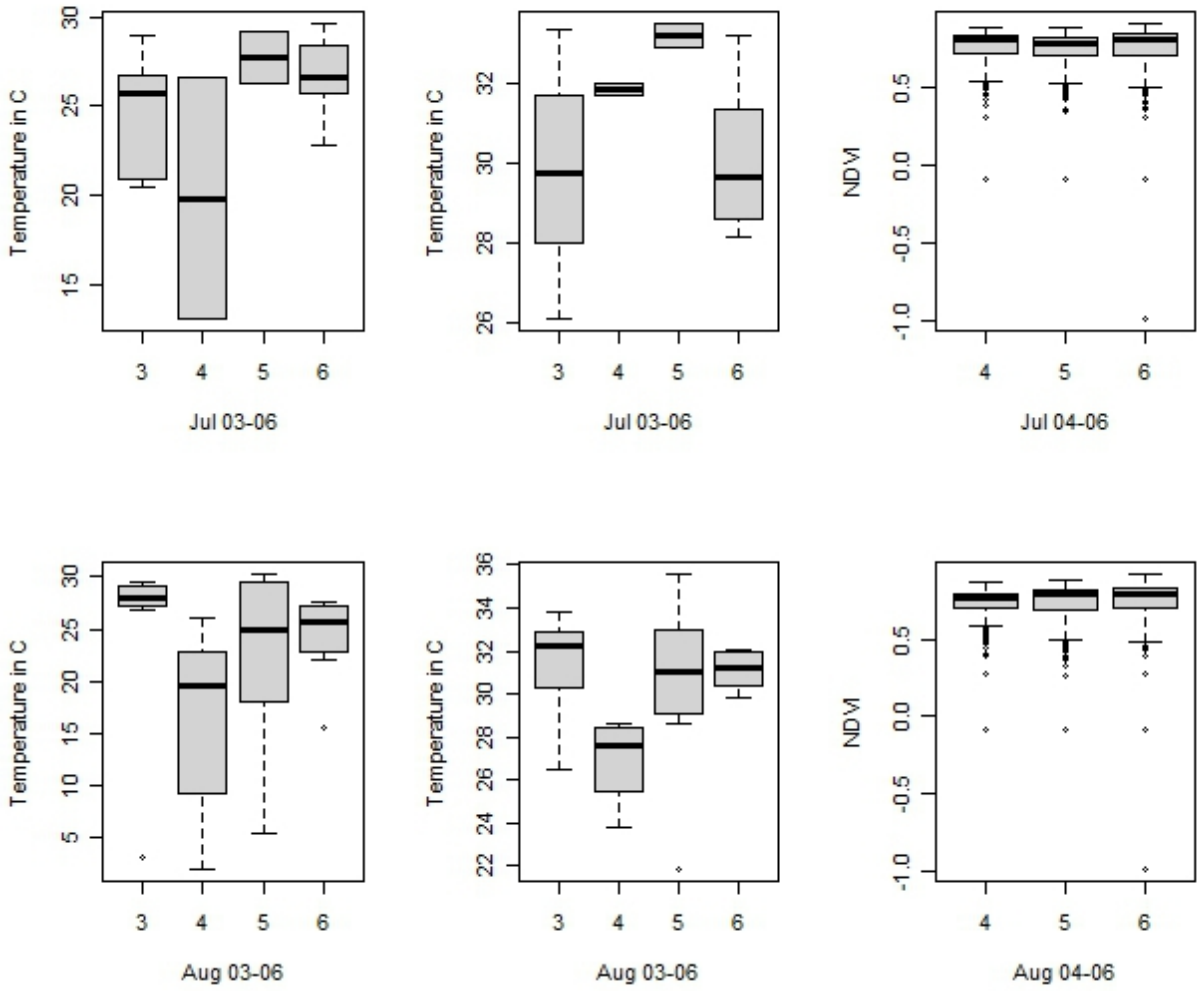

Figure 35. From left to right and top to bottom are box plots representing the distribution of mean daytime surface temperature, maximum daytime surface temperature and NDVI for the months of July and August respectively

August. The mean and average temperatures for the months of July and August were found to be similar. The temperature profile September correlates with July and August. While the temperature profiles for October correlate more closely with May, exhibiting more variation, but yet maintaining monthly average temperature across all years.

In general, from the analysis of daytime temperature it is evident that maximum variation in the average maximum temperature was during the month of May and minimum variation in the average maximum temperature was in the month of October. The months of July to September exhibited maximum temperatures in varying years. In the case of nighttime temperatures, August and September were found to exhibit maximum variation. Average maximum nighttime temperatures were in the months of July, August and September and the minimum nighttime temperatures were observed in October.

Space-Time analysis

The spatio temporal pattern of UHI was analyzed using a four dimensional visualization technique. This visualization was done using ArcScene. In this analysis ASTER false color composite (FCC) of band (3, 2, 1) was used as a base image along the x and y plane of the visualization interface. The months from January to December were projected along the z plane. The result from the model derived UHIs, i.e., the center of UHI was plotted onto this x, y and z plane while colors and sizes were used to represent the fourth dimensions, i.e., the intensity of UHI. This technique provided a visual understanding of the behavior and intensity of UHI in space and in time. The results obtained from this analysis are presented in Tables 31 to 32.

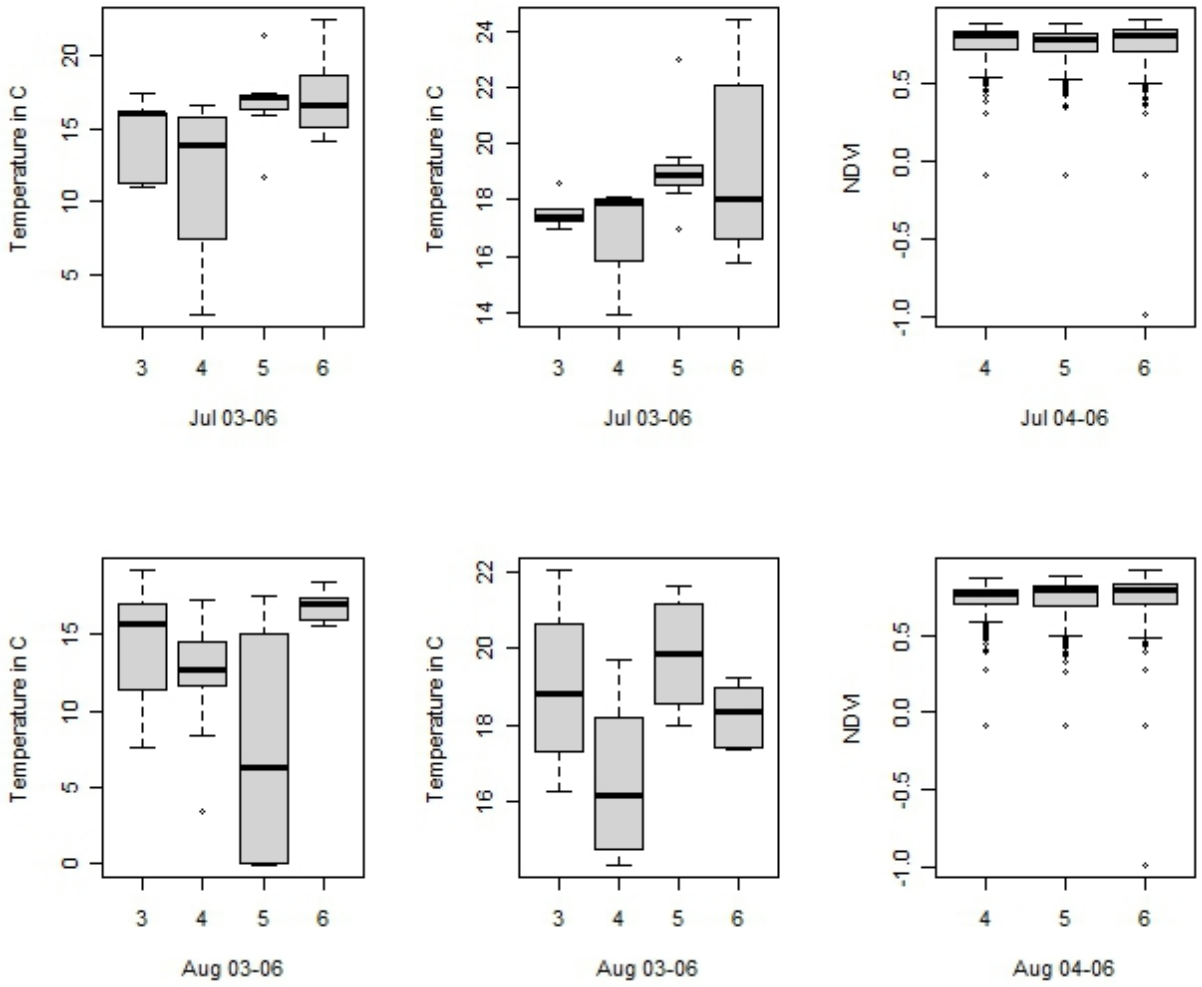

Figure 36. From left to right and top to bottom are box plots representing the distribution of mean nighttime surface temperature, maximum nighttime surface temperature and NDVI for the months of July and August respectively

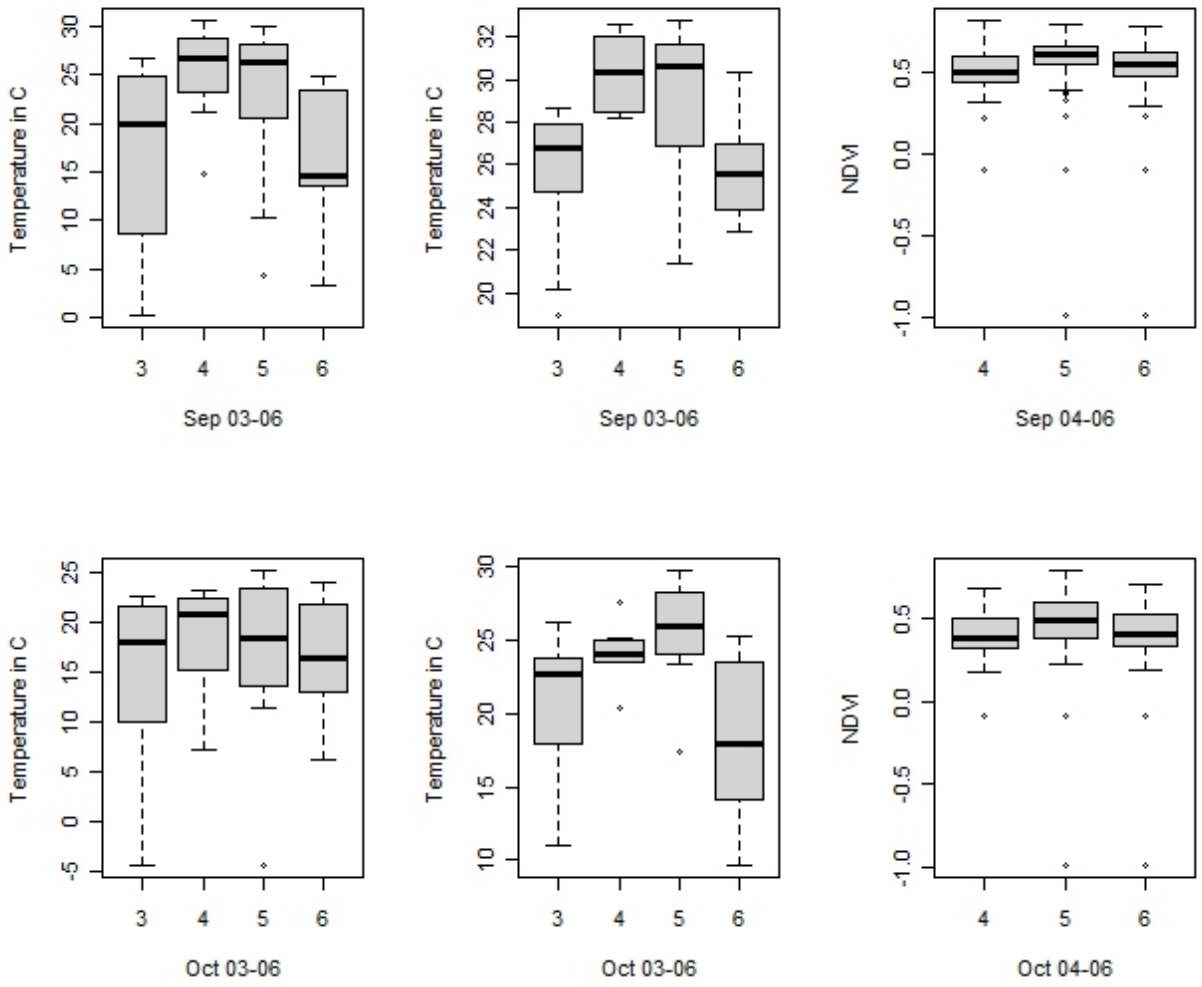

Figure 37. From left to right and top to bottom are box plots representing the distribution of mean daytime surface temperature, maximum daytime surface temperature and NDVI for the months of September and October respectively

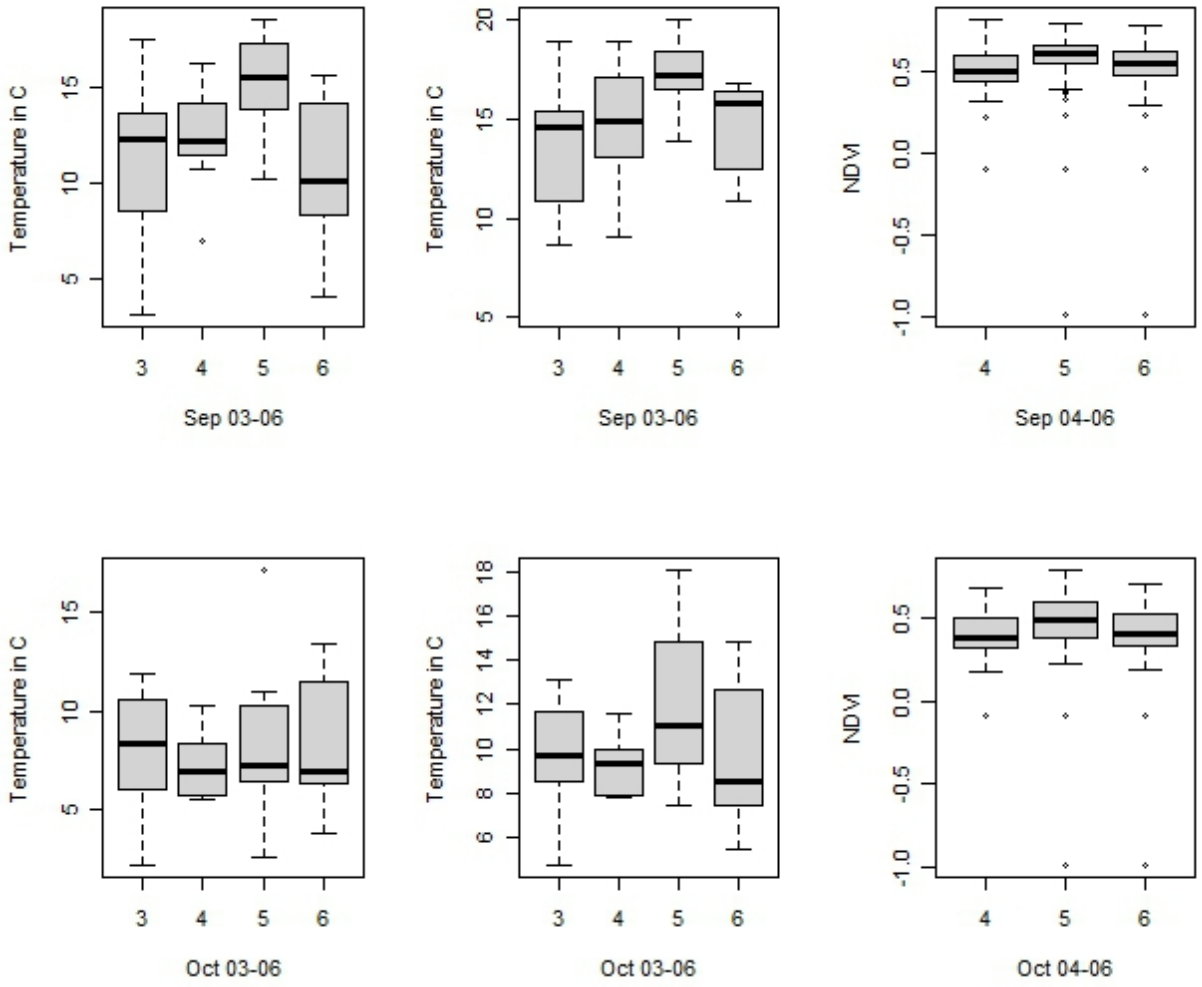

Figure 38. From left to right and top to bottom are box plots representing the distribution of mean nighttime surface temperature, maximum nighttime surface temperature and NDVI for the months of September and October respectively

Table 31

Modeled day time location and intensity of UHI

Date	Lat	Long	Mean Temp	Max Temp	Intensity
3-Apr-03	578515.4	4424080.1	13.1	25.9	13
26-Apr-03	573200.5	4421954.1	22.1	24.5	2
27-Apr-03	574263.5	4421954.1	21.8	25.1	3
5-May-03	573200.5	4426206.0	23.9	26.9	3
13-May-03	574263.5	4420891.2	18.3	24.1	6
20-Jun-03	575326.4	4420891.2	27.1	30.0	3
27-Jun-03	577452.4	4416639.3	30.2	33.0	3
16-Jul-03	575326.4	4425143.1	25.9	28.9	3
17-Jul-03	578515.4	4434709.8	27.5	32.7	5
19-Jul-03	574263.5	4424080.1	29.1	33.5	4
25-Jul-03	574263.5	4423017.1	26.2	29.9	4
18-Aug-03	573200.5	4423017.1	28.2	32.4	4
19-Aug-03	573200.5	4421954.1	27.1	31.0	4
20-Aug-03	574263.5	4420891.2	29.7	33.9	4
23-Aug-03	574263.5	4421954.1	29.0	32.8	4
25-Aug-03	571074.6	4436835.7	29.7	33.3	4
5-Sep-03	574263.5	4430457.9	0.4	27.0	27
6-Sep-03	572137.5	4424080.1	23.6	28.3	5
18-Sep-03	573200.5	4421954.1	26.1	28.2	2
20-Sep-03	571074.6	4420891.2	23.2	25.5	2
21-Sep-03	579578.3	4437898.7	25.7	27.9	2
24-Sep-03	572137.5	4420891.2	24.5	26.6	2
12-Oct-03	574263.5	4420891.2	22.5	23.9	1

Table 31 – continued from previous page

Date	Lat	Long	Mean Temp	Max Temp	Intensity
15-Oct-03	574263.5	4420891.2	17.4	18.4	1
19-Nov-03	581704.3	4426206.0	12.4	13.2	1
23-Mar-04	568948.6	4416639.3	9.7	15.6	6
5-Apr-04	572137.5	4414513.3	12.0	18.3	6
28-Apr-04	572137.5	4412387.4	13.9	24.7	11
3-May-04	573200.5	4417702.3	16.8	19.7	3
28-May-04	570011.6	4412387.4	1.9	27.7	26
31-May-04	574263.5	4421954.1	16.1	25.1	9
19-Jun-04	567885.7	4423017.1	21.2	26.9	6
20-Jun-04	574263.5	4423017.1	25.7	29.4	4
23-Jun-04	576389.4	4426206.0	26.6	30.2	4
15-Jul-04	573200.5	4425143.1	13.2	31.8	19
28-Jul-04	573200.5	4426206.0	26.7	32.1	5
6-Aug-04	575326.4	4426206.0	19.8	28.6	9
10-Sep-04	573200.5	4421954.1	29.0	31.5	2
19-Sep-04	577452.4	4423017.1	27.7	29.6	2
2-Dec-04	571074.6	4406009.6	7.4	8.2	1
3-Mar-05	576389.4	4420891.2	3.2	7.7	4
24-Mar-05	574263.5	4417702.3	14.1	15.2	1
4-Apr-05	568948.6	4413450.4	20.7	26.0	5
8-Apr-05	574263.5	4423017.1	21.0	22.6	2
4-May-05	571074.6	4423017.1	18.6	22.6	4
6-May-05	570011.6	4424080.1	15.4	27.3	12
29-May-05	571074.6	4423017.1	19.7	31.5	12
31-May-05	573200.5	4425143.1	16.8	28.2	11

Table 31 – continued from previous page

Date	Lat	Long	Mean Temp	Max Temp	Intensity
16-Jun-05	576389.4	4421954.1	26.5	29.8	3
17-Jun-05	580641.3	4437898.7	23.0	28.9	6
29-Jul-05	573200.5	4423017.1	26.4	33.6	7
21-Aug-05	573200.5	4425143.1	30.3	35.7	5
2-Sep-05	573200.5	4425143.1	28.2	31.4	3
3-Sep-05	575326.4	4441087.6	27.8	31.1	3
4-Sep-05	573200.5	4425143.1	27.3	30.8	3
11-Sep-05	571074.6	4423017.1	29.9	32.3	2
13-Sep-05	570011.6	4425143.1	30.1	32.9	3
29-Sep-05	574263.5	4419828.2	19.9	21.5	2
1-Oct-05	576389.4	4420891.2	11.6	27.2	16
26-Jan-06	574263.5	4420891.2	5.9	7.0	1
23-Feb-06	573200.5	4418765.2	9.3	10.4	1
18-Mar-06	571074.6	4414513.3	4.0	11.2	7
4-Apr-06	573200.5	4423017.1	16.0	17.9	2
9-Apr-06	574263.5	4423017.1	19.8	21.6	2
18-Apr-06	574263.5	4423017.1	23.5	26.3	3
19-Apr-06	576389.4	4421954.1	21.6	25.8	4
23-Apr-06	572137.5	4418765.2	22.7	26.4	4
27-Apr-06	575326.4	4426206.0	11.1	25.2	14
20-May-06	575326.4	4425143.1	25.2	28.2	3
23-May-06	572137.5	4419828.2	23.3	28.3	5
3-Jun-06	574263.5	4425143.1	27.4	30.6	3
5-Jun-06	564696.7	4419828.2	17.9	31.9	14
14-Jun-06	570011.6	4427269.0	20.6	32.9	12

Table 31 – continued from previous page

Date	Lat	Long	Mean Temp	Max Temp	Intensity
5-Jul-06	575326.4	4425143.1	25.5	29.6	4
7-Jul-06	576389.4	4423017.1	29.7	33.3	4
15-Jul-06	579578.3	4433646.8	29.7	32.8	3
4-Aug-06	572137.5	4423017.1	27.5	32.2	5
12-Aug-06	577452.4	4431520.9	27.1	30.9	4
15-Aug-06	573200.5	4424080.1	27.8	32.2	4
16-Aug-06	575326.4	4427269.0	15.8	30.0	14
20-Aug-06	573200.5	4419828.2	25.9	30.2	4
6-Sep-06	576389.4	4427269.0	24.9	29.0	4
9-Sep-06	574263.5	4423017.1	23.6	30.5	7
25-Sep-06	579578.3	4420891.2	21.3	24.0	3
27-Sep-06	574263.5	4418765.2	25.0	26.8	2
6-Oct-06	575326.4	4419828.2	18.4	20.1	2
7-Oct-06	578515.4	4416639.3	21.4	22.6	1
13-Oct-06	574263.5	4418765.2	12.3	13.5	1
22-Nov-06	571074.6	4419828.2	8.8	11.0	2
23-Nov-06	575326.4	4416639.3	10.6	12.4	2

Table 32

Modeled night time location and intensity of UHI

Date	Lat	Long	Mean Temp	Max Temp	Intensity
15-Apr-03	575326.4	4427269.0	9.0	13.8	4.8
16-Apr-03	573200.5	4434709.8	8.6	15.2	6.6

Table 32 – continued from previous page

Date	Lat	Long	Mean Temp	Max Temp	Intensity
23-May-03	575326.4	4427269.0	8.3	9.3	1.0
24-May-03	573200.5	4418765.2	5.2	10.1	4.9
2-Jun-03	573200.5	4419828.2	9.1	10.2	1.2
10-Jun-03	572137.5	4423017.1	14.4	15.7	1.3
21-Jun-03	572137.5	4426206.0	12.8	14.3	1.5
22-Jun-03	572137.5	4423017.1	14.3	15.6	1.4
17-Jul-03	572137.5	4424080.1	11.2	17.6	6.4
20-Jul-03	572137.5	4420891.2	17.6	18.8	1.2
25-Jul-03	574263.5	4428332.0	16.2	17.4	1.2
29-Jul-03	565759.7	4435772.8	11.5	17.1	5.7
30-Jul-03	571074.6	4424080.1	16.3	17.8	1.6
1-Aug-03	573200.5	4424080.1	17.8	20.0	2.2
13-Aug-03	571074.6	4425143.1	7.7	16.4	8.7
17-Aug-03	562570.8	4419828.2	10.1	21.6	11.5
19-Aug-03	573200.5	4426206.0	15.7	17.8	2.0
20-Aug-03	571074.6	4420891.2	15.1	17.5	2.3
21-Aug-03	574263.5	4420891.2	19.3	20.8	1.5
24-Aug-03	570011.6	4419828.2	15.9	18.0	2.1
25-Aug-03	573200.5	4427269.0	17.2	20.0	2.8
28-Aug-03	573200.5	4425143.1	11.5	22.2	10.6
5-Sep-03	570011.6	4419828.2	11.6	12.5	0.9
6-Sep-03	572137.5	4421954.1	13.2	14.6	1.4
7-Sep-03	572137.5	4424080.1	13.3	14.9	1.6
11-Sep-03	573200.5	4425143.1	17.6	19.1	1.5
17-Sep-03	574263.5	4426206.0	13.8	15.5	1.7

Table 32 – continued from previous page

Date	Lat	Long	Mean Temp	Max Temp	Intensity
18-Sep-03	573200.5	4427269.0	13.7	15.4	1.7
20-Sep-03	573200.5	4428332.0	3.3	10.4	7.1
21-Sep-03	572137.5	4425143.1	6.9	9.5	2.5
24-Sep-03	573200.5	4427269.0	10.1	11.6	1.4
26-Sep-03	573200.5	4425143.1	7.3	8.8	1.5
9-Oct-03	571074.6	4424080.1	10.7	11.9	1.1
13-Oct-03	573200.5	4424080.1	8.2	9.4	1.2
3-Nov-03	574263.5	4436835.7	12.4	13.9	1.4
20-Nov-03	577452.4	4430457.9	5.3	6.2	1.0
3-Jun-04	566822.7	4414513.3	11.4	12.4	1.0
7-Jun-04	573200.5	4426206.0	15.1	17.9	2.8
23-Jun-04	574263.5	4427269.0	8.4	14.6	6.2
24-Jun-04	575326.4	4429394.9	15.0	17.8	2.8
30-Jun-04	571074.6	4411324.4	7.7	15.3	7.7
1-Jul-04	573200.5	4425143.1	2.4	17.9	15.5
16-Jul-04	571074.6	4424080.1	16.7	18.3	1.6
18-Jul-04	572137.5	4427269.0	15.1	18.2	3.0
28-Jul-04	573200.5	4424080.1	12.8	14.1	1.2
1-Aug-04	572137.5	4424080.1	13.6	19.1	5.5
2-Aug-04	577452.4	4428332.0	3.6	16.4	12.8
7-Aug-04	572137.5	4425143.1	12.6	14.5	1.9
9-Aug-04	573200.5	4428332.0	14.6	18.0	3.3
16-Aug-04	568948.6	4425143.1	11.7	14.5	2.8
22-Aug-04	566822.7	4419828.2	13.2	15.1	1.9
23-Aug-04	573200.5	4423017.1	17.4	18.3	1.0

Table 32 – continued from previous page

Date	Lat	Long	Mean Temp	Max Temp	Intensity
31-Aug-04	573200.5	4421954.1	14.8	16.2	1.4
2-Sep-04	572137.5	4426206.0	16.4	18.1	1.7
10-Sep-04	571074.6	4425143.1	14.2	15.5	1.3
11-Sep-04	571074.6	4426206.0	15.3	17.2	1.9
13-Sep-04	574263.5	4423017.1	15.4	18.7	3.3
15-Sep-04	578515.4	4421954.1	12.3	19.0	6.7
18-Sep-04	573200.5	4426206.0	11.2	13.2	2.0
20-Sep-04	573200.5	4426206.0	11.9	14.1	2.2
26-Sep-04	573200.5	4421954.1	12.7	14.1	1.4
27-Sep-04	572137.5	4421954.1	11.6	13.2	1.6
30-Sep-04	573200.5	4423017.1	7.2	9.2	2.1
1-Oct-04	574263.5	4426206.0	8.5	10.1	1.6
4-Oct-04	576389.4	4434709.8	7.1	9.5	2.4
6-Nov-04	576389.4	4436835.7	2.7	3.9	1.2
16-Apr-05	575326.4	4431520.9	6.4	8.6	2.2
20-Apr-05	573200.5	4433646.8	11.8	15.0	3.2
1-May-05	568948.6	4419828.2	3.3	4.7	1.4
6-May-05	572137.5	4424080.1	6.6	8.0	1.5
7-May-05	574263.5	4421954.1	4.0	10.7	6.7
17-May-05	572137.5	4420891.2	7.9	9.0	1.1
29-May-05	573200.5	4421954.1	10.6	11.8	1.2
31-May-05	572137.5	4426206.0	13.6	14.6	1.0
17-Jun-05	572137.5	4421954.1	13.0	14.1	1.1
18-Jun-05	574263.5	4421954.1	12.2	14.2	2.0
19-Jun-05	572137.5	4424080.1	14.4	15.7	1.3

Table 32 – continued from previous page

Date	Lat	Long	Mean Temp	Max Temp	Intensity
23-Jun-05	572137.5	4420891.2	17.4	18.3	0.8
4-Jul-05	572137.5	4404946.6	17.3	19.1	1.7
9-Jul-05	573200.5	4427269.0	17.3	19.2	1.9
10-Jul-05	573200.5	4426206.0	16.0	18.4	2.4
23-Jul-05	572137.5	4425143.1	21.5	23.2	1.7
29-Jul-05	574263.5	4424080.1	11.8	17.1	5.3
30-Jul-05	572137.5	4424080.1	17.5	19.0	1.4
31-Jul-05	574263.5	4429394.9	17.0	19.7	2.7
4-Aug-05	580641.3	4423017.1	0.1	20.8	20.8
10-Aug-05	570011.6	4429394.9	12.6	21.8	9.1
17-Aug-05	572137.5	4421954.1	17.7	19.2	1.5
28-Aug-05	580641.3	4423017.1	0.3	18.2	17.8
1-Sep-05	574263.5	4427269.0	15.9	17.2	1.3
2-Sep-05	574263.5	4419828.2	17.4	18.5	1.1
4-Sep-05	572137.5	4427269.0	15.1	17.0	1.9
5-Sep-05	575326.4	4431520.9	15.4	17.6	2.1
6-Sep-05	573200.5	4426206.0	16.1	17.8	1.7
11-Sep-05	573200.5	4426206.0	18.6	20.1	1.5
12-Sep-05	573200.5	4425143.1	17.4	18.6	1.1
13-Sep-05	573200.5	4427269.0	18.1	19.5	1.4
18-Sep-05	573200.5	4425143.1	14.0	15.7	1.7
22-Sep-05	574263.5	4427269.0	13.9	17.1	3.3
1-Oct-05	572137.5	4426206.0	9.8	11.2	1.4
6-Oct-05	571074.6	4428332.0	17.3	18.2	1.0
8-Oct-05	573200.5	4417702.3	2.8	9.3	6.5

Table 32 – continued from previous page

Date	Lat	Long	Mean Temp	Max Temp	Intensity
15-Oct-05	574263.5	4427269.0	11.1	12.3	1.2
5-Apr-06	576389.4	4428332.0	2.7	3.8	1.1
9-Apr-06	573200.5	4423017.1	1.1	2.6	1.5
10-Apr-06	572137.5	4423017.1	2.7	4.1	1.4
24-Apr-06	572137.5	4419828.2	9.9	11.1	1.2
27-Apr-06	573200.5	4425143.1	4.3	5.8	1.5
3-May-06	572137.5	4425143.1	10.5	11.1	0.6
21-May-06	573200.5	4425143.1	9.8	10.8	1.0
23-May-06	572137.5	4426206.0	8.4	9.9	1.5
5-Jun-06	573200.5	4424080.1	13.2	14.5	1.3
6-Jun-06	574263.5	4424080.1	8.5	16.1	7.6
8-Jun-06	573200.5	4419828.2	17.3	18.1	0.8
30-Jun-06	575326.4	4426206.0	15.9	17.3	1.4
6-Jul-06	573200.5	4424080.1	14.2	15.9	1.7
7-Jul-06	572137.5	4425143.1	15.2	16.8	1.6
17-Jul-06	571074.6	4425143.1	22.6	24.6	2.0
19-Jul-06	568948.6	4425143.1	18.8	22.3	3.5
23-Jul-06	575326.4	4417702.3	16.0	17.3	1.2
24-Jul-06	572137.5	4423017.1	17.4	19.1	1.8
5-Aug-06	571074.6	4421954.1	18.6	19.4	0.8
13-Aug-06	572137.5	4415576.3	16.1	17.6	1.4
16-Aug-06	571074.6	4424080.1	17.2	18.5	1.3
21-Aug-06	571074.6	4421954.1	15.8	17.5	1.8
4-Sep-06	572137.5	4421954.1	8.3	14.1	5.8
7-Sep-06	574263.5	4424080.1	8.7	16.7	8.0

Table 32 – continued from previous page

Date	Lat	Long	Mean Temp	Max Temp	Intensity
8-Sep-06	572137.5	4428332.0	14.0	16.3	2.3
15-Sep-06	574263.5	4429394.9	10.2	15.6	5.4
16-Sep-06	572137.5	4426206.0	14.6	16.2	1.6
17-Sep-06	573200.5	4427269.0	15.7	17.0	1.2
26-Sep-06	573200.5	4425143.1	10.3	11.0	0.8
29-Sep-06	568948.6	4418765.2	4.3	5.3	1.0
2-Oct-06	572137.5	4426206.0	13.5	15.0	1.5
7-Oct-06	571074.6	4423017.1	7.7	9.1	1.5
8-Oct-06	571074.6	4427269.0	6.6	8.2	1.6

From the results it was observed that, the UHI derived from the MODIS data was contrary to the expectation that land cover of a certain type would radiate relative heat given a constant temperature. From earlier analysis by Rajasekar and Weng (2009a) using high resolution LST images, minor variation in the UHI centers was evident. This variation was attributed to the change in land use and land cover. But unlike the results from high resolution image analysis, in this study, the variation in UHI centers were more than 5 kilometers. Additionally, this variation in the centers of UHI is evident in both daytime and nighttime surface temperatures and does not have a pattern corresponding to either month or season. This variation could be either due to the effect of scattered cloud-cover, especially near the actual center of UHI, leading to a shift. This variation in UHI centers could also be due to the nature of the sensor. Regarding the latter, since spatial resolution of MODIS LST is 1 km x 1 km, there are more chances of mixed pixel effects and subsequent dilution of actual surface temperature.

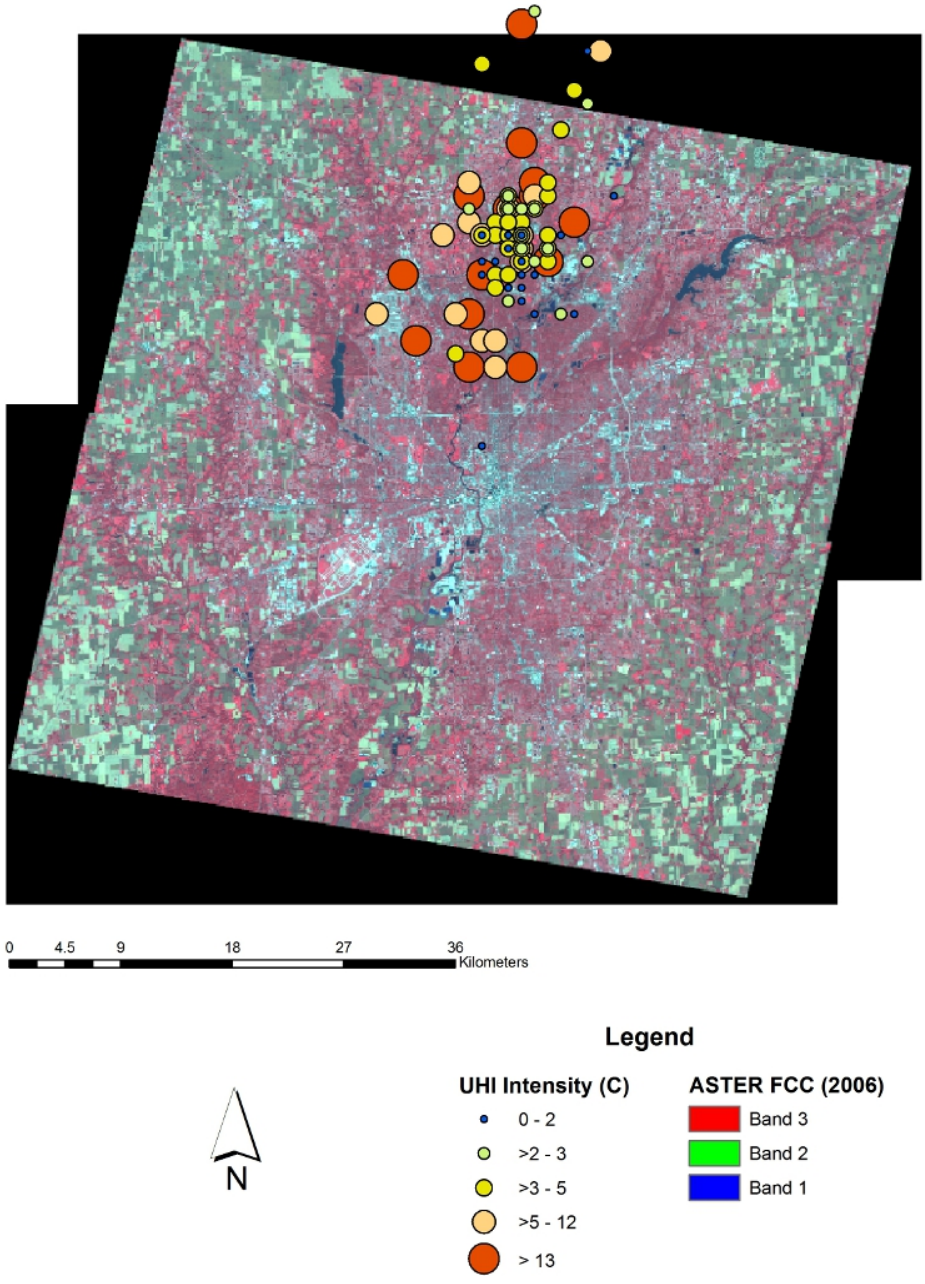

Figure 39. Daytime UHI projected over the ASTER false color composite (FCC)

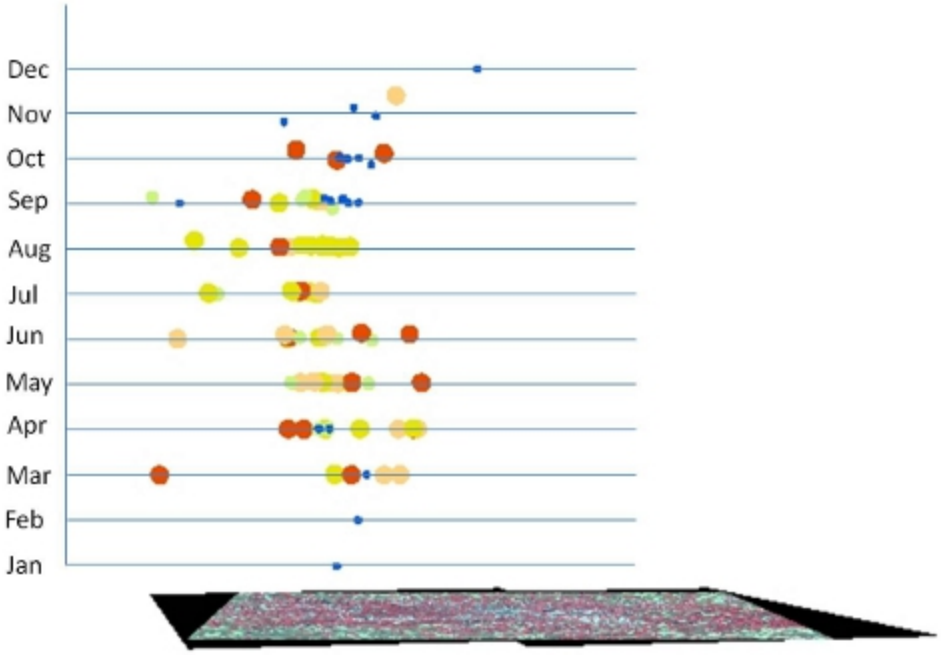

Figure 40. Daytime UHI along the north - south direction presented in 3D perspective

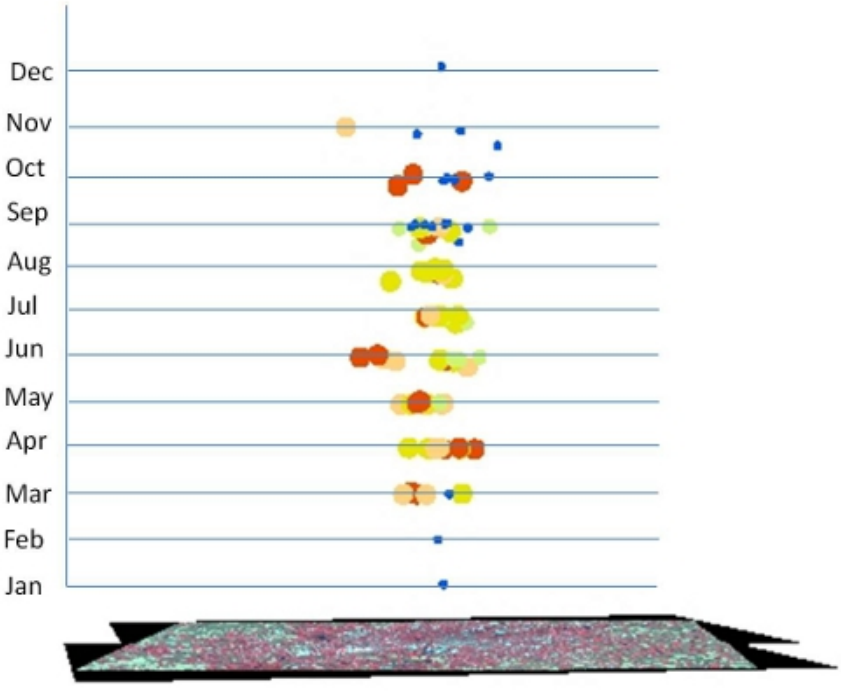

Figure 41. Daytime UHI along the east - west direction presented in 3D perspective

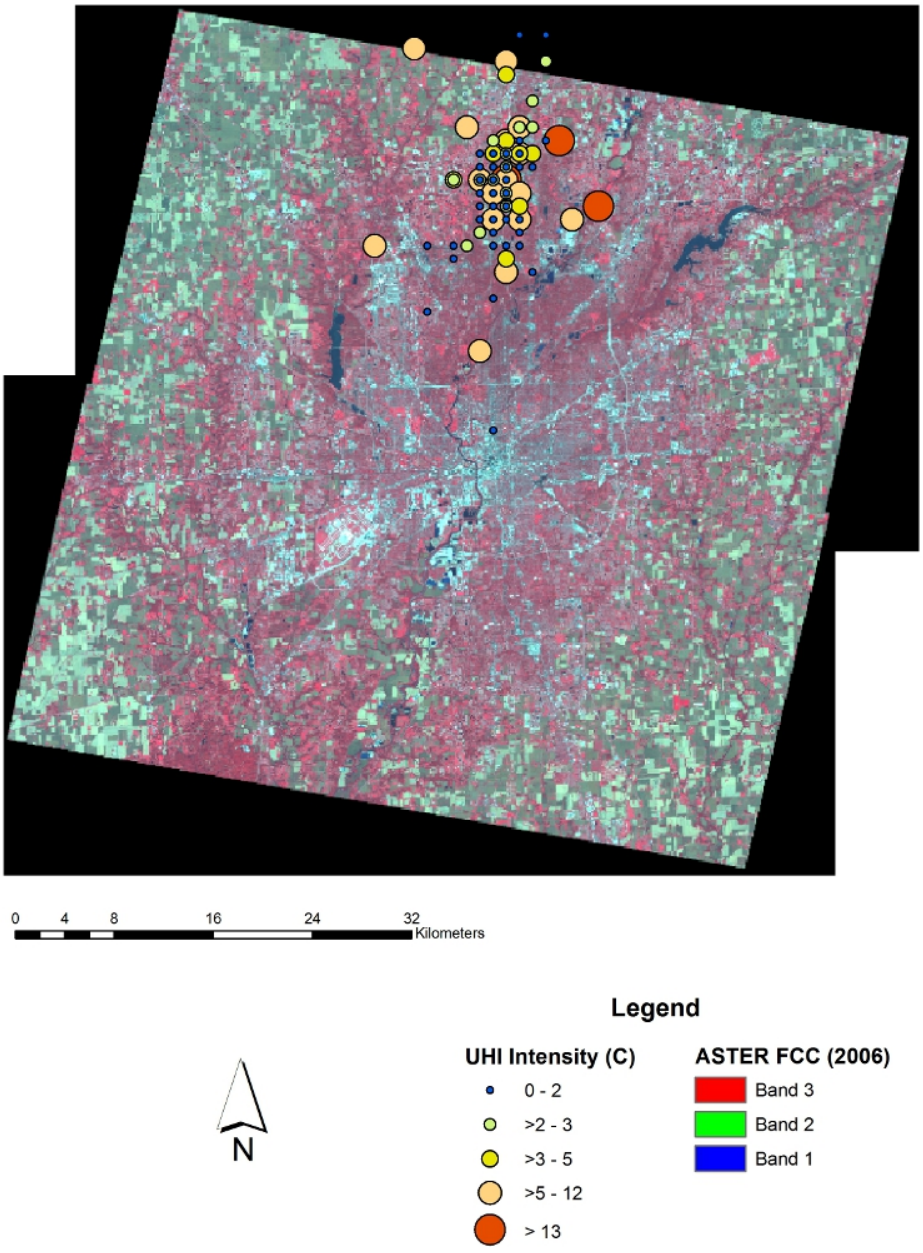

Figure 42. Nighttime UHI projected over the ASTER FCC

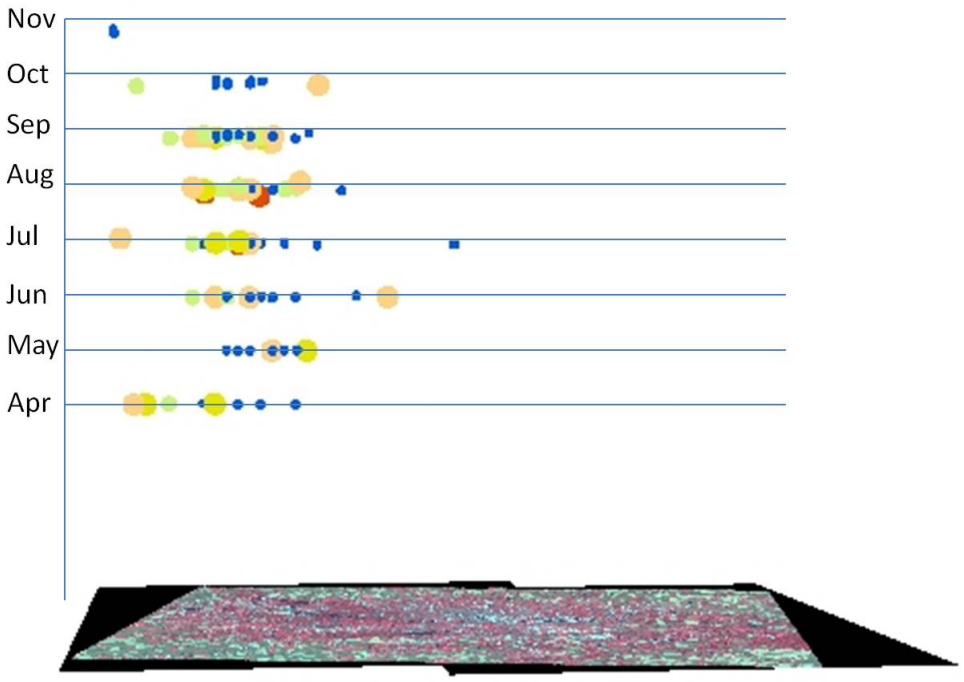

Figure 43. Nighttime UHI along the north - south direction presented in 3D perspective

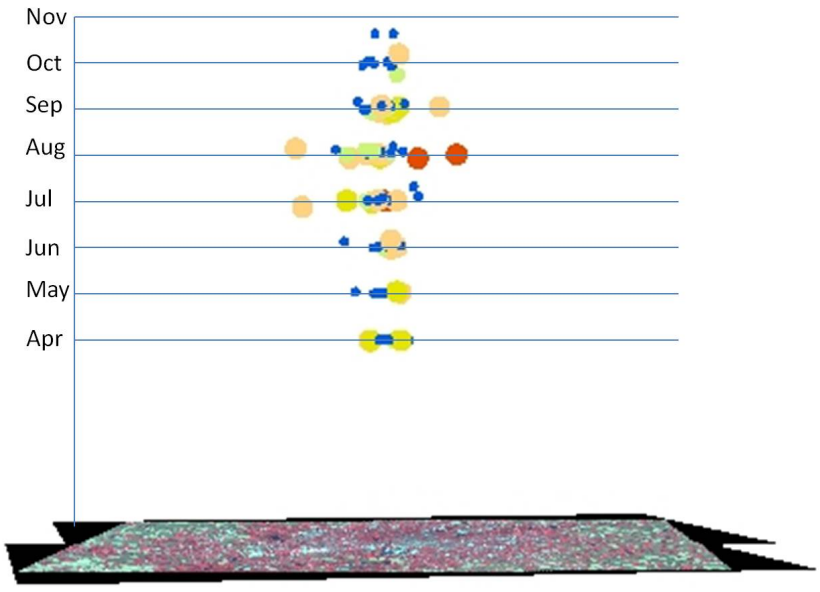

Figure 44. Nighttime UHI along the east - west direction presented in 3D perspective

Figures 39 through 41 make it evident that the change in center of UHI for daytime images across all months are greater along the North-South direction rather than East-West direction. One of the main reasons for such occurrences could be the clear variation in the land use and land cover pattern to the North of Indianapolis.

The city of Indianapolis has been undergoing rapid development and therefore expansion, over the last decade. There is evidence of a slow transition whereby peri-urban areas become urban and surrounding rural areas slowly sub-urbanize. This development has also brought about land cover transition in and around the city. Such land cover transition, especially from pervious surfaces (less heat radiation) to impervious surfaces (relatively more heat radiation) is greater to the northern part of the city. There are many reasons for expansion of the city northwards rather than to along the south, one being the proximity to Chicago. On one hand the northern part of the city is rich in forested areas on both the East and West. On the other hand, there are also two lakes present in the northeast and northwest of the city (refer Figure 39). These conditions, along with the land cover restriction and high real estate prices compared with the regional economy, make these places less attractive for rapid development. The restriction in land cover, presence of forested lands and water bodies lead to a relatively cooler surface temperature in northwestern and northeastern parts of Indianapolis, in comparison to central and northern areas of the city. Therefore, there is evidence of high variation in the location of the centre of UHI along the North-South in comparison with East-West direction. Similar variation is also evident with nighttime UHI (refer Figure 42).

The results of the daytime analysis indicate that variation in UHI magnitude is high during spring, summer and autumn months. The magnitude of UHI is particularly larger during summers, while, results from nighttime UHI analysis indicate that there are less variations in UHI magnitudes across all seasons. More than 50% of the nighttime UHI has a magnitude of 1-2 C. During autumn, especially in the months of September and October, there is increased variation in the magnitude of daytime UHI ranging from 1 C

to over 13 C, whereas such clear transitions are not evident for the nighttime UHI.

To further understand the locations of UHIs, the centroids of the heat islands were projected onto a high resolution visible imagery as provided by Google Earth and visualized. The centroids of the UHIs were classified into categories based on their intensity. Within the 3D representation the x, y and z were substituted with the location parameter (x, y) and intensity values (z) to analyze the characteristics of UHIs. The results from this analysis are presented in Figures 45 through 48. The results indicate the absence of a correlation between the UHI centroids and the month/seasons. This is probabiliy due to the fact that many of the images which were suitable for analysis are from late spring to early fall. Much of the variation in LULC observations around Marion County is experienced during winters and early spring. Most of the images from these seasons were not used for the analysis due to the presence of cloud cover in excess of 30%.

From the results it is evident that most of modeled UHIs had their centroids located to the North of Interstate-69. Some of the earlier studies carried out by Rajasekar and Weng (2009b); Weng et al. (2011) focusing on implementation of non-parametric modeling on medium resolution images such as Landsat and ASTER indicate the presence of the center of UHI close to Interstate-65. An analysis of MODIS imagery elucidates that only one scenario, in the month of December, exhibited similarity to the results from medium resolution images.

The variations in results presented in this study are likely to be due to two reasons. First, the change in resolution, i.e., from 15 m in the case of medium resolution images to 1 km in case of MODIS, has an effect on the characteristics of UHI. It is possible to capture the micro characteristics of the urban landscape with the increase in resolution (i.e., decrease in scale). Nevertheless, the use of medium resolution imagery may limit the extent of the study area (Rajasekar and Weng, 2009b). Second, the change in the centroids of UHI from medium resolution images could be due to the inclusion of a larger area, which may have influenced the characteristics of the UHI. While using low resolution

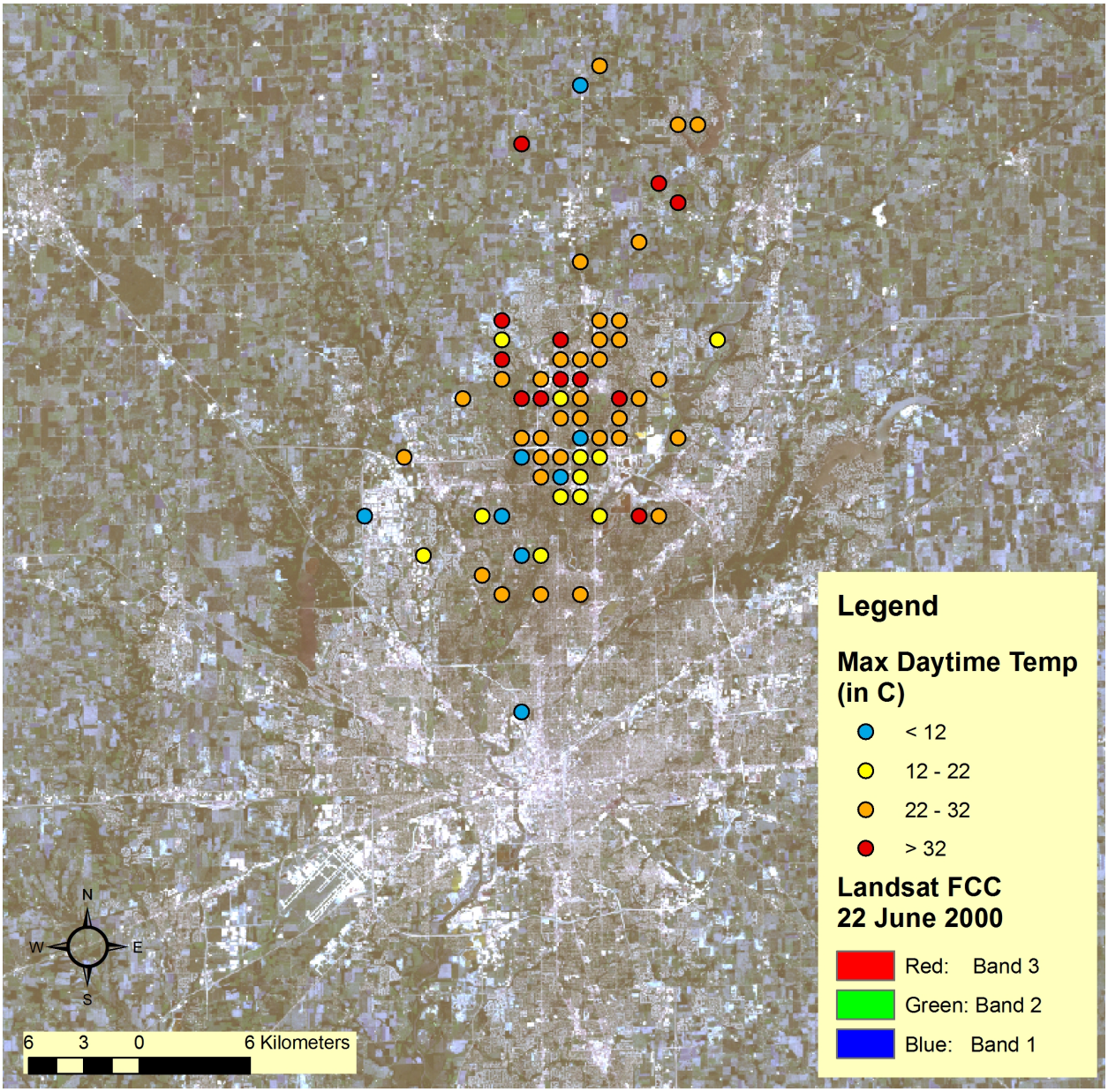

Figure 45. Centroids of UHI maximum temperature: A representation over Marion County

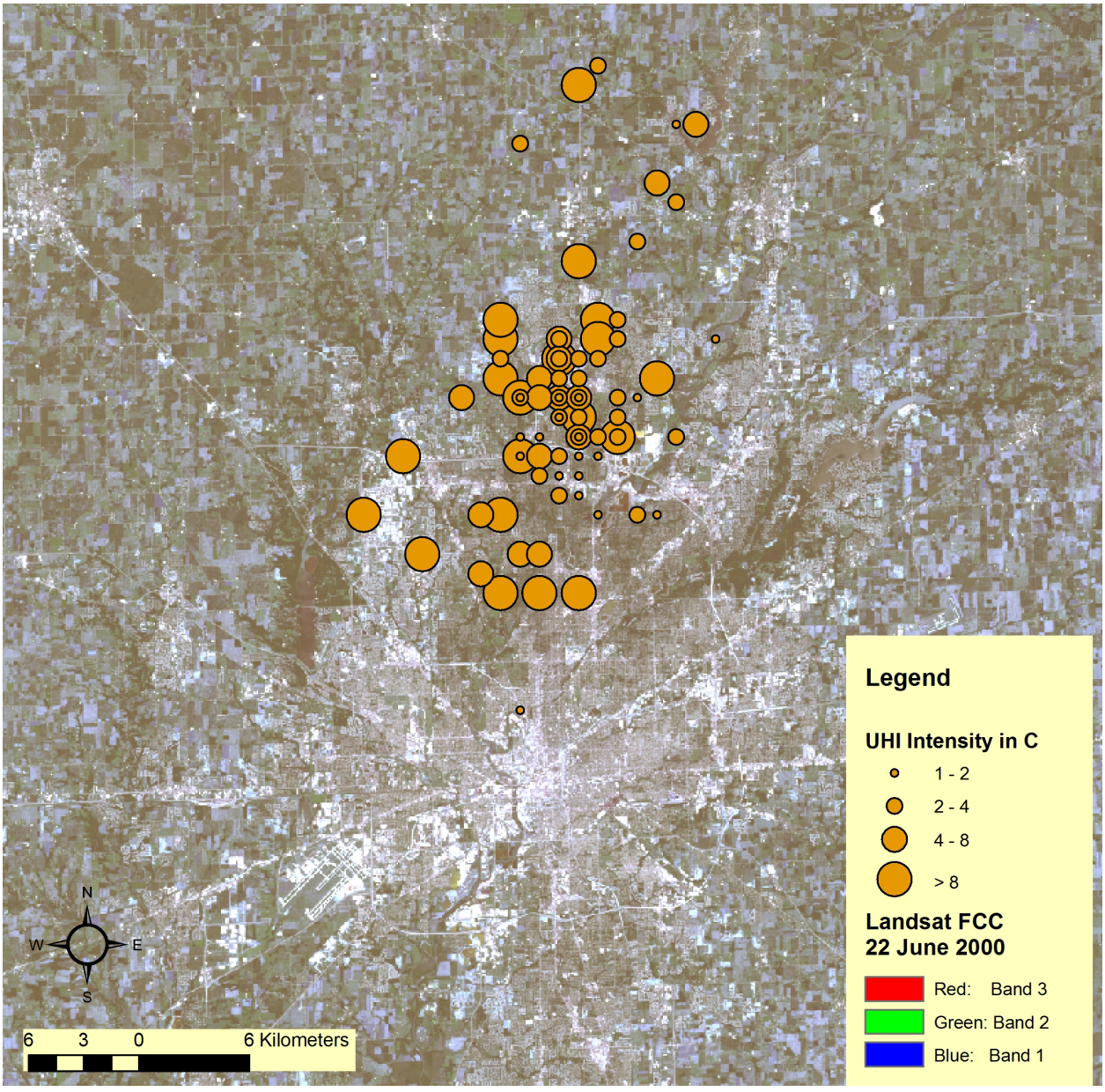

Figure 46. Centroids of UHI intensity: A representation over Marion County

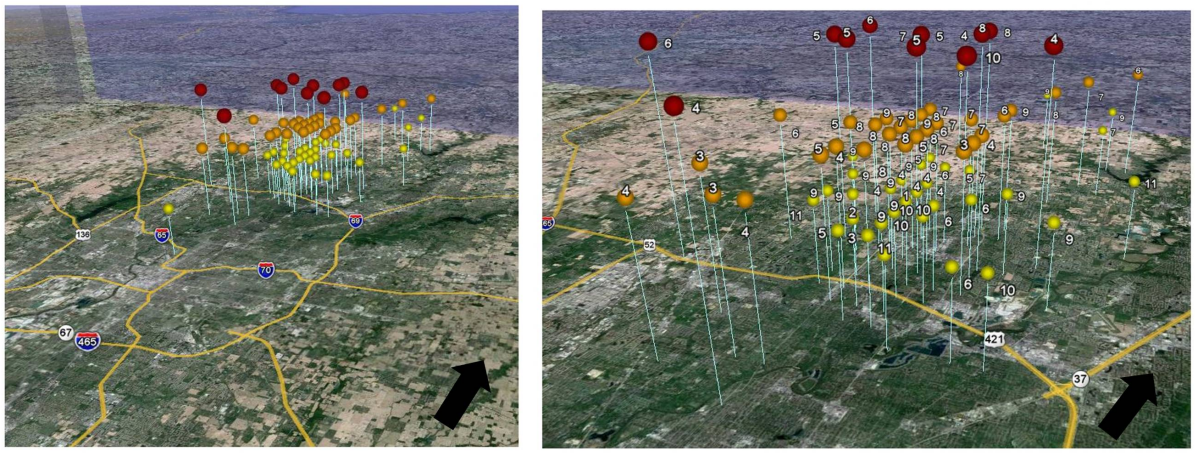

Figure 47. Centroids of UHI with intensity: A view from west of Marion County. The red centroids are of UHI intensity > 8 C, the orange centroids are of UHI intensity > 4 to 8 and the yellow centroids are of UHI intensity 0 to 4. The numbers displayed within the image correspond to the month in which the LST was acquired (Image source: Google)

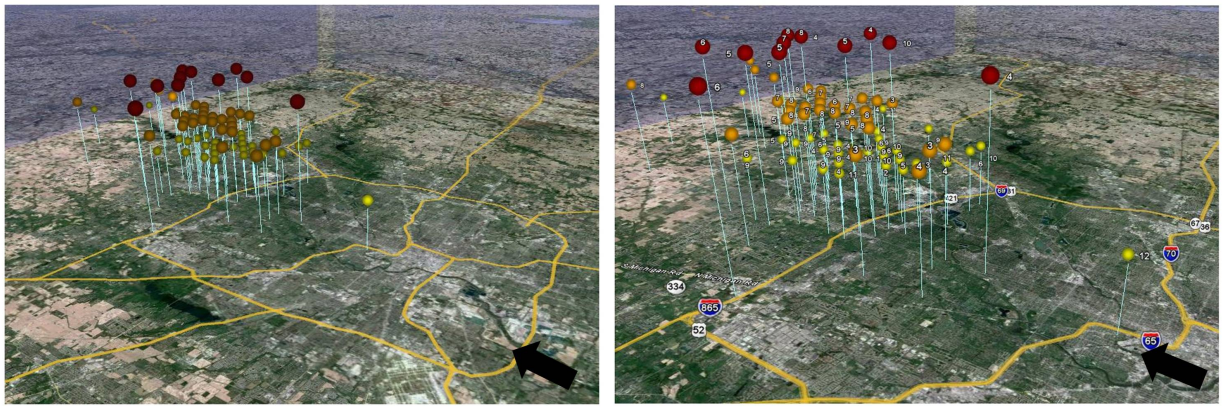

Figure 48. Centroids of UHI with intensity: A view from east of Marion County. The red centroids are of UHI intensity > 8 C, the orange centroids are of UHI intensity > 4 to 8 and the yellow centroids are of UHI intensity 0 to 4 C. The numbers displayed within the image correspond to the month in which the LST was acquired (Image source: Google)

images the possibility of capturing micro variations in the surface heat signature is drastically reduced. This uncertainty coming from mixed pixels is complimented by the option of covering a larger area. Depending upon the study area, the use of low resolution images such as MODIS may provide us with a better understanding of the phenomenon at a broad scale.

Even though this research concentrated on the theory of modeling UHI and used MODIS LST as case, a detailed analysis of MODIS LST with respect to the study area is required for further understanding the behavior of UHI in space and over time

5.4 Summary

In this research, varying information sources from the raw data have been developed to analyze the behavior of UHI in space and over time. Three main data sets that were extracted from the remotely sensed images are LULC, vegetation and surface temperature. The variables which were extracted from secondary information include population density grid. This research analyzed images of varying spatial and temporal resolution for modeling and monitoring the UHI phenomenon.

The techniques of Bertin's visual variables were effective in identifying urban regions which contribute to the heat island effect. In spite of advancements in the field of personal computing, the time required for the software to run the animation was too high, making these techniques less efficient for personal computing based analysis. The land use and land cover that were analyzed within this study included residential areas, commercial areas, roads, open areas and water bodies. The results indicate that urban land cover has a significant effect on temperature profiles. The results indicate that, even though land surface temperature is based on the capacity of the surface to absorb and radiate heat, the presence or absence of certain land cover elements within a defined space will have an effect on its radiation profile. For example, it was noted that at a macro level, that residential areas which were closer to commercial buildings and open impervious

parking spaces tend to be influenced by the surrounding higher temperature irrespective of their green surrounding. This can also be due to the mixed pixel effects but the degree of influence needs to be analyzed in much detail.

In this research, association rule mining algorithm was successfully modified to include spatial information. Additionally, in order to compare different spatial datasets representing the same region over space but from different time, a standardization procedure was developed and implemented. In this study LST as derived from three sensors were converted into interval data for use within the association mining algorithm. This was made possible through quantile classification of the data sets. To have a deeper insight , the results from quantile classification were compared with equal interval classification results to throw light on the effect of classification on the results of association mining algorithm. The association rule mining algorithm was executed by considering various permutations and combinations of datasets. The initial model was experimented using LST and NDVI information from ASTER in relation to the land use land cover and demographic indicators. Similarly, the succeeding models were experimented taking into consideration the LST and NDVI information from Landsat and MODIS in relation with land use land cover and demographic indicators. The results indicate that while generalization of rules is possible using low resolution images specific rules could only be extracted using medium resolution images. On the other hand, attempts to extract specific rules will lead to low support of the rules due to the complexity of the urban terrain.

Within the macro model, a total of 2922 MODIS LST images were considered for analysis. From this large image set only a portion was suitable for analysis as the area was prone to frequent cloud cover. The LST with minimum cloud cover (< 30%) was used for characterizing UHI using the non-parametric kernel convolution model as described within the section on methodology. The non-parametric modeling aided in characterizing the UHI in space. The kernel convolution process does have its limitations. One such

limitation is the sensitivity of parameterization algorithm to the local mean (in this case mean LST). Variation in mean temperature will have an impact on the model results.

Therefore, the algorithm may not be best suitable for characterizing UHI over a large area. Results from characterization of UHI for Marion County and its surrounding areas were classified into three categories. They were positive heat islands, negative heat islands and absence of heat islands. The characterized LST images were then analyzed with respect to monthly average NDVI to identify patterns. Due to the low resolution of LST and possible mixed pixel effect no strong correlation between LST and NDVI was evident. Nevertheless, when a similar approach is carried for medium to high resolution images the possibility of a correlation is likely to exist. From the analysis of daytime temperatures it was evident that maximum variation in the average maximum temperature was during the month of May and minimum variation in the average maximum temperature is in the month of October. The months of July to September exhibited maximum temperatures sometimes, but were not constant across time. In the case of nighttime temperatures, the months of August and September were found to exhibit the maximum variation. The average maximum nighttime temperatures were found to be in the months of July, August and September and the minimum nighttime temperatures were observed in the month of October. The results obtained were then analyzed for spatio temporal patterning of UHI using visualization techniques. It was evident from the results that changes in center of

UHI for daytime images across all months are more along the North-South direction in comparison to the East-West direction. One of the main reasons for such an occurrence could be the clear variation in the land use and land cover pattern along the North of Indianapolis. The results from the daytime analysis indicate that variation in UHI magnitude is high during the spring, summer and autumn months. The magnitude of UHI is more during the summers. While, results from nighttime UHI analysis indicate that there are less variations in nighttime UHI magnitude across all seasons. More than 50% of the nighttime UHI has a magnitude of range 1-2 C. During autumn, especially

in the months of September and October, there are indications of high variation in the magnitude of daytime UHI ranging from 1 C to over 13 C, whereas such clear transitions are not evident within the nighttime UHI.

The next chapter briefly summarizes conclusions, describes the significance of this research and its possible contribution to the academia. A section within the chapter also outlines future research possibility using methodologies experimented with in this research.

CHAPTER 6

CONCLUSION

The effect of urban heat islands in space and in time was analyzed within this research using exploratory and quantitative models. Visualization techniques including animation was experimented with to develop a mechanism to view and understand the UHI over a city. Association rule mining models were implemented to analyze the relationship between remote sensing images and GIS data. This model was implemented using three different remote sensing images i.e., ASTER, Landsat and MODIS. The effect of the spatial resolution on the model and the phenomenon were analyzed in detail to determine variables which strongly associate with LULC in space and in time. Non-parametric process convolution model was developed and was used to characterize UHI from MODIS time series images. The resulting characterized images were used to study the relationship between LULC and UHI. This chapter highlights the outcomes of the research, its key contribution to the scientific community and discusses the way forward.

This chapter is divided into three sections. Section 6.1 summarizes the results and their conclusion. Section 6.2 provides an overview of the research and discusses the problems and pitfalls that were experienced during the course of this research. This section also provides possible options to avoid such problems if the elements of this research need to be replicated. Section 6.3 of this chapter provides the future research direction. This section first highlights the possible research that could be carried out within the urban heat island framework using the models and methodologies that were

developed within this research. The later part of this section highlights the application of the theoretical frameworks which were developed on other applications and research agendas in the field of spatial science.

6.1 Conclusion

Exploratory data analysis

Within exploratory analysis, maximum, minimum and mean temperatures obtained for land cover types such as residential, commercial, water bodies, open lands and roads were analyzed. A thermal image was superimposed over high resolution true color composite image to create a false three-dimensional composite. In this image, colors of objects in the image were true color and their extrusion along third dimension was done using LST.

Results indicate that around 50% of residential areas are in mean temperature range.. In spite of their green surroundings residential areas that were near to commercial buildings and open impervious parking spaces had higher surface temperatures.

Commercial buildings within downtown Indianapolis exhibited more heat and RCA Dome had the least skin temperature in that area. This can be attributed to the color and structure of the roof and the material used for its construction. Open parking areas also exhibited relatively high temperature. Skin temperature around downtown was found to be above local mean except for the RCA dome at central Indianapolis. Additionally, all sky scrapers around central Indianapolis exhibited temperature lesser than mean temperature of Marion County due to their roof type. Also most of these buildings are relatively tall therefore the shadow cast by them limits the sun's heat from reaching the ground. Detailed analysis of the aerial image helped conclude that roof type negatively affects heat radiation budget of buildings, while air conditioning elements over roof tops positively affects the radiation.

Road sections and water bodies near the downtown Indianapolis were analyzed.

Water bodies exhibited less heat and the temperature profile of roads were equivalent to mean heat level (Marion County). It was deduced that the location of roads and material used for construction are key indicators which affect radiation.

Association rule mining

An algorithm to extract association information from spatial dataset (inclusive of raster and vector data) was developed and implemented. In this analysis, the datasets used were normalized to facilitate comparison. The LST was derived from three different sensors namely ASTER, Landsat and MODIS. This was considered for analysis along with land use land cover (raster) and demographic information (vector).

In order to successfully execute the association mining, rational data were converted into interval data types. Sensitivity analysis brought out results that the clearest classification of the LST images was possible through quantile classification. While equal interval classification made the outliers or small scale anomalies which are inclusive of variations evident.. Natural breaks and standard deviations classifications were also experimented with but they did not demonstrate satisfactory results. The numbers of classes were limited to 10 to avoid over fitting and under fitting of results. NLCD 2000 and Land Zoning Map were used without much modification. Demographic information was normalized to a scale of 1 to 10 to match the raster data classification.

Results from the analysis of ASTER derived information indicate that association of LST with NDVI is not linear. This can be due to the nature of vegetation cover. A crop can have a poor health therefore a low NDVI but can still provide sufficient roughness over its surface to prevent absorption or radiation of heat. Land cover type namely deciduous forest (DE), emergent wetlands (EW), open water (OW), shrubs (SS) and woody wetlands (WW) were found to be associated with low LST. The woody wetlands were found to be more strongly associated with low LST than open waters. Land cover classes including pastures (PA), evergreen forest (EV), grasslands (GR), and developed low intensity (DLI)

along with developed medium/high intensity demonstrated partial association with Low LST.

ASTER-derived LST was found to be strongly associated with land use including airport, agriculture, low density housing, industrial, park and special uses. The occurrence of agriculture and airport within the same classification is mainly a seasonal characteristic. LST of higher temperature were found to be associated with commercial zones, central business district, hospitals, high-density housings, medium-density housings, university and historical preservations.

Demographic indicators especially medium family size was found to be associated with higher LST. Also, low to medium-LST demonstrated a strong association with the following indicators namely low-intensity developed land which includes areas with a mixture of constructed materials and vegetation, high NDVI in the range of 0.18 to 3.00, high average household size, low vacant areas (less than 10%) and low-population density. This infers that households with large family size generally prefer to stay in suburban areas or areas with more open space or areas with high green space. These spaces have low radiation capacity and therefore may contribute little to the local heat effect. It was also found that majority of people who have relatively large family size and living in areas with relatively low-thermal radiation zones were people with mean age range of 31 to 40. These areas were also found to be consisting of fully occupied buildings with high confidence (91.3%). Highly-developed areas (NLCD) where people reside or work in high numbers are found to have strong association with relatively higher land surface thermal characteristics. This relationship exists with support of around 19.6% and confidence of 84.2%. These highly-developed areas (NLCD) were also found to be mostly composed of low-density housing (Zone).

The results from the Landsat ETM+ derived LST and NDVI information indicated similar characteristics as that of ASTER. Additional association rules captured using Landsat data include the association of LST with DHI, DMI and DLI land cover classes

with confidence of 83%, 96% and 98% respectively. LST was found to exhibit a strong association with deciduous forest (confidence of 92%), evergreen forest (84%), grassland (81%), developed open spaces (90%), pastures (96%), crops (89%) and shrubs (95%). Barren land and emergent wetlands were also found to be associated with temperature ranges similar to that of woody wetlands with confidence of 99% and 95% respectively.

The mining algorithm aided in capturing the association of Landsat derived LST with vegetation, high intensity developed, low density housing, high family size, high household size and low population density with high confidence (>80%). Degrees of association of indicators varied with variation in LST. This variation was more evident within demographic indicators such as average family size, average household and population density. In 20% of the cases, associations of indicators with LST were not constant. In around 50% of the cases, association of LST with family size, household size, median age and high population density were found to exhibit an inverse relationship. From these results, it was inferred that people who are in their mid 20s to early 30s have relatively small family/household size prefer to stay in highly populated areas. These areas are usually towards the city center and are composed of less tree cover thereby contributing to more radiation. Overall the rules indicate that population density is associated with LST. But, this association holds true only for temperatures within a certain range (low to medium). Beyond specific ranges the existence of relationships have weak confidence levels (below 10%) therefore reducing the possibility of generalizing many of the rules that were extracted.

The variation in results from ASTER and Landsat derived LST may be due to the spectral characteristics of the sensors. Since there is a lack of strong rules to support the LST with NDVI, in future studies land cover characteristics have to be studied in detail with respect to their radiation properties and possible percentage of mixed pixels within the derived information to arrive at generalized rules for particular months/seasons within a year.

Unlike ASTER and Landsat, the LST and NDVI information derived from MODIS demonstrated association. Rules derived indicate the presence of a linear relationship between NDVI and LST. Even though many of the NDVI classes were associated with more than one LST classes, in general low NDVI classes were associated with high LST classes and vice versa with confidence ranging between 76

The inverse linear relationship between MODIS derived NDVI and LST was also evident within the association mining results obtained through the quantile classification dataset. In this case, even through a linear relationship was evident; the association of each of the NDVI classes was evident with more than one LST class. Based on the results obtained from ASTER, Landsat and MODIS data one can infer that NDVI is associated with LST but the relationship is usually non-linear in high resolution images and tends to become linear with the lower resolution images. Furthermore, the NDVI of a particular range were not found to exhibit similar thermal absorption or radiation characteristics. The nature of the relationship between NDVI and LST was made evident through the results of the association mining algorithm. Nevertheless, a detailed characteristic of different urban features will have to be mapped at both low and high scales to generalize their thermal behavior.

The LST dataset and land use zoning were able to demonstrate strong association rules in comparison with the land cover dataset. From the results it was evident that agriculture zone was associated with medium LST with confidence of 94%. Central business district and historical preservation areas exhibited association with high LST with a confidence of 91% and 100% respectively.

Descriptive analysis

Total of 2,922 MODIS LST images were analyzed for the study of UHI in and around the city of Indianapolis. From this large image set only a portion was suitable for analysis as the area was prone to frequent cloud cover. Further, the MODIS algorithm has trouble

characterizing LST over areas which are covered with snow or water cover. Therefore it was ensured that the images selected for analysis did not exceed a maximum of 30

The availability of cloud free images varied within the study area. This situation was the worst for the months of January and February when the snow cover is usually high. Summer showers also have an impact on LST especially during the months of May, June and July. For the city of Indianapolis and its surrounding, the best time to acquire the LST image for UHI analysis are the months of April followed by August to October.

The results from selected LST indicate a variation in the intensity. The variations in mean and maximum temperatures were evident within the daytime and nighttime images. The results from daytime temperatures indicate that the variations in mean temperatures are greater than the variations in maximum temperatures. Variation in the mean daytime temperature is more during spring and summer months in comparison with autumn and winter months.

The results from the nighttime temperatures exhibited less variation in comparison to results from daytime temperatures. In the case of nighttime LST, maximum variation was evident for the month of April followed by July and October. These are transition months between seasons i.e. from winter to spring, summer to autumn and autumn to winter. From the results, it can be inferred that the nighttime temperature patterns are sensitive to the change in seasonal temperatures.

It was also evident from the results that the magnitudes of LST temperature difference are higher during daytime in comparison with nighttime. The magnitude of temperature difference is highest during June for daytime LST and it is highest during the month of August for nighttime LST. The average magnitude is around 9.2 C with a variation of 3.5 for daytime LST and the average magnitude is 2.7 C with variation of less than 1 C for nighttime LST. This magnitude may not be necessarily corresponding to the magnitude of UHI but provides us with a range of variation possible over the study area irrespective of the month, season or year. The variation in temperature is a matter of concern as old

people and children are vulnerable to these variations. They are likely to experience severe stress in these high magnitude heat pockets.

The process of kernel convolution aided in characterizing the image while maintaining its mean temperature. This process demonstrates the effectiveness of the algorithm to identify the presence of UHI phenomenon by exaggerating and smoothing the background noise where necessary. The degree of such smoothing can be controlled by the users based on their knowledge and understanding of the phenomenon. This degree of smoothing varies from 0 to 100, where 0 is likely to produce an image similar to the original LST and the number 100 is likely to produce an image where the variation within the image is equal to the mean. The results from the convolution maintained the mean temperature of the LST images while characterizing the heat island through reducing/exaggerating the variation between the maximum and minimum temperatures.

Analysis of modeled LST exhibited an average difference of 14 C between maximum daytime and maximum nighttime temperatures across all seasons. The diurnal temperature is highest during the months of April where the difference is around 18 C and is least during the July where the difference is around 10 C. It should be noted that corresponding day and night images were not available for the months of January, February and December.

Results from kernel convolution helped characterize LST as positive heat islands, negative heat islands and absence of heat islands. Positive heat islands are heat islands where the central core of the island is hotter than its surroundings. Negative heat islands are heat islands where the central core of the island is colder than the surrounding. From the results it is evident that the presence of heat island or absence of heat island does not have any correlation with either the month or the season but is only proportional to the number of relatively cloud free images which were used for analysis.

Analysis of May and June daytime modeled surface temperature characteristics with respect to NDVI indicates that no strong correlation exists. Results from nighttime tem-

perature analysis indicate that difference between average of mean nighttime temperature and average of maximum nighttime temperature is very low for May and June. Furthermore, variations evident within nighttime temperatures for a given month are higher in comparison to daytime temperature. This variation is higher for June in comparison with May. One of the possible reasons for much variation in surface temperatures could be due to use of air conditioning systems (centralized systems which are located on the roof of buildings) contributing to skin temperature. In general, from analysis of daytime temperature, the highest variation in average maximum temperature was evident for the month of May and least variation in average maximum temperature was during month of October. In the case of nighttime temperatures, the months of August and September were found to exhibit maximum variation. Average maximum nighttime temperatures were found to be in the months of July, August and September and minimum nighttime temperatures were observed in the month of October.

The spatio-temporal pattern of the UHI was analyzed using a four-dimensional visualization technique. This visualization was done using Arc Scene. The result from the model derived UHIs i.e. the center of the UHI was plotted and colors, sizes were used to represent the fourth dimension i.e the intensity of UHI. This technique provided a visual understanding of the behavior and intensity of UHI in space and in time.

The changes in center of UHI for daytime images across all months are more along the North-South direction in comparison to the East-West direction. One of the main reasons for such occurrences could be the clear variation in land use and land cover pattern along the North of Indianapolis. The city of Indianapolis has been undergoing rapid development. These developments have brought about land cover transition in and around the city. Land cover transition especially from pervious surfaces (less heat radiation) to impervious surfaces (relatively more heat radiation) is more along the northern part of the city in comparison to its southern Part. There are many reasons for the expansion of the city northwards rather than along the south. One of the reasons

is proximity to Chicago. The northern part of the city is rich in forested areas on both east and west also, there are also two lakes present in the northeast and northwest of the city. These conditions along with land cover restrictions and high real estate prices in comparison to the regional economy make these places less attractive for rapid development. The restriction in land cover, presence of forested lands and water bodies lead to relatively cooler surface temperature in comparison to the central and northern areas of the city. Therefore, there are evidences of high variation in the location of UHI along the North-South in comparison with East-West direction. Similar variation is also evident within nighttime UHI.

The spatio-temporal analysis of UHI including its magnitude and distribution aided in visualizing the behavior of the phenomenon over space and time. The results indicate that during autumn, especially in the months of September and October, there are variation in the magnitude of daytime UHI ranging from 1 C to over 13 CO ; while, the results from nighttime UHI analysis indicates no such seasonal dependence exists. More than 50% of the nighttime UHI has a magnitude of range 1-2 C. Such spatio-temporal knowledge has the potential to be extended further and can be used for various applications including land use land cover planning, building design and city planning.

6.2 Discussions

Exploratory data analysis

This dissertation has aided in addressing the issue of UHI not only with respect to bio-physical dimensions but also from the human environment interaction perspective. The latter is more relevant to the current scenario with increase in the overall energy consumption and its demand. Other factors such as quality of the environment especially the increase in pollution within urban areas adds to the existing stress. The association study which was researched upon as a part of this study would aid in addressing certain

indirect relationships of UHI with respect to other phenomena. The models developed within this research are expected to aid environmental scientists in examining the UHI phenomenon not only at a local level but also at a global level.

The method developed using abstract modeling is an effective means for dissemination of UHI information to the local users. It can be used in future to help users to have a virtual walk over the city of Indianapolis and relate to the difference in heat radiated by the various familiar landmarks around the downtown Indianapolis. Later, the presentation can be further improved upon by displaying parallel information (along with the current one) of depicting the city with actual terrain elevation; this would facilitate the common public in relating to the places and objects.

Association rule mining

The association mining algorithms extended to the spatial data sets have the potential to extract knowledge from nominal, ordinal, interval and ratio data sets. Nevertheless, selection of appropriate classification type has an effect on the results. In this study several classification types were explored before using quantile and equal interval classification for the study of UHI. The use of similar classification methods may prove to be effective in understanding the association within spatial data, but there are likely chances that other methods of classification may also prove to be more effective depending upon the data that needs to be analyzed, this could be the possibility of further research.

In this study, vector information was converted to raster information for standardizing input data sets. Such rules can also be executed for vector datasets only where such conversion may not be necessary. It is to be noted that normalization is the key to association mining of the spatial data sets. There is possibility of high variation in radiance/ reflectance of elements over space in time. This problem was address through normalization of the indicators. Normalization has ensured effective comparison of the elements in this study, while opening scope of further comparisons in future research.

Also, in case of spatial data analysis the relationship between support and confidence was found to be inversely proportional. This was mainly due to the high variation in land use land cover within urban sprawl. In this study, as a sample case, the Aprori algorithm for information mining was used. This algorithm was selected based on its effectiveness in capturing the support and confidence within the given data set. But, other algorithms of association mining can also be explored in future and they may prove to be equally effective depending upon the objective of the study.

The rules obtained were inferred and discussed within this study based on a comprehensive knowledge of the study area. Such inferences are required to rationalize and throw light on the support and confidence obtained for any given data sets. Lack of comprehensive knowledge of the study area may lead to an inability to extract knowledge from the support and confidence information. Even though much of the process can be automated, the rationalization of the information obtained to generate knowledge about the urban phenomenon still depends upon scientist expertise. Therefore, there is a strong need for the identification and documentation of the mixed pixel effects. This can only be documented through ground verification with respect to indentified rules. Such documentation might provide urban scientists with rich source of information to base their knowledge extraction processes. Due to the complexity of the urban terrain with variation in the type of construction materials used within the built environment, the process of ground verification and contextualizing the information will be a continuous process.

Descriptive analysis

Number of images that can be obtained from MODIS sensor is quite large. LST image product of MODIS aids in UHI monitoring. Daytime and nighttime image products also provide an option of studying diurnal characteristics of UHI. But unfortunately, the presence of clouds, water on ground and snow cover (depending upon geographical area)

will pose problem in continuous monitoring of UHI. In this research, characterization of negative heat island effect and absence of heat island in observed images was mostly due to the presence of scattered clouds, water on ground and snow cover. In this study, high variation was identified during months of April. This can be due to the seasonal transition i.e. transition from winter to spring where there could be days of cold weather followed by pleasant weather. Such variations might impact the characteristics of the LST. For Indianapolis, the transition from winter to spring is usually complete by April end. This led to little variation during the month of May. In case of June and July, these are summer months which are characterized by summer showers including extreme conditions favoring tornados along the periurban areas of Indianapolis. Such weather does not last for long time but contributes to high variation in the mean temperatures. The results indicate that such variations can lead to an average temperature difference of over 12 C.

Contrary to the expectation that land cover of certain type would radiate relative heat given a constant temperature, UHI derived from MODIS data did vary spatially. From earlier analysis using high resolution LST there was evidence of minor variation in center of UHI. This variation was attributed to change in land use and land cover. But unlike results from high resolution image analysis, variation in center of UHI has been more than 5 kilometers in case of MODIS. This variation in center of UHI is evident in both daytime and nighttime surface temperature and does not have a pattern corresponding to either the month or the season. Therefore, this variation could be either due to the scattered effect of cloud on certain areas, especially near the actual center of UHI leading to the shift or this could be due to the nature of the sensor. Regarding the later, since MODIS LST is of 1 km x 1 km resolution there are more chances of mixed pixel effect and subsequent dilution of the actual surface temperature. The mixed pixel effect and the low resolution of the MODIS LST product are some of the reasons for not being able to establish its relationship with the associated NDVI product from MODIS. ct are some

of the reasons for not being able to establish its relationship with the associated NDVI product from MODIS.

Overall this research aided in effective characterization of UHI and its spatio-temporal analysis. Research achievements include (1) an association rule mining algorithm for quantitative analysis of the relationship between Land Surface Temperature (LST) and bio-physical parameters, (2) a non-parametric process convolution model to effectively characterize and analyze UHI and (3) a technique to visualize the urban heat. The intellectual merits of these methods are two-fold; first, it will be a forerunner in the development and implementation of association rule mining algorithm within remote sensing image analysis framework. Second, since most of the existing UHI models are parametric in nature, this non-parametric approach is expected to overcome many existing problems within characterization and analysis. The parametric models pose problems (in terms of efficiency, since the implementation of such models is time consuming and needs human intervention) while analyzing UHI effect from multiple imageries. These proposed models are expected to aid in effective spatial characterization, facilitate temporal analysis and monitoring of UHI phenomenon.

6.3 Future Research

The application of methods developed can range from research within the urban heat island framework to research within spatial science in general. Listed below are different areas of future research that are possible using the methods which were experimented and discussed within this research.

Further directions for research within the UHI framework include the ground verification of results that were obtained through this study. Much of the association relationships that were established within this study are based on satellite measurements and other secondary source of information. Even though most of the discussions in this study are based on the proficient knowledge of the study area there is need for verification of

satellite derived land surface temperature with actual readings from different elements on the ground. This would help in identifying the extent of variation within satellite derived LST at varying scale and in quantification of mixed pixel effects.

Within this study the urban heat island effect was analyzed for the city of Indianapolis, Indiana in space and over time. There is need for such analysis across all major cities across the world. The possibility for automation through using a non-parametric approach can be exploited to study the phenomenon across space and time for cities within United States and elsewhere. Functional description of the phenomenon can be useful in comparing qualitative and quantitative aspects of the phenomenon between any two cities. This will throw light on UHI research and help streamlining the mitigating efforts.

Visualization and cut-fill techniques which were discussed within this research are models that could be used for knowledge dissemination activities such as education and city wide awareness generation programs. While numerical models and heat island quantification methods can help research scientists in understanding the phenomenon, visualization techniques such as animation are some of the best methods to enable the dissemination of the identified knowledge to concerned stakeholder (who may not understand scientific language) for actions. In this case, such techniques could be used for educating students, citizens, urban managers and urban administrators in understanding and locating the UHI effect within their cities.

The broad range of research which is currently being carried out in the area of urban heat island study concentrates on the effect of radiant heat of different materials based on the tests conducted within laboratories or controlled environment. Such research aids in identifying elements that are required to cool a particular building or an area. On the other hand, these types of research do not address the urban heat island effect on a larger scale i.e. at city level. The collective behavior of all urban elements behaves in a different manner with respect to their relative position in space and time as opposed to the behavior of an individual element. The non-parametric model developed and

discussed within this research context could be useful in identifying the behavior of urban space as a whole and could aid in better planning of urban land use and land cover to minimize the urban heat island effect.

Researches have been carried out to study relationships between energy consumption pattern of a city and its demographic variation. The methods discussed within this research could be extended further to analyze the relationship between energy consumption, demographic variation and urban heat island effect. The results from such study can help urban managers and policy makers to relook at the design of a city in order to conserve energy especially during peak summers.

The past two decades have been termed as the decades of urbanization especially within developing countries by the United Nations. The rapid migrations of people from rural areas to urban centers have contributed to phenomenal growth within cities. Such rapid growth has lead to change in land use and land cover, especially, as much of the peri-urban areas are being converted into urban areas. Such changes are difficult to track by urban managers. The situation gets complicated with much of the urban spaces being defined based on political or administrative boundaries rather than environmental boundaries. Such demarcations make it difficult for bringing about policy level intervention to address land use and land cover change. On a parallel front, there is also much confusion within the research community regarding the classification of urban sprawl. One solution to the above mentioned problem could be creation of environmental boundaries to monitor the changes. The non-parametric kernel convolution model can therefore aid urban researchers in automated classification of the urban sprawl with respect to their heat signatures since surface temperatures can be associated to land use and land cover change.

Broader applications of the models discussed within this research are also possible for areas beyond the UHI framework. The method of association rule mining for spatial datasets discussed within this research can have wide areas of applications within spatial

science including quantification of relationships between spatial datasets especially nominal data types. The non-parametric kernel convolution models which were discussed with respect to UHI phenomenon can be used for characterizing and modeling other continuous phenomenon such as air pollution within cities in space and over time. A range of such modeling can be used for hazard risk modeling especially to study the extent of dispersion of chemical/nuclear hazards. The characterization and functional transformation of images has a great amount of application in the areas of data compression and timely information extraction.

REFERENCES

Akai, Y., Kanzaki, T., Shimota, A., and Ichikawa, Y. (2002). Radio acoustic sounding in urban meteorological observations. *Journal of Atmospheric & Oceanic Technology*, 19(8):1193.

Arnfield, A. J. (2003). Two decades of urban climate research: a review of turbulence, exchanges of energy and water, and the urban heat island. *International Journal of Climatology*, 23(1):1–26.

Atkinson, B. W. (2003). Numerical modelling of urban heat-island intensity. *Boundary–Layer Meteorology*, 109(109):285–310.

Balling, R. C. and Brazel, S. W. (1998). High-resolution surface temperature patterns in a complex urban terrain. *Photogrammetric Engineering and Remote Sensing*, 54(9):1289–1293.

Borgelt, C. and Kruse, R. (2002). *Graphical Models: Methods for Data Analysis and Mining*. John Wiley & Sons, Ltd.

Bottyán, Z. and Unger, J. (2003). A multiple linear statistical model for estimating the mean maximum urban heat island. *Theoretical and Applied Climatology*, 75:233–243.

Bowman, A. W. and Azzalini, A. (1997). *Applied smoothing techniques for data analysis*. Oxford Statistical Science Series. Clarendon Press. Oxford, New York, USA.

Bretz, S., Akbari, H., and A, R. (1998). Practical issues for urban solar-reflective materials to mitigate urban heat islands. *Atmospheric Environment*, 32:95–101.

Brunsdon, C., Macgill, J., Openshaw, S., Turner, A., and I. Turton, I. (1999). Testing space-time and more complex hyperspace geographical analysis tools. In *Proceedings of 7th GISRUK conference, UK.*

Cabena, P. (1998). *Discovering data mining from concept to implementation*. Prentice hall.

Cenedese, A. and Monti, P. (2003). Interaction between an inland urban heat island and a sea-breeze flow: A laboratory study. *Journal of Applied Meteorology*, 42(11):1569–1583.

Chen, X., Vierling, L., and Deering, D. (2005). A simple and effective radiometric correction method to improve landscape change detection across sensors and across time. *Remote Sensing of Environment*, 98:63–79.

Childs, P. P. and Raman, S. (2005). Observations and numerical simulations of urban heat island and sea breeze circulations over new york city. *Pure & Applied Geophysics*, 162(10):1955–1980.

Chin, H.-N. S., Leach, M. J., Sugiyama, G. A., Jr., J. M. L., Walker, H., and Nasstrom, J. S. (2005). Evaluation of an urban canopy parameterization in a mesoscale model using VTMX and URBAN 2000 data. *American Meteorological Society*, 133:2043–2068.

Dash, P., Göttsche, F. M., Olesen, F. S., and Fischer, H. (2002). Land surface temperature and emissivity estimation from passive sensor data: theory and practice–current trends. *International Journal of Remote Sensing*, 13:2563–2594.

de Assis, E. S. and Frota, A. B. (1999). Urban bioclimatic design stratergies for a tropical city. *Atmospheric Environment*, 33:4135–4142.

de Schiller, S. and Evans, J. M. (1996). Training architects and planners to design with urban microclimates. *Atmospheric Environment*, 30:449–454.

DiBias, D., MacEachren, A. M., Krygier, J. B., and Reeves, C. (1992). Animation and the role of map design in scientific visualization. *Cartography and Geographic Information Systems*, 19:201–214, 265–266.

Ding, Q., Ding, Q., and Perrizo, W. (2002). Association rule mining on remotely sensed images using p–trees. *Lecture notes in computer science, Advances in knowledge discovery and data mining*, 2336:66–79.

Ding, Q., Ding, Q., and Perrizo, W. (2003). Association rule mining on remotely sensed images. In *Advances in Knowledge Discovery and Data Mining : 6th Pacific-Asia Conference, PAKDD 2002, Taipel, Taiwan*, Lecture Notes in Computer Science. Springer Berlin / Heidelberg.

Doran, J. C., Fast, J. D., and Horel, J. (2002). The vtmx 2000 campaign. *Bulletin of the American Meteorological Society*, 83(4):537.

Dousset, B. and Gourmelon, F. (2003). Satellite multi-sensor data analysis of urban surface temperatures and landcover. *ISPRS Journal of Photogrammetry and Remote Sensing*, 58(1-2):43–54.

Du, Y., Teillet, P. M., and Cihlar, J. (2002). Radiometric normalization of multitemporal high-resolution satellite images with quality control for land cover change detection. *Remote Sensing of Environment*, 82:123–134.

Eliasson, I. (1996). Urban nocturnal temperatures, street geometry and land use. *Atmospheric environment*, 30:379–392.

Emeis, S. and Schafer, K. (2006). Remote sensing methods to investigate boundary-layer structures relevant to air pollution in cities. *Boundary-Layer Meteorology*, 121(2):377–385.

Estiville-Castro, V. and Lee, I. (2004). Clustering with obstacles for geographical data mining. *ISPRS Journal of photogrammetry and remote sensing*, 59:21–34.

Fast, J. D., Torcolini, J. C., and Redman, R. (2005). Pseudovertical temperature profiles and the urban heat island measured by a temperature datalogger network in phoenix, arizona. *American Meteorological Society*, 44:3–13.

Fayyad, U. M. and Smyth, P. (1999). Cataloging and mining massive datasets for science data analysis. *Journal of Computation and Graphical Statistics*, 8:589–608.

Foody, G. M. (2003). Uncertainty, knowledge discovery and data mining in GIS. *Progress in physical geography*, 27, no 1:113–121(9).

Friedl, M. A. (2002). Forward and inverse modeling of land surface energy balance using surface energy temperature measurements. *Remote sensing of environment*, 79:344–354.

Gaffin, S., Rosenzweig, C., and Parshall, L. (2006). New york city urban heat island reconnaissance: Preliminary findings on street trees, parks and various urban surfaces using mobile sensors. Technical report, Center for Climate Systems Research, Columbia University.

Gallo, K. P. and Owen, T. W. (1998). Assessment of urban heat islands: A multi-sensor perspective for the dallas-ft. worth, usa region. *Geocarto Internationa*, 13(4):35–41.

Gallo, K. P. and Owen, T. W. (1999). Satellite-based adjustments for the urban heat island temperature bias. *Journal of Applied Meteorology*, 38(6):806–813.

Gedzelman, S. D., Austin, S., Cermak, R., Stefano, N., Partridge, S., Quesenberry, S., and Robinson, D. A. (2003). Mesoscale aspects of the urban heat island around new york city. *Theoretical & Applied Climatology*, 75(1/2):29–42.

Ghiaus, C., Allard, F., Santamouris, M., Georgakis, C., and Nicol, F. (2006). Urban environment influence on natural ventilation potential. *Building and Environment*, 41(4):395.

Gillies, R. R., Kustas, W. P., and Humes, K. S. (1997). A verification of the 'triangle' method for obtaining surface soil water content and energy fluxes from remote measurements of the normalized difference vegetation index (ndvi) and surface e. *International Journal of Remote Sensing*, 18(15):3145–3166.

Golany, G. S. (1996). Urban design morphology and thermal performance. *Atmospheric Environment*, 30:455–465.

Golden, J. S. (2004). The built environment induced urban heat island effect in rapidly urbanizing arid regions – a sustainable urban engineering complexity. *Environmental Sciences*, 1(4):321–333.

Goward, S. N., Xue, Y., and Czajkowski, K. P. (2002). Evaluating land surface moisture conditions from the remotely sensed temperature/vegetation index measurements: An exploration with the simplified simple biosphere model. *Remote Sensing of Environment*, 79(2-3):225–242.

Grant, R. H. and Wong, K. (1999). Ozone profiles over a suburban neighbourhood. *Atmospheric Environment*, 33:51–63.

Grimmond, C. S. B. (2006). Progress in measuring and observing the urban atmosphere. *Theoretical & Applied Climatology*, 84(1-3):3–22.

Groth, R. (1999). *Data mining : a hands - on approach for business professionals*. Prentice hall.

Guhathakurta, S. and Gober, P. (2007). The impact of the phoenix urban heat island on residential water use. *Journal of the American Planning Association*, 73(3):317–329.

Hall, D. J., Walker, S., and Spanton, A. M. (1999). Dispersion from courtyards and other enclosed spaces. *Atmospheric Environment*, 33:1187–1203.

Halverson, J. B. (2006). 2005's violent second wind. *Weatherwise*, 59(2):66–67.

Hand, D., Mannila, H., and Smyth, P. (2001). *Principles of Data Mining*, volume 1. A Bradford Book, The MIT Press.

Harrower, M. (2004). A look at the history and future of animated maps. *Cartographica*, 39:33–42.

Haute, A. R. (1988). A soil-adjusted vegetation index (savi). *Remote Sensing of Environment*, 25:295–309.

Hawkins, T. W., Brazel, A. J., Stefanov, W. L., Bigler, W., and Saffell, E. M. (2004). The role of rural variability in urban heat island determination for phoenix, arizona. *Journal of Applied Meteorology*, 43:476–486.

Heckel, M. and Zendulka, J. (2004). Data mining and its use in texture analysis. *Fundamenta Informaticae*, 60:173–186.

Hoyano, A., Asano, K., and Kanamaru, T. (1999). Analysis of the sensible heat flux from the exterior surface of buildings using tiem sequential thermography. *Atmospheric Environment*, 33:3941–3951.

Hudischewskyj, A. B., Douglas, S. G., and Lundgren, J. R. (2001). Meteorological and air quality modeling to further examine the effects of urban heat island mitigation measures on several cities in the northeastern U.S. Technical report, ICF Consulting, Systems Applications International, Inc.

Hung, T., Uchihama, D., Ochi, S., and Yasuoka, Y. (2006). Assessment with satellite data of the urban heat island effect in Asian mega cities. *International Journal of Applied Earth Observation and Geoinformation*, 8:34–48.

Jenerette, G. D., Harlan, S. L., Brazel, A., Jones, N., Larsen, L., and Stefanov, W. L. (2007). Regional relationships between surface temperature, vegetation, and human settlement in a rapidly urbanizing ecosystem. *Landscape Ecology*, 22(3):353–365.

Jin, M., E.Dickinson, R., and Zhang, D.-L. (2005). The footprint of urban areas on global climate as characterized by MODIS. *American Meteorological Society*, 18:1551–1565.

Jung, A., Kardevan, P., and Tokei, L. (2005). Detection of urban effect on vegetation in a less built-up Hungarian city by hyperspectral remote sensing. *Physics & Chemistry of the Earth – Parts A/B/C*, 30(1–3):255–259.

Kafatos, M., Wang, X. S., Li, Z., Yang, R., and Ziskin, D. (1998). Information technology implementation for a distributed data system serving earth scientists: seasonal to interannual ESIP. In *Tenth International Conference on Scientific and Statistical Database Management*.

Kato, S. and Yamaguchi, Y. (2005). Analysis of urban heat-island effect using aster and etm+ data: Seperation of antropogenic heat discharge and natural heat radiation from sensible heat flux. *Remote Sensing of Environment*, 99(1/2):44–54.

Khaikine, M. N., Kuznetsova, I. N., Kadygrov, E. N., and Miller, E. A. (2006). Investigation of temporal-spatial parameters of an urban heat island on the basis of passive microwave remote sensing. *Theoretical and Applied Climatology*, 84(1–3):161–169.

Khan, S. M. and Simpson, R. W. (2001). Effect of a heat island on the meteorology of a complex urban airshed. *Boundary–Layer Meteorology*, 100(100):487–506.

Kikegawaa, Y., Genchib, Y., Yoshikadoc, H., and Kondod, H. (2003). Development of a numerical simulation system toward comprehensive assessments of urban warming countermeasures including their impacts upon the urban buildings energy–demands. *Applied Energy*, 76:449–456.

Kim, Y.-H. and Baik, J.-J. (2005). Spatial and temporal structure of the urban heat island in Seoul. *American Meteorological Society*, 44:591–605.

Klosgen, W. and M.Zytkow, J. (2002). *Handbook of Data Mining and Knowledge Discovery*. Oxford university press.

Koperski, K., Marchisio, G. B., and Meyer, K. (2002). Inforrmation fusion and mining from satellite imagery and gis data. Technical report, Insightful Corporation.

Kullback, S. and Leibler, R. A. (1951). On information and sufficiency. *Annals of Mathematical Statistics*, 22:79–86.

Lagouarde, J.-P., Moreau, P., Irvine, M., Bonnefond, J.-M., Voogt, J. A., and Solliec, F. (2004). Airborne experimental measurements of the angular variations in surface temperature over urban areas: case study of marseille (france). *Remote Sensing of Environment*, 93(4):443–462.

Lam, N. S.-N. and Quattrochi, D. A. (1992). On the issues of scale, resolution, and fractal analysis in the mapping science. *Professional Geographer*, 44:88–98.

Lambin, E. F. and Ehrlich, D. (1996). The surface temperature-vegetation index space for land cover and land-cover change analysis. *International Journal of Remote Sensing*, 17(3):463–487.

Lensky, I. M. and Drori, R. (2007). A satellite-based parameter to monitor the aerosol impact on convective clouds. *Journal of Applied Meteorology & Climatology*, 46(5):660–666.

Li, F., Jackson, T. J., Kustas, W. P., Schmugge, T. J., French, A. N., Cosh, M. H., and Bindlish, R. (2003). Deriving land surface temperature from lansat 5 and 7 during SMEX02/SMACEX. *Remote Sensing of Environment*, 92:521–534.

Liu, H. and Weng, Q. (2008). Seasonal variations in the relationship between landscape pattern and land surface temperature in Indianapolis, U.S.A. *Environmental Monitoring and Assessment*, 144:199–219.

Lo, C. P. (1995). Automated population and dwelling unit estimation from high resolution satellite images: A GIS approach. *Internbation Journal of Remote Sensing*, 16:17–34.

Lo, C. P., Quattrochi, D. A., and Luvall, J. C. (1997). Application of high-resolution thermal infrered remote sensing and GIS to assess the urban heat island effect. *International Journal of Remote Sensing*, 18(2):287–304.

Lu, D. and Weng, Q. (2006). Spectral mixture analysis of ASTER images for examining the relationship between urban thermal features and biophysical descriptors in Indianapolis, Indiana, USA. *Remote Sensing of Environment*, 104:157–167.

Lyman, P., Varian, H. R., Dunn, J., Strygin, A., and Swearingen, K. (2000). How much information? Technical report, University of California at Berkeley.

MacEachren, A. M. and Kraak, M.-J. (1997). Exploratory cartographic visualization: Advancing the agenda. *Computers & Geosciences*, 23:335–343.

Markham, B. L. and Barker, J. L. (1985). Spectral characterization of the landsat thematic mapper sensors. *International Journal of Remote Sensing*, 6:697–716.

Masson, V. (2006). Urban surface modeling and the meso–scale impact of cities. *Theoretical and Applied Climatology*, 84(1–3):35–45.

Mihalakakou, G., Flocas, H. A., Santamouris, M., and Helmis, C. G. (2002). Application of neural networks to the simulation of the heat island over Athens, Greece, using synoptic types as a predictor. *American Meteorological Society*, 41:519–527.

Mihalakakou, G., Santamouris, M., Papanikolaou, N., Cartalis, C., and Tsangrassoulis, A. (2004). Simulation of the urban heat island phenomenon in mediterranean climates. *Pure and Applied Geophysics*, 161:429–451.

Miller, H. J. and Han, J. (2001). *Geographic Data Mining and Knowledge Discovery*. Taylor & Francis, London and Newyork.

Offerle, B., Grimmond, C. S. B., Fortuniak, K., Keysik, K., and Oke, T. R. (2006). Temporal variations in heat fluxes over a central european city centre. *Theoretical & Applied Climatology*, 84(1-3):103–115.

Oke, T. R. (1987). *Boundary layer climates*. London: Routledge.

Oke, T. R. (2006). Initial guidance to obtain representative meteorological observations at urban sites. Technical report, World Meteorological Organization.

Oke, T. R., Borrego, C., and Norman, A. L. (2004). Sitting and exposure of meteorological instruments at urban sites. In *27th NATO/CCMS International Technical Meeting on Air Pollution Modelling and its Application, Banff, 25-29 October, 2004*.

Openshaw, S. (1999). Geographical data mining: Key design issues. In *Geocomputation*, number 99, page 14.

Owen, T. W., Carlson, T. N., and Gillies, R. R. (1998). An assessment of satellite remotely-sensed land cover parameters in quantitatively describing the climatic effect of urbanization. *International Journal of Remote Sensing*, 19(9):1663–1681.

Paciorek, C. J. and Schervish, M. J. (2006). Spatial modelling using a new class of nonstationary covariance functions. *EnvironMetrics*, 17:483–506.

Paolini, L., Grings, F., Sobrino, J. A., Munoz, J. C. J., and Karszenbaum, H. (2006). Radiometric correction effects in landsat multi-date/multi-sensorchange detection studies. *International Journal of Remote Sensing*, 27:685–704.

Patz, J. A., Campbell-Lendrum, D., Holloway, T., and Foley, J. A. (2005). Impact of regional climate change on human health. *Nature*, 438(7066):310–317.

Pryor, S. C., Barthelmie, R. J., and Kjellstm, E. (2005). Potential climate change impact on wind energy resources in northern Europe: analyses using a regional climate model. *Climate Dynamics 25(7/8), 815-835.*, 25(7/8):815–835.

Quattrochi, D. and Ridd, M. (1994). Measurement and analysis of thermal energy responses from discrete urban surfaces using remote sensing data. *International Journal of Remote Sensing*, 15:1991–2022.

Rajasekar, U. and Weng, Q. (2009a). Spatio-temporal modeling and analysis of urban heat islands by using landsat tm and etm+ imagery. *International Journal of Remote Sensing*, 30:1297–1311.

Rajasekar, U. and Weng, Q. (2009b). Urban heat island monitoring and analysis by data mining of modis imageries. *ISPRS Journal of Photogrammetry and Remote Sensing*, 64(1):86–96.

Rosenzweig, C., Soleck, W., and Slosberg, R. (2006). Mitigating new york city heat island with urban forestry, living roofs and light surfaces. Technical report, New York state energy research and development authority.

Rotach, M. W., Vogt, R., Bernhofer, C., Batchvarova, E., Christen, A., Clappier, A., Feddersen, B., Gryning, S.-E., Martucci, G., Mayer, H., Mitev, V., Oke, T. R., Parlow, E., Richner, H., Roth, M., Roulet, Y.-A., Ruffieux, D., Salmond, J. A., Schatzmann, M., and Voogt, J. A. (2005). BUBBLE - an Urban Boundary Layer Meteorology Project . *Theoretical and Applied Climatology*, 81(3):231–261.

Rozoff, C. M., Cotton, W. R., and Adegoke, J. O. (2003). Simulation of st. louis, missouri, land use impacts on thunderstorms. *Journal of Applied Meteorology*, 42(6):716–.

Samenow, J. . (2007). Beating the Heat: EPA Role in Saving Lives in Vulnerable Urban Areas. Technical report, Climate Change Division, EPA.

Sarrat, C., Lemonsu, A., Masson, V., and Guedalia, D. (2006). Impact of urban heat island on regional atmospheric pollution. *Atmospheric Environment*, 40(10):1743–1758.

Scheeringa, K. (2006). Indiana state climate office (ISCO), Purdue university, revised on december 2002. http://shadow.agry.purdue.edu/toolbox/narrative.html, accessed on October 23, 2006.

Scherer, D., Fehrenbach, U., Beha, D. H., and Parlow, E. (1999). Improved concepts and methods in analysis and evaluation of the urban climate for optimizing urban planning processes. *Atmospheric Environment*, 33:4185–4193.

Schroeder, T. A., Cohen, W. B., Song, C., Canty, M. J., and Yang, Z. (2006). Radiometric correction of multi-temporal landsat data for characterization of early successional forest patterns in western oregon. *Remote Sensing of Environment*, 103:16–26.

Silverstein, C., Brin, S., and Motwani, R. (1997). Beyond market baskets: Generalizing association rules to dependence rules. In *The ACM SIGMOD International Conference on Management of Data*, pages 255–264.

Simpson, J. R. and McPherson, E. G. (1998). Simulation of tree shade impacts on residential energy use for space conditioning in sacremento. *Atmospheric Environment*, 32:69–74.

Snyder, W. C., Wan, Z., Zhang, Y., and Feng, Y. Z. (1998). Classification–based emissivity for land surface temperature measurement from space. *International Journal of Remote Sensing*, 19:2753–2774.

Sobrino, J. A., Jimenez-Munoz, J. C., and Paolini, L. (2004). Land surface temperature retrieval from landsat tm 5. *Remote Sensing of Environment*, 90(4):434–440.

Sobrino, J. A. and Raissouni, N. (2000). Toward remote sensing methods for land cover dynamic monitoring: application to morocco. *International Journal of Remote Sensing*, 21(2):353–366.

Souch, C. and Grimmond, C. (2004). Applied climatology: Heat waves. *Progress in Physical Geography*, 28(4):599–606.

Soux, A., Voogt, J. A., and Oke, T. R. (2004). A model to calculate what a remote sensor 'sees' of an urban surface. *Boundary-Layer Meteorology*, 112(2):401–424.

Stathopoulou, M., Cartalis, C., and Keramitsoglou, I. (2004). Mapping micro-urban heat islands using NOAA/AVHRR images and CORINE land cover: an application to coastal cities of Greece. *International Journal of Remote Sensing*, 25(12):2301–2316.

Streutker, D. R. (2002). A remote sensing study of the urban heat island of Houston, Texas. *International Journal of Remote Sensing*, 23:2595–2608.

Streutker, D. R. (2003). Satellite-measured growth of the urban heat island of Houston, Texas. *Remote Sensing of Environment*, 85:282–289.

Taha, H. (1997). Modeling the impacts of large-scale albedo changes on ozone air quality in the south coast air basin. *Atmospheric Environment*, 31:1667–1676.

Taha, H., Kalkstein, L. S., Sheridan, S., and Wong, E. (2004). The potential of urban environmental control in alleviating heat-wave health effects in five us regions. In *16th Symposium on Biometeorology and Aerobiology, American Meteorological Society, Vancouver, BC*.

Takahara, Y., Shiba, N., and Liu, Y. (2002). General system theoretic approach to data mining system. *International Journal of General Systems*, 31(3):245–264.

Tan, P. N., Steinbach, M., and Kumar, V. (2002). Finding spatio-temporal patterns in earth science data. NASA grant project, University of Minnesota.

Taylor, J. S. and Cristianini, N. (2004). *Kernel Methods for Pattern Analysis*. Cambridge University Press, Cambridge, United Kingdom.

Tešić, J., Newsam, S., and Manjunath, B. S. (2003). Mining image datasets using perceptual association rules. In *Proceedings of SIAM Sixth Workshop on Mining Scientific and Engineering Datasets*, volume Proceedings of SIAM Sixth Workshop on Mining Scientific and Engineering Datasets.

Velickov, S., Solomatine, P. D., Yu, X., and Price, K. R. (2000). Application of data mining techniques for remote sensing image. In *4th International conference on hydroinformatics*.

Vogelmann, J. E., Helder, D., Morfitta, R., Choatea, M. J., Merchant, J. W., and Bulley, H. (2001). Effects of landsat 5 thematic mapper and landsat 7 enhanced thematic mapper plus radiometric and geometric calibrations and corrections on landscape characterization. *Remote Sensing of Environment*, 78:55–70.

Voogt, J. A. (2005). How researchers measure urban heat island. Technical report, University of Western Ontario.

Voogt, J. A. and Oke, T. R. (1998a). Effects of urban surface geometry on remotely-sensed surface temperature. *International Journal of Remote Sensing*, 19(5):895–920.

Voogt, J. A. and Oke, T. R. (1998b). Radiometric temperatures of urban canyon walls obtained from vehicle traverses. *Theoretical and Applied Climatology*, 60(1):199–217.

Voogt, J. A. and Oke, T. R. (2003). Thermal remote sensing of urban cities. *Remote Sensing of Environment*, 86(3):370–384.

Weng, Q. (2001). A remote sensing - GIS evaluation of urban expansion and its impact on surface temperature in the Zhujiang Delta, China. *International Journal of Remote Sensing*, 22:1999–2014.

Weng, Q. (2003). Fractal analysis of satellite-detected urban heat island effect. *Photogrammetric Engineering & Remote Sensing*, 69:555–566.

Weng, Q. and Lu, D. (2008). A sub-pixel analysis of urbanization effect on land surface temperature and its interplay with impervious surface and vegetation coverage in indianapolis, united states. *International Journal of Applied Earth Observation and Geoinformation*, Accepted, May 2007.

Weng, Q., Lu, D., and Liang, B. (2006). Urban surface biophysical descriptors and land surface temperature variations. *Photogrammetric Engineering & Remote Sensing*, 72:1275–1286.

Weng, Q., Lu, D., and Schubring, J. (2004). Estimation of land surface temperature - vegetation abundance relationship for urban heat island studies. *Journal of Environmental Management*, 70:145–156.

Weng, Q., Rajasekar, U., and Hu, X. (2011). Modeling urban heat islands with multi-temporal aster images. *IEEE Transactions on Geosciences and Remote Sensing*, accepted.

Weng, Q. and Yang, S. (2006). Urban air pollution patterns, land use and thermal landscape: An examination of the linkage using GIS. *Environmental montioring and assessment*, 117:463–489.

Wukelic, G. E., Gibbons, D. E., Martucci, L. M., and Foote, H. P. (1989). Radiometric calibration of landsat thematic mapper thermal band. *Remote Sensing of Environment*, 28:339–347.

Xiao, H. and Weng, Q. (2007). The impact of land use and land cover changes on land surface temperature in a karst area of china. *Journal of Environmental Management*, 85:245–257.

Xiao, R. B., Weng, Q., Ouyang, Z., Li, W., Schienke, E. W., and Zhang, Z. (2008). Land surface temperature variation and major factors in Beijing, China. *Photogrammetric Engineering & Remote Sensing*, 74(4):451–461.

Zhang, C. and Zhang, S. (2002). *Association Rule Mining*. Springer.

APPENDIX

The below set of lists indicate the selected (confidence over 80%) results from Association mining Algorithm

Table 33

Selected results from the association mining algorithm

Association Rules
General Rules obtained
ATE6 <- ATQ10 (10.2/100735, 8.9/87148, 86.5, 7.594, 0.0)
ATE5 <- ATQ6 (10.2/100726, 10.2/100726, 100.0, 1.788, 0.0)
ATE5 <- ATQ7 (10.4/102279, 10.4/102279, 100.0, 1.788, 0.0)
ATE5 <- ATQ8 (10.4/102233, 10.4/102233, 100.0, 1.788, 0.0)
ANE7 <- ANQ7 (10.3/100986, 10.3/100986, 100.0, 2.582, 0.0)
ANE7 <- ANQ5 (11.0/107780, 11.0/107780, 100.0, 2.582, 0.0)
LTE6 <- LNQ8 (10.9/106713, 9.1/89130, 83.5, 1.252, 0.0)
LTE6 <- LTQ5 (11.0/107972, 11.0/107972, 100.0, 1.499, 0.0)
LTE6 <- LTQ7 (11.4/112526, 11.4/112526, 100.0, 1.499, 0.0)
LTE6 <- LTQ4 (11.5/113156, 11.5/113156, 100.0, 1.499, 0.0)
LTE6 <- LTQ3 (14.5/142583, 14.5/142583, 100.0, 1.499, 0.0)
LTE7 <- LTQ8 ATE5 (10.4/101758, 10.4/101758, 100.0, 3.654, 0.0)
LTE7 <- LTQ8 (13.2/130229, 13.2/130229, 100.0, 3.654, 0.0)
LNE5 <- LNQ3 (10.4/102465, 10.4/102465, 100.0, 1.947, 0.0)
LNE5 <- LNQ4 (10.5/102826, 10.5/102826, 100.0, 1.947, 0.0)
LNE6 <- LNQ8 (10.9/106713, 10.9/106713, 100.0, 2.239, 0.0)
LNE5 <- LNQ5 (12.4/121894, 12.4/121894, 100.0, 1.947, 0.0)

Table 33 – continued from previous page

Association Rules
LNE6 <- LNQ7 (12.8/125336, 12.8/125336, 100.0, 2.239, 0.0)
LNE6 <- LNQ7 LTE6 (10.2/100044, 10.2/100044, 100.0, 2.239, 0.0)
MTE8 <- MTQ6 (10.8/105932, 10.8/105932, 100.0, 2.392, 0.0)
MTE8 <- MTQ5 (10.8/106177, 10.8/106177, 100.0, 2.392, 0.0)
MTE8 <- MTQ7 (11.4/111713, 10.4/102680, 91.9, 2.199, 0.0)
MTE9 <- MTQ8 (11.4/111646, 11.4/111646, 100.0, 3.554, 0.0)
MNE8 <- MNQ5 (10.1/98936, 8.6/84892, 85.8, 3.636, 0.0)
MNE8 <- MNQ6 (10.2/99787, 10.2/99787, 100.0, 4.238, 0.0)
MNE7 <- MNQ4 (11.2/109752, 11.2/109752, 100.0, 5.156, 0.0)
LTE6 <- ATQ4 (10.1/99764, 9.3/91066, 91.3, 1.369, 0.0)
LTE6 <- ATQ6 (10.2/100726, 8.3/81497, 80.9, 1.213, 0.0)
LNE5 <- ANQ2 (10.7/104917, 8.7/85458, 81.5, 1.586, 0.0)
LNE5 <- CO (14.6/143496, 12.1/119043, 83.0, 1.615, 0.0)
LTE6 <- DA (14.7/144951, 13.4/131655, 90.8, 1.362, 0.0)
LNE6 <- ANE8 (18.8/184954, 15.5/152667, 82.5, 1.848, 0.0)
LTE6 <- ANE8 (18.8/184954, 15.1/148881, 80.5, 1.207, 0.0)
LTE6 <- ATE4 (27.5/270101, 24.8/243673, 90.2, 1.353, 0.0)
LTE6 <- LO (27.8/273198, 25.0/245706, 89.9, 1.348, 0.0)
LTE6 <- LNE6 (44.7/438967, 36.7/360870, 82.2, 1.233, 0.0)
ATE5 <- LTQ7 (11.4/112526, 9.3/91075, 80.9, 1.447, 0.0)
LTE6 <- LNQ8 LNE6 (10.9/106713, 9.1/89130, 83.5, 1.252, 0.0)
LTE6 <- ATQ6 ATE5 (10.2/100726, 8.3/81497, 80.9, 1.213, 0.0)
ATE5 <- LTQ7 LTE6 (11.4/112526, 9.3/91075, 80.9, 1.447, 0.0)
LNE6 <- ANE8 ATE5 (12.0/118412, 10.0/98397, 83.1, 1.861, 0.0)
LTE6 <- ANE8 LNE6 (15.5/152667, 13.0/128087, 83.9, 1.258, 0.0)

Table 33 – continued from previous page

Association Rules
LNE6 <- ANE8 LTE6 (15.1/148881, 13.0/128087, 86.0, 1.927, 0.0)
LTE6 <- MNE8 LNE6 (10.2/100212, 8.4/82620, 82.4, 1.236, 0.0)
LTE6 <- MNE9 LNE6 (12.5/122623, 10.5/103054, 84.0, 1.260, 0.0)
LTE6 <- MTE7 ANE7 (10.0/98531, 8.1/79530, 80.7, 1.210, 0.0)
LTE6 <- MTE7 LNE6 (12.9/127003, 11.2/109844, 86.5, 1.297, 0.0)
LTE6 <- ATE4 ANE7 (12.9/127292, 12.2/119877, 94.2, 1.412, 0.0)
LTE6 <- ATE4 MTE8 (11.2/109953, 10.2/100411, 91.3, 1.369, 0.0)
LTE6 <- ATE4 LNE6 (14.1/138771, 13.4/131962, 95.1, 1.426, 0.0)
LTE6 <- ATE4 LNE5 (12.5/122687, 10.7/105331, 85.9, 1.287, 0.0)
LTE6 <- ANE7 LNE6 (18.5/181980, 15.0/147926, 81.3, 1.219, 0.0)
LTE6 <- LDH LNE6 (22.9/225520, 18.4/180641, 80.1, 1.201, 0.0)
LTE6 <- MTE8 LNE6 (18.0/177063, 14.6/143081, 80.8, 1.212, 0.0)
LTE6 <- ANE8 LNE6 ATE5 (10.0/98397, 8.2/80627, 81.9, 1.229, 0.0)
LTE6 <- ATE4 LO (12.2/119521, 11.6/113548, 95.0, 1.424, 0.0)
LTE6 <- LO ANE7 (11.4/111685, 10.3/101053, 90.5, 1.357, 0.0)
LTE6 <- LO LDH (12.0/118262, 10.9/106708, 90.2, 1.353, 0.0)
LTE6 <- LO MTE8 (11.5/112631, 10.3/101123, 89.8, 1.346, 0.0)
LTE6 <- LO LNE6 (19.8/194389, 18.2/179158, 92.2, 1.382, 0.0)
LTE6 <- LO ATE5 (14.4/141875, 12.7/125129, 88.2, 1.322, 0.0)
LTE6 <- LO LNE6 ATE5 (10.7/104703, 9.6/94535, 90.3, 1.354, 0.0)
ATE5 <- HI LDH (19.6/192183, 16.5/161818, 84.2, 1.506, 0.0)
ATE5 <- HI LDH LNE6 (11.6/113550, 9.8/96107, 84.6, 1.514, 0.0)
ATE5 <- HI LDH LTE6 (12.2/119479, 10.2/99974, 83.7, 1.496, 0.0)
ATE5 <- HI LNE6 LTE6 (12.0/117630, 9.7/95254, 81.0, 1.448, 0.0)

Table 33 – continued from previous page

Association Rules
ASTER
AF7 <- ATE4 (27.5/270101, 23.1/226859, 84.0, 1.092, 0.0)
AF7 <- ATE4 LO (12.2/119521, 10.1/98790, 82.7, 1.075, 0.0)
AF7 <- ATE4 MA5 (16.6/162965, 15.2/149079, 91.5, 1.190, 0.0)
AF7 <- ATE4 ANE7 (12.9/127292, 10.9/107564, 84.5, 1.099, 0.0)
AF7 <- ATE4 AH8 (14.0/137539, 13.9/136149, 99.0, 1.287, 0.0)
AF7 <- ATE4 AH8 V1 (12.6/124336, 12.6/124047, 99.8, 1.297, 0.0)
AF7 <- ATE4 AH8 MA5 (10.8/105773, 10.7/105267, 99.5, 1.294, 0.0)
AF7 <- ATE4 PD1 (15.1/148200, 13.5/133014, 89.8, 1.167, 0.0)
AF7 <- ATE4 PD1 V1 (12.1/119038, 11.7/115306, 96.9, 1.260, 0.0)
AF7 <- ATE4 PD1 MA5 (10.6/104685, 9.9/97261, 92.9, 1.208, 0.0)
AF7 <- ATE4 V1 (19.2/188661, 17.5/172175, 91.3, 1.187, 0.0)
AF7 <- ATE4 V1 MA5 (12.3/120788, 11.8/115696, 95.8, 1.246, 0.0)
AH8 <- ATE4 V1 MA5 (12.3/120788, 10.0/97907, 81.1, 1.928, 0.0)
AH8 <- ATE4 PD1 V1 AF7 (11.7/115306, 9.6/94007, 81.5, 1.939, 0.0)
AH8 <- ATE4 V1 MA5 AF7 (11.8/115696, 10.0/97907, 84.6, 2.013, 0.0)
V1 <- ATE4 PD1 (15.1/148200, 12.1/119038, 80.3, 1.405, 0.0)
V1 <- ATE4 AH8 (14.0/137539, 12.6/124336, 90.4, 1.582, 0.0)
V1 <- ATE4 PD1 MA5 (10.6/104685, 8.7/85980, 82.1, 1.437, 0.0)
V1 <- ATE4 PD1 AF7 (13.5/133014, 11.7/115306, 86.7, 1.517, 0.0)
V1 <- ATE4 AH8 MA5 (10.8/105773, 10.0/97907, 92.6, 1.620, 0.0)
V1 <- ATE4 AH8 AF7 (13.9/136149, 12.6/124047, 91.1, 1.594, 0.0)
V1 <- ATE4 AH8 MA5 AF7 (10.7/105267, 10.0/97907, 93.0, 1.627, 0.0)
ATE5 <- HI LDH (19.6/192183, 16.5/161818, 84.2, 1.506, 0.0)

Table 33 – continued from previous page

Association Rules
ATE5 <- HI ANE7 AF7 (10.6/104520, 8.6/84087, 80.5, 1.439, 0.0)
ATE5 <- HI LDH V1 (10.9/106804, 9.0/88724, 83.1, 1.486, 0.0)
ATE5 <- HI LDH MA5 (11.3/111152, 9.6/94700, 85.2, 1.524, 0.0)
ATE5 <- HI LDH AF7 (15.4/151267, 13.0/127460, 84.3, 1.507, 0.0)
AF7 <- ANE8 ATE5 (12.0/118412, 9.7/94928, 80.2, 1.042, 0.0)
AF7 <- AH7 ATE5 (19.1/187922, 17.0/167054, 88.9, 1.156, 0.0)
AF7 <- PD2 ATE5 (22.5/221568, 18.2/179325, 80.9, 1.052, 0.0)
AF7 <- PD1 ATE5 (19.4/190637, 15.7/154773, 81.2, 1.056, 0.0)
AF7 <- AH8 ATE5 (23.1/227415, 21.8/214016, 94.1, 1.224, 0.0)
AF7 <- ATE5 V1 (30.9/303901, 26.2/257187, 84.6, 1.100, 0.0)
AF7 <- ATE5 MA5 (32.5/319732, 28.4/279442, 87.4, 1.136, 0.0)
AF7 <- HI PD2 ATE5 (11.1/109405, 9.1/89031, 81.4, 1.058, 0.0)
AF7 <- HI ATE5 V1 (12.0/118279, 9.8/96786, 81.8, 1.064, 0.0)
AF7 <- HI ATE5 MA5 (13.4/131688, 11.5/112765, 85.6, 1.113, 0.0)
AF7 <- AH7 PD2 ATE5 (10.9/106767, 9.5/92983, 87.1, 1.132, 0.0)
AF7 <- AH7 LDH ATE5 (10.3/101400, 9.0/88508, 87.3, 1.135, 0.0)
AF7 <- AH7 ATE5 MA5 (11.4/111805, 10.7/105556, 94.4, 1.228, 0.0)
AF7 <- V2 ATE5 MA5 (10.9/106952, 9.5/93004, 87.0, 1.131, 0.0)
AF7 <- PD2 LDH ATE5 (13.2/129756, 10.8/106493, 82.1, 1.067, 0.0)
AF7 <- PD2 ATE5 V1 (12.7/125038, 10.7/105418, 84.3, 1.096, 0.0)
AF7 <- PD2 ATE5 MA5 (12.5/123239, 11.3/111540, 90.5, 1.177, 0.0)
AF7 <- ANE7 ATE5 V1 (12.4/122348, 10.5/103252, 84.4, 1.097, 0.0)
AF7 <- ANE7 ATE5 MA5 (12.8/126310, 11.3/110777, 87.7, 1.140, 0.0)
AF7 <- LDH AH8 ATE5 (10.9/107078, 10.1/99352, 92.8, 1.207, 0.0)
AF7 <- LDH ATE5 V1 (15.8/155298, 13.2/130196, 83.8, 1.090, 0.0)

Table 33 – continued from previous page

Association Rules
AF7 <- LDH ATE5 MA5 (15.9/156318, 13.7/134884, 86.3, 1.122, 0.0)
AF7 <- PD1 ATE5 V1 MA5 (10.2/100550, 9.6/94286, 93.8, 1.219, 0.0)
AF7 <- AH8 ATE5 V1 MA5 (13.1/129245, 13.1/129245, 100.0, 1.300, 0.0)
AF7 <- PD1 AH8 ATE5 (12.0/117488, 11.8/116383, 99.1, 1.288, 0.0)
AF7 <- PD1 ATE5 V1 (14.4/141721, 12.9/126481, 89.2, 1.161, 0.0)
AF7 <- PD1 ATE5 MA5 (13.3/130556, 12.0/118424, 90.7, 1.180, 0.0)
AF7 <- AH8 ATE5 V1 (16.8/165003, 16.6/162978, 98.8, 1.284, 0.0)
AF7 <- AH8 ATE5 MA5 (16.5/162130, 16.2/158962, 98.0, 1.275, 0.0)
AF7 <- ATE5 V1 MA5 (19.3/190110, 17.5/171841, 90.4, 1.175, 0.0)
AF7 <- PD1 AH8 ATE5 V1 (11.1/108840, 11.0/108109, 99.3, 1.292, 0.0)
AF7 <- PD1 AH8 ATE5 MA5 (10.0/98508, 10.0/98134, 99.6, 1.295, 0.0)
AH8 <- PD1 ATE5 V1 MA5 (10.2/100550, 9.2/90134, 89.6, 2.132, 0.0)
AH8 <- PD1 ATE5 MA5 AF7 (12.0/118424, 10.0/98134, 82.9, 1.971, 0.0)
AH8 <- PD1 ATE5 V1 AF7 (12.9/126481, 11.0/108109, 85.5, 2.033, 0.0)
V1 <- AH8 ATE5 MA5 AF7 (16.2/158962, 13.1/129245, 81.3, 1.423, 0.0)
V1 <- PD1 ATE5 AF7 (15.7/154773, 12.9/126481, 81.7, 1.430, 0.0)
V1 <- PD1 AH8 ATE5 MA5 (10.0/98508, 9.2/90134, 91.5, 1.601, 0.0)
V1 <- PD1 AH8 ATE5 AF7 (11.8/116383, 11.0/108109, 92.9, 1.625, 0.0)
V1 <- PD1 AH8 ATE5 (12.0/117488, 11.1/108840, 92.6, 1.621, 0.0)
MA5 <- PD1 AH8 ATE5 AF7 (11.8/116383, 10.0/98134, 84.3, 1.452, 0.0)
MA5 <- PD1 AH8 ATE5 V1 AF7 (11.0/108109, 9.2/90134, 83.4, 1.435, 0.0)
MA5 <- PD1 AH8 ATE5 (12.0/117488, 10.0/98508, 83.8, 1.443, 0.0)
MA5 <- PD1 AH8 ATE5 V1 (11.1/108840, 9.2/90134, 82.8, 1.426, 0.0)

Landsat

Table 33 – continued from previous page

Association Rules
LTE6 <- DA (14.7/144951, 13.4/131655, 90.8, 1.362, 0.0)
LTE6 <- LO (27.8/273198, 25.0/245706, 89.9, 1.348, 0.0)
LTE6 <- LNE6 (44.7/438967, 36.7/360870, 82.2, 1.233, 0.0)
AF7 <- LTE6 (66.7/655610, 54.7/537622, 82.0, 1.066, 0.0)
LTE6 <- DA PD1 (10.8/106481, 9.8/96594, 90.7, 1.360, 0.0)
LTE6 <- DA V1 (12.5/122856, 11.4/112015, 91.2, 1.367, 0.0)
V1 <- DA LTE6 (13.4/131655, 11.4/112015, 85.1, 1.489, 0.0)
AF7 <- DA LTE6 (13.4/131655, 12.4/122376, 93.0, 1.209, 0.0)
LTE6 <- DA AF7 (13.6/133918, 12.4/122376, 91.4, 1.370, 0.0)
V1 <- MA6 LTE6 (13.0/127675, 11.2/109709, 85.9, 1.503, 0.0)
LTE6 <- LO PD2 (14.1/138254, 12.8/125380, 90.7, 1.360, 0.0)
LTE6 <- LO LDH (12.0/118262, 10.9/106708, 90.2, 1.353, 0.0)
LTE6 <- LO PD1 (10.5/103120, 9.5/93863, 91.0, 1.365, 0.0)
LTE6 <- LO AH8 (11.0/107809, 10.0/98081, 91.0, 1.364, 0.0)
LTE6 <- LO LNE6 (19.8/194389, 18.2/179158, 92.2, 1.382, 0.0)
LTE6 <- LO V1 (17.6/172889, 16.0/157454, 91.1, 1.365, 0.0)
LTE6 <- LO MA5 (15.1/148463, 13.6/134080, 90.3, 1.354, 0.0)
AF7 <- LO LTE6 (25.0/245706, 20.3/199374, 81.1, 1.055, 0.0)
LTE6 <- LO AF7 (22.3/219361, 20.3/199374, 90.9, 1.363, 0.0)
LTE6 <- AH7 LNE6 (15.8/155432, 12.7/125096, 80.5, 1.207, 0.0)
AF7 <- AH7 LTE6 (20.3/199615, 18.4/181146, 90.7, 1.180, 0.0)
LTE6 <- PD2 LNE6 (21.5/211378, 17.8/175165, 82.9, 1.242, 0.0)
AF7 <- PD2 LTE6 (26.9/264594, 21.9/215636, 81.5, 1.060, 0.0)
LTE6 <- LDH LNE6 (22.9/225520, 18.4/180641, 80.1, 1.201, 0.0)

Table 33 – continued from previous page

Association Rules
AF7 <- LDH LTE6 (27.8/273294, 23.2/228319, 83.5, 1.086, 0.0)
LTE6 <- PD1 AH8 (24.6/242282, 20.1/198008, 81.7, 1.225, 0.0)
LTE6 <- PD1 LNE6 (16.0/157191, 14.3/140384, 89.3, 1.339, 0.0)
LTE6 <- PD1 V1 (30.1/296095, 24.6/241638, 81.6, 1.224, 0.0)
AF7 <- PD1 LTE6 (31.2/306913, 26.8/263042, 85.7, 1.114, 0.0)
LTE6 <- AH8 LNE6 (18.8/184715, 16.1/158717, 85.9, 1.288, 0.0)
LTE6 <- AH8 V1 (32.6/320583, 26.6/261918, 81.7, 1.225, 0.0)
V1 <- AH8 LTE6 (31.5/309625, 26.6/261918, 84.6, 1.480, 0.0)
AF7 <- AH8 LTE6 (31.5/309625, 30.9/303595, 98.1, 1.275, 0.0)
LTE6 <- LNE6 V1 (28.5/279805, 24.4/240018, 85.8, 1.286, 0.0)
LTE6 <- LNE6 MA5 (25.2/247380, 21.1/207228, 83.8, 1.256, 0.0)
AF7 <- LNE6 LTE6 (36.7/360870, 30.5/300003, 83.1, 1.081, 0.0)
LTE6 <- LNE6 AF7 (36.5/358358, 30.5/300003, 83.7, 1.255, 0.0)
AF7 <- LNE5 LTE6 (27.4/269615, 22.1/217363, 80.6, 1.048, 0.0)
AF7 <- V1 LTE6 (43.3/425435, 38.5/378231, 88.9, 1.156, 0.0)
AF7 <- MA5 LTE6 (40.3/396349, 36.3/356383, 89.9, 1.169, 0.0)
LTE6 <- DA PD1 AF7 (10.4/102377, 9.5/93026, 90.9, 1.362, 0.0)
AF7 <- DA V1 LTE6 (11.4/112015, 10.9/106893, 95.4, 1.241, 0.0)
LTE6 <- DA V1 AF7 (11.9/116873, 10.9/106893, 91.5, 1.371, 0.0)
V1 <- DA LTE6 AF7 (12.4/122376, 10.9/106893, 87.3, 1.528, 0.0)
AF7 <- MA6 V1 LTE6 (11.2/109709, 9.4/92522, 84.3, 1.097, 0.0)
LTE6 <- MA6 V1 AF7 (11.7/114972, 9.4/92522, 80.5, 1.207, 0.0)
V1 <- MA6 LTE6 AF7 (10.1/99010, 9.4/92522, 93.4, 1.635, 0.0)
LTE6 <- LO PD2 LNE6 (10.8/106057, 10.0/97959, 92.4, 1.385, 0.0)
AF7 <- LO PD2 LTE6 (12.8/125380, 10.5/103584, 82.6, 1.074, 0.0)

Table 33 – continued from previous page

Association Rules
LTE6 <- LO PD2 AF7 (11.5/113411, 10.5/103584, 91.3, 1.369, 0.0)
AF7 <- LO LDH LTE6 (10.9/106708, 9.0/88913, 83.3, 1.083, 0.0)
LTE6 <- LO AH8 AF7 (10.7/105314, 9.8/96112, 91.3, 1.368, 0.0)
LTE6 <- LO LNE6 V1 (12.6/123693, 11.7/114983, 93.0, 1.394, 0.0)
LTE6 <- LO LNE6 MA5 (10.5/103590, 9.7/95831, 92.5, 1.387, 0.0)
AF7 <- LO LNE6 LTE6 (18.2/179158, 14.9/146051, 81.5, 1.060, 0.0)
LTE6 <- LO LNE6 AF7 (16.0/157491, 14.9/146051, 92.7, 1.390, 0.0)
AF7 <- LO V1 LTE6 (16.0/157454, 14.0/137972, 87.6, 1.139, 0.0)
LTE6 <- LO V1 AF7 (15.3/150560, 14.0/137972, 91.6, 1.374, 0.0)
AF7 <- LO MA5 LTE6 (13.6/134080, 12.2/119892, 89.4, 1.163, 0.0)
LTE6 <- LO MA5 AF7 (13.5/132298, 12.2/119892, 90.6, 1.359, 0.0)
AF7 <- HI LDH LTE6 (12.2/119479, 10.0/98315, 82.3, 1.070, 0.0)
AF7 <- HI LNE6 LTE6 (12.0/117630, 9.8/96292, 81.9, 1.064, 0.0)
AF7 <- HI V1 LTE6 (10.6/104651, 9.0/88651, 84.7, 1.102, 0.0)
AF7 <- HI MA5 LTE6 (10.9/107069, 9.6/94324, 88.1, 1.146, 0.0)
LTE6 <- AH7 PD2 LNE6 (10.1/98893, 8.3/81139, 82.0, 1.230, 0.0)
AF7 <- AH7 PD2 LTE6 (11.9/117422, 10.5/103497, 88.1, 1.146, 0.0)
AF7 <- AH7 LNE6 LTE6 (12.7/125096, 11.5/112668, 90.1, 1.171, 0.0)
LTE6 <- AH7 LNE6 AF7 (14.1/138928, 11.5/112668, 81.1, 1.216, 0.0)
AF7 <- AH7 MA5 LTE6 (11.5/113498, 11.0/108507, 95.6, 1.243, 0.0)
AF7 <- V2 MA5 LTE6 (11.2/110031, 9.5/92926, 84.5, 1.098, 0.0)
LTE6 <- PD2 LDH LNE6 (13.4/131707, 11.0/108518, 82.4, 1.235, 0.0)
AF7 <- PD2 LDH LTE6 (14.9/146866, 12.3/121114, 82.5, 1.072, 0.0)
LTE6 <- PD2 LNE6 V1 (13.7/134823, 11.6/113662, 84.3, 1.264, 0.0)
LTE6 <- PD2 LNE6 MA5 (11.2/110115, 9.3/91441, 83.0, 1.245, 0.0)

Table 33 – continued from previous page

Association Rules
AF7 <- PD2 LNE6 LTE6 (17.8/175165, 14.7/144267, 82.4, 1.071, 0.0)
LTE6 <- PD2 LNE6 AF7 (17.6/172521, 14.7/144267, 83.6, 1.254, 0.0)
AF7 <- PD2 V1 LTE6 (16.4/161336, 13.9/136410, 84.6, 1.099, 0.0)
AF7 <- PD2 MA5 LTE6 (14.4/141896, 13.3/130347, 91.9, 1.195, 0.0)
V1 <- LDH AH8 LTE6 (12.0/118297, 9.7/95397, 80.6, 1.411, 0.0)
AF7 <- LDH AH8 LTE6 (12.0/118297, 11.8/115717, 97.8, 1.272, 0.0)
LTE6 <- LDH LNE6 V1 (15.1/148508, 12.4/122079, 82.2, 1.233, 0.0)
AF7 <- LDH LNE6 LTE6 (18.4/180641, 15.5/152161, 84.2, 1.095, 0.0)
LTE6 <- LDH LNE6 AF7 (19.1/187555, 15.5/152161, 81.1, 1.216, 0.0)
AF7 <- LDH V1 LTE6 (18.7/183627, 16.4/161313, 87.8, 1.142, 0.0)
AF7 <- LDH MA5 LTE6 (16.0/157124, 14.3/140492, 89.4, 1.163, 0.0)
LTE6 <- PD1 AH8 V1 (22.9/225413, 19.2/188944, 83.8, 1.257, 0.0)
V1 <- PD1 AH8 LTE6 (20.1/198008, 19.2/188944, 95.4, 1.670, 0.0)
LTE6 <- PD1 AH8 MA5 (21.0/206482, 16.9/166542, 80.7, 1.209, 0.0)
MA5 <- PD1 AH8 LTE6 (20.1/198008, 16.9/166542, 84.1, 1.448, 0.0)
AF7 <- PD1 AH8 LTE6 (20.1/198008, 20.0/196774, 99.4, 1.292, 0.0)
LTE6 <- PD1 AH8 AF7 (24.4/240066, 20.0/196774, 82.0, 1.229, 0.0)
LTE6 <- PD1 LNE6 V1 (12.7/125228, 11.6/114111, 91.1, 1.366, 0.0)
V1 <- PD1 LNE6 LTE6 (14.3/140384, 11.6/114111, 81.3, 1.422, 0.0)
LTE6 <- PD1 LNE6 MA5 (10.9/106859, 9.8/95944, 89.8, 1.346, 0.0)
AF7 <- PD1 LNE6 LTE6 (14.3/140384, 12.5/122709, 87.4, 1.137, 0.0)
LTE6 <- PD1 LNE6 AF7 (13.8/135777, 12.5/122709, 90.4, 1.355, 0.0)
AF7 <- PD1 LNE5 LTE6 (15.2/149035, 12.9/126443, 84.8, 1.103, 0.0)
LTE6 <- PD1 V1 MA5 (21.5/211230, 17.6/173272, 82.0, 1.230, 0.0)
V1 <- PD1 MA5 LTE6 (22.0/215830, 17.6/173272, 80.3, 1.405, 0.0)

Table 33 – continued from previous page

Association Rules
AF7 <- PD1 V1 LTE6 (24.6/241638, 22.9/225538, 93.3, 1.214, 0.0)
LTE6 <- PD1 V1 AF7 (27.7/272013, 22.9/225538, 82.9, 1.243, 0.0)
V1 <- PD1 LTE6 AF7 (26.8/263042, 22.9/225538, 85.7, 1.500, 0.0)
AF7 <- PD1 MA5 LTE6 (22.0/215830, 20.0/196316, 91.0, 1.183, 0.0)
LTE6 <- AH8 LNE6 V1 (15.5/152673, 13.7/134961, 88.4, 1.325, 0.0)
V1 <- AH8 LNE6 LTE6 (16.1/158717, 13.7/134961, 85.0, 1.488, 0.0)
LTE6 <- AH8 LNE6 MA5 (13.6/134020, 11.8/116157, 86.7, 1.299, 0.0)
AF7 <- AH8 LNE6 LTE6 (16.1/158717, 15.9/156010, 98.3, 1.278, 0.0)
LTE6 <- AH8 LNE6 AF7 (18.3/180375, 15.9/156010, 86.5, 1.297, 0.0)
V1 <- AH8 LNE5 LTE6 (14.0/137649, 11.8/116121, 84.4, 1.476, 0.0)
AF7 <- AH8 LNE5 LTE6 (14.0/137649, 13.7/134681, 97.8, 1.272, 0.0)
LTE6 <- AH8 V1 MA5 (25.8/254043, 20.9/205926, 81.1, 1.215, 0.0)
V1 <- AH8 MA5 LTE6 (23.8/233509, 20.9/205926, 88.2, 1.543, 0.0)
AF7 <- AH8 V1 LTE6 (26.6/261918, 26.5/260633, 99.5, 1.294, 0.0)
LTE6 <- AH8 V1 AF7 (32.3/317931, 26.5/260633, 82.0, 1.229, 0.0)
V1 <- AH8 LTE6 AF7 (30.9/303595, 26.5/260633, 85.8, 1.502, 0.0)
AF7 <- AH8 MA5 LTE6 (23.8/233509, 23.6/231708, 99.2, 1.290, 0.0)
LTE6 <- LNE6 V1 MA5 (16.8/164994, 14.5/142553, 86.4, 1.295, 0.0)
AF7 <- LNE6 V1 LTE6 (24.4/240018, 21.6/212321, 88.5, 1.150, 0.0)
LTE6 <- LNE6 V1 AF7 (24.9/245227, 21.6/212321, 86.6, 1.298, 0.0)
AF7 <- LNE6 MA5 LTE6 (21.1/207228, 19.1/187921, 90.7, 1.179, 0.0)
LTE6 <- LNE6 MA5 AF7 (22.6/222591, 19.1/187921, 84.4, 1.266, 0.0)
AF7 <- LNE5 V1 LTE6 (17.2/169311, 15.5/152166, 89.9, 1.169, 0.0)
AF7 <- LNE5 MA5 LTE6 (17.6/173203, 15.6/153524, 88.6, 1.153, 0.0)
AF7 <- V1 MA5 LTE6 (27.6/271457, 25.8/253943, 93.5, 1.216, 0.0)

Table 33 – continued from previous page

Association Rules
PD1 <- DA V1 LTE6 AF7 (10.9/106893, 8.8/86476, 80.9, 1.958, 0.0)
AH8 <- DA V1 LTE6 AF7 (10.9/106893, 8.8/86317, 80.8, 1.921, 0.0)
AF7 <- LO LNE6 V1 LTE6 (11.7/114983, 10.2/100321, 87.2, 1.135, 0.0)
LTE6 <- LO LNE6 V1 AF7 (10.9/107580, 10.2/100321, 93.3, 1.398, 0.0)
AF7 <- PD2 LDH LNE6 LTE6 (11.0/108518, 9.1/89692, 82.7, 1.075, 0.0)
LTE6 <- PD2 LDH LNE6 AF7 (11.0/108275, 9.1/89692, 82.8, 1.242, 0.0)
AF7 <- PD2 LDH V1 LTE6 (10.4/101765, 8.7/85882, 84.4, 1.097, 0.0)
AF7 <- PD2 LNE6 V1 LTE6 (11.6/113662, 9.8/96305, 84.7, 1.102, 0.0)
LTE6 <- PD2 LNE6 V1 AF7 (11.6/113609, 9.8/96305, 84.8, 1.271, 0.0)
LTE6 <- PD2 LNE6 MA5 AF7 (10.3/101278, 8.6/84246, 83.2, 1.247, 0.0)
V1 <- LDH AH8 LTE6 AF7 (11.8/115717, 9.7/94921, 82.0, 1.435, 0.0)
AF7 <- LDH LNE6 V1 LTE6 (12.4/122079, 10.9/107376, 88.0, 1.144, 0.0)
LTE6 <- LDH LNE6 V1 AF7 (13.2/129669, 10.9/107376, 82.8, 1.242, 0.0)
AF7 <- LDH LNE6 MA5 LTE6 (10.0/98769, 9.2/90062, 91.2, 1.186, 0.0)
LTE6 <- LDH LNE6 MA5 AF7 (11.4/112309, 9.2/90062, 80.2, 1.202, 0.0)
AF7 <- LDH V1 MA5 LTE6 (11.0/107682, 10.1/98848, 91.8, 1.194, 0.0)
V1 <- PD1 AH8 LNE5 LTE6 (10.0/98347, 9.6/94264, 95.8, 1.677, 0.0)
AH8 <- PD1 LNE5 V1 LTE6 (11.7/114684, 9.6/94264, 82.2, 1.955, 0.0)
PD1 <- AH8 LNE5 V1 LTE6 (11.8/116121, 9.6/94264, 81.2, 1.965, 0.0)
MA5 <- PD1 AH8 LNE5 LTE6 (10.0/98347, 8.4/82564, 84.0, 1.445, 0.0)
AF7 <- PD1 AH8 LNE5 LTE6 (10.0/98347, 10.0/97988, 99.6, 1.296, 0.0)
LTE6 <- PD1 AH8 V1 MA5 (19.3/190011, 16.0/157666, 83.0, 1.244, 0.0)
MA5 <- PD1 AH8 V1 LTE6 (19.2/188944, 16.0/157666, 83.4, 1.437, 0.0)
V1 <- PD1 AH8 MA5 LTE6 (16.9/166542, 16.0/157666, 94.7, 1.656, 0.0)
AH8 <- PD1 V1 MA5 LTE6 (17.6/173272, 16.0/157666, 91.0, 2.164, 0.0)

Table 33 – continued from previous page

Association Rules
AF7 <- PD1 AH8 V1 LTE6 (19.2/188944, 19.1/188237, 99.6, 1.295, 0.0)
LTE6 <- PD1 AH8 V1 AF7 (22.8/224326, 19.1/188237, 83.9, 1.258, 0.0)
V1 <- PD1 AH8 LTE6 AF7 (20.0/196774, 19.1/188237, 95.7, 1.674, 0.0)
AH8 <- PD1 V1 LTE6 AF7 (22.9/225538, 19.1/188237, 83.5, 1.985, 0.0)
AF7 <- PD1 AH8 MA5 LTE6 (16.9/166542, 16.9/166015, 99.7, 1.296, 0.0)
LTE6 <- PD1 AH8 MA5 AF7 (20.9/205353, 16.9/166015, 80.8, 1.212, 0.0)
MA5 <- PD1 AH8 LTE6 AF7 (20.0/196774, 16.9/166015, 84.4, 1.452, 0.0)
AH8 <- PD1 MA5 LTE6 AF7 (20.0/196316, 16.9/166015, 84.6, 2.012, 0.0)
AF7 <- PD1 LNE6 V1 LTE6 (11.6/114111, 10.8/106470, 93.3, 1.213, 0.0)
LTE6 <- PD1 LNE6 V1 AF7 (11.9/116491, 10.8/106470, 91.4, 1.370, 0.0)
V1 <- PD1 LNE6 LTE6 AF7 (12.5/122709, 10.8/106470, 86.8, 1.518, 0.0)
AF7 <- PD1 LNE5 V1 LTE6 (11.7/114684, 11.0/108363, 94.5, 1.229, 0.0)
V1 <- PD1 LNE5 LTE6 AF7 (12.9/126443, 11.0/108363, 85.7, 1.499, 0.0)
AF7 <- PD1 LNE5 MA5 LTE6 (11.0/108230, 9.9/97635, 90.2, 1.173, 0.0)
AF7 <- PD1 V1 MA5 LTE6 (17.6/173272, 16.9/165896, 95.7, 1.245, 0.0)
LTE6 <- PD1 V1 MA5 AF7 (20.4/200817, 16.9/165896, 82.6, 1.239, 0.0)
V1 <- PD1 MA5 LTE6 AF7 (20.0/196316, 16.9/165896, 84.5, 1.479, 0.0)
LTE6 <- AH8 LNE6 V1 MA5 (11.8/116281, 10.4/102534, 88.2, 1.322, 0.0)
V1 <- AH8 LNE6 MA5 LTE6 (11.8/116157, 10.4/102534, 88.3, 1.544, 0.0)
AF7 <- AH8 LNE6 V1 LTE6 (13.7/134961, 13.7/134250, 99.5, 1.294, 0.0)
LTE6 <- AH8 LNE6 V1 AF7 (15.4/151581, 13.7/134250, 88.6, 1.328, 0.0)
V1 <- AH8 LNE6 LTE6 AF7 (15.9/156010, 13.7/134250, 86.1, 1.506, 0.0)
AF7 <- AH8 LNE6 MA5 LTE6 (11.8/116157, 11.7/115324, 99.3, 1.291, 0.0)
LTE6 <- AH8 LNE6 MA5 AF7 (13.5/132784, 11.7/115324, 86.9, 1.302, 0.0)
MA5 <- AH8 LNE5 V1 LTE6 (11.8/116121, 9.6/94788, 81.6, 1.405, 0.0)

Table 33 – continued from previous page

Association Rules
V1 <- AH8 LNE5 MA5 LTE6 (10.9/106904, 9.6/94788, 88.7, 1.551, 0.0)
AF7 <- AH8 LNE5 V1 LTE6 (11.8/116121, 11.8/115712, 99.6, 1.296, 0.0)
V1 <- AH8 LNE5 LTE6 AF7 (13.7/134681, 11.8/115712, 85.9, 1.503, 0.0)
AF7 <- AH8 LNE5 MA5 LTE6 (10.9/106904, 10.8/106035, 99.2, 1.290, 0.0)
AF7 <- AH8 V1 MA5 LTE6 (20.9/205926, 20.9/205926, 100.0, 1.300, 0.0)
LTE6 <- AH8 V1 MA5 AF7 (25.8/254043, 20.9/205926, 81.1, 1.215, 0.0)
V1 <- AH8 MA5 LTE6 AF7 (23.6/231708, 20.9/205926, 88.9, 1.555, 0.0)
AH8 <- V1 MA5 LTE6 AF7 (25.8/253943, 20.9/205926, 81.1, 1.929, 0.0)
AF7 <- LNE6 V1 MA5 LTE6 (14.5/142553, 13.5/132698, 93.1, 1.210, 0.0)
LTE6 <- LNE6 V1 MA5 AF7 (15.6/153053, 13.5/132698, 86.7, 1.300, 0.0)
AF7 <- LNE5 V1 MA5 LTE6 (12.1/118755, 11.4/111636, 94.0, 1.222, 0.0)
AH8 <- PD1 LNE5 V1 LTE6 AF7 (11.0/108363, 9.6/94100, 86.8, 2.066, 0.0)
PD1 <- AH8 LNE5 V1 LTE6 AF7 (11.8/115712, 9.6/94100, 81.3, 1.968, 0.0)
AF7 <- PD1 AH8 V1 MA5 LTE6 (16.0/157666, 16.0/157666, 100.0, 1.300, 0.0)
LTE6 <- PD1 AH8 V1 MA5 AF7 (19.3/190011, 16.0/157666, 83.0, 1.244, 0.0)
MA5 <- PD1 AH8 V1 LTE6 AF7 (19.1/188237, 16.0/157666, 83.8, 1.442, 0.0)
V1 <- PD1 AH8 MA5 LTE6 AF7 (16.9/166015, 16.0/157666, 95.0, 1.662, 0.0)
AH8 <- PD1 V1 MA5 LTE6 AF7 (16.9/165896, 16.0/157666, 95.0, 2.261, 0.0)
AF7 <- AH8 LNE6 V1 MA5 LTE6 (10.4/102534, 10.4/102534, 100.0, 1.300, 0.0)
LTE6 <- AH8 LNE6 V1 MA5 AF7 (11.8/116281, 10.4/102534, 88.2, 1.322, 0.0)
V1 <- AH8 LNE6 MA5 LTE6 AF7 (11.7/115324, 10.4/102534, 88.9, 1.556, 0.0)
MA5 <- AH8 LNE5 V1 LTE6 AF7 (11.8/115712, 9.6/94788, 81.9, 1.410, 0.0)
V1 <- AH8 LNE5 MA5 LTE6 AF7 (10.8/106035, 9.6/94788, 89.4, 1.564, 0.0)
AH8 <- LNE5 V1 MA5 LTE6 AF7 (11.4/111636, 9.6/94788, 84.9, 2.020, 0.0)

Table 33 – continued from previous page

Association Rules
MODIS
AF7 <- MTE7 (26.6/261789, 24.3/238419, 91.1, 1.184, 0.0)
MA5 <- MTE7 PD1 AH8 V1 (12.8/125730, 11.7/114539, 91.1, 1.568, 0.0)
V1 <- MTE7 PD1 AH8 MA5 (12.2/119506, 11.7/114539, 95.8, 1.677, 0.0)
AH8 <- MTE7 PD1 V1 MA5 (12.0/117747, 11.7/114539, 97.3, 2.314, 0.0)
PD1 <- MTE7 AH8 V1 MA5 (12.6/123391, 11.7/114539, 92.8, 2.247, 0.0)
AF7 <- MTE7 PD1 AH8 V1 (12.8/125730, 12.8/125730, 100.0, 1.300, 0.0)
V1 <- MTE7 PD1 AH8 AF7 (13.3/130697, 12.8/125730, 96.2, 1.683, 0.0)
AH8 <- MTE7 PD1 V1 AF7 (14.2/140045, 12.8/125730, 89.8, 2.136, 0.0)
PD1 <- MTE7 AH8 V1 AF7 (14.0/137150, 12.8/125730, 91.7, 2.219, 0.0)
AF7 <- MTE7 PD1 AH8 MA5 (12.2/119506, 12.2/119506, 100.0, 1.300, 0.0)
MA5 <- MTE7 PD1 AH8 AF7 (13.3/130697, 12.2/119506, 91.4, 1.574, 0.0)
AH8 <- MTE7 PD1 MA5 AF7 (13.6/134018, 12.2/119506, 89.2, 2.121, 0.0)
PD1 <- MTE7 AH8 MA5 AF7 (13.9/136546, 12.2/119506, 87.5, 2.118, 0.0)
AF7 <- MTE7 PD1 V1 MA5 (12.0/117747, 11.7/115460, 98.1, 1.275, 0.0)
MA5 <- MTE7 PD1 V1 AF7 (14.2/140045, 11.7/115460, 82.4, 1.419, 0.0)
V1 <- MTE7 PD1 MA5 AF7 (13.6/134018, 11.7/115460, 86.2, 1.507, 0.0)
PD1 <- MTE7 V1 MA5 AF7 (13.9/136988, 11.7/115460, 84.3, 2.040, 0.0)
AF7 <- MTE7 AH8 V1 MA5 (12.6/123391, 12.6/123391, 100.0, 1.300, 0.0)
MA5 <- MTE7 AH8 V1 AF7 (14.0/137150, 12.6/123391, 90.0, 1.549, 0.0)
V1 <- MTE7 AH8 MA5 AF7 (13.9/136546, 12.6/123391, 90.4, 1.581, 0.0)
AH8 <- MTE7 V1 MA5 AF7 (13.9/136988, 12.6/123391, 90.1, 2.143, 0.0)
PD1 <- MTE7 AH8 (15.8/155077, 13.3/130697, 84.3, 2.040, 0.0)
V1 <- MTE7 PD1 (17.2/169298, 15.1/148212, 87.5, 1.532, 0.0)

Table 33 – continued from previous page

Association Rules
MA5 <- MTE7 PD1 (17.2/169298, 13.9/136305, 80.5, 1.386, 0.0)
AF7 <- MTE7 PD1 (17.2/169298, 16.1/158603, 93.7, 1.218, 0.0)
V1 <- MTE7 AH8 (15.8/155077, 14.0/137401, 88.6, 1.550, 0.0)
MA5 <- MTE7 AH8 (15.8/155077, 13.9/136546, 88.1, 1.516, 0.0)
AF7 <- MTE7 AH8 (15.8/155077, 15.8/154826, 99.8, 1.298, 0.0)
AF7 <- MTE7 V1 (19.3/189407, 17.9/175757, 92.8, 1.207, 0.0)
AF7 <- MTE7 MA5 (19.4/190514, 18.8/184830, 97.0, 1.262, 0.0)
AF7 <- MNE9 MTE7 (15.9/156022, 14.5/142614, 91.4, 1.189, 0.0)
V1 <- MNE9 MTE7 PD1 (10.3/101730, 9.0/88922, 87.4, 1.529, 0.0)
AF7 <- MNE9 MTE7 PD1 (10.3/101730, 9.7/95647, 94.0, 1.223, 0.0)
AF7 <- MNE9 MTE7 V1 (11.8/115609, 11.0/107672, 93.1, 1.211, 0.0)
AF7 <- MNE9 MTE7 MA5 (11.4/111807, 11.0/108617, 97.1, 1.263, 0.0)
V1 <- MTE7 PD1 AH8 (13.3/130697, 12.8/125730, 96.2, 1.683, 0.0)
AH8 <- MTE7 PD1 V1 (15.1/148212, 12.8/125730, 84.8, 2.018, 0.0)
PD1 <- MTE7 AH8 V1 (14.0/137401, 12.8/125730, 91.5, 2.215, 0.0)
MA5 <- MTE7 PD1 AH8 (13.3/130697, 12.2/119506, 91.4, 1.574, 0.0)
AH8 <- MTE7 PD1 MA5 (13.9/136305, 12.2/119506, 87.7, 2.085, 0.0)
PD1 <- MTE7 AH8 MA5 (13.9/136546, 12.2/119506, 87.5, 2.118, 0.0)
AF7 <- MTE7 PD1 AH8 (13.3/130697, 13.3/130697, 100.0, 1.300, 0.0)
AH8 <- MTE7 PD1 AF7 (16.1/158603, 13.3/130697, 82.4, 1.960, 0.0)
PD1 <- MTE7 AH8 AF7 (15.8/154826, 13.3/130697, 84.4, 2.043, 0.0)
V1 <- MTE7 PD1 MA5 (13.9/136305, 12.0/117747, 86.4, 1.511, 0.0)
PD1 <- MTE7 V1 MA5 (14.4/141520, 12.0/117747, 83.2, 2.014, 0.0)
AF7 <- MTE7 PD1 V1 (15.1/148212, 14.2/140045, 94.5, 1.229, 0.0)
V1 <- MTE7 PD1 AF7 (16.1/158603, 14.2/140045, 88.3, 1.545, 0.0)

Table 33 – continued from previous page

Association Rules
AF7 <- MTE7 PD1 MA5 (13.9/136305, 13.6/134018, 98.3, 1.279, 0.0)
MA5 <- MTE7 PD1 AF7 (16.1/158603, 13.6/134018, 84.5, 1.455, 0.0)
MA5 <- MTE7 AH8 V1 (14.0/137401, 12.6/123391, 89.8, 1.546, 0.0)
V1 <- MTE7 AH8 MA5 (13.9/136546, 12.6/123391, 90.4, 1.581, 0.0)
AH8 <- MTE7 V1 MA5 (14.4/141520, 12.6/123391, 87.2, 2.074, 0.0)
AF7 <- MTE7 AH8 V1 (14.0/137401, 14.0/137150, 99.8, 1.298, 0.0)
V1 <- MTE7 AH8 AF7 (15.8/154826, 14.0/137150, 88.6, 1.550, 0.0)
AF7 <- MTE7 AH8 MA5 (13.9/136546, 13.9/136546, 100.0, 1.300, 0.0)
MA5 <- MTE7 AH8 AF7 (15.8/154826, 13.9/136546, 88.2, 1.518, 0.0)
AF7 <- MTE7 V1 MA5 (14.4/141520, 13.9/136988, 96.8, 1.259, 0.0)
AF7 <- MTE7 PD1 AH8 V1 MA5 (11.7/114539, 11.7/114539, 100.0, 1.300, 0.0)
MA5 <- MTE7 PD1 AH8 V1 AF7 (12.8/125730, 11.7/114539, 91.1, 1.568, 0.0)
V1 <- MTE7 PD1 AH8 MA5 AF7 (12.2/119506, 11.7/114539, 95.8, 1.677, 0.0)
AH8 <- MTE7 PD1 V1 MA5 AF7 (11.7/115460, 11.7/114539, 99.2, 2.360, 0.0)
PD1 <- MTE7 AH8 V1 MA5 AF7 (12.6/123391, 11.7/114539, 92.8, 2.247, 0.0)
AF7 <- MNE9 MTE8 (10.2/100296, 8.3/81395, 81.2, 1.055, 0.0)
AF7 <- LO MTE8 (11.5/112631, 9.4/92354, 82.0, 1.066, 0.0)
AF7 <- AH7 MTE8 (13.6/133606, 12.4/121518, 91.0, 1.183, 0.0)
AF7 <- PD2 MTE8 (17.5/172286, 14.9/146314, 84.9, 1.104, 0.0)
AF7 <- LDH MTE8 (16.0/156977, 12.9/127260, 81.1, 1.054, 0.0)
AF7 <- MTE8 AH8 (17.4/171315, 16.6/162737, 95.0, 1.235, 0.0)
AF7 <- MTE8 V1 (23.0/226348, 19.9/195353, 86.3, 1.122, 0.0)
AF7 <- MTE8 MA5 (24.0/236244, 20.7/203778, 86.3, 1.122, 0.0)
AF7 <- PD1 MTE8 V1 (10.9/107240, 9.7/95597, 89.1, 1.159, 0.0)
AF7 <- PD1 MTE8 MA5 (11.2/110034, 9.2/90399, 82.2, 1.068, 0.0)

Table 33 – continued from previous page

Association Rules
V1 <- MTE8 AH8 MA5 (12.6/123716, 10.1/99085, 80.1, 1.401, 0.0)
AF7 <- PD2 MTE8 V1 (10.5/102856, 9.0/88698, 86.2, 1.121, 0.0)
AF7 <- MTE8 AH8 V1 (12.8/125629, 12.6/124315, 99.0, 1.287, 0.0)
AF7 <- MTE8 AH8 MA5 (12.6/123716, 12.4/121711, 98.4, 1.279, 0.0)
AF7 <- MTE8 V1 MA5 (14.2/140054, 13.2/129690, 92.6, 1.204, 0.0)
AF7 <- MTE8 AH8 V1 MA5 (10.1/99085, 10.1/99085, 100.0, 1.300, 0.0)
V1 <- MTE8 AH8 MA5 AF7 (12.4/121711, 10.1/99085, 81.4, 1.424, 0.0)
AF7 <- MTE9 AH7 (10.0/98638, 8.5/83629, 84.8, 1.102, 0.0)

Table 34

Marion County and its surrounding eight Counties daytime LST image characteristics: Before and after kernel convolution

	Temperature Before (K)		Temperature After (K)		
Date	Maximum	Mean	Maximum	Mean	%Cloud
1-Jan-03	268.0	47.1	81.0	40.0	82.1
2-Jan-03	0.0	0.0	3.4	0.4	100.0
3-Jan-03	0.0	0.0	0.0	0.0	100.0
4-Jan-03	272.8	235.7	258.0	203.2	13.0
5-Jan-03	0.0	0.0	0.0	0.0	100.0
6-Jan-03	276.3	93.1	202.7	84.7	66.0
7-Jan-03	0.0	0.0	3.4	0.4	100.0
8-Jan-03	0.0	0.0	4.0	0.5	100.0
9-Jan-03	283.3	280.3	281.6	279.8	0.5

Table 34 – continued from previous page

	Temperature Before (K)		Temperature After (K)		
Date	Maximum	Mean	Maximum	Mean	%Cloud
10-Jan-03	275.4	37.4	70.7	30.9	86.4
11-Jan-03	272.2	81.9	134.7	81.5	69.8
12-Jan-03	271.8	5.4	97.3	23.7	98.0
13-Jan-03	0.0	0.0	29.9	3.1	100.0
14-Jan-03	0.0	0.0	7.8	0.6	100.0
15-Jan-03	0.0	0.0	13.3	2.2	100.0
16-Jan-03	0.0	0.0	0.0	0.0	100.0
17-Jan-03	268.7	264.3	263.2	257.5	0.1
18-Jan-03	0.0	0.0	3.8	0.1	100.0
19-Jan-03	263.6	57.6	188.3	63.4	77.9
20-Jan-03	0.0	0.0	0.0	0.0	100.0
21-Jan-03	0.0	0.0	45.8	10.5	100.0
22-Jan-03	0.0	0.0	0.0	0.0	100.0
23-Jan-03	0.0	0.0	26.0	3.9	100.0
24-Jan-03	261.8	1.0	48.5	5.4	99.6
25-Jan-03	272.1	230.9	263.5	223.1	14.5
26-Jan-03	0.0	0.0	4.0	0.2	100.0
27-Jan-03	0.0	0.0	0.0	0.0	100.0
28-Jan-03	268.2	1.5	97.1	19.3	99.4
29-Jan-03	0.0	0.0	0.0	0.0	100.0
30-Jan-03	274.2	36.6	208.0	69.2	86.6
31-Jan-03	0.0	0.0	0.0	0.0	100.0
2-Feb-03	0.0	0.0	0.0	0.0	100.0
3-Feb-03	0.0	0.0	0.0	0.0	100.0

Table 34 – continued from previous page

	Temperature Before (K)		Temperature After (K)		
Date	Maximum	Mean	Maximum	Mean	%Cloud
4-Feb-03	0.0	0.0	0.0	0.0	100.0
5-Feb-03	276.1	130.8	158.8	122.0	52.4
6-Feb-03	0.0	0.0	0.0	0.0	100.0
7-Feb-03	271.2	132.4	239.2	131.7	50.6
8-Feb-03	271.4	50.5	209.7	65.2	81.3
9-Feb-03	273.2	4.6	70.7	11.2	98.3
10-Feb-03	0.0	0.0	0.0	0.0	100.0
11-Feb-03	268.8	265.3	265.1	258.4	0.2
12-Feb-03	268.2	28.1	115.6	41.1	89.5
13-Feb-03	274.0	201.7	246.7	185.5	25.9
14-Feb-03	0.0	0.0	0.0	0.0	100.0
15-Feb-03	0.0	0.0	0.0	0.0	100.0
16-Feb-03	0.0	0.0	0.0	0.0	100.0
17-Feb-03	0.0	0.0	0.0	0.0	100.0
18-Feb-03	0.0	0.0	0.0	0.0	100.0
19-Feb-03	0.0	0.0	0.0	0.0	100.0
20-Feb-03	279.2	271.2	273.4	261.4	1.7
21-Feb-03	0.0	0.0	0.0	0.0	100.0
22-Feb-03	0.0	0.0	0.0	0.0	100.0
23-Feb-03	0.0	0.0	6.4	0.3	100.0
24-Feb-03	0.0	0.0	6.1	1.1	100.0
25-Feb-03	261.8	7.9	22.5	8.0	97.0
26-Feb-03	0.0	0.0	3.2	0.1	100.0
27-Feb-03	0.0	0.0	0.0	0.0	100.0

Table 34 – continued from previous page

	Temperature Before (K)		Temperature After (K)		
Date	Maximum	Mean	Maximum	Mean	%Cloud
28-Feb-03	0.0	0.0	7.3	0.3	100.0
1-Mar-03	0.0	0.0	0.0	0.0	100.0
2-Mar-03	0.0	0.0	0.0	0.0	100.0
3-Mar-03	270.0	118.7	224.7	123.2	55.7
4-Mar-03	0.0	0.0	0.0	0.0	100.0
5-Mar-03	0.0	0.0	0.0	0.0	100.0
6-Mar-03	274.2	242.8	265.3	234.1	10.5
7-Mar-03	278.7	150.9	196.8	131.0	45.3
8-Mar-03	275.9	7.3	38.7	9.8	97.3
9-Mar-03	278.2	3.4	32.8	5.8	98.8
10-Mar-03	275.9	195.2	268.6	180.8	28.8
11-Mar-03	0.0	0.0	22.9	4.7	100.0
12-Mar-03	0.0	0.0	0.0	0.0	100.0
13-Mar-03	0.0	0.0	0.0	0.0	100.0
14-Mar-03	288.2	267.9	273.9	260.6	5.7
15-Mar-03	294.5	184.6	254.0	179.1	36.6
16-Mar-03	300.0	296.2	296.6	295.7	0.3
17-Mar-03	290.5	4.7	9.2	2.6	98.4
18-Mar-03	0.0	0.0	2.5	0.4	100.0
19-Mar-03	0.0	0.0	0.0	0.0	100.0
20-Mar-03	297.5	222.7	238.6	226.0	24.2
22-Mar-03	293.1	272.7	286.5	248.1	5.8
23-Mar-03	299.4	295.2	296.5	291.8	0.3
24-Mar-03	299.0	199.3	256.7	193.8	32.7

Table 34 – continued from previous page

	Temperature Before (K)		Temperature After (K)		
Date	Maximum	Mean	Maximum	Mean	%Cloud
25-Mar-03	0.0	0.0	52.6	6.2	100.0
26-Mar-03	0.0	0.0	6.3	1.0	100.0
27-Mar-03	291.5	37.2	84.8	40.4	87.1
28-Mar-03	0.0	0.0	0.0	0.0	100.0
29-Mar-03	0.0	0.0	0.0	0.0	100.0
30-Mar-03	0.0	0.0	7.0	1.2	100.0
31-Mar-03	292.5	273.4	275.1	254.5	5.1
1-Apr-03	299.5	296.1	297.0	296.2	0.0
2-Apr-03	300.5	183.3	259.3	177.7	38.4
3-Apr-03	303.8	296.6	298.8	296.0	1.0
4-Apr-03	291.4	7.4	12.1	7.0	97.4
5-Apr-03	0.0	0.0	0.0	0.0	100.0
6-Apr-03	0.0	0.0	0.0	0.0	100.0
7-Apr-03	0.0	0.0	0.0	0.0	100.0
11-Apr-03	297.7	294.1	295.2	294.0	0.0
12-Apr-03	302.7	291.9	294.8	290.2	1.8
13-Apr-03	299.8	296.4	297.0	296.4	0.0
14-Apr-03	305.3	256.5	281.6	251.0	14.7
15-Apr-03	303.7	289.1	298.8	287.2	3.4
16-Apr-03	300.3	18.6	112.5	34.6	93.8
17-Apr-03	0.0	0.0	0.1	0.0	100.0
18-Apr-03	298.6	276.9	280.7	252.8	6.2
19-Apr-03	0.0	0.0	4.0	0.2	100.0
20-Apr-03	0.0	0.0	7.4	0.6	100.0

Table 34 – continued from previous page

	Temperature Before (K)		Temperature After (K)		
Date	Maximum	Mean	Maximum	Mean	%Cloud
21-Apr-03	0.0	0.0	0.0	0.0	100.0
22-Apr-03	0.0	0.0	0.0	0.0	100.0
23-Apr-03	301.4	290.0	292.1	286.0	1.9
24-Apr-03	0.0	0.0	0.0	0.0	100.0
25-Apr-03	0.0	0.0	0.0	0.0	100.0
26-Apr-03	302.3	296.0	297.5	295.9	0.0
27-Apr-03	301.5	297.2	298.1	297.1	0.0
28-Apr-03	303.7	143.6	253.0	139.0	51.8
29-Apr-03	302.9	298.1	295.7	273.6	0.0
30-Apr-03	0.0	0.0	22.7	4.8	100.0
1-May-03	0.0	0.0	0.0	0.0	100.0
2-May-03	0.0	0.0	0.0	0.0	100.0
3-May-03	299.1	194.9	218.4	190.2	33.7
4-May-03	0.0	0.0	0.0	0.0	100.0
5-May-03	304.1	298.3	299.8	297.5	0.0
6-May-03	301.8	156.1	262.1	153.3	47.6
7-May-03	0.0	0.0	6.0	0.7	100.0
8-May-03	0.0	0.0	0.6	0.0	100.0
9-May-03	302.4	12.5	13.4	9.0	95.8
10-May-03	0.0	0.0	0.0	0.0	100.0
11-May-03	289.3	12.0	53.6	19.3	95.8
12-May-03	297.5	197.5	276.6	191.0	32.5
13-May-03	301.2	295.9	297.1	295.7	0.0
14-May-03	0.0	0.0	0.3	0.0	100.0

Table 34 – continued from previous page

	Temperature Before (K)		Temperature After (K)		
Date	Maximum	Mean	Maximum	Mean	%Cloud
15-May-03	297.2	12.5	51.3	18.2	95.7
16-May-03	299.8	41.1	144.4	54.7	86.1
17-May-03	0.0	0.0	0.0	0.0	100.0
18-May-03	0.0	0.0	0.0	0.0	100.0
19-May-03	0.0	0.0	0.0	0.0	100.0
20-May-03	0.0	0.0	0.0	0.0	100.0
21-May-03	301.8	180.6	226.8	169.7	38.7
22-May-03	300.5	248.5	281.4	237.2	15.9
23-May-03	302.6	141.8	238.5	134.4	52.5
24-May-03	301.0	225.4	277.3	206.9	24.0
25-May-03	0.0	0.0	0.0	0.0	100.0
26-May-03	301.5	21.4	66.5	28.9	92.8
27-May-03	301.5	20.1	78.2	31.6	93.3
28-May-03	0.0	0.0	0.0	0.0	100.0
29-May-03	297.5	212.7	255.5	171.3	27.5
30-May-03	0.0	0.0	0.0	0.0	100.0
31-May-03	0.0	0.0	0.0	0.0	100.0
1-Jun-03	304.5	247.0	277.3	238.8	16.3
2-Jun-03	0.0	0.0	0.0	0.0	100.0
3-Jun-03	0.0	0.0	0.0	0.0	100.0
4-Jun-03	294.3	3.9	56.3	11.5	98.7
5-Jun-03	302.5	292.8	295.2	287.2	1.3
6-Jun-03	0.0	0.0	0.1	0.0	100.0
7-Jun-03	294.7	3.3	43.4	8.6	98.9

Table 34 – continued from previous page

	Temperature Before (K)		Temperature After (K)		
Date	Maximum	Mean	Maximum	Mean	%Cloud
8-Jun-03	0.0	0.0	0.0	0.0	100.0
9-Jun-03	302.1	113.3	176.9	123.1	62.0
10-Jun-03	0.0	0.0	0.0	0.0	100.0
11-Jun-03	0.0	0.0	4.0	0.7	100.0
12-Jun-03	0.0	0.0	0.0	0.0	100.0
13-Jun-03	302.5	102.1	126.3	92.7	65.7
14-Jun-03	0.0	0.0	0.0	0.0	100.0
15-Jun-03	305.3	6.6	92.5	22.6	97.8
16-Jun-03	0.0	0.0	8.3	1.0	100.0
17-Jun-03	307.7	105.8	203.0	108.2	65.1
19-Jun-03	0.0	0.0	0.0	0.0	100.0
20-Jun-03	308.7	301.8	303.0	301.4	0.1
21-Jun-03	310.0	273.9	300.9	276.0	9.8
22-Jun-03	315.6	305.2	306.5	302.3	0.9
23-Jun-03	309.7	241.9	297.2	259.4	20.3
26-Jun-03	0.0	0.0	0.0	0.0	100.0
27-Jun-03	312.7	305.5	306.0	304.9	0.0
28-Jun-03	307.7	149.6	228.5	147.2	50.8
29-Jun-03	312.6	258.9	296.9	230.8	15.9
30-Jun-03	302.2	25.5	96.8	39.0	91.5
1-Jul-03	308.0	46.7	179.3	72.8	84.7
2-Jul-03	302.5	18.5	94.8	36.6	93.8
3-Jul-03	311.1	91.0	171.1	92.3	70.3
4-Jul-03	305.4	75.8	226.5	99.4	75.0

Table 34 – continued from previous page

	Temperature Before (K)		Temperature After (K)		
Date	Maximum	Mean	Maximum	Mean	%Cloud
5-Jul-03	302.0	179.3	280.5	162.6	40.0
6-Jul-03	305.6	140.2	233.1	146.7	53.5
7-Jul-03	0.0	0.0	5.7	0.6	100.0
8-Jul-03	306.5	26.3	113.6	44.6	91.3
9-Jul-03	260.3	1.0	43.9	8.8	99.6
10-Jul-03	297.4	2.2	40.2	8.5	99.2
11-Jul-03	300.5	174.5	274.7	193.7	40.9
12-Jul-03	306.8	223.0	257.5	217.0	25.7
13-Jul-03	306.3	200.1	230.5	203.6	33.1
14-Jul-03	307.3	270.7	297.1	269.6	10.5
15-Jul-03	0.0	0.0	0.0	0.0	100.0
16-Jul-03	307.1	300.3	301.8	299.9	0.0
17-Jul-03	313.4	303.8	305.4	303.6	0.2
18-Jul-03	0.0	0.0	0.0	0.0	100.0
19-Jul-03	314.1	303.8	306.4	303.5	0.0
20-Jul-03	301.4	47.5	152.5	59.6	84.1
21-Jul-03	0.0	0.0	0.4	0.0	100.0
22-Jul-03	303.3	161.8	204.2	162.1	45.5
23-Jul-03	293.0	18.4	73.9	17.8	93.7
24-Jul-03	313.5	289.3	301.3	291.1	4.0
25-Jul-03	308.0	301.0	302.8	300.6	0.0
26-Jul-03	303.9	14.8	200.8	48.6	95.1
27-Jul-03	297.8	76.6	127.7	81.8	74.1
28-Jul-03	0.0	0.0	0.0	0.0	100.0

Table 34 – continued from previous page

	Temperature Before (K)		Temperature After (K)		
Date	Maximum	Mean	Maximum	Mean	%Cloud
29-Jul-03	308.5	286.7	298.7	291.0	4.6
30-Jul-03	311.1	290.6	299.6	291.9	3.6
31-Jul-03	311.1	280.0	291.6	279.1	7.3
1-Aug-03	302.3	216.1	293.6	231.2	27.9
2-Aug-03	0.0	0.0	9.8	1.6	100.0
3-Aug-03	299.5	110.9	159.9	111.0	62.6
4-Aug-03	306.3	175.5	221.2	174.6	41.6
5-Aug-03	305.6	234.3	265.5	236.8	21.8
6-Aug-03	301.8	46.0	156.8	53.6	84.6
7-Aug-03	308.3	273.6	294.9	274.7	9.5
8-Aug-03	300.0	13.5	100.6	22.5	95.5
9-Aug-03	0.0	0.0	3.8	0.5	100.0
10-Aug-03	270.5	33.9	45.3	27.8	87.2
11-Aug-03	306.4	188.0	232.3	169.7	37.4
12-Aug-03	299.3	86.3	188.5	98.2	70.7
13-Aug-03	298.6	0.6	107.5	12.5	99.8
14-Aug-03	302.8	144.3	243.6	149.6	51.9
15-Aug-03	301.4	73.3	204.3	77.1	75.5
16-Aug-03	307.4	207.2	255.8	211.5	31.3
17-Aug-03	296.0	4.8	147.2	44.5	98.4
18-Aug-03	312.4	303.1	305.3	302.7	0.0
19-Aug-03	308.8	302.4	304.0	301.8	0.0
20-Aug-03	314.3	305.1	306.9	304.6	0.1
21-Aug-03	305.6	200.4	294.4	209.9	33.7

Table 34 – continued from previous page

	Temperature Before (K)		Temperature After (K)		
Date	Maximum	Mean	Maximum	Mean	%Cloud
22-Aug-03	0.0	0.0	57.2	5.3	100.0
23-Aug-03	311.9	303.9	305.8	303.5	0.0
24-Aug-03	304.3	261.9	295.8	268.7	12.7
25-Aug-03	312.8	303.1	305.9	303.6	0.8
26-Aug-03	308.7	300.7	301.6	300.8	0.7
27-Aug-03	307.7	209.0	297.8	199.8	30.8
28-Aug-03	303.6	192.5	285.3	207.5	36.1
29-Aug-03	0.0	0.0	28.0	2.1	100.0
30-Aug-03	0.0	0.0	3.5	0.2	100.0
31-Aug-03	0.0	0.0	0.0	0.0	100.0
1-Sep-03	0.0	0.0	0.0	0.0	100.0
2-Sep-03	0.0	0.0	0.0	0.0	100.0
3-Sep-03	305.2	31.1	231.6	61.2	89.6
4-Sep-03	298.9	123.0	144.5	116.4	58.0
5-Sep-03	305.8	279.8	299.2	276.4	6.2
6-Sep-03	306.7	298.8	301.2	298.2	0.1
7-Sep-03	297.3	10.8	199.2	51.1	96.3
8-Sep-03	301.7	79.3	136.1	66.1	73.1
9-Sep-03	303.3	228.9	263.6	225.1	23.4
10-Sep-03	307.0	263.6	290.2	259.6	12.5
11-Sep-03	300.1	245.6	293.5	257.9	17.4
12-Sep-03	307.0	296.5	298.2	293.5	1.4
13-Sep-03	304.4	273.9	291.7	277.4	8.4
14-Sep-03	300.0	7.9	37.1	10.0	97.3

Table 34 – continued from previous page

	Temperature Before (K)		Temperature After (K)		
Date	Maximum	Mean	Maximum	Mean	%Cloud
15-Sep-03	303.4	278.3	285.2	274.7	6.3
16-Sep-03	307.3	298.1	300.8	299.4	1.0
17-Sep-03	306.9	282.2	299.1	282.1	6.3
18-Sep-03	304.7	300.1	301.2	299.9	0.0
19-Sep-03	0.0	0.0	0.0	0.0	100.0
20-Sep-03	302.4	297.5	298.5	297.1	0.0
21-Sep-03	305.3	298.5	300.5	299.0	0.5
22-Sep-03	294.0	35.9	126.2	58.6	87.7
23-Sep-03	300.1	246.5	274.5	259.6	16.4
24-Sep-03	303.5	298.7	299.6	298.4	0.0
25-Sep-03	294.1	233.3	282.0	221.3	19.5
26-Sep-03	0.0	0.0	0.7	0.0	100.0
27-Sep-03	297.2	291.6	293.0	292.0	0.5
28-Sep-03	0.0	0.0	3.8	0.3	100.0
29-Sep-03	289.5	113.3	116.6	103.8	60.3
30-Sep-03	295.7	281.8	291.2	281.8	3.3
1-Oct-03	294.2	271.4	287.2	266.9	6.4
2-Oct-03	293.7	284.3	286.8	284.0	1.6
3-Oct-03	0.0	0.0	0.0	0.0	100.0
4-Oct-03	0.0	0.0	10.4	0.8	100.0
5-Oct-03	297.0	64.2	144.1	52.5	78.1
6-Oct-03	298.1	295.1	295.5	295.0	0.0
7-Oct-03	301.5	296.2	297.5	296.5	0.5
8-Oct-03	302.5	287.0	298.2	289.5	4.0

Table 34 – continued from previous page

	Temperature Before (K)		Temperature After (K)		
Date	Maximum	Mean	Maximum	Mean	%Cloud
9-Oct-03	0.0	0.0	0.0	0.0	100.0
10-Oct-03	0.0	0.0	6.9	1.0	100.0
11-Oct-03	301.0	229.6	263.9	222.4	22.9
12-Oct-03	300.8	296.2	296.9	296.0	0.0
13-Oct-03	298.6	296.3	296.9	296.0	0.0
14-Oct-03	0.0	0.0	0.0	0.0	100.0
15-Oct-03	293.5	290.7	291.4	290.7	0.1
16-Oct-03	297.0	267.3	291.3	265.4	8.7
17-Oct-03	0.0	0.0	47.0	9.0	100.0
18-Oct-03	294.0	275.4	282.6	271.2	5.2
19-Oct-03	298.7	295.4	295.6	295.3	0.0
20-Oct-03	294.5	11.8	139.4	41.7	95.9
21-Oct-03	0.0	0.0	0.0	0.0	100.0
22-Oct-03	288.1	53.8	74.1	49.5	81.2
23-Oct-03	294.0	286.9	288.5	284.1	1.3
24-Oct-03	292.3	288.7	290.1	287.9	0.4
25-Oct-03	0.0	0.0	0.0	0.0	100.0
26-Oct-03	289.8	285.0	286.8	277.5	0.4
27-Oct-03	0.0	0.0	7.5	1.2	100.0
28-Oct-03	0.0	0.0	0.0	0.0	100.0
29-Oct-03	286.2	284.1	284.2	282.6	0.0
30-Oct-03	295.7	293.0	293.3	292.9	0.1
31-Oct-03	0.0	0.0	0.0	0.0	100.0
1-Nov-03	0.0	0.0	0.8	0.1	100.0

Table 34 – continued from previous page

	Temperature Before (K)		Temperature After (K)		
Date	Maximum	Mean	Maximum	Mean	%Cloud
2-Nov-03	298.2	164.1	226.1	167.1	44.5
3-Nov-03	297.2	196.0	274.9	188.7	33.7
4-Nov-03	299.4	296.6	297.1	296.8	0.0
5-Nov-03	0.0	0.0	0.0	0.0	100.0
6-Nov-03	0.0	0.0	0.1	0.0	100.0
7-Nov-03	0.0	0.0	0.0	0.0	100.0
8-Nov-03	280.0	10.3	100.8	26.7	96.3
9-Nov-03	284.6	282.6	282.8	282.5	0.0
10-Nov-03	286.2	52.5	106.1	50.5	81.5
11-Nov-03	0.0	0.0	0.0	0.0	100.0
12-Nov-03	269.3	0.8	26.2	3.4	99.7
13-Nov-03	282.8	279.3	280.2	276.9	0.5
14-Nov-03	0.0	0.0	0.0	0.0	100.0
15-Nov-03	0.0	0.0	2.4	0.5	100.0
16-Nov-03	0.0	0.0	0.0	0.0	100.0
17-Nov-03	0.0	0.0	41.7	11.8	100.0
18-Nov-03	0.0	0.0	0.0	0.0	100.0
19-Nov-03	288.4	285.4	286.2	285.6	0.2
20-Nov-03	289.8	240.8	285.1	246.1	15.8
21-Nov-03	289.7	26.5	130.5	38.9	90.8
22-Nov-03	290.3	152.4	224.8	154.4	46.8
23-Nov-03	0.0	0.0	12.6	1.5	100.0
24-Nov-03	0.0	0.0	0.0	0.0	100.0
25-Nov-03	0.0	0.0	0.0	0.0	100.0

Table 34 – continued from previous page

	Temperature Before (K)		Temperature After (K)		
Date	Maximum	Mean	Maximum	Mean	%Cloud
26-Nov-03	283.0	38.9	222.3	63.7	86.1
27-Nov-03	0.0	0.0	2.4	0.2	100.0
28-Nov-03	0.0	0.0	0.0	0.0	100.0
29-Nov-03	0.0	0.0	0.5	0.0	100.0
30-Nov-03	283.6	245.1	281.6	238.6	12.9
1-Dec-03	281.8	279.2	279.8	279.4	0.2
2-Dec-03	0.0	0.0	35.0	3.4	100.0
3-Dec-03	0.0	0.0	0.0	0.0	100.0
4-Dec-03	0.0	0.0	0.0	0.0	100.0
5-Dec-03	0.0	0.0	0.0	0.0	100.0
6-Dec-03	280.8	162.9	226.4	141.2	41.7
7-Dec-03	278.7	93.8	170.2	85.2	66.1
8-Dec-03	0.0	0.0	0.5	0.1	100.0
9-Dec-03	0.0	0.0	0.0	0.0	100.0
10-Dec-03	270.7	27.9	41.0	19.4	89.6
11-Dec-03	0.0	0.0	0.0	0.0	100.0
12-Dec-03	274.9	28.2	81.9	33.8	89.7
13-Dec-03	0.0	0.0	0.0	0.0	100.0
14-Dec-03	0.0	0.0	0.0	0.0	100.0
15-Dec-03	0.0	0.0	0.0	0.0	100.0
16-Dec-03	0.0	0.0	0.0	0.0	100.0
25-Dec-03	274.8	48.5	226.8	76.9	82.3
26-Dec-03	279.3	206.0	253.2	212.4	25.7
27-Dec-03	280.9	278.5	280.0	278.8	0.2

Table 34 – continued from previous page

	Temperature Before (K)		Temperature After (K)		
Date	Maximum	Mean	Maximum	Mean	%Cloud
28-Dec-03	285.3	101.9	180.8	102.4	63.9
29-Dec-03	0.0	0.0	0.0	0.0	100.0
30-Dec-03	277.9	159.6	242.1	163.0	42.2
31-Dec-03	282.5	280.7	281.0	280.6	0.0
1-Jan-04	0.0	0.0	0.8	0.1	100.0
2-Jan-04	0.0	0.0	0.0	0.0	100.0
3-Jan-04	279.5	8.7	30.6	9.2	96.9
4-Jan-04	277.1	21.9	69.8	29.7	91.9
5-Jan-04	0.0	0.0	0.0	0.0	100.0
6-Jan-04	264.8	1.5	23.7	5.4	99.4
7-Jan-04	271.8	6.7	26.1	7.3	97.5
8-Jan-04	0.0	0.0	0.0	0.0	100.0
9-Jan-04	0.0	0.0	0.0	0.0	100.0
10-Jan-04	273.6	208.5	246.8	198.7	23.4
11-Jan-04	0.0	0.0	0.0	0.0	100.0
12-Jan-04	0.0	0.0	0.0	0.0	100.0
13-Jan-04	0.0	0.0	57.8	13.5	100.0
14-Jan-04	278.6	271.1	273.7	269.0	2.0
15-Jan-04	0.0	0.0	5.1	0.9	100.0
16-Jan-04	261.4	4.2	16.5	3.1	98.4
17-Jan-04	0.0	0.0	0.0	0.0	100.0
18-Jan-04	0.0	0.0	0.0	0.0	100.0
19-Jan-04	271.6	50.8	177.2	63.8	81.3
20-Jan-04	0.0	0.0	0.0	0.0	100.0

Table 34 – continued from previous page

	Temperature Before (K)		Temperature After (K)		
Date	Maximum	Mean	Maximum	Mean	%Cloud
21-Jan-04	0.0	0.0	0.0	0.0	100.0
22-Jan-04	270.7	12.5	52.0	21.2	95.4
23-Jan-04	0.0	0.0	0.0	0.0	100.0
24-Jan-04	0.0	0.0	6.9	0.8	100.0
25-Jan-04	0.0	0.0	3.6	1.0	100.0
26-Jan-04	0.0	0.0	0.0	0.0	100.0
27-Jan-04	265.2	26.2	98.9	35.1	90.0
28-Jan-04	264.9	58.0	198.3	68.8	77.9
29-Jan-04	0.0	0.0	0.0	0.0	100.0
30-Jan-04	0.0	0.0	0.2	0.0	100.0
31-Jan-04	262.0	183.9	240.1	166.1	28.8
1-Feb-04	0.0	0.0	0.0	0.0	100.0
2-Feb-04	0.0	0.0	3.0	0.3	100.0
3-Feb-04	0.0	0.0	0.0	0.0	100.0
4-Feb-04	273.5	91.4	115.0	81.9	66.4
7-Feb-04	0.0	0.0	0.0	0.0	100.0
8-Feb-04	0.0	0.0	0.0	0.0	100.0
9-Feb-04	0.0	0.0	50.9	5.0	100.0
10-Feb-04	277.7	263.3	273.0	264.2	3.8
11-Feb-04	277.0	236.3	263.3	233.6	13.9
12-Feb-04	273.4	114.4	159.9	122.1	57.9
13-Feb-04	0.0	0.0	0.0	0.0	100.0
14-Feb-04	275.7	114.5	165.6	99.5	58.2
15-Feb-04	277.3	6.5	119.1	25.0	97.6

Table 34 – continued from previous page

	Temperature Before (K)		Temperature After (K)		
Date	Maximum	Mean	Maximum	Mean	%Cloud
16-Feb-04	269.9	1.5	5.8	1.3	99.4
17-Feb-04	0.0	0.0	0.0	0.0	100.0
18-Feb-04	0.0	0.0	0.0	0.0	100.0
19-Feb-04	284.6	14.2	30.7	12.1	95.0
20-Feb-04	0.0	0.0	0.0	0.0	100.0
21-Feb-04	0.0	0.0	0.0	0.0	100.0
22-Feb-04	283.8	111.2	179.7	112.8	60.5
23-Feb-04	0.0	0.0	0.0	0.0	100.0
24-Feb-04	0.0	0.0	0.0	0.0	100.0
25-Feb-04	282.7	280.0	280.4	279.6	0.1
26-Feb-04	285.3	271.9	277.0	265.4	3.3
27-Feb-04	287.3	283.9	284.8	284.1	0.3
28-Feb-04	289.0	222.2	262.6	209.0	22.2
29-Feb-04	0.0	0.0	6.1	0.4	100.0
1-Mar-04	0.0	0.0	0.0	0.0	100.0
2-Mar-04	0.0	0.0	6.9	0.6	100.0
3-Mar-04	0.0	0.0	0.0	0.0	100.0
4-Mar-04	0.0	0.0	0.0	0.0	100.0
5-Mar-04	293.6	289.9	291.0	289.4	0.4
6-Mar-04	0.0	0.0	26.0	2.7	100.0
7-Mar-04	287.6	202.4	238.8	196.7	28.8
8-Mar-04	0.0	0.0	0.3	0.0	100.0
9-Mar-04	0.0	0.0	23.3	3.2	100.0
10-Mar-04	287.3	103.6	208.2	113.6	63.6

Table 34 – continued from previous page

	Temperature Before (K)		Temperature After (K)		
Date	Maximum	Mean	Maximum	Mean	%Cloud
11-Mar-04	290.5	286.1	287.3	286.6	0.4
12-Mar-04	278.6	60.6	235.6	74.8	78.1
13-Mar-04	287.6	251.6	281.1	242.1	11.4
14-Mar-04	0.0	0.0	0.2	0.0	100.0
15-Mar-04	292.6	239.2	241.5	224.1	17.2
16-Mar-04	0.0	0.0	4.2	0.4	100.0
17-Mar-04	0.0	0.0	0.0	0.0	100.0
18-Mar-04	0.0	0.0	0.0	0.0	100.0
19-Mar-04	285.5	0.3	115.4	12.7	99.9
20-Mar-04	293.3	13.2	16.3	9.5	95.5
21-Mar-04	0.0	0.0	0.0	0.0	100.0
22-Mar-04	287.2	270.4	282.1	259.1	4.5
23-Mar-04	291.2	288.4	288.6	287.5	0.1
24-Mar-04	293.8	2.2	21.0	4.7	99.2
25-Mar-04	0.0	0.0	16.9	3.2	100.0
26-Mar-04	0.0	0.0	0.0	0.0	100.0
27-Mar-04	291.2	0.8	1.6	0.6	99.7
28-Mar-04	297.0	25.4	106.3	46.4	91.4
29-Mar-04	0.0	0.0	0.0	0.0	100.0
30-Mar-04	0.0	0.0	0.0	0.0	100.0
31-Mar-04	0.0	0.0	22.0	3.0	100.0
1-Apr-04	289.9	158.3	153.3	123.1	44.5
2-Apr-04	286.4	1.6	60.5	12.2	99.4
3-Apr-04	291.9	149.3	227.3	147.0	47.9

Table 34 – continued from previous page

	Temperature Before (K)		Temperature After (K)		
Date	Maximum	Mean	Maximum	Mean	%Cloud
4-Apr-04	290.6	159.3	222.7	148.1	44.4
5-Apr-04	296.5	290.7	291.3	289.9	0.4
6-Apr-04	295.2	248.7	276.1	216.3	14.9
7-Apr-04	301.0	115.8	193.7	118.0	60.5
8-Apr-04	297.3	294.0	294.3	291.3	0.0
9-Apr-04	297.2	161.0	254.1	159.7	45.2
10-Apr-04	0.0	0.0	96.3	15.3	100.0
11-Apr-04	0.0	0.0	0.0	0.0	100.0
12-Apr-04	0.0	0.0	0.0	0.0	100.0
13-Apr-04	0.0	0.0	0.0	0.0	100.0
14-Apr-04	300.1	289.4	291.6	286.3	2.2
15-Apr-04	298.3	119.2	172.1	105.1	59.6
16-Apr-04	306.2	251.7	281.1	244.0	16.8
17-Apr-04	307.2	264.0	303.8	249.4	12.8
18-Apr-04	305.6	151.4	211.5	145.4	49.6
19-Apr-04	0.0	0.0	0.0	0.0	100.0
20-Apr-04	0.0	0.0	0.0	0.0	100.0
21-Apr-04	0.0	0.0	0.0	0.0	100.0
22-Apr-04	0.0	0.0	0.0	0.0	100.0
23-Apr-04	0.0	0.0	6.7	1.2	100.0
24-Apr-04	0.0	0.0	0.0	0.0	100.0
25-Apr-04	297.2	43.0	97.7	38.4	85.4
26-Apr-04	297.9	240.6	286.0	240.0	18.2
27-Apr-04	291.5	61.7	172.3	78.7	78.5

Table 34 – continued from previous page

	Temperature Before (K)		Temperature After (K)		
Date	Maximum	Mean	Maximum	Mean	%Cloud
28-Apr-04	302.1	297.9	297.7	296.1	0.1
29-Apr-04	291.9	4.9	79.9	18.7	98.3
30-Apr-04	301.7	79.5	124.6	82.9	73.3
1-May-04	0.0	0.0	2.8	0.2	100.0
2-May-04	0.0	0.0	2.9	0.4	100.0
3-May-04	297.7	292.0	292.7	291.5	0.0
21-May-04	296.0	1.4	30.5	5.8	99.5
22-May-04	0.0	0.0	0.0	0.0	100.0
23-May-04	0.0	0.0	0.5	0.0	100.0
24-May-04	294.0	30.7	125.1	58.8	89.4
25-May-04	0.0	0.0	2.0	0.1	100.0
26-May-04	294.1	28.9	118.3	35.9	90.1
27-May-04	300.9	81.8	200.6	84.1	72.6
28-May-04	307.5	300.4	300.7	298.0	0.0
29-May-04	308.2	294.1	300.1	292.0	2.3
30-May-04	0.0	0.0	2.3	0.2	100.0
31-May-04	302.2	296.8	298.0	296.5	0.0
1-Jun-04	310.8	296.1	303.8	285.5	2.0
2-Jun-04	299.2	176.1	258.9	185.8	40.4
3-Jun-04	304.1	93.8	191.1	98.8	68.7
4-Jun-04	301.5	104.9	146.3	93.2	64.6
5-Jun-04	303.3	49.1	88.5	51.2	83.6
6-Jun-04	304.2	97.2	197.6	76.8	67.6
7-Jun-04	304.8	194.7	281.7	203.1	35.5

Table 34 – continued from previous page

	Temperature Before (K)		Temperature After (K)		
Date	Maximum	Mean	Maximum	Mean	%Cloud
8-Jun-04	311.5	196.4	248.7	213.4	35.8
9-Jun-04	0.0	0.0	34.6	4.7	100.0
10-Jun-04	0.0	0.0	0.0	0.0	100.0
11-Jun-04	295.5	12.0	45.1	18.4	95.9
12-Jun-04	0.0	0.0	0.0	0.0	100.0
13-Jun-04	297.6	7.2	89.1	21.4	97.5
14-Jun-04	306.4	269.4	294.6	276.1	10.8
15-Jun-04	0.0	0.0	4.5	0.5	100.0
16-Jun-04	294.3	98.0	160.4	80.3	66.1
17-Jun-04	305.3	77.1	141.0	77.3	74.4
18-Jun-04	298.4	64.9	167.3	68.8	78.0
19-Jun-04	311.0	298.0	299.8	297.5	1.0
20-Jun-04	309.8	300.4	302.4	300.1	0.1
21-Jun-04	299.3	12.3	132.9	32.9	95.8
22-Jun-04	0.0	0.0	8.5	1.9	100.0
23-Jun-04	308.9	300.7	303.0	300.6	0.2
24-Jun-04	310.8	300.6	302.3	301.2	1.0
25-Jun-04	0.0	0.0	0.0	0.0	100.0
26-Jun-04	311.9	268.0	289.3	274.2	11.1
27-Jun-04	304.7	204.5	291.1	218.6	31.8
28-Jun-04	302.8	13.7	171.8	32.0	95.5
29-Jun-04	308.1	273.5	297.3	248.0	9.1
30-Jun-04	312.5	301.8	303.6	302.3	0.8
1-Jul-04	313.7	268.6	302.6	275.1	12.0

Table 34 – continued from previous page

	Temperature Before (K)		Temperature After (K)		
Date	Maximum	Mean	Maximum	Mean	%Cloud
2-Jul-04	302.4	190.6	252.1	204.4	36.2
3-Jul-04	0.0	0.0	0.0	0.0	100.0
4-Jul-04	297.8	73.4	214.5	88.4	75.2
5-Jul-04	310.6	217.0	261.4	232.4	28.3
6-Jul-04	304.2	195.1	265.9	186.5	35.0
7-Jul-04	303.7	102.9	193.2	109.9	65.4
8-Jul-04	303.1	114.1	127.7	91.6	61.7
9-Jul-04	298.7	3.4	30.3	8.8	98.9
10-Jul-04	0.0	0.0	11.1	3.3	100.0
11-Jul-04	294.5	6.1	53.5	20.8	97.9
12-Jul-04	306.5	105.3	189.9	105.4	65.1
13-Jul-04	307.8	239.5	291.3	222.1	20.9
14-Jul-04	309.0	251.3	286.2	254.5	16.4
15-Jul-04	312.1	301.4	304.6	298.7	0.3
16-Jul-04	306.0	249.6	276.4	236.7	17.1
17-Jul-04	306.9	244.3	282.2	238.4	18.7
18-Jul-04	294.8	14.2	20.9	10.4	95.2
19-Jul-04	309.8	257.5	294.5	265.1	14.7
20-Jul-04	299.8	119.2	257.9	148.8	59.9
21-Jul-04	0.0	0.0	0.0	0.0	100.0
22-Jul-04	303.9	192.6	277.5	214.4	35.7
23-Jul-04	303.8	111.8	225.4	119.8	62.4
24-Jul-04	302.3	17.2	105.6	31.5	94.2
25-Jul-04	0.0	0.0	2.1	0.3	100.0

Table 34 – continued from previous page

	Temperature Before (K)		Temperature After (K)		
Date	Maximum	Mean	Maximum	Mean	%Cloud
26-Jul-04	0.0	0.0	0.0	0.0	100.0
27-Jul-04	293.1	13.3	89.3	47.2	95.5
28-Jul-04	311.2	302.3	304.9	301.8	0.0
29-Jul-04	0.0	0.0	1.6	0.1	100.0
30-Jul-04	0.0	0.0	0.0	0.0	100.0
31-Jul-04	303.5	130.0	201.9	117.5	56.4
1-Aug-04	304.5	165.3	238.2	172.0	44.8
2-Aug-04	310.3	283.2	299.4	279.4	6.5
3-Aug-04	300.2	50.7	164.6	72.8	82.9
4-Aug-04	296.8	11.7	18.3	7.7	96.0
5-Aug-04	305.2	289.3	296.1	288.3	2.9
6-Aug-04	309.9	299.0	301.3	297.9	0.2
7-Aug-04	309.5	297.1	298.1	296.7	0.9
8-Aug-04	304.4	76.9	149.9	95.7	74.1
9-Aug-04	304.8	89.3	131.1	79.4	70.0
10-Aug-04	302.2	253.9	291.9	248.3	14.4
11-Aug-04	294.0	13.5	34.8	17.9	95.4
12-Aug-04	296.3	64.6	154.4	70.8	77.8
13-Aug-04	302.2	131.1	181.5	110.1	55.7
14-Aug-04	292.2	16.1	76.0	36.2	94.4
15-Aug-04	309.3	272.6	287.7	276.1	9.1
16-Aug-04	297.8	43.5	102.5	51.9	85.1
17-Aug-04	304.3	181.0	267.0	195.3	39.5
18-Aug-04	302.4	12.5	118.7	29.4	95.8

Table 34 – continued from previous page

	Temperature Before (K)		Temperature After (K)		
Date	Maximum	Mean	Maximum	Mean	%Cloud
19-Aug-04	298.8	74.5	247.5	99.5	74.9
20-Aug-04	0.0	0.0	0.0	0.0	100.0
21-Aug-04	303.9	296.5	297.4	296.8	0.7
22-Aug-04	310.0	299.7	300.8	299.9	0.8
23-Aug-04	307.4	246.1	271.3	250.9	18.1
24-Aug-04	299.1	14.9	69.9	31.5	95.0
25-Aug-04	0.0	0.0	8.9	1.3	100.0
26-Aug-04	0.0	0.0	0.0	0.0	100.0
27-Aug-04	293.6	1.1	24.1	3.9	99.6
28-Aug-04	293.7	4.0	69.9	10.7	98.6
29-Aug-04	0.0	0.0	17.5	1.2	100.0
30-Aug-04	300.3	72.6	138.9	91.9	75.4
31-Aug-04	308.4	278.6	297.8	274.7	7.4
1-Sep-04	307.7	219.0	252.9	226.5	26.7
2-Sep-04	306.9	296.8	299.4	298.1	1.4
3-Sep-04	300.7	38.1	77.8	46.8	87.1
4-Sep-04	298.4	1.7	60.3	18.1	99.4
5-Sep-04	309.3	208.7	239.7	222.4	30.9
6-Sep-04	301.6	42.9	238.0	74.7	85.7
7-Sep-04	304.5	199.8	270.0	180.6	33.1
8-Sep-04	0.0	0.0	11.8	0.5	100.0
9-Sep-04	300.4	66.9	94.8	73.3	77.4
10-Sep-04	309.6	303.3	304.4	303.0	0.0
11-Sep-04	299.2	57.2	145.9	69.2	80.7

Table 34 – continued from previous page

	Temperature Before (K)		Temperature After (K)		
Date	Maximum	Mean	Maximum	Mean	%Cloud
12-Sep-04	309.3	183.4	230.3	204.1	39.1
13-Sep-04	300.8	139.9	269.9	147.5	53.1
14-Sep-04	306.5	81.5	165.4	92.7	72.9
15-Sep-04	301.5	75.1	216.7	110.4	74.9
16-Sep-04	0.0	0.0	0.0	0.0	100.0
17-Sep-04	301.7	241.4	295.6	237.5	18.6
18-Sep-04	302.8	160.6	292.8	172.9	45.6
19-Sep-04	306.7	301.5	302.6	301.5	0.2
20-Sep-04	304.5	301.2	301.6	300.8	0.0
21-Sep-04	309.6	304.9	305.2	304.2	0.0
22-Sep-04	307.6	304.2	305.0	304.1	0.0
23-Sep-04	309.7	303.4	304.1	303.1	0.7
24-Sep-04	0.0	0.0	4.7	1.0	100.0
25-Sep-04	302.5	59.7	222.3	76.4	79.7
26-Sep-04	302.2	172.7	274.4	172.3	42.0
27-Sep-04	302.1	229.3	276.5	228.0	23.4
28-Sep-04	305.3	299.1	300.6	298.6	0.7
29-Sep-04	296.1	111.6	261.8	120.3	61.9
30-Sep-04	302.5	234.3	273.2	230.0	21.1
1-Oct-04	302.0	102.7	113.2	81.9	65.4
2-Oct-04	0.0	0.0	0.5	0.1	100.0
3-Oct-04	300.3	297.4	298.0	297.1	0.0
4-Oct-04	299.2	145.3	255.3	147.3	50.9
5-Oct-04	299.6	295.2	296.2	295.0	0.4

Table 34 – continued from previous page

	Temperature Before (K)		Temperature After (K)		
Date	Maximum	Mean	Maximum	Mean	%Cloud
6-Oct-04	300.8	298.1	298.0	296.9	0.0
7-Oct-04	301.2	157.3	222.2	149.9	46.5
8-Oct-04	0.0	0.0	0.0	0.0	100.0
9-Oct-04	295.6	19.4	42.2	15.1	93.4
10-Oct-04	298.9	284.7	295.4	284.8	3.7
11-Oct-04	295.0	22.2	80.2	27.7	92.3
12-Oct-04	295.8	3.4	36.4	4.5	98.9
13-Oct-04	0.0	0.0	2.2	0.4	100.0
14-Oct-04	0.0	0.0	0.0	0.0	100.0
15-Oct-04	0.0	0.0	0.0	0.0	100.0
16-Oct-04	0.0	0.0	4.0	0.9	100.0
17-Oct-04	290.8	280.4	288.7	264.6	2.9
18-Oct-04	0.0	0.0	0.0	0.0	100.0
19-Oct-04	0.0	0.0	0.0	0.0	100.0
20-Oct-04	0.0	0.0	0.0	0.0	100.0
21-Oct-04	293.2	29.1	32.4	17.7	90.0
22-Oct-04	295.5	268.1	284.3	251.7	8.5
23-Oct-04	0.0	0.0	0.0	0.0	100.0
24-Oct-04	294.6	292.7	293.0	292.6	0.0
25-Oct-04	298.2	295.6	296.1	295.7	0.2
26-Oct-04	0.0	0.0	0.0	0.0	100.0
27-Oct-04	0.0	0.0	0.0	0.0	100.0
28-Oct-04	291.1	36.6	126.2	38.8	87.3
29-Oct-04	294.9	7.0	95.9	18.2	97.6

Table 34 – continued from previous page

	Temperature Before (K)		Temperature After (K)		
Date	Maximum	Mean	Maximum	Mean	%Cloud
30-Oct-04	299.0	296.1	296.8	296.2	0.1
31-Oct-04	0.0	0.0	0.5	0.0	100.0
1-Nov-04	0.0	0.0	6.9	1.8	100.0
2-Nov-04	0.0	0.0	0.0	0.0	100.0
3-Nov-04	0.0	0.0	0.0	0.0	100.0
4-Nov-04	0.0	0.0	0.0	0.0	100.0
5-Nov-04	287.9	275.5	283.7	278.2	3.6
6-Nov-04	291.9	290.2	290.4	290.1	0.0
7-Nov-04	292.5	254.8	287.7	263.6	11.9
8-Nov-04	287.7	104.0	111.7	87.4	63.4
9-Nov-04	286.1	239.6	262.5	241.6	15.5
10-Nov-04	289.4	48.8	82.2	45.0	83.0
11-Nov-04	0.0	0.0	0.0	0.0	100.0
12-Nov-04	283.2	111.9	242.3	150.1	60.0
13-Nov-04	284.8	283.1	283.4	283.1	0.0
14-Nov-04	282.0	105.3	135.0	98.6	62.3
15-Nov-04	0.0	0.0	0.0	0.0	100.0
16-Nov-04	0.0	0.0	0.0	0.0	100.0
17-Nov-04	0.0	0.0	0.0	0.0	100.0
18-Nov-04	0.0	0.0	3.0	0.3	100.0
19-Nov-04	0.0	0.0	3.9	0.3	100.0
20-Nov-04	0.0	0.0	0.0	0.0	100.0
21-Nov-04	0.0	0.0	29.7	5.0	100.0
22-Nov-04	284.9	2.4	14.6	2.7	99.1

Table 34 – continued from previous page

	Temperature Before (K)		Temperature After (K)		
Date	Maximum	Mean	Maximum	Mean	%Cloud
23-Nov-04	0.0	0.0	0.0	0.0	100.0
24-Nov-04	268.6	63.3	159.7	61.7	75.9
25-Nov-04	280.5	244.4	270.2	230.4	12.4
26-Nov-04	0.0	0.0	0.0	0.0	100.0
27-Nov-04	0.0	0.0	0.0	0.0	100.0
28-Nov-04	0.0	0.0	0.0	0.0	100.0
29-Nov-04	252.9	1.7	2.7	1.3	99.3
30-Nov-04	0.0	0.0	0.0	0.0	100.0
1-Dec-04	281.2	279.0	277.9	267.0	0.2
2-Dec-04	282.6	281.2	281.2	281.0	0.0
3-Dec-04	282.3	203.4	272.4	209.6	27.5
4-Dec-04	280.6	111.2	135.6	73.0	60.1
5-Dec-04	283.9	136.7	259.1	184.9	51.5
6-Dec-04	0.0	0.0	0.0	0.0	100.0
7-Dec-04	288.4	23.0	32.6	19.9	91.7
8-Dec-04	285.4	235.0	279.4	235.6	17.0
9-Dec-04	0.0	0.0	0.0	0.0	100.0
10-Dec-04	0.0	0.0	0.9	0.1	100.0
11-Dec-04	0.0	0.0	0.0	0.0	100.0
12-Dec-04	0.0	0.0	0.1	0.0	100.0
13-Dec-04	0.0	0.0	0.5	0.0	100.0
14-Dec-04	273.7	48.8	86.6	39.1	82.1
15-Dec-04	276.5	267.2	272.1	255.8	2.7
16-Dec-04	0.0	0.0	0.0	0.0	100.0

Table 34 – continued from previous page

	Temperature Before (K)		Temperature After (K)		
Date	Maximum	Mean	Maximum	Mean	%Cloud
17-Dec-04	279.1	225.9	249.7	202.8	18.6
18-Dec-04	0.0	0.0	16.2	3.7	100.0
19-Dec-04	267.0	45.5	91.8	56.6	82.8
20-Dec-04	0.0	0.0	0.0	0.0	100.0
21-Dec-04	279.9	162.0	229.6	159.8	41.8
22-Dec-04	0.0	0.0	0.0	0.0	100.0
23-Dec-04	267.0	238.5	236.2	208.7	9.7
24-Dec-04	0.0	0.0	0.0	0.0	100.0
25-Dec-04	0.0	0.0	0.0	0.0	100.0
26-Dec-04	265.8	1.5	149.7	32.7	99.4
27-Dec-04	262.9	55.4	165.7	60.1	78.8
28-Dec-04	0.0	0.0	16.0	1.9	100.0
29-Dec-04	276.7	33.6	159.9	52.8	87.8
30-Dec-04	0.0	0.0	0.0	0.0	100.0
31-Dec-04	0.0	0.0	0.0	0.0	100.0
1-Jan-05	0.0	0.0	0.0	0.0	100.0
2-Jan-05	0.0	0.0	0.6	0.0	100.0
3-Jan-05	0.0	0.0	0.0	0.0	100.0
4-Jan-05	0.0	0.0	0.0	0.0	100.0
5-Jan-05	0.0	0.0	0.0	0.0	100.0
6-Jan-05	0.0	0.0	0.0	0.0	100.0
7-Jan-05	0.0	0.0	0.0	0.0	100.0
8-Jan-05	0.0	0.0	0.0	0.0	100.0
9-Jan-05	275.1	27.7	38.1	21.5	89.9

Table 34 – continued from previous page

	Temperature Before (K)		Temperature After (K)		
Date	Maximum	Mean	Maximum	Mean	%Cloud
10-Jan-05	0.0	0.0	0.0	0.0	100.0
11-Jan-05	0.0	0.0	0.2	0.0	100.0
12-Jan-05	0.0	0.0	0.0	0.0	100.0
13-Jan-05	0.0	0.0	1.3	0.1	100.0
14-Jan-05	275.2	90.5	163.6	84.9	67.0
15-Jan-05	275.1	66.9	86.3	51.4	75.6
16-Jan-05	263.9	9.2	62.8	15.7	96.5
17-Jan-05	266.8	209.3	230.9	192.8	20.4
18-Jan-05	265.7	105.2	198.1	117.9	59.8
19-Jan-05	0.0	0.0	0.0	0.0	100.0
20-Jan-05	0.0	0.0	5.0	0.4	100.0
22-Jan-05	0.0	0.0	0.0	0.0	100.0
23-Jan-05	266.8	210.9	229.2	210.5	20.4
24-Jan-05	273.6	147.2	179.6	113.4	45.8
25-Jan-05	277.3	168.1	236.1	164.8	38.9
26-Jan-05	0.0	0.0	0.0	0.0	100.0
27-Jan-05	273.0	11.0	151.3	25.9	95.9
28-Jan-05	0.0	0.0	0.0	0.0	100.0
29-Jan-05	0.0	0.0	9.5	1.2	100.0
30-Jan-05	277.1	22.6	178.2	42.7	91.8
31-Jan-05	0.0	0.0	0.0	0.0	100.0
1-Feb-05	280.0	174.0	229.4	170.9	37.3
2-Feb-05	0.0	0.0	0.0	0.0	100.0
3-Feb-05	282.5	239.7	270.5	229.0	14.3

Table 34 – continued from previous page

	Temperature Before (K)		Temperature After (K)		
Date	Maximum	Mean	Maximum	Mean	%Cloud
4-Feb-05	284.0	181.4	277.3	172.1	35.7
5-Feb-05	286.4	283.0	283.6	274.9	0.1
6-Feb-05	0.0	0.0	0.0	0.0	100.0
7-Feb-05	0.0	0.0	0.0	0.0	100.0
8-Feb-05	0.0	0.0	0.0	0.0	100.0
9-Feb-05	262.5	7.7	13.4	6.3	97.1
10-Feb-05	0.0	0.0	0.0	0.0	100.0
11-Feb-05	276.8	21.4	183.7	35.4	92.2
12-Feb-05	284.1	72.9	238.9	102.2	74.1
13-Feb-05	0.0	0.0	0.0	0.0	100.0
14-Feb-05	0.0	0.0	0.0	0.0	100.0
15-Feb-05	291.8	188.7	280.6	199.6	34.7
16-Feb-05	280.3	5.0	17.5	7.3	98.2
17-Feb-05	278.8	121.8	165.3	118.3	55.9
18-Feb-05	278.0	26.2	144.8	46.9	90.5
19-Feb-05	282.3	109.9	222.4	128.1	60.6
20-Feb-05	0.0	0.0	0.0	0.0	100.0
21-Feb-05	0.0	0.0	0.0	0.0	100.0
22-Feb-05	0.0	0.0	0.0	0.0	100.0
23-Feb-05	0.0	0.0	0.0	0.0	100.0
24-Feb-05	0.0	0.0	2.3	0.3	100.0
25-Feb-05	0.0	0.0	0.0	0.0	100.0
26-Feb-05	286.2	246.6	278.1	248.5	13.0
27-Feb-05	0.0	0.0	0.0	0.0	100.0

Table 34 – continued from previous page

	Temperature Before (K)		Temperature After (K)		
Date	Maximum	Mean	Maximum	Mean	%Cloud
28-Feb-05	0.0	0.0	0.2	0.0	100.0
1-Mar-05	0.0	0.0	0.0	0.0	100.0
2-Mar-05	280.4	142.7	201.4	129.7	48.5
3-Mar-05	283.5	280.0	280.7	280.0	0.2
4-Mar-05	0.0	0.0	0.0	0.0	100.0
5-Mar-05	0.0	0.0	0.0	0.0	100.0
6-Mar-05	287.8	45.2	166.9	63.9	84.2
7-Mar-05	0.0	0.0	0.0	0.0	100.0
8-Mar-05	0.0	0.0	4.0	0.4	100.0
9-Mar-05	283.2	11.7	78.7	28.3	95.8
10-Mar-05	0.0	0.0	0.0	0.0	100.0
11-Mar-05	0.0	0.0	0.0	0.0	100.0
12-Mar-05	0.0	0.0	0.0	0.0	100.0
13-Mar-05	281.0	18.9	25.5	14.9	93.2
14-Mar-05	286.6	53.4	217.3	80.2	81.3
15-Mar-05	284.2	257.9	282.4	259.5	8.7
16-Mar-05	291.3	250.8	269.4	249.1	12.5
17-Mar-05	291.8	118.4	225.7	134.4	59.2
18-Mar-05	0.0	0.0	25.9	7.1	100.0
19-Mar-05	272.6	6.4	10.9	4.3	97.6
20-Mar-05	0.0	0.0	0.0	0.0	100.0
21-Mar-05	283.1	0.5	9.2	1.4	99.8
22-Mar-05	0.0	0.0	0.0	0.0	100.0
23-Mar-05	0.0	0.0	0.1	0.0	100.0

Table 34 – continued from previous page

	Temperature Before (K)		Temperature After (K)		
Date	Maximum	Mean	Maximum	Mean	%Cloud
24-Mar-05	290.5	287.8	288.2	287.6	0.0
25-Mar-05	0.0	0.0	0.0	0.0	100.0
26-Mar-05	0.0	0.0	0.0	0.0	100.0
27-Mar-05	0.0	0.0	0.0	0.0	100.0
28-Mar-05	289.5	27.9	159.0	33.9	90.2
29-Mar-05	296.6	246.8	273.3	243.7	15.5
30-Mar-05	300.1	229.6	286.5	244.2	22.3
31-Mar-05	0.0	0.0	13.0	1.0	100.0
1-Apr-05	0.0	0.0	0.0	0.0	100.0
2-Apr-05	285.0	23.9	163.8	44.1	91.6
3-Apr-05	297.9	262.2	278.6	260.9	10.6
4-Apr-05	301.5	298.7	299.0	298.3	0.0
5-Apr-05	302.8	101.5	192.4	119.0	66.0
6-Apr-05	0.0	0.0	0.0	0.0	100.0
7-Apr-05	0.0	0.0	0.0	0.0	100.0
8-Apr-05	299.8	294.5	295.5	294.5	0.1
9-Apr-05	299.2	221.5	278.8	224.6	24.7
10-Apr-05	307.1	239.1	261.3	228.4	20.5
11-Apr-05	0.0	0.0	0.0	0.0	100.0
12-Apr-05	0.0	0.0	0.0	0.0	100.0
13-Apr-05	289.8	0.3	140.1	29.9	99.9
14-Apr-05	299.5	281.1	290.2	270.6	4.5
15-Apr-05	303.6	297.4	299.1	297.4	0.2
16-Apr-05	303.8	300.3	301.5	300.2	0.0

Table 34 – continued from previous page

	Temperature Before (K)		Temperature After (K)		
Date	Maximum	Mean	Maximum	Mean	%Cloud
17-Apr-05	308.2	275.8	295.5	271.6	8.5
18-Apr-05	306.5	303.3	304.0	303.3	0.0
19-Apr-05	308.0	212.8	255.6	208.3	29.6
20-Apr-05	303.4	65.2	250.5	110.1	78.2
21-Apr-05	0.0	0.0	0.0	0.0	100.0
22-Apr-05	0.0	0.0	0.0	0.0	100.0
23-Apr-05	0.0	0.0	0.3	0.0	100.0
24-Apr-05	283.5	1.1	92.5	13.3	99.6
25-Apr-05	295.9	287.8	289.6	288.6	0.6
26-Apr-05	0.0	0.0	0.0	0.0	100.0
27-Apr-05	286.1	15.2	52.7	24.8	94.6
28-Apr-05	0.0	0.0	0.0	0.0	100.0
29-Apr-05	0.0	0.0	0.0	0.0	100.0
30-Apr-05	291.9	8.4	65.1	11.4	97.1
1-May-05	292.4	54.6	171.4	64.8	81.1
2-May-05	0.0	0.0	6.9	2.9	100.0
3-May-05	297.3	257.0	270.9	250.1	11.9
4-May-05	299.4	294.1	295.5	293.9	0.4
5-May-05	306.0	227.2	274.7	215.1	24.2
6-May-05	305.7	295.8	300.2	294.3	1.8
7-May-05	295.0	1.1	66.2	12.5	99.6
8-May-05	308.3	212.4	285.9	221.6	29.4
9-May-05	300.5	27.6	172.2	46.2	90.7
10-May-05	312.3	300.3	303.3	300.5	1.8

Table 34 – continued from previous page

	Temperature Before (K)		Temperature After (K)		
Date	Maximum	Mean	Maximum	Mean	%Cloud
11-May-05	302.5	15.7	129.9	29.2	94.8
12-May-05	296.2	6.4	37.6	8.7	97.8
13-May-05	302.8	232.8	286.9	227.5	22.3
14-May-05	0.0	0.0	0.0	0.0	100.0
15-May-05	0.0	0.0	0.0	0.0	100.0
16-May-05	292.0	3.6	27.4	5.9	98.8
17-May-05	299.4	116.9	156.3	113.0	60.1
18-May-05	298.1	117.2	252.1	117.9	60.2
19-May-05	0.0	0.0	0.0	0.0	100.0
20-May-05	295.1	1.7	51.2	11.6	99.4
21-May-05	0.0	0.0	13.8	2.8	100.0
22-May-05	305.3	292.2	298.7	293.4	2.5
23-May-05	304.4	155.4	251.4	155.6	48.1
24-May-05	304.6	251.8	279.9	242.4	15.7
25-May-05	300.3	125.4	215.4	119.0	57.8
26-May-05	304.7	25.2	96.6	38.1	91.6
27-May-05	303.2	151.1	238.6	152.6	49.5
28-May-05	307.6	137.3	152.8	126.0	54.2
29-May-05	310.7	300.7	304.4	299.8	1.5
30-May-05	0.0	0.0	16.5	2.4	100.0
31-May-05	311.9	295.6	301.1	295.1	2.9
1-Jun-05	0.0	0.0	0.0	0.0	100.0
2-Jun-05	0.0	0.0	0.0	0.0	100.0
3-Jun-05	0.0	0.0	21.9	3.3	100.0

Table 34 – continued from previous page

	Temperature Before (K)		Temperature After (K)		
Date	Maximum	Mean	Maximum	Mean	%Cloud
4-Jun-05	309.4	126.4	205.0	122.0	58.4
5-Jun-05	309.1	204.3	265.7	184.6	33.2
6-Jun-05	313.5	199.9	292.8	224.8	35.2
7-Jun-05	312.0	38.8	130.0	53.5	87.3
8-Jun-05	302.5	1.7	61.8	16.3	99.4
9-Jun-05	311.3	15.1	98.2	26.1	95.1
10-Jun-05	0.0	0.0	11.9	2.8	100.0
11-Jun-05	0.0	0.0	0.6	0.0	100.0
12-Jun-05	270.1	16.5	20.2	9.6	93.8
13-Jun-05	309.4	242.2	289.5	244.7	20.5
14-Jun-05	308.1	301.6	300.7	287.7	0.6
15-Jun-05	304.4	55.3	183.5	71.7	81.5
16-Jun-05	308.7	301.3	302.8	301.1	0.0
17-Jun-05	309.5	297.9	300.4	296.8	1.4
18-Jun-05	302.0	50.7	70.3	43.5	83.0
19-Jun-05	298.1	12.7	173.8	25.0	95.7
20-Jun-05	309.3	96.6	181.3	125.1	68.0
21-Jun-05	307.0	205.9	282.7	205.9	32.1
22-Jun-05	315.1	173.8	288.7	176.4	43.8
23-Jun-05	313.5	307.1	307.8	306.6	0.2
24-Jun-05	305.9	68.7	241.9	92.9	77.4
25-Jun-05	312.4	251.9	298.0	245.8	18.4
26-Jun-05	305.5	86.6	202.1	93.0	71.4
27-Jun-05	313.0	165.8	184.9	138.5	46.3

Table 34 – continued from previous page

	Temperature Before (K)		Temperature After (K)		
Date	Maximum	Mean	Maximum	Mean	%Cloud
28-Jun-05	296.8	18.7	86.8	30.1	93.7
29-Jun-05	306.6	88.1	209.3	117.4	71.0
30-Jun-05	297.5	27.2	92.6	36.1	90.8
1-Jul-05	308.4	14.1	187.9	47.5	95.3
2-Jul-05	310.0	233.1	259.0	234.6	22.6
3-Jul-05	311.8	248.9	284.4	250.1	18.2
4-Jul-05	301.7	8.2	84.6	17.9	97.3
5-Jul-05	0.0	0.0	25.0	6.0	100.0
6-Jul-05	312.9	236.1	285.3	231.9	22.9
7-Jul-05	293.1	2.2	62.8	12.5	99.2
8-Jul-05	313.4	194.6	267.3	210.4	36.3
9-Jul-05	311.8	61.6	260.5	95.6	79.6
10-Jul-05	309.7	132.3	243.2	153.4	56.2
11-Jul-05	0.0	0.0	0.0	0.0	100.0
12-Jul-05	0.0	0.0	0.0	0.0	100.0
13-Jul-05	0.0	0.0	0.0	0.0	100.0
14-Jul-05	0.0	0.0	0.0	0.0	100.0
15-Jul-05	297.8	2.0	10.1	2.5	99.3
16-Jul-05	279.8	2.1	8.8	2.7	99.2
17-Jul-05	0.0	0.0	2.7	0.2	100.0
18-Jul-05	303.4	115.7	204.2	130.2	61.4
19-Jul-05	306.5	111.3	238.3	146.7	63.0
20-Jul-05	303.2	89.0	188.7	115.7	70.3
21-Jul-05	304.5	183.5	253.6	195.4	38.7

Table 34 – continued from previous page

	Temperature Before (K)		Temperature After (K)		
Date	Maximum	Mean	Maximum	Mean	%Cloud
22-Jul-05	313.2	226.7	280.3	217.0	25.3
23-Jul-05	302.2	166.2	279.8	172.6	44.7
24-Jul-05	305.3	172.9	275.0	178.7	42.5
25-Jul-05	310.9	231.7	297.8	244.7	24.1
26-Jul-05	304.3	184.9	286.7	202.5	38.7
27-Jul-05	303.5	79.7	189.6	79.6	73.1
28-Jul-05	302.5	104.0	218.5	113.5	65.0
29-Jul-05	313.3	303.9	306.5	303.3	0.0
30-Jul-05	302.9	263.3	296.2	269.3	12.0
31-Jul-05	314.7	305.5	305.6	304.5	0.1
1-Aug-05	310.9	287.6	300.9	291.7	5.5
2-Aug-05	315.8	305.9	305.5	304.8	0.5
3-Aug-05	315.3	291.0	304.5	293.7	4.9
4-Aug-05	303.7	141.6	280.0	146.9	52.9
5-Aug-05	0.0	0.0	0.0	0.0	100.0
6-Aug-05	0.0	0.0	0.0	0.0	100.0
7-Aug-05	310.7	250.3	289.2	250.1	17.5
8-Aug-05	299.3	58.6	240.1	81.0	80.3
9-Aug-05	311.4	274.6	296.8	278.7	9.9
10-Aug-05	301.7	28.7	201.9	60.3	90.4
11-Aug-05	303.7	183.1	267.7	160.3	39.2
12-Aug-05	308.5	245.2	300.6	254.0	19.4
13-Aug-05	299.0	12.7	157.1	48.6	95.7
14-Aug-05	0.0	0.0	0.1	0.0	100.0

Table 34 – continued from previous page

	Temperature Before (K)		Temperature After (K)		
Date	Maximum	Mean	Maximum	Mean	%Cloud
15-Aug-05	0.0	0.0	0.0	0.0	100.0
16-Aug-05	0.0	0.0	0.3	0.0	100.0
17-Aug-05	308.3	288.0	299.6	282.3	4.4
18-Aug-05	0.0	0.0	0.0	0.0	100.0
19-Aug-05	302.3	44.9	246.8	83.5	84.7
20-Aug-05	302.2	82.4	160.0	67.6	72.5
21-Aug-05	315.0	305.7	308.5	305.1	0.0
22-Aug-05	307.7	300.5	302.1	299.7	0.0
23-Aug-05	305.8	227.2	280.9	225.5	23.3
24-Aug-05	306.9	270.2	299.0	270.0	9.1
25-Aug-05	313.5	303.1	304.3	303.0	0.6
26-Aug-05	0.0	0.0	0.2	0.0	100.0
27-Aug-05	302.3	16.4	57.6	19.9	94.5
28-Aug-05	310.2	173.6	217.3	155.4	41.7
29-Aug-05	296.6	5.0	13.5	3.9	98.3
30-Aug-05	0.0	0.0	0.0	0.0	100.0
31-Aug-05	301.9	290.8	293.7	285.9	2.0
1-Sep-05	308.4	267.1	299.7	267.8	11.4
2-Sep-05	308.9	302.5	304.3	302.2	0.0
3-Sep-05	310.9	301.7	303.1	301.5	0.3
4-Sep-05	309.6	301.8	303.7	301.5	0.1
5-Sep-05	305.3	290.5	298.5	283.7	3.2
6-Sep-05	310.6	302.1	301.9	301.2	0.4
7-Sep-05	305.4	266.3	287.4	253.9	11.4

Table 34 – continued from previous page

	Temperature Before (K)		Temperature After (K)		
Date	Maximum	Mean	Maximum	Mean	%Cloud
8-Sep-05	307.1	240.3	280.4	238.7	20.5
9-Sep-05	304.1	170.3	263.9	200.3	43.3
10-Sep-05	308.8	277.7	300.5	281.5	8.2
11-Sep-05	309.5	304.0	305.3	303.8	0.0
12-Sep-05	310.7	284.3	303.2	288.4	6.7
13-Sep-05	309.7	304.4	305.8	304.1	0.0
14-Sep-05	0.0	0.0	6.2	0.8	100.0
15-Sep-05	0.0	0.0	0.0	0.0	100.0
16-Sep-05	0.0	0.0	7.7	1.1	100.0
17-Sep-05	304.7	188.1	274.1	194.0	36.9
18-Sep-05	302.3	216.2	252.1	199.3	27.2
19-Sep-05	298.0	123.8	201.9	110.0	58.0
20-Sep-05	0.0	0.0	0.0	0.0	100.0
21-Sep-05	302.8	73.9	260.1	90.6	75.4
22-Sep-05	305.4	287.9	300.9	267.7	4.5
23-Sep-05	0.0	0.0	0.0	0.0	100.0
24-Sep-05	293.6	1.7	4.2	1.4	99.4
25-Sep-05	0.0	0.0	0.0	0.0	100.0
26-Sep-05	0.0	0.0	11.4	1.5	100.0
27-Sep-05	302.9	299.2	299.6	298.9	0.0
28-Sep-05	304.1	299.1	299.9	299.3	0.3
29-Sep-05	298.0	293.9	294.5	293.7	0.0
30-Sep-05	299.0	294.4	295.4	294.6	0.3
1-Oct-05	304.1	299.3	300.2	294.3	0.1

Table 34 – continued from previous page

	Temperature Before (K)		Temperature After (K)		
Date	Maximum	Mean	Maximum	Mean	%Cloud
2-Oct-05	0.0	0.0	15.0	4.5	100.0
3-Oct-05	306.5	299.5	299.3	280.3	0.9
4-Oct-05	304.4	289.8	301.8	284.9	4.0
5-Oct-05	307.1	294.7	302.1	298.0	2.7
6-Oct-05	300.3	187.6	234.6	154.0	36.7
7-Oct-05	296.5	229.3	273.9	237.4	21.6
8-Oct-05	293.8	23.3	168.5	39.2	92.0
9-Oct-05	293.1	144.5	252.0	150.0	50.2
10-Oct-05	288.3	0.3	1.5	0.3	99.9
11-Oct-05	0.0	0.0	0.0	0.0	100.0
12-Oct-05	0.0	0.0	0.0	0.0	100.0
13-Oct-05	294.6	5.3	30.5	8.2	98.2
14-Oct-05	300.4	292.5	296.3	293.9	1.4
15-Oct-05	299.9	296.5	297.1	296.4	0.1
16-Oct-05	295.1	125.7	261.3	122.5	57.1
17-Oct-05	298.0	177.7	285.3	197.2	39.6
18-Oct-05	300.1	297.4	298.6	297.2	0.0
19-Oct-05	300.9	233.7	292.1	254.5	20.9
20-Oct-05	0.0	0.0	0.0	0.0	100.0
21-Oct-05	0.0	0.0	0.0	0.0	100.0
22-Oct-05	289.0	50.0	154.8	51.3	82.6
23-Oct-05	0.0	0.0	0.0	0.0	100.0
24-Oct-05	0.0	0.0	10.0	1.9	100.0
25-Oct-05	283.3	1.3	50.4	12.6	99.5

Table 34 – continued from previous page

	Temperature Before (K)		Temperature After (K)		
Date	Maximum	Mean	Maximum	Mean	%Cloud
26-Oct-05	0.0	0.0	78.6	11.0	100.0
27-Oct-05	279.6	0.5	9.8	2.1	99.8
28-Oct-05	287.7	99.8	177.6	106.1	65.1
29-Oct-05	291.0	289.4	289.9	289.3	0.0
30-Oct-05	289.1	220.4	263.1	214.5	22.9
31-Oct-05	0.0	0.0	15.4	5.2	100.0
1-Nov-05	287.5	16.8	28.1	16.0	94.1
2-Nov-05	292.6	290.6	290.8	290.5	0.0
3-Nov-05	289.3	60.9	77.8	36.9	78.6
4-Nov-05	293.9	214.6	239.2	181.3	25.9
5-Nov-05	0.0	0.0	15.4	1.6	100.0
6-Nov-05	287.1	4.9	23.8	5.3	98.3
7-Nov-05	0.0	0.0	0.1	0.0	100.0
8-Nov-05	291.5	0.8	10.6	1.2	99.7
9-Nov-05	0.0	0.0	1.8	0.1	100.0
10-Nov-05	285.3	213.3	276.0	219.8	24.6
11-Nov-05	286.3	129.0	214.5	137.1	54.6
12-Nov-05	292.6	290.7	291.1	290.6	0.1
13-Nov-05	291.7	133.3	228.6	130.8	54.0
14-Nov-05	287.4	232.8	261.3	210.4	18.5
16-Nov-05	0.0	0.0	0.0	0.0	100.0
17-Nov-05	275.2	26.9	117.5	52.6	90.2
18-Nov-05	280.0	163.3	231.4	159.5	41.1
19-Nov-05	281.1	1.1	110.1	27.6	99.6

Table 34 – continued from previous page

	Temperature Before (K)		Temperature After (K)		
Date	Maximum	Mean	Maximum	Mean	%Cloud
20-Nov-05	286.9	239.1	278.1	219.0	15.9
21-Nov-05	0.0	0.0	0.0	0.0	100.0
22-Nov-05	0.0	0.0	2.7	0.6	100.0
23-Nov-05	0.0	0.0	0.0	0.0	100.0
24-Nov-05	277.3	99.1	186.0	92.6	64.0
25-Nov-05	277.0	102.5	136.2	88.6	62.8
26-Nov-05	0.0	0.0	0.0	0.0	100.0
27-Nov-05	262.9	39.5	81.8	29.3	84.8
28-Nov-05	0.0	0.0	2.0	0.2	100.0
29-Nov-05	0.0	0.0	0.0	0.0	100.0
30-Nov-05	277.6	21.1	102.6	28.4	92.3
1-Dec-05	257.3	0.5	17.5	5.1	99.8
2-Dec-05	273.4	44.0	112.5	51.6	83.7
3-Dec-05	0.0	0.0	0.0	0.0	100.0
4-Dec-05	0.0	0.0	0.0	0.0	100.0
5-Dec-05	271.4	14.8	90.8	22.7	94.5
6-Dec-05	267.3	1.8	52.7	5.8	99.3
7-Dec-05	272.6	124.0	180.1	120.3	54.3
8-Dec-05	0.0	0.0	0.0	0.0	100.0
9-Dec-05	0.0	0.0	0.0	0.0	100.0
10-Dec-05	269.8	108.2	156.0	103.2	59.6
11-Dec-05	272.1	9.0	51.7	13.4	96.7
12-Dec-05	273.8	270.0	267.1	255.1	0.2
13-Dec-05	0.0	0.0	0.0	0.0	100.0

Table 34 – continued from previous page

	Temperature Before (K)		Temperature After (K)		
Date	Maximum	Mean	Maximum	Mean	%Cloud
14-Dec-05	0.0	0.0	0.0	0.0	100.0
15-Dec-05	0.0	0.0	0.0	0.0	100.0
16-Dec-05	274.1	78.4	86.6	62.5	71.1
17-Dec-05	274.7	191.4	247.6	181.8	29.6
18-Dec-05	264.8	213.5	255.9	205.4	18.8
19-Dec-05	266.1	237.2	251.7	214.8	9.9
20-Dec-05	270.6	261.4	263.3	249.7	2.3
21-Dec-05	273.6	212.9	243.8	190.1	21.5
22-Dec-05	272.0	26.6	149.6	43.1	90.2
23-Dec-05	276.6	74.3	165.3	65.8	72.9
24-Dec-05	0.0	0.0	0.0	0.0	100.0
25-Dec-05	0.0	0.0	0.0	0.0	100.0
26-Dec-05	0.0	0.0	0.0	0.0	100.0
27-Dec-05	282.1	279.9	280.9	279.0	0.2
28-Dec-05	0.0	0.0	0.0	0.0	100.0
29-Dec-05	0.0	0.0	0.0	0.0	100.0
30-Dec-05	0.0	0.0	0.0	0.0	100.0
31-Dec-05	0.0	0.0	0.0	0.0	100.0
1-Jan-06	0.0	0.0	0.0	0.0	100.0
2-Jan-06	0.0	0.0	0.0	0.0	100.0
3-Jan-06	0.0	0.0	0.0	0.0	100.0
4-Jan-06	283.2	3.8	118.9	18.8	98.7
5-Jan-06	0.0	0.0	0.0	0.0	100.0
6-Jan-06	0.0	0.0	0.0	0.0	100.0

Table 34 – continued from previous page

	Temperature Before (K)		Temperature After (K)		
Date	Maximum	Mean	Maximum	Mean	%Cloud
7-Jan-06	279.7	275.6	276.5	276.0	0.6
8-Jan-06	0.0	0.0	0.0	0.0	100.0
9-Jan-06	0.0	0.0	0.0	0.0	100.0
10-Jan-06	0.0	0.0	0.0	0.0	100.0
11-Jan-06	0.0	0.0	0.0	0.0	100.0
12-Jan-06	284.8	283.2	283.5	283.1	0.0
13-Jan-06	0.0	0.0	0.0	0.0	100.0
14-Jan-06	0.0	0.0	8.5	2.5	100.0
15-Jan-06	274.8	7.5	57.4	20.4	97.3
16-Jan-06	283.8	277.2	280.4	277.4	1.4
17-Jan-06	0.0	0.0	0.0	0.0	100.0
18-Jan-06	0.0	0.0	0.0	0.0	100.0
19-Jan-06	283.0	175.5	265.3	190.5	37.5
20-Jan-06	0.0	0.0	0.0	0.0	100.0
21-Jan-06	0.0	0.0	37.5	3.5	100.0
22-Jan-06	0.0	0.0	0.0	0.0	100.0
23-Jan-06	282.3	262.3	279.9	239.3	6.4
24-Jan-06	281.2	276.6	279.3	276.1	0.9
25-Jan-06	276.8	4.7	51.9	14.7	98.3
26-Jan-06	281.9	279.5	280.0	279.4	0.0
27-Jan-06	278.0	7.4	111.2	22.4	97.3
28-Jan-06	288.1	45.7	114.6	41.2	84.0
29-Jan-06	0.0	0.0	8.2	0.7	100.0
30-Jan-06	0.0	0.0	0.0	0.0	100.0

Table 34 – continued from previous page

	Temperature Before (K)		Temperature After (K)		
Date	Maximum	Mean	Maximum	Mean	%Cloud
31-Jan-06	0.0	0.0	0.0	0.0	100.0
1-Feb-06	0.0	0.0	0.0	0.0	100.0
2-Feb-06	0.0	0.0	0.0	0.0	100.0
3-Feb-06	0.0	0.0	0.0	0.0	100.0
4-Feb-06	0.0	0.0	0.0	0.0	100.0
5-Feb-06	0.0	0.0	0.0	0.0	100.0
6-Feb-06	275.0	265.4	271.2	262.3	2.5
7-Feb-06	273.6	41.3	151.8	63.9	84.8
8-Feb-06	281.1	55.3	148.4	62.3	80.1
9-Feb-06	0.0	0.0	15.6	1.1	100.0
10-Feb-06	279.0	12.6	74.5	20.7	95.5
11-Feb-06	0.0	0.0	0.2	0.0	100.0
12-Feb-06	0.0	0.0	1.0	0.1	100.0
13-Feb-06	276.1	78.7	130.2	64.0	70.9
14-Feb-06	284.3	257.3	279.5	263.5	8.7
15-Feb-06	0.0	0.0	1.0	0.0	100.0
16-Feb-06	0.0	0.0	0.0	0.0	100.0
17-Feb-06	277.9	1.3	9.0	3.1	99.5
18-Feb-06	0.0	0.0	14.7	2.1	100.0
19-Feb-06	275.7	45.2	103.6	49.2	83.5
20-Feb-06	279.4	252.4	267.2	239.5	8.9
21-Feb-06	0.0	0.0	95.8	21.9	100.0
22-Feb-06	0.0	0.0	1.2	0.1	100.0
23-Feb-06	284.9	282.9	283.4	282.8	0.0

Table 34 – continued from previous page

	Temperature Before (K)		Temperature After (K)		
Date	Maximum	Mean	Maximum	Mean	%Cloud
24-Feb-06	284.5	277.7	279.6	274.1	1.2
25-Feb-06	282.9	265.4	275.5	252.3	5.6
26-Feb-06	283.9	168.9	228.5	172.2	39.8
27-Feb-06	0.0	0.0	7.1	0.7	100.0
28-Feb-06	284.6	2.7	103.6	25.9	99.1
1-Mar-06	0.0	0.0	5.5	0.7	100.0
2-Mar-06	0.0	0.0	40.2	8.5	100.0
3-Mar-06	283.5	1.1	15.3	1.9	99.6
4-Mar-06	286.4	281.9	282.6	279.5	0.9
5-Mar-06	0.0	0.0	0.0	0.0	100.0
6-Mar-06	0.0	0.0	0.0	0.0	100.0
7-Mar-06	286.8	149.9	224.6	160.6	47.2
8-Mar-06	0.0	0.0	0.0	0.0	100.0
9-Mar-06	0.0	0.0	0.0	0.0	100.0
10-Mar-06	0.0	0.0	0.0	0.0	100.0
11-Mar-06	0.0	0.0	3.8	0.3	100.0
12-Mar-06	293.8	17.4	49.7	19.4	94.0
13-Mar-06	0.0	0.0	74.3	13.8	100.0
14-Mar-06	286.7	274.2	282.5	277.6	3.2
15-Mar-06	289.7	285.7	286.6	286.0	0.3
16-Mar-06	287.2	7.0	117.5	25.0	97.5
17-Mar-06	290.3	285.2	286.3	285.6	0.5
18-Mar-06	286.2	283.9	284.2	283.5	0.0
19-Mar-06	290.9	106.5	253.4	122.0	62.8

Table 34 – continued from previous page

	Temperature Before (K)		Temperature After (K)		
Date	Maximum	Mean	Maximum	Mean	%Cloud
20-Mar-06	0.0	0.0	0.0	0.0	100.0
21-Mar-06	0.0	0.0	1.2	0.0	100.0
22-Mar-06	279.5	266.9	273.3	269.6	3.3
23-Mar-06	0.0	0.0	6.9	1.0	100.0
24-Mar-06	0.0	0.0	0.0	0.0	100.0
25-Mar-06	0.0	0.0	8.9	1.1	100.0
26-Mar-06	291.9	214.4	230.4	189.9	25.5
27-Mar-06	282.9	3.2	60.9	13.1	98.9
28-Mar-06	0.0	0.0	0.1	0.0	100.0
29-Mar-06	0.0	0.0	1.1	0.1	100.0
30-Mar-06	299.5	236.6	273.1	237.1	20.0
31-Mar-06	0.0	0.0	2.1	0.2	100.0
1-Apr-06	0.0	0.0	0.0	0.0	100.0
2-Apr-06	0.0	0.0	1.7	0.1	100.0
3-Apr-06	0.0	0.0	0.0	0.0	100.0
4-Apr-06	293.9	289.8	290.8	289.7	0.0
5-Apr-06	295.6	292.1	292.6	291.1	0.0
6-Apr-06	0.0	0.0	0.0	0.0	100.0
7-Apr-06	297.8	277.1	284.0	267.0	5.7
8-Apr-06	291.9	273.0	281.3	264.6	4.9
9-Apr-06	298.3	293.5	294.5	293.4	0.0
10-Apr-06	297.8	186.1	247.7	182.6	36.4
11-Apr-06	292.4	5.2	71.0	27.7	98.2
12-Apr-06	300.1	206.4	265.8	197.1	30.6

Table 34 – continued from previous page

	Temperature Before (K)		Temperature After (K)		
Date	Maximum	Mean	Maximum	Mean	%Cloud
13-Apr-06	308.0	262.4	291.0	262.3	13.4
14-Apr-06	0.0	0.0	0.0	0.0	100.0
15-Apr-06	304.5	126.1	228.8	136.2	58.0
16-Apr-06	301.1	132.8	283.8	156.0	55.4
17-Apr-06	0.0	0.0	103.5	14.4	100.0
18-Apr-06	303.8	298.0	299.3	297.8	0.0
19-Apr-06	302.8	297.9	298.8	297.8	0.0
20-Apr-06	0.0	0.0	0.0	0.0	100.0
21-Apr-06	0.0	0.0	0.0	0.0	100.0
22-Apr-06	307.3	271.2	293.2	269.8	9.8
23-Apr-06	303.7	297.2	299.4	297.4	0.7
24-Apr-06	301.9	204.5	256.0	208.5	30.8
25-Apr-06	0.0	0.0	0.0	0.0	100.0
26-Apr-06	294.8	277.2	286.8	279.1	4.6
27-Apr-06	304.8	289.2	297.8	289.1	3.4
28-Apr-06	302.8	299.0	300.4	298.8	0.0
29-Apr-06	0.0	0.0	0.0	0.0	100.0
30-Apr-06	0.0	0.0	0.0	0.0	100.0
1-May-06	0.0	0.0	0.2	0.0	100.0
2-May-06	296.7	76.5	116.2	72.8	73.9
3-May-06	0.0	0.0	0.5	0.0	100.0
4-May-06	295.5	4.2	44.7	11.4	98.6
5-May-06	299.7	72.2	206.9	100.1	75.5
6-May-06	305.1	287.7	295.0	282.9	3.6

Table 34 – continued from previous page

	Temperature Before (K)		Temperature After (K)		
Date	Maximum	Mean	Maximum	Mean	%Cloud
7-May-06	299.1	126.6	236.9	133.8	56.6
8-May-06	306.0	193.1	266.4	169.9	35.5
9-May-06	0.0	0.0	1.6	0.1	100.0
10-May-06	0.0	0.0	0.0	0.0	100.0
11-May-06	0.0	0.0	0.0	0.0	100.0
12-May-06	0.0	0.0	0.0	0.0	100.0
13-May-06	0.0	0.0	0.0	0.0	100.0
15-May-06	0.0	0.0	0.0	0.0	100.0
16-May-06	0.0	0.0	0.2	0.0	100.0
17-May-06	301.7	226.0	289.3	223.3	24.0
18-May-06	0.0	0.0	60.0	8.8	100.0
19-May-06	300.3	258.3	293.3	237.2	12.5
20-May-06	308.1	299.6	301.1	299.3	0.0
21-May-06	298.6	162.6	279.6	166.5	44.6
22-May-06	306.6	235.1	280.4	237.4	21.5
23-May-06	306.1	299.4	301.3	299.1	0.6
24-May-06	0.0	0.0	2.3	0.3	100.0
25-May-06	300.5	34.4	180.1	53.0	88.4
26-May-06	301.2	15.8	30.9	20.1	94.7
27-May-06	0.0	0.0	0.0	0.0	100.0
28-May-06	301.8	10.0	160.2	33.2	96.7
29-May-06	315.1	261.0	303.0	267.6	15.6
30-May-06	291.3	7.3	39.2	14.1	97.4
31-May-06	306.5	15.0	135.0	30.7	95.1

Table 34 – continued from previous page

	Temperature Before (K)		Temperature After (K)		
Date	Maximum	Mean	Maximum	Mean	%Cloud
1-Jun-06	0.0	0.0	6.7	0.8	100.0
2-Jun-06	0.0	0.0	0.0	0.0	100.0
3-Jun-06	310.2	300.0	303.5	300.7	0.8
4-Jun-06	307.4	284.1	292.3	280.4	5.3
5-Jun-06	312.7	298.7	304.9	297.4	1.9
6-Jun-06	309.4	221.2	279.0	218.1	27.0
7-Jun-06	304.5	39.5	82.4	43.5	86.8
8-Jun-06	0.0	0.0	22.9	3.9	100.0
9-Jun-06	0.0	0.0	3.3	0.3	100.0
10-Jun-06	0.0	0.0	0.0	0.0	100.0
11-Jun-06	0.0	0.0	0.0	0.0	100.0
12-Jun-06	302.8	148.0	196.6	159.1	50.3
13-Jun-06	302.3	92.0	179.5	120.5	68.8
14-Jun-06	313.0	298.1	305.6	298.3	2.5
15-Jun-06	301.0	103.4	263.0	127.9	65.4
16-Jun-06	310.0	49.0	170.1	64.7	83.8
17-Jun-06	0.0	0.0	10.5	2.3	100.0
18-Jun-06	0.0	0.0	0.0	0.0	100.0
19-Jun-06	305.7	202.3	291.0	192.8	33.0
20-Jun-06	0.0	0.0	0.0	0.0	100.0
21-Jun-06	307.8	29.8	138.6	62.5	90.2
22-Jun-06	302.8	43.6	178.2	68.6	85.5
23-Jun-06	0.0	0.0	0.0	0.0	100.0
24-Jun-06	304.7	240.5	298.8	232.0	20.2

Table 34 – continued from previous page

	Temperature Before (K)		Temperature After (K)		
Date	Maximum	Mean	Maximum	Mean	%Cloud
25-Jun-06	310.9	225.3	277.0	195.4	25.9
26-Jun-06	296.3	8.7	147.7	46.2	97.1
27-Jun-06	306.9	252.4	289.5	242.9	16.3
28-Jun-06	310.3	278.6	299.7	276.8	8.0
29-Jun-06	302.9	138.5	244.5	174.8	53.5
30-Jun-06	313.2	280.9	302.6	275.4	7.7
1-Jul-06	300.9	65.4	168.3	76.3	78.0
2-Jul-06	312.0	118.2	271.5	137.8	61.2
3-Jul-06	303.8	97.1	268.8	120.5	67.8
4-Jul-06	0.0	0.0	0.3	0.0	100.0
5-Jul-06	308.5	300.5	302.5	300.3	0.1
6-Jul-06	310.3	299.7	302.2	300.5	0.9
7-Jul-06	313.5	304.5	306.3	304.2	0.1
8-Jul-06	306.8	301.2	301.7	300.5	0.0
9-Jul-06	312.5	186.3	282.9	189.0	38.9
10-Jul-06	0.0	0.0	85.2	15.7	100.0
11-Jul-06	0.0	0.0	0.0	0.0	100.0
12-Jul-06	0.0	0.0	0.0	0.0	100.0
13-Jul-06	301.5	39.4	120.0	57.2	86.8
14-Jul-06	0.0	0.0	7.9	0.5	100.0
15-Jul-06	312.8	304.3	305.4	304.0	0.3
16-Jul-06	317.2	260.7	291.1	256.2	14.5
17-Jul-06	307.9	286.1	301.0	287.4	5.7
18-Jul-06	311.1	191.2	285.7	191.0	37.2

Table 34 – continued from previous page

	Temperature Before (K)		Temperature After (K)		
Date	Maximum	Mean	Maximum	Mean	%Cloud
19-Jul-06	310.7	295.7	302.4	297.3	2.9
20-Jul-06	0.0	0.0	0.0	0.0	100.0
21-Jul-06	0.0	0.0	3.8	0.1	100.0
22-Jul-06	301.7	115.7	215.6	121.5	61.0
23-Jul-06	311.0	300.7	300.8	299.8	0.7
24-Jul-06	304.5	248.2	295.6	256.0	17.0
25-Jul-06	312.8	291.9	302.7	275.5	4.2
26-Jul-06	0.0	0.0	0.0	0.0	100.0
27-Jul-06	297.5	5.6	10.4	3.8	98.1
28-Jul-06	303.1	96.3	185.7	113.1	67.8
29-Jul-06	304.5	6.6	69.5	14.5	97.8
30-Jul-06	309.2	219.7	292.1	228.0	27.6
31-Jul-06	303.5	143.7	267.7	159.3	52.3
1-Aug-06	313.5	291.8	300.0	292.9	4.5
2-Aug-06	305.3	241.3	297.1	252.7	20.0
3-Aug-06	0.0	0.0	0.0	0.0	100.0
4-Aug-06	311.3	302.1	305.2	302.0	0.2
5-Aug-06	313.2	296.6	302.9	298.1	1.6
6-Aug-06	309.9	126.3	265.3	152.5	58.0
7-Aug-06	0.0	0.0	58.2	5.0	100.0
8-Aug-06	300.0	3.9	55.9	9.7	98.7
9-Aug-06	0.0	0.0	0.0	0.0	100.0
10-Aug-06	0.0	0.0	0.0	0.0	100.0
11-Aug-06	0.0	0.0	0.3	0.0	100.0

Table 34 – continued from previous page

	Temperature Before (K)		Temperature After (K)		
Date	Maximum	Mean	Maximum	Mean	%Cloud
12-Aug-06	311.2	301.1	303.5	301.1	0.4
13-Aug-06	309.6	295.4	299.7	285.7	2.3
14-Aug-06	0.0	0.0	0.0	0.0	100.0
15-Aug-06	311.3	302.9	305.1	302.5	0.0
16-Aug-06	309.5	294.4	302.7	292.5	2.5
17-Aug-06	293.8	1.9	46.2	10.4	99.3
18-Aug-06	0.0	0.0	0.0	0.0	100.0
19-Aug-06	303.9	158.6	221.6	151.6	47.2
20-Aug-06	309.2	301.5	303.2	300.9	0.0
21-Aug-06	312.5	172.5	282.6	205.0	42.9
22-Aug-06	0.0	0.0	0.0	0.0	100.0
23-Aug-06	0.0	0.0	0.0	0.0	100.0
24-Aug-06	297.0	13.3	144.6	24.3	95.5
25-Aug-06	296.7	66.1	193.2	74.1	77.6
26-Aug-06	0.0	0.0	31.7	2.9	100.0
27-Aug-06	0.0	0.0	1.8	0.2	100.0
28-Aug-06	0.0	0.0	0.4	0.0	100.0
29-Aug-06	0.0	0.0	0.0	0.0	100.0
30-Aug-06	300.5	21.4	57.4	27.4	92.8
31-Aug-06	0.0	0.0	0.0	0.0	100.0
1-Sep-06	0.0	0.0	0.0	0.0	100.0
2-Sep-06	299.4	52.7	130.4	49.7	82.1
3-Sep-06	301.7	277.8	293.9	275.4	5.9
4-Sep-06	0.0	0.0	0.0	0.0	100.0

Table 34 – continued from previous page

	Temperature Before (K)		Temperature After (K)		
Date	Maximum	Mean	Maximum	Mean	%Cloud
5-Sep-06	300.5	88.1	105.0	67.8	70.2
6-Sep-06	307.5	299.8	301.8	299.4	0.2
7-Sep-06	307.3	296.3	297.3	293.1	1.4
8-Sep-06	305.2	291.4	298.7	294.0	2.9
9-Sep-06	308.9	301.8	303.4	301.2	0.2
10-Sep-06	300.6	258.8	295.6	253.0	12.9
11-Sep-06	304.9	90.9	149.1	97.6	69.5
12-Sep-06	0.0	0.0	0.0	0.0	100.0
13-Sep-06	292.5	10.8	18.1	7.8	96.3
14-Sep-06	296.7	65.8	130.3	62.4	77.6
15-Sep-06	304.7	298.9	298.6	296.5	0.1
16-Sep-06	295.8	28.7	202.7	64.0	90.2
17-Sep-06	301.7	121.3	253.3	131.4	59.5
18-Sep-06	0.0	0.0	0.8	0.1	100.0
19-Sep-06	0.0	0.0	53.2	6.2	100.0
20-Sep-06	298.7	128.6	181.9	118.5	55.9
21-Sep-06	295.7	272.2	289.1	264.0	6.7
22-Sep-06	0.0	0.0	0.0	0.0	100.0
23-Sep-06	0.0	0.0	0.0	0.0	100.0
24-Sep-06	291.5	1.1	40.7	4.6	99.6
25-Sep-06	300.8	296.1	297.0	295.9	0.1
26-Sep-06	299.9	295.0	296.2	293.4	0.5
27-Sep-06	303.7	299.0	299.8	298.8	0.0
28-Sep-06	289.2	57.6	113.6	49.0	79.9

Table 34 – continued from previous page

	Temperature Before (K)		Temperature After (K)		
Date	Maximum	Mean	Maximum	Mean	%Cloud
29-Sep-06	297.0	256.9	290.5	250.4	12.2
30-Sep-06	296.1	151.4	210.7	138.8	48.3
1-Oct-06	302.1	297.1	298.2	297.5	0.4
2-Oct-06	302.6	237.8	296.0	254.8	20.2
3-Oct-06	297.8	51.7	121.3	50.1	82.4
4-Oct-06	303.8	183.6	258.1	172.1	38.7
5-Oct-06	0.0	0.0	0.0	0.0	100.0
6-Oct-06	296.4	292.4	293.1	292.2	0.0
7-Oct-06	298.3	295.3	295.6	295.0	0.0
8-Oct-06	301.5	296.8	297.6	296.6	0.2
9-Oct-06	301.3	246.0	287.5	243.5	17.0
10-Oct-06	299.2	61.7	190.9	62.9	79.2
11-Oct-06	286.4	15.5	31.0	14.9	94.2
12-Oct-06	280.4	50.9	76.8	51.8	81.6
13-Oct-06	288.9	286.1	286.5	285.9	0.0
14-Oct-06	289.8	287.6	287.8	287.5	0.0
15-Oct-06	0.0	0.0	1.2	0.1	100.0
16-Oct-06	0.0	0.0	0.0	0.0	100.0
17-Oct-06	292.7	14.1	83.2	25.9	95.2
18-Oct-06	0.0	0.0	2.7	0.4	100.0
19-Oct-06	0.0	0.0	0.0	0.0	100.0
20-Oct-06	284.7	5.6	70.8	20.7	98.0
21-Oct-06	289.8	180.2	244.7	189.7	37.4
22-Oct-06	0.0	0.0	0.0	0.0	100.0

Table 34 – continued from previous page

	Temperature Before (K)		Temperature After (K)		
Date	Maximum	Mean	Maximum	Mean	%Cloud
23-Oct-06	0.0	0.0	7.3	0.9	100.0
24-Oct-06	288.5	240.3	254.4	228.7	15.6
25-Oct-06	289.2	125.7	241.5	130.3	56.2
26-Oct-06	0.0	0.0	0.0	0.0	100.0
27-Oct-06	0.0	0.0	0.0	0.0	100.0
28-Oct-06	285.2	282.6	282.6	281.6	0.1
29-Oct-06	291.0	288.3	288.6	288.2	0.0
30-Oct-06	288.9	16.8	105.7	36.7	94.1
31-Oct-06	0.0	0.0	0.0	0.0	100.0
1-Nov-06	0.0	0.0	0.0	0.0	100.0
2-Nov-06	282.7	259.1	272.2	260.6	7.6
3-Nov-06	284.1	280.8	281.3	280.9	0.2
4-Nov-06	0.0	0.0	0.4	0.0	100.0
5-Nov-06	0.0	0.0	6.0	1.0	100.0
6-Nov-06	0.0	0.0	0.0	0.0	100.0
7-Nov-06	0.0	0.0	0.0	0.0	100.0
8-Nov-06	0.0	0.0	0.0	0.0	100.0
9-Nov-06	293.6	286.4	289.9	285.7	1.7
10-Nov-06	293.2	60.2	128.4	75.2	79.3
11-Nov-06	0.0	0.0	0.0	0.0	100.0
12-Nov-06	0.0	0.0	0.6	0.0	100.0
13-Nov-06	0.0	0.0	0.0	0.0	100.0
14-Nov-06	280.7	1.1	2.0	0.9	99.6
15-Nov-06	0.0	0.0	0.0	0.0	100.0

Table 34 – continued from previous page

	Temperature Before (K)		Temperature After (K)		
Date	Maximum	Mean	Maximum	Mean	%Cloud
16-Nov-06	0.0	0.0	0.0	0.0	100.0
17-Nov-06	0.0	0.0	0.0	0.0	100.0
18-Nov-06	284.6	166.3	208.9	154.5	41.2
19-Nov-06	0.0	0.0	0.0	0.0	100.0
20-Nov-06	282.0	196.6	256.7	201.6	29.9
21-Nov-06	284.3	273.0	274.8	257.6	3.2
22-Nov-06	285.3	283.1	284.0	282.9	0.3
23-Nov-06	287.3	285.2	285.4	284.7	0.0
24-Nov-06	288.7	286.4	287.9	286.6	0.2
25-Nov-06	284.6	1.1	38.8	8.3	99.6
26-Nov-06	0.0	0.0	0.0	0.0	100.0
27-Nov-06	0.0	0.0	0.0	0.0	100.0
28-Nov-06	289.0	34.2	48.8	27.1	88.1
29-Nov-06	0.0	0.0	0.0	0.0	100.0
30-Nov-06	0.0	0.0	2.9	0.5	100.0
1-Dec-06	0.0	0.0	0.0	0.0	100.0
2-Dec-06	278.9	135.9	223.0	129.2	50.9
3-Dec-06	0.0	0.0	2.8	0.4	100.0
4-Dec-06	272.7	4.6	7.6	4.4	98.3
5-Dec-06	276.3	232.6	241.5	220.4	15.3
6-Dec-06	0.0	0.0	0.8	0.0	100.0
7-Dec-06	271.4	1.8	16.9	4.9	99.3
8-Dec-06	271.7	211.4	257.7	202.9	21.8
9-Dec-06	278.2	229.0	245.8	212.6	17.1

Table 34 – continued from previous page

	Temperature Before (K)		Temperature After (K)		
Date	Maximum	Mean	Maximum	Mean	%Cloud
10-Dec-06	282.7	273.7	276.8	264.4	2.7
11-Dec-06	0.0	0.0	0.0	0.0	100.0
12-Dec-06	0.0	0.0	0.0	0.0	100.0
13-Dec-06	283.9	232.1	257.0	234.1	17.8
14-Dec-06	282.3	22.3	164.6	40.2	92.0
15-Dec-06	282.8	272.1	276.7	260.6	3.3
16-Dec-06	0.0	0.0	0.0	0.0	100.0